The Role of Non-Classical Monocytes and the CX3CL1/CX3CR1 Axis in the Immune Response to Myocardial Ischemia-Reperfusion

Sarah Alice Marsh

Thesis Submitted for the Degree of

Doctor of Philosophy

Institute of Genetic Medicine
Faculty of Medical Sciences
Newcastle University

May 2020

Contents

List of Figures

List of Tables

List of Abbreviations

ACE : Angiotensin Converting Enzyme

ACS : Acute Coronary Syndrome

ADAM10/17 : A Disintegrin And Metalloproteinase domain-containing protein 10/17

Angina Pectoris : AP

BAFF : B-Cell Activating Factor

Bcl-2 : B-cell lymphoma 2

Bcl-XL : B-cell lymphoma-extra large

BCR : B-Cell Receptor

CAD : Coronary Artery Disease

CK-MB : Creatine Kinase Myocardial Band

cMoP : common monocyte progenitor

cTn : Cardiac Troponin

DAMP : Damage-Associated Molecular Pattern

DC : dendritic cell

ECG : Electrocardiogram

ECM : extracellular matrix

EGFR : Epidermal Growth Factor Receptor

ESGL-1 : E-Selectin Glycoprotein Ligand-1

GlyCam-1 : Glycosylation-dependent Cell-adhesion Molecule-1

Hif1α : hypoxia-inducible factor-1α

HMGB1 : High Mobility Group Box 1

HPSC : Haematopoietic Stem Cell

ICAM-1 : Intercellular Adhesion Molecule 1

ICAM-2 : Intracellular Adhesion Molecule 2

IkB : inhibitor of κB

IL-10 : Interleukin 10

IL-1α : Interleukin 1 alpha

IL-1β : Interleukin 1 Beta

IL-6 : Interleukin 6

IL-8 : Interleukin 8

LAD : Left Anterior Descending coronary artery

LCA : Left Coronary Artery

LFA-1 : lymphocyte function antigen-1

LV : Left Ventricle

LVEF : Left Ventricular Ejection Fraction

MAC : Membrane Attack Complex

MI : Myocardial Infarction

MM6 : MonoMac6

MPTP : Mitochondrial Permeability Transition Pore

MRI : Magnetic Resonance Imaging

MVO : Microvascular Obstruction

NEMO : NFκB Essential Modulator

NFκB : nuclear factor kappa-light-chain-enhancer of activated B cells

NSTEMI : Non-ST-Elevation Myocardial Infarction

PECAM : Platelet/Endothelial Cell Adhesion Molecule 1

PI3K : phosphoinositide 3-kinase

PPCI : Primary Percutaneous Coronary Intervention

PSGL-1 : P-Selectin Glycoprotein Ligand-1

RANKL : Receptor Activator of NFκB Ligand

RCA : Right Coronary Artery

RhoA : Ras homolog gene family member A

ROS : Reactive Oxygen Species

SNS : Sympathetic Nervous System

STEMI : ST-Elevation Myocardial Infarction

TAD : Transactivation Domain

TAK-1 : Transforming growth factor beta-Activated Kinase 1

TCR : T-Cell Receptor

TGF-β : Transforming Growth Factor Beta

TLR : Toll-Like Receptor

TNF-α : tumor necrosis factor alpha

VCAM-1 : Vascular Cell Adhesion Protein 1

VLA-4 : Very Late Antigen 4

α-SMA : alpha-smooth muscle actin

Abstract

Myocardial Infarction is a leading cause of morbidity and mortality worldwide. Over the past decade, STEMI patient prognosis has improved in line with the increased clinical use of reperfusion therapy by primary percutaneous coronary intervention. Despite advances in treatment however, the mortality rate following STEMI remains up to 43.1%, due to a range of short and long term complications. Novel treatment options are therefore required to improve outcome following MI.

In the immune response to MI, monocytes are rapidly recruited to the injured tissue where they contribute to the inflammatory milieu. While the function of classical monocytes in this response has been well described, the role of the non-classical monocyte subset is poorly defined. These cells express high levels of the fractalkine receptor, CX3CR1, which has increasingly been implicated in cardiac ischemia-reperfusion (I/R) injury. Expression of the fractalkine ligand, CX3CL1, also known as Fractalkine (FKN) is elevated in mouse models of MI, and neutralization of the ligand leads to improved survival. Similarly, in MI and heart failure patients, plasma levels of the soluble form of CX3CL1 are increased. The aim of this project was therefore to investigate non-classical monocyte behaviour and function following cardiac I/R, with relation to CX3CR1 expression, in both STEMI patients and a mouse model of cardiac I/R. The research presented in this thesis describes the distinct dynamics of $CX3CR1^{hi}$ non-classical monocytes in STEMI patients immediately following reperfusion. These cells show an increased depletion in patients with larger infarcts and lower left ventricular ejection fraction, thereby acting as a potential prognostic biomarker of myocardial outcome. In complementary pre-clinical mouse studies of cardiac I/R, this project established that monocyte adherence in the coronary vessel endothelium occurs over a post-reperfusion timeframe which corresponds approximately to the 90 min post-reperfusion drop in circulating non-classical monocytes in STEMI patients. Investigation of CX3CR1 function using a *Cx3cr1* knockout mouse demonstrated that infarct-triggered monocyte recruitment and later decrease in myocardial function are not significantly affected by loss of the *Cx3cr1* gene. Research into the signalling pathways downstream of CX3CR1 activation identified the pro-inflammatory NFκB pathway as a possible contributor to non-classical monocyte function. Based on this

study, the CX3CL1/CX3CR1 axis appears to have an important role in mediating the acute post-reperfusion dynamics and function of circulating non-classical monocytes following human cardiac I/R. Unexpectedly, however, loss of *Cx3cr1* in pre-clinical mouse models does not appear to compromise intra-myocardial monocyte recruitment or heart function following cardiac I/R.

Acknowledgements

I would firstly like to thank the MRC for funding me to conduct this research through a prestigious DiMeN DTP MRC grant.

I would like to express my sincere gratitude to my two supervisors Professor Helen Arthur and Professor Simi Ali, who gave me the opportunity to carry out this research. I would like to thank Helen for providing her valuable expertise in the field of Cardiovascular Research whilst also being a highly attentive supervisor that has guided me throughout this project. I would like to equally thank Simi for her continued support and encouragement not only throughout this PhD project but also extending over the past 6 years back to my undergraduate research project. My experience with Simi sparked both inspiration and confidence to pursue a PhD in the field of Immunology. The clinical component of this thesis would not have been possible without the involvement and expertise of Professor Ioakim Spyridopoulos. I would therefore like to express sincere thanks to Kim for allowing me to carry out this clinical work, as well as providing positive and motivational words of wisdom throughout. I would like to thank Steve Boag for collecting the retrospective data presented in this work, and the Freeman Hospital for permitting the prospective study. I would like to thank past and present members of the HMA lab. In particular, a huge appreciation to Dr. Rachael Redgrave whose work as a heart microsurgeon was integral for generating a considerable amount of the data presented here. I would also like to thank Dr. Esha Singh who has taught me a valuable knowledge and skill of microscopy to study the heart. I would like to thank Dr. Catherine Park for her valuable contribution to the final chapter of this research. The time and patience that she kindly spent in teaching me her knowledge and skills of protein and gene expression analysis is hugely appreciated. I would also like to thank PhD student Lilia for her contribution to the mouse cardiac I/R work. My gratitude extends to all other individuals that have made this work possible, including the FCCF facility and the IGM staff.

Above all I would like to thank my family and friends for their unconditional love, encouragement and support over the past 3.5 years. You have kept me sane throughout the most challenging journey!

Chapter 1.0. Introduction

1.1 Myocardial Infarction

1.1.1 Coronary Artery Disease & Atherosclerosis

Coronary Artery Disease (CAD) is a chronic inflammatory disease, characterized by remodeling and narrowing of the coronary arteries supplying oxygen and nutrients to the heart tissue. The predominant cause of CAD is atherosclerosis, a progressive chronic inflammatory condition driven by an interplay of genetic and environmental factors [1, 2]. The atherosclerotic process begins with the development of a lipid-rich atherosclerotic lesion known as the fatty streak, in which high numbers of extracellular lipids and lipid-laden macrophages (foam cells), occupy the sub-endothelial space, which is capped by fibrous connective tissue [3]. Thereafter, an inflammatory response occurs, which is characterized by the recruitment and accumulation of other leukocytes including lymphocytes and mast cells in the sub-endothelial space. Interaction between monocytes, macrophages, foam cells, and T-cells initiates a cellular and humoral immune response, leading to a chronic inflammatory state and the release of pro-inflammatory mediators and growth factors. This drives further leukocyte recruitment and the migration of smooth muscle cells from the medial layer of the artery into the intima, leading to a transition from a fatty streak to a more complex lesion. Smooth muscle cells present in the intima media produce extracellular matrix molecules, creating a fibrous cap that covers the lesion. Foam cells inside the fibrous cap die and release lipids that accumulate in the extracellular space, forming a lipid-rich pool within the necrotic core. The result of this process is formation of the second atherosclerotic lesion known as the fibrous plaque [4, 5]. Two types of plaque, stable and unstable, are defined, depending on the balance between the formation and degradation of the fibrous cap [6]. Stable plaques have an intact, thick fibrous cap composed of smooth muscle cells in a matrix rich in type I and III collagen. Protrusion of a stable plaque into the lumen of the artery produces flow-limiting stenosis, leading to tissue ischemia and usually stable angina [7].

1.1.2 Myocardial Infarction

While stable atherosclerotic plaques usually manifest as stable angina, myocardial infarction arises from an unstable, vulnerable plaque. Such lesions possess a much thinner fibrous cap made mostly of type I collagen and few or no smooth muscle cells, with abundant macrophages and proinflammatory and pro-thrombotic molecules. These plaques are more prone to erosion or rupture, exposing the core of the plaque to circulating coagulation proteins, causing thrombosis, sudden occlusion of the artery lumen, and a resulting myocardial infarction (MI) [8, 9]. MI is defined as myocardial death due to prolonged ischaemia, and the extent of necrosis is dependent upon the location and size of the affected artery, duration of coronary occlusion, the presence of collateral flow, and the integrity of the fibrinolytic system [10]. Depending on these factors, the same pathological process leads to one of three clinical outcomes; ST-elevation myocardial infarction (STEMI), non-ST elevation myocardial infarction (NSTEMI), and unstable angina (UA), collectively termed Acute Coronary Syndromes (ACS).

1.1.3 Myocardial Infarction Diagnosis & Classification

Diagnosis of STEMI and NSTEMI involves the clinical assessment of a range of markers including electrocardiogram (ECG), elevated levels of the biomarkers cardiac troponin (cTn) or creatine kinase myocardial band (CK-MB), echocardiogram, and a range of imaging techniques including magnetic resonance imaging (MRI) [11]. Elevated levels of blood cTn or CK-MB reflect myocardial injury and the subsequent necrosis of myocardial cells [12-14]. Although these markers do not explain the underlying mechanism, cTn (I or T) is highly specific to myocardial tissue and demonstrates high clinical sensitivity. Patients without such elevated biomarker values in the blood hours after the initial onset of ischemic chest pain are diagnosed with UA [15]. Differential diagnosis of STEMI or NSTEMI is made on the basis of ST segment elevation observed on an ECG at presentation, which is crucial for deciding immediate treatment strategies such as reperfusion therapy [11]. In the context of MI, ST segment elevation is usually indicative of complete occlusion of the infarct related artery, and

therefore requires rapid intervention to open the occluded vessel (reperfusion therapy), unlike NSTEMI, where reperfusion is less urgent.

1.1.4 Treatment of Myocardial Infarction

The predominant aims of MI treatment are to re-establish myocardial perfusion, minimize the myocardial damage sustained, and prevent subsequent complications. The therapeutic management of MI is tailored to the patient's final diagnosis. Given the differences in the underlying pathophysiology, different treatment strategies are adopted for STEMI, NSTEMI, and UA. In STEMI patients, there is usually total occlusion of the infarct-related artery, and therefore requires immediate reperfusion therapy to retrieve normal coronary blood flow and minimize acute ischemic myocardial injury. Primary percutaneous coronary intervention (PPCI) and thrombolysis are two commonly used reperfusion strategies, both of which must be administered promptly and effectively after the onset of acute MI to salvage myocardium, limit MI size, preserve left ventricular systolic function, and prevent long term development of heart failure and therefore reduce mortality [16]. The importance of PPCI in salvaging myocardial tissue is illustrated in Figure 1.1. Critically, longer intervals between the onset of STEMI patient symptoms such as chest pain, and complete restoration of coronary reperfusion, known as the 'onset-to-balloon time', have been shown to correlate directly with mortality and morbidity in STEMI patients [17]. While thrombolysis can be administered quickly and performed relatively easily, PPCI is superior at reducing mortality and major cardiovascular events, achieving effective reperfusion in over 90-95% of cases, and is therefore the current gold-standard method for treating acute STEMI providing it can be performed expeditiously [18, 19]. European guidelines recommend PPCI over thrombolytic therapy in all patients wherever possible, within a 90 minute interval between the first qualified medical contact and the procedure, known as the 'door-to-balloon' interval [20].

During PPCI, the infarct related artery is directly opened through a procedure known as angioplasty, to restore blood flow to the myocardium. A catheter is firstly inserted through a small puncture in either the radial or femoral artery, and advanced over a guide wire into the coronary artery and past the occlusion. Once the catheter has

engaged in the coronary ostium and diagnostic angiograms have been obtained, weight-based IV anti-coagulants such as unfractionated heparin, bivalirudin, or low-molecular-weight heparin therapy may be administered to prevent any blood clotting [21]. To open the blocked artery, a wire mounted balloon is then threaded over this wire and inflated at the site of occlusion for pre-dilation of the vessel. In the majority of cases, a metallic stent of appropriate length is deployed, and expanded with the balloon to help maintain vessel patency [22].

Anti-ischemic therapies including Nitroglycerin and β-blockers are routinely used in MI patients to reduce oxygen demand or increase oxygen supply [23]. Nitroglycerin is a vasodilator that reduces myocardial oxygen demand by decreasing ventricular preload via venodilation, and enhances myocardial oxygen delivery by dilating large coronary arteries and improving collateral flow to ischemic areas. β-blockers inhibit β1-adrenergic receptors in the myocardium and decrease myocardial contractility and heart rate, thereby reducing myocardial oxygen demand.

1.1.5 Myocardial Reperfusion Injury

Following the onset of acute MI, timely and effective reperfusion therapy using either PPCI or thrombolytic therapy is effective at reducing acute myocardial ischemic injury, salvaging viable myocardium, limiting MI size, preserving LV systolic function, and preventing heart failure. Reperfusion therapy has therefore significantly improved clinical outcome and patient survival following acute MI [24, 25]. However, this process of reperfusion itself can independently induce cardiomyocyte death, by a process known as ischaemia reperfusion (I/R) injury [26, 27]. This is believed to be a result of free radicals, calcium build-up, acidosis, inflammation and accumulation of neutrophils, all of which accumulate to the opening of the mitochondrial permeability transition pore (MPTP) [24, 27]. Dying cardiomyocytes also release Damage-associated molecular patterns (DAMP)s following myocardial injury which activate the immune response and contribute to reperfusion injury.

Four major components of myocardial I/R injury are recognised; reperfusion arrhythmias, myocardial stunning, microvascular obstruction (MVO), and lethal

myocardial ischemia reperfusion injury. The first two of these are transient and reversible, in contrast to the latter two which are irreversible and contribute up to 50% of the final infarct size (Figure 1.1) [24, 27, 28]. Historical efforts to therapeutically target myocardial reperfusion injury have proved disappointing to date, and the varying susceptibility of an individual to reperfusion injury alongside the narrow window of opportunity in which to intervene, adds to the complexity of this process. Despite this, more recent studies using a variety of novel treatments have shown promise in proof-of-concept trials to minimize the impact of reperfusion injury, and clinical trials are currently underway to investigate the effects of these strategies on clinical outcomes in PPCI patients [24, 29-32].

1.1.6 Clinical Outcomes of MI

Acute MI and its accompanying adverse sequelae remains one of the greatest causes of morbidity and mortality worldwide. Despite advances in treatment, the UK reports one heart attack occurring every three minutes, and over half a million individuals being diagnosed with subsequent heart failure [33]. Progression to heart failure after MI is multifactorial, depending on the extent of myocardial damage at the time of MI, recurrent myocardial ischemia, infarct size, ventricular remodelling, stunned myocardium, MVO, and mechanical complications [34, 35]. Aside from the loss of myocardial tissue directly damaged during the initial insult of acute MI, one of the most critical complications of MI and prevailing cause of heart failure is adverse left ventricular remodelling [36]. Immediately post-myocardial infarction, the heart undergoes remodelling to attempt to maintain cardiac function and output. In around 30% of cases, dependent on infarct size, this remodelling process is maladaptive, causing a further decline in cardiac function. Such patients are at the greatest risk of symptomatic heart failure or sudden death due to lethal arrhythmia [37]. Multiple major mechanisms contribute to adverse left ventricular remodelling including early sub-acute phase infarct expansion, subsequent infarct extension into adjacent non-infarcted myocardium, late chronic phase hypertrophy and dilatation in the remote myocardium, and scar formation. Left ventricular dysfunction is the strongest predictor of mortality following STEMI, and approximately 40% of MI patients will develop left ventricular systolic dysfunction, with or without subsequent clinical heart failure [38].

Many of the therapies targeting the prevention of heart failure are therefore designed to attenuate the adverse remodelling process. While there is no approved treatment for preventing adverse remodelling follow MI [39], increasing evidence supports the use of both Angiotensin converting enzyme (ACE) inhibitors and β-adrenergic blockers to inhibit progressive LV remodelling and improve clinical outcome in MI [40, 41]. Arrhythmic complications are another deleterious consequence of acute MI, commonly including bradycardia, and supraventricular and ventricular tachycardia [42]. Studies continue to report that the majority of acute MI patients are complicated by cardiac arrhythmias [43, 44]. Atrial fibrillation is frequently associated with severe left ventricle (LV) damage and heart failure, and requires prompt treatment using direct current cardioversion [45].

1.1.7 Therapeutic Targeting of Myocardial Ischemia-Reperfusion Injury

Currently, the treatment of myocardial ischemia reperfusion injury is primarily supportive, as no specific target-oriented therapy has been validated so far. Therapeutic approaches to protect against myocardial ischemia-reperfusion injury however remain an active area of investigation given the detrimental effects of this phenomenon. Despite a significant amount of research as well as encouraging preclinical results with multiple agents, most of the clinical trials to prevent reperfusion injury have been disappointing [46].

Various studies have shown that damage caused by myocardial ischemia-reperfusion can be prevented or limited by non-pharmacological strategies [47], such as ischemic pre-conditioning [48, 49], ischemic post-conditioning, and remote ischemic conditioning [50-52], as well as hyperthermia [53], though none of these strategies have translated into routine clinical practice.

A number of promising pharmalogical agents to protect from myocardial I/R injury have also been described. Na+/H+ exchange inhibitors including Cariporide and SM-20550 demonstrate an attenuation of I/R injury as determined by improved LV function, reduced infarct size, and minimized myocardial remodelling [54-56]. The rationale behind these agents is to prevent the build-up of intracellular calcium resulting from

inhibition of Na+/K+-ATPase and by the hyperactivation of Na+/H+ exchanger in cardiomyocytes during ischemia and reperfusion. Atrial natriuretic peptide (ANP) and phosphodiesterase 5 (PDE5) inhibitors have also shown beneficial effects in preventing myocardial ischemia reperfusion injury; clinical studies of PDE5 inhibitors appear to act similar to cardiac pre-conditioning [57], while administration of ANP intravenously at the time of reperfusion reduces infarct size and improves ventricular function in porcine models [58]. A large number of clinical trials have also investigated the effect of Glucose-insulin-potassium (GIK) therapy which demonstrate that this approach may be more effective at reducing infarct size when administered to STEMI patients in the ambulance prior to reperfusion [59]. Through its function as an insulinotropic incretin, the Glucagon-like peptide-1 (GLP-1) receptor agonist known as Exenatide offers protection during I/R, which has now been translated into the clinical setting whereby Exenatide is administered during reperfusion [60]. Intracoronary adenosine has been widely evaluated in clinical studies, demonstrating cardioprotection at higher doses in patients with previous infarctions [61], and in patients receiving primary angioplasty within the first 3 h after the onset of pain, as determined by reduced infarct size and improved LVEF at 6 months [62]. The mPTP inhibitor Cyclosporine-A has also shown to be a promising intervention to limit infarct size in pilot studies [63], though these findings have not been replicated in more recent research [64, 65]. The beneficial effect of β-blockers on LV remodeling, re-infarction, life-threatening arrhythmias, and mortality is well documented. Notably, a clinical study aimed to determine the effect of intravenous metoprolol on infarct size when administered immediately prior to reperfusion, showed cardioprotection of this β-blocker via an increase in myocardial salvage without complications [66]. Other β-blockers such as nebivolol have also shown cardioprotective potential [67], however sufficient pre-clinical investigation, including reproducible results in multiple animal models, is required before large-scale clinical testing. Glycoprotein IIb/IIIa inhibitors were developed for the reduction of thrombotic events due to their potent effect on platelets and platelet-leukocyte aggregates implicated in ischemia-reperfusion injury. Clinical trials investigating abciximab showed that this potent glycoprotein IIb/IIIa inhibitor can reduce infarct size and lead to improved clinical outcomes when administered early to MI patients [68] or via an intracoronary route [69]. Over recent years there has been a renewed interest in nitrates and nitroglycerin, as several

clinical studies have shown the potential of nitrates to limit myocardial infarct size [70], and a pre-conditioning mimetic action of nitroglycerin [71].

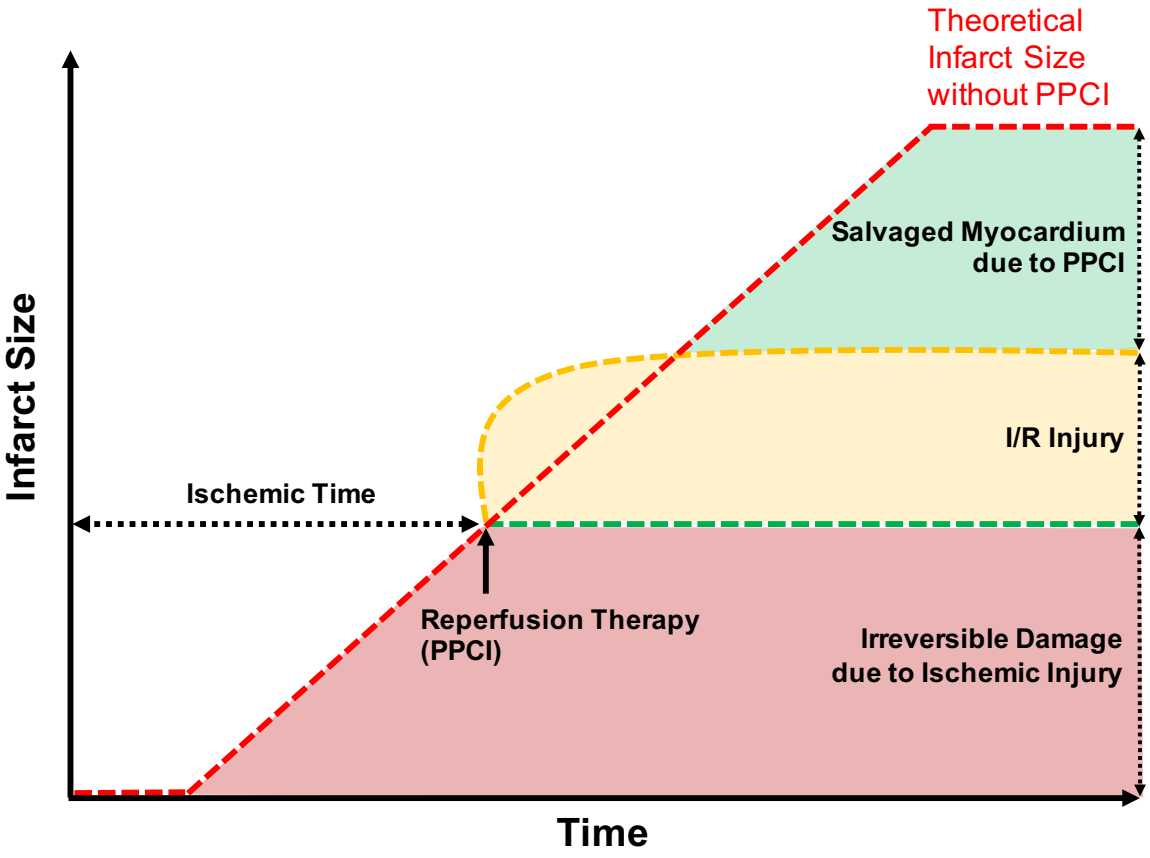

Figure 1. 1. The contribution of acute myocardial ischemic injury, PPCI, and I/R injury to final patient infarct size.

The red dashed line illustrates the development of infarct size over time without reperfusion therapy (PPCI). Myocardial Ischemia leads to irreversible damage of cardiac tissue which continues until the entire area at risk has undergone infarction. The yellow dashed line illustrates the extent of damage with PPCI treatment. Reperfusion leads to I/R injury, which has shown to compromise the benefit of reperfusion and contribute up to 50% of total infarct size. The green dashed line demonstrates the theoretical infarct size following PPCI in the absence of subsequent I/R injury. The theoretical infarct size without PPCI represents the worst outcome. Adapted from [24].

1.2 The Immune System in Myocardial Infarction

As the human heart has negligible endogenous regenerative capacity, repair and remodelling of the infarcted myocardium requires a tightly regulated immune response [72]. Repair of the infarcted myocardium occurs as a sequence of three distinct and overlapping phases; the inflammatory phase, the proliferative phase, and the maturation phase. Sudden coronary artery occlusion causes rapid ischemia of the myocardium and cardiomyocyte death within the ischemic area. Myocardial necrosis triggers an inflammatory reaction that clears the wound from dead cells and matrix debris, while activating proliferative and reparative pathways critical for collagenous scar formation at the injured site [73]. Importantly, the molecular and cellular changes associated with infarct healing directly influence ventricular remodelling and therefore affect prognosis in MI patients [74]. In particular, the timing of the events that occur in the immune response to myocardial injury during the inflammatory, proliferative, and maturation phases is critical to infarct healing. There is evidence that perturbations in both the balance and transition between the pro-inflammatory and the anti-inflammatory reparative phases can exacerbate acute myocardial IRI, and contribute to post-MI adverse LV remodeling. Adverse LV remodelling is a process whereby the LV undergoes geometric and functional changes following acute MI, including dilation/thinning of the infarcted tissue and hypertrophy of non-infarcted myocardium, resulting in reduced left ventricular ejection fraction (LVEF) and therefore a poorer clinical prognosis. Understanding the role of immune cells in MI is therefore critical for the development of therapeutic strategies aimed at preventing adverse remodeling of the infarcted heart.

1.2.1 Inflammatory Phase

Acute sudden death of cardiomyocytes in the infarcted heart rapidly activates several innate immune pathways that trigger an intense, but transient inflammatory response which occurs at day 1-3/5 following MI [75] (Figure 1.2). The generation of DAMPs by necrotic cells and matrix fragments activates membrane-bound Toll-Like Receptors (TLR)s in a number of cell types including resident cardiac macrophages, cardiomyocytes, vascular cells, fibroblasts, and infiltrating leukocytes (Figure 1.2).

Activation of TLRs induces cytokine production and leukocyte recruitment to the site of injury. Specifically, TLR2 and TLR4 have pro-inflammatory functions during myocardial injury; genetic knockout or antibody inhibition of TLR2 leads to reduced infarct size, improved cardiac function, and attenuated myocardial inflammation [76, 77], while TLR4 KO mice show reduced infarct size, attenuated adverse remodelling, and decreased inflammation [78, 79]. Other prominent features of the early inflammatory response include activation of the complement cascade, generation of reactive oxygen species (ROS), and upregulation of cytokine cascades. An initial role for complement was inferred from the deposition of complement components, namely C3 fragments, within the myocardium of experimental models of MI [80]. The complement cascade is acutely activated within hours of MI, as supported by augmented expression of complement genes in ischemia and reperfusion [81]. During this process, C3 and C5 cleavage fragments contribute to initiation of the immune response in IRI by chemoattraction of immune cells and membrane attack complex (MAC) formation on cells within the ischemic region. Importantly, the depletion or inhibition of complement prior to myocardial I/R has shown to impair LV function and accelerate progression towards heat failure, thus supporting an important involvement of the complement system in the immune response to MI [82]. Other important stimuli in the early inflammatory response after necrotic myocardial injury include reactive oxygen species (ROS) [83], cardiomyocyte-derived High Mobility Group Box (HMGB1) [84], Interleukin 1 alpha (IL-1α) [85] and extracellular RNAs [86]. Activation of these innate signalling pathways converges onto the activation of the key transcription factor, nuclear factor kappa-light-chain-enhancer of activated B cells (NFκB), which induces gene transcription of factors promoting inflammation including cytokines, chemokines, and adhesion molecules, by multiple cell types including endothelial cells, fibroblasts, cardiomyocytes, resident cardiac mast cells, and macrophages [87]. Upregulation of proinflammatory cytokines, namely tumor necrosis factor alpha (TNFα), Interleukin 1 Beta (IL-1β) and Interleukin 6 (IL-6), and chemokines, is the hallmark of the inflammatory phase of infarct healing, which generates chemotactic gradients that recruit leukocyte subpopulations to the infarcted area via interactions with corresponding chemokine receptors. Increased synthesis of TNFα, IL-1β and members of the IL-6 family, induce endothelial cell adhesion molecule synthesis and activate leukocyte integrins, mediating strong adhesive interactions that ultimately

lead to extravasation of inflammatory cells into the infarct. IL-1-mediated signalling in particular has a central role in the activation of the proinflammatory response following MI. The release of active IL-1β is dependent on the action of the inflammasome, a key molecular platform required for caspase-1 activation and subsequent generation of bioactive IL-1β from pro-IL-1β. Once active, IL-1β signalling is an important source of cytokine and chemokine synthesis and mediates inflammatory cell infiltration into the infarcted myocardium. Following MI, the expression of chemokines including neutrophil chemoattractant IL-8 [88], and the mononuclear cell chemoattractant CCL2, are upregulated in the infarcted area [89]. Chemokines released in the infarct are immobilized by binding to glycosaminoglycans on the endothelial surface and in the extracellular matrix, which generates localized high chemokine concentrations in areas of injury and provides directional signals for extravasation of leukocyte subpopulations into the infarcted myocardium [90]. This inflammatory response to cardiac I/R occurs at day 1-4 following MI, which transitions and overlaps into the proliferative phase around day 4 onwards.

1.2.2 Suppression of Inflammation

While the intense myocardial inflammatory response is essential for cardiac repair, unrestrained activity, temporal prolongation, or spatial expansion of the inflammatory response is implicated in the pathogenesis of adverse remodelling and heart failure in patients with acute MI [91-93]. Excessive early inflammation may augment matrix degradation causing cardiac rupture, while prolongation of the inflammatory reaction may impair collagen deposition leading to formation of a scar with reduced tensile strength, thus increasing chamber dilation. An excessive, persistent or expanded pro-inflammatory response to cardiac I/R may worsen adverse LV remodelling by activating proteases [94]; increasing cytokine expression which may induce cardiomyocyte apoptosis and suppress contractility; increasing matrix deposition which may result in a stiffer ventricle and causes diastolic dysfunction [95], and the activation of cardiac fibroblasts in the infarct border zone which may expand fibrosis into viable tissue. Defective containment of the inflammatory reaction may lead to extension of the inflammatory infiltrate into the non-infarcted myocardium, enhancing fibrosis and worsening diastolic function [96]. Experimental studies have

demonstrated that myocardial expression levels of pro-inflammatory cytokines (IL-6, TNF-α, and IL-1β) at 8 and 20 weeks after AMI in a rat model, were significantly associated with left ventricular end-diastolic volume [97]. Similarly, in STEMI patients, IL-1β levels measured at pre-, 2, and 7 days post-PPCI were able to predict indexed left ventricular end-systolic volume and left ventricular end-diastolic volume values measured by CMR at 1 year [98]. In mouse models of MI, an excessive or pro-longed inflammatory classical monocyte response has shown to contribute to inappropriate tissue destruction, infarct size, cardiac dysfunction, and adverse ventricular remodelling [99-104]. Furthermore, clinical studies have shown that elevated concentrations of inflammatory phase circulating monocytes and neutrophils following acute MI are associated with adverse remodelling and development of heart failure [105, 106].

Optimum repair of infarcted myocardial tissue and the prevention of adverse LV remodelling following MI is therefore critically dependent on the timely suppression and containment of inflammation. Suppression of the inflammatory response occurs as necrotic cells and cell fragments are cleared from the infarct, around day 3-4 following MI. Although many cell types contribute to the resolution of myocardial inflammation, reparative M2 macrophage, and Treg populations in particular contribute to inflammatory suppression following MI. Neutrophils undergo apoptosis and are phagocytosed by macrophages, and there is a shift from inflammatory monocytes and M1 macrophages to a repertoire of reparative monocytes and M2 macrophages. Reparative macrophages and lymphocytes produce anti-inflammatory mediators including IL-10 and Transforming Growth Factor Beta (TGF-β), which are essential for repressing the synthesis of pro-inflammatory cytokines and chemokines [107].

1.2.3 Proliferative Phase

Transition to the proliferative/reparative phase following suppression of inflammation begins around day 4/5 following MI and can continue for weeks [75] (Figure 1.2). This stage is characterised by fibroblast migration, proliferation, and transdifferentiation into a myofibroblast phenotype. A combination of growth factors, cytokines, TGF-β1/Smad3 signalling, angiotensin II, and altered composition of the extracellular matrix (ECM) are particularly important reparative and fibrogenic mediators, inducing transdifferentiation of fibroblasts to secretory myofibroblasts. Infarct myofibroblasts express and secrete contractile proteins including alpha-smooth muscle actin (α-SMA), and synthesize and deposit ECM proteins, beginning from the infarct border zone and progressing toward the core infarct area as the cells migrate along the newly synthesized ECM matrix [99, 108-110]. Myofibroblasts produce and deposit large amounts of interstitial collagens (initially type III and later on, during the infarct healing, type I collagen), which is crucial for increasing tensile strength and preventing ventricular wall rupture [111]. Fibroblast proliferation and activation is also associated with extensive angiogenic signalling, which stimulates endothelial cell proliferation and infiltration to establish a microvascular network to the infarct area and thus provide adequate oxygen and nutrients to myofibroblasts in the metabolically active infarct [112]. As the infarct is filled with matrix, cellular proliferation is suppressed and transition to the maturation phase follows. Although the initial reparative fibrosis is crucial for preventing rupture of the ventricular wall, an exaggerated fibrotic response or fibrosis outside the injured area is detrimental; enhanced fibrosis during the proliferative phase contributes to stiffening of the left ventricle, reduced LV compliance, and adverse left ventricular remodelling, particularly if myofibroblasts remain in non-injured areas of the heart. Conversely, interference with the reparative response promotes infarct expansion, ventricular wall thinning, dilation, systolic dysfunction and propensity to rupture [113].

1.2.4 Maturation phase

The final stage of infarct healing is the maturation phase, whereby matrix cross-linking leads to the formation of a dense collagenous scar, marking the end stage of myocardial infarct repair. This occurs from weeks to months following MI [75]. Fibroblasts become quiescent and undergo apoptosis, resulting in the suppression of collagen-based matrix synthesis and deposition which is critical to prevent exaggerated fibrosis and adverse remodelling. Temporary infarct vascular networks produced during the reparative phase then either undergo apoptosis or acquire a muscular coat [114, 115].

As with all stages of infarct healing, it is critical that the transition from the proliferative to the maturation phase occurs at an appropriate time; if the maturation phase begins too early the scar matrix may still be inadequate, and collagen deposition will cease as myofibroblasts disappear, resulting in an unstable scar prone to rupture. Conversely, a delay in the events of maturation, allows for prolonged tissue degradation and collagen formation, creating a larger scar area more likely to cause cardiac failure.

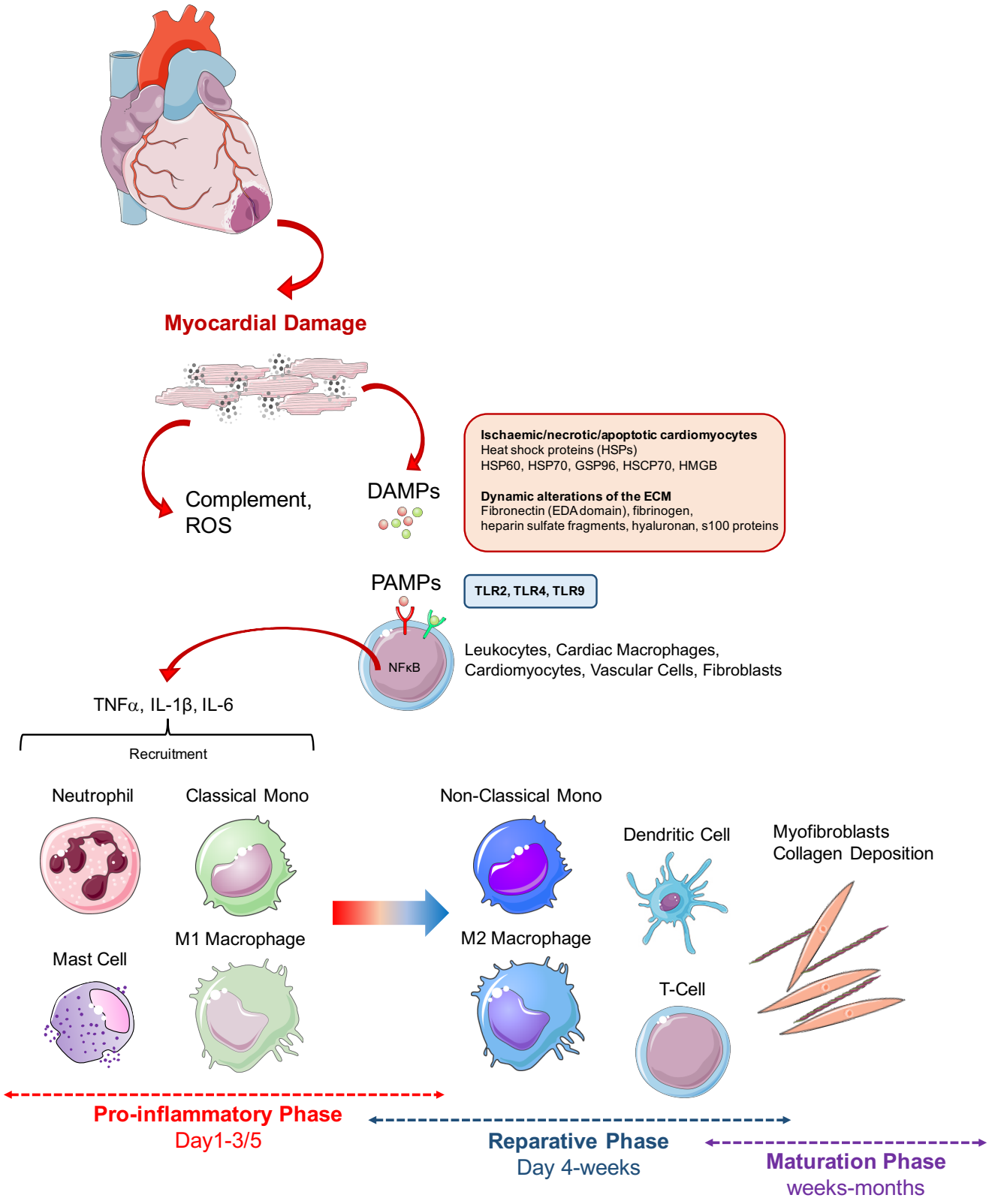
Myocardial Damage
Complement, ROS
DAMPs
Ischaemic/necrotic/apoptotic cardiomyocytes
Heat shock proteins (HSPs)
HSP60, HSP70, GSP96, HSCP70, HMGB
Dynamic alterations of the ECM
Fibronectin (EDA domain), fibrinogen,
heparin sulfate fragments, hyaluronan, s100 proteins
PAMPs
TLR2, TLR4, TLR9
NFκB
Leukocytes, Cardiac Macrophages,
Cardiomyocytes, Vascular Cells, Fibroblasts
TNFα, IL-1β, IL-6
Recruitment
Neutrophil
Classical Mono
Non-Classical Mono
Dendritic Cell
Myofibroblasts
Collagen Deposition
Mast Cell
M1 Macrophage
M2 Macrophage
T-Cell
Pro-inflammatory Phase
Day1-3/5
Reparative Phase
Day 4-weeks
Maturation Phase
weeks-months

Figure 1. 2. Activation of the immune response and leukocyte recruitment by myocardial DAMPs following myocardial infarction.

Activation of innate signalling pathways converges onto the activation of the key transcription factor NFκB which induces gene transcription of factors promoting inflammation including cytokines, chemokines, and adhesion molecules, by multiple cell types including endothelial cells, fibroblasts, cardiomyocytes, resident cardiac mast cells, and macrophages. Upregulation of proinflammatory cytokines (namely TNF-α, IL-1β, and IL-6) and chemokines is the hallmark of the inflammatory phase of infarct healing (day 1-3/5 post-MI), which induce endothelial cell adhesion molecule synthesis and activate leukocyte integrins, mediating strong adhesive interactions that ultimately lead to extravasation of inflammatory cells into the infarct. Neutrophils, classical monocytes and M1 Macrophages dominate the inflammatory phase of repair. These cells give rise to non-classical monocytes and M2 macrophages which promote the second anti-inflammatory, proliferative phase of repair (around day 4 to weeks post-MI). Myofibroblasts mediate collagen production and deposition to promote fibrosis and prevent cardiac rupture. The third stage of infarct healing is the maturation phase, whereby matrix cross-linking leads to the formation of a dense collagenous scar, marking the end stage of myocardial infarct repair. This final stage continues for weeks to months following MI.

1.3 Monocytes

1.3.1 Monocytes: An Overview

Monocytes are members of the mononuclear phagocyte system, a critical component of the innate immune system. Derived in the bone marrow from haematopoietic stem cells (HPSC), monocytes circulate the blood and spleen, occupying a central role in homeostasis, inflammation, and immune defence [116]. Monocytes can phagocytose and present antigens, secrete chemokines, and proliferate in response to infection and injury [117]. Once recruited to tissues, monocytes contribute to tissue repair as well as providing a progenitor pool of cells capable of differentiating into macrophages and dendritic cells [118, 119]. The heterogeneous, plastic nature of monocytes permits their context-dependent functions which are attributed to different subpopulations of these cells [120, 121]. The functions of monocyte subpopulations have been studied most extensively using mouse models of heath and disease.

1.3.2 Monocyte Development and Heterogeneity

Monocytes develop in the bone marrow from HPSCs following a transition through several intermediate progenitor stages of the common myeloid progenitor, the granulocyte/macrophage progenitor, and the monocyte/dendritic cell (DC) progenitor [122]. Current nomenclature divides monocytes into two main subpopulations in both humans and mice, known as classical and non-classical monocytes [123]. Human classical and non-classical monocytes are defined by their differential expression of CD14 and CD16, while mouse monocyte subpopulations are classified according to differential expression of Ly6C. Classical monocytes ($CD14^{++}CD16^{-}$ in humans, $Ly6C^{hi}$ in mouse) characteristically express high levels of CCR2 and low levels of the fractalkine receptor, CX3CR1. In contrast, non-classical monocytes ($CD14^{+}$ $CD16^{++}$ in humans, $Ly6C^{lo}$ in mouse) express high levels of CX3CR1, and low levels of CCR2. A third subset of intermediate monocytes has also been described in humans ($CD14^{++}$ $CD16^{+}$), which express these surface markers at levels between the classical and non-classical subsets [124]. Previous studies grouped intermediate monocytes with the non-classical subset due to their high expression of CX3CR1, however increasing

evidence suggests that human intermediate monocytes are a third, distinct monocyte population [125]. In addition to having their own distinct immune cell marker expression profile, monocyte subpopulations also perform unique functions. Accurate classification of these distinct monocyte subpopulations is therefore crucial for understanding the specific functions of each monocyte population.

1.3.3 Origin of Non-Classical Monocytes

It currently remains unclear whether non-classical monocytes arise from an independent bone marrow monocyte progenitor distinct from that of classical monocytes, or whether classical Ly6C^{hi}CCR2^{hi} monocytes serve as an intermediate lineage for the subsequent generation of non-classical Ly6C^{lo}CX3CR1^{hi} monocytes. A number of murine studies support the notion that myeloid precursors in the bone marrow initially give rise to classical Ly6C^{hi}CCR2^{hi} monocytes, which subsequently transition into non-classical Ly6C^{lo}CX3CR1^{hi} monocytes over time [126-131]. In this manner, mouse blood monocyte subpopulations represent stages of a developmental sequence. In vitro studies suggest that this transition is performed over 24-48h, whereby Ly6C^{hi} monocytes gradually down-regulate Ly6C expression while still in the blood stream [132, 133]. Under steady state conditions, in vivo peripheral blood monocytes were estimated to have a similar average transit time in the circulation of ~25h [134]. In the absence of inflammation, murine classical Ly6C^{hi}CCR2^{hi} monocytes have been shown to return to the bone marrow from the circulation [127]. Research suggests that classical Ly6C^{hi} monocytes can downregulate their Ly6C expression, and move between blood and bone marrow [135], however whether this loss of Ly6C expression corresponds to a conversion of monocyte subset is unclear, and does not exclude the existence of an alternative route for non-classical Ly6C^{lo} development independent of the classical Ly6C^{hi} monocyte population. For example, selective impairment of Ly6C^{hi} monocytes in *Irf8*$^{-/-}$ mutant mice or *Klf4*$^{-/-}$ cells suggests an independent developmental pathway for non-classical Ly6C^{lo} monocytes, whereby dramatically reduced numbers of classical Ly6C^{hi} monocytes in the bone marrow does not affect the counts of Ly6C^{lo} non-classical monocytes [136, 137]. Such findings support a route of Ly6C^{lo} monocyte development which is independent from that of the Ly6C^{hi} population in the blood or bone marrow, or originating from the common

monocyte progenitor (cMoP). Other explanations for such findings may include an increased survival of Ly6C^{lo} monocytes in these models.

Many of the specific factors that drive differentiation of monocytes into three distinct subsets are unknown; however, the transcription factor Nur77, encoded by the NR4A1 gene, plays a crucial role in non-classical Ly6C monocyte development; *Nur77*$^{-/-}$ mice show an absence of patrolling non-classical Ly6C^{lo} monocytes in the blood, spleen, and bone marrow, and Ly6C^{lo} patrolling monocytes remaining in the bone marrow undergo apoptosis due to arrest in the S-phase of cell cycle progression [138]. Human non-classical CD14^{+}CD16^{++} monocytes (equivalent to mouse Ly6C^{lo} patrolling monocytes) also express high levels of Nur77, and are likely to have a common function [138, 139].

1.3.4 Monocyte Function in Steady State

During resting state, classical monocytes are abundant in the blood and in several non-inflamed organs including the spleen, lung, liver, and brain. Following injury or infection, these pools of classical monocytes can readily extravasate to the site of injury [140]. In contrast, Ly6C^{hi}-derived Ly6C^{lo} non-classical monocytes predominantly remain in the vascular system, and have a lifespan of several days in both humans [141] and mice [142, 143].

Total monocytes typically comprise ~4% of all circulating leukocytes in mice, which is made up of ~60% classical monocytes and ~40% non-classical monocytes [144]. Mouse Ly6C^{hi} monocytes have a half-life of ~22h, while Ly6C^{hi}-dervived Ly6C^{lo} monocytes have a half-life of ~2.2 days [128, 141]. Of this peripheral blood monocyte population in mice, 40% are circulating while 60% are marginating [145]. In humans, total monocytes occupy ~10% of all circulating leukocytes, which is comprised of an approximate ratio of 85% classical monocytes, 5% intermediate monocytes, and 10% non-classical monocytes in the blood. As seen in mouse, human circulating classical monocytes have a shorter life-span (24h) than intermediate and non-classical monocytes, which circulate for approximately 4 days and 7 days, respectively [141]. The bone marrow is the primary organ responsible for maintaining monocyte numbers

in the circulation during basal conditions. The egress of bone marrow Ly6C^{hi} monocytes during steady state requires the engagement of the chemokine receptor CCR2 [146]. By contrast, most Ly6C^{lo} monocytes gain access to the bloodstream independently of CCR2 and rely on the transcription factor NR4A1 for the differentiation of circulating Ly6C^{hi} monocytes into Ly6C^{lo} monocytes as previously described [138]. In this sense, Ly6C^{lo} non-classical monocytes are not necessarily derived from the bone marrow directly, but instead originate from bone marrow Ly6C^{hi} monocytes following their release into the blood. Ly6C^{hi} classical and Ly6C^{lo} non-classical monocytes exhibit different behaviour during homeostatic conditions; in the absence of inflammation, Ly6C^{hi} classical monocytes return to the bone marrow from the circulation, however steady state Ly6C^{lo} non-classical monocytes engage in long-term migration along the endothelium with or against blood flow, in a process termed patrolling [147, 148]. This unique patrolling of the luminal endothelium by Ly6C^{lo} non-classical monocytes provides a timely mechanism of surveillance for the immune system to respond to inflammatory stimuli following injury or infection. The patrolling behaviour of Ly6C^{lo} non-classical monocytes is mediated through the interaction of CX3CR1 with its ligand, CX3CL1, expressed by endothelial cells. This patrolling of non-classical monocytes is a significantly slower process (~12μm/min) that the rolling behaviour of classical monocytes in the circulation [149]. Deletion of CX3CR1 reduces the patrolling of Ly6C^{lo} monocytes [150] and results in overall fewer circulating Ly6C^{lo} monocytes, possibly due to reduced monocyte survival resulting from CX3CR1-dependent expression of anti-apoptotic protein B-cell lymphoma 2 (BCL-2) [151]. This CX3CL1/CX3CR1 interaction promotes further adhesion of patrolling non-classical monocytes to the vascular endothelium via the lymphocyte function antigen-1 (LFA-1) which is an integrin comprising CD11a and CD18 that interact with Intercellular Adhesion Molecule 1 (ICAM1) and Intracellular Adhesion Molecule 2 (ICAM2) on the endothelial cell surface [150]. ICAM1 and ICAM2 behave in a mutually redundant fashion to facilitate LFA-1 dependent monocyte adhesion, and ICAM1/2 double knockout mice demonstrate a dramatically reduced frequency of non-classical monocyte adhesion to the vasculature [125]. In vivo inhibition of LFA-1 using anti-CD11a/CD18 antibodies also leads to the prolonged dissociation of non-classical monocytes from the endothelium and abolishes patrolling behaviour [152]. Expression of CX3CR1 and LFA-1 by non-classical monocytes is therefore crucial to their

patrolling behaviour. Transcriptomic and functional comparison studies suggest that human $CD14^{-}CD16^{++}$ non-classical monocytes are the human counterpart to these patrolling $Ly6C^{lo}$ monocytes in mouse [124, 139, 153], which also exhibit patrolling behaviour when infused into mice [154]. Further details on the role of CX3CR1 expression in non-classical monocyte function are described in section 1.4.

1.3.5 The Monocyte Response Following Myocardial Infarction

The importance of monocytes and macrophages following MI has been extensively demonstrated in mouse models of MI. In mouse models of cardiac injury, monocyte depletion increases mortality and reduces ventricular function [113], suggesting that monocytes are necessary for effective wound healing and repair of heart tissue. Following MI in mice, monocytes are preferentially released from the spleen, which is highly sensitive to ischaemic myocardial injury and can rapidly mobilize this reservoir of monocytes to be recruited to the myocardium via CCL2 and angiotensin II signals. The vasoconstrictive hormone angiotensin II is particularly important in promoting the splenic release of $Ly6C^{hi}$ monocytes [155]. MI also induces the exit of HSPCs from the bone marrow via sympathetic nervous system (SNS) signalling pathways, which seed the spleen and provide a sustained boost in monocyte production [156].

Nahrendorf et al describe the migration of monocytes released from the bone marrow and spleen to the injured myocardium as a biphasic response, governed by the actions of chemokines. Classical and non-classical monocyte subpopulations express a different repertoire of chemokine receptors, allowing their differential recruitment from the bone marrow and into tissues. Classical monocytes express high levels of CCR2, and migrate from the bone marrow into the circulation predominantly in response to CCL2, and also CCL7 and CCL12. As expected, CCR2 deficient mice show an 80% reduction in classical $Ly6C^{hi}$ monocyte emigration from the bone marrow, while the distribution of non-classical $Ly6C^{lo}$ monocytes is relatively normal [157]. Classical $Ly6C^{hi}$ monocytes dominate the first phase (day 1-4) of the monocyte response following MI in mouse, and differentiate into M1 pro-inflammatory macrophages that exhibit phagocytic and proteolytic functions to remove debris in the injured infarct tissue [158]. The emigration of $Ly6C^{lo}$ non-classical monocytes from the bone marrow

and their recruitment to the injured myocardium is however less clearly defined. As previously described, non-classical monocytes express high levels of CX3CR1 and primarily exhibit patrolling behaviour along the vasculature by responding to endothelial expressed CX3CL1. In the inflammation that ensues following MI, vascular endothelial cells upregulate the expression of CX3CL1, allowing patrolling non-classical monocytes to firmly arrest and adhere to the vascular lumen. This interaction permits the subsequent extravasation of non-classical monocytes into the injured myocardial tissue. In the later stages of repair, pro-inflammatory $Ly6C^{hi}$ monocytes and M1 macrophages can also differentiate into pro-fibrotic $Ly6C^{lo}$ monocytes and M2 macrophages via TGF-β activation and have attenuated inflammatory properties [158], highlighting the plasticity of the monocyte/macrophage lineage. M2-like pro-fibrotic macrophages promote the reparative phase of healing by stimulating myofibroblast accumulation, angiogenesis, and collagen deposition [158]. This temporal biphasic monocyte response in mouse models of MI has also been reported to occur in human MI, whereby an initial rise of inflammatory classical $CD14^{++}CD16^{-}$ monocytes at day 2-3 is followed by the sequential recruitment of non-classical $CD14^{+}CD16^{++}$ monocytes at day 4-5 [159]. This study was however limited to observed changes in monocyte counts in the blood. Studies of monocytes in human heart tissue following MI are limited due to the unavailability of tissue specimens, however an autopsy study by Van der Laan et al showed that $CD14^{+}$ cells accumulate in distinct regions of the infarcted myocardium in different phases of healing following acute MI; $CD14^{+}$ cells were recruited in the post-MI inflammatory phase (12h–5 days post-MI) and predominantly accumulated in the infarct border zone. In the subsequent proliferative phase (5–14 days post-MI), $CD14^{+}$ cells almost exclusively invaded the infarct core. This study noted that there was an abundant population of the $CD14^{+}CD16^{-}$ classical monocyte subset in the border zone in the inflammatory phase after MI, whereas comparable proportions of classical $CD14^{+}$ $CD16^{-}$ and non-classical $CD14^{+}$ $CD16^{+}$ monocytes were present in the infarct in the proliferative phase.

Importantly, disruption of the finely tuned balance between the early classical monocyte and subsequent non-classical monocyte response is highly detrimental to infarct healing [113]; an excessive or prolonged inflammatory classical monocyte response contributes to inappropriate tissue destruction, infarct size, cardiac

dysfunction, and adverse ventricular remodelling [99-104], while disruption of the phase 2 non-classical monocyte response hinders the formation and remodeling of granulation tissue. Nur77 deficient mice which lack non-classical Ly6C^{lo} monocytes demonstrate adverse cardiac remodelling post-MI [160], highlighting the importance of the Ly6C^{lo} non-classical monocyte response. Furthermore, in the absence of classical Ly6C^{hi} monocytes, the half-life of non-classical Ly6C^{lo} monocytes is increased from around 2.5 days to 11 days [128], indicating an increased surveillance function of non-classical patrolling monocytes in the vasculature when the classical monocyte population has been disrupted or recruited to inflammatory sites.

Nahrendorf et al describe Ly6C^{lo} monocyte infiltration into the myocardium occurring in the second proliferative/reparative phase (day 5-9) of infarct healing. This traditional concept of a biphasic monocyte model of infarct healing has been challenged in recent years by new insights into monocyte behaviour, particularly of the non-classical monocyte subpopulation. This evidence has suggested a much earlier role of non-classical monocytes than that originally thought; real-time imaging revealed a rapid infiltration of CX3CR1^{+} monocytes into the injured site within several minutes after acute MI [161]. Such findings suggested that following cardiac I/R, monocytes are recruited rapidly (<15min) from the vascular reservoir and then later from the spleen. These early non-classical monocytes are postulated to actively attract neutrophils to the infarct, as observed in lung inflammation [162]. Furthermore, Li et al have shown by intravital 2-photon imaging of the beating heart that CX3CR1^{hi} monocytes are rapidly recruited to the heart within one hour of reperfusion, and displayed rolling, adhesion, and intraluminal crawling behavior characteristic of non-classical monocytes [163]. The dynamics of non-classical monocytes in response to cardiac I/R are therefore not clearly understood and further research is required to define their exact kinetics following reperfusion.

Research has also demonstrated that human non-classical monocytes have a greater inflammatory profile than previously believed. Non-classical monocytes have traditionally been viewed as the anti-inflammatory, pro-fibrotic subpopulation of monocytes, however research has now shown that upon activation, non-classical monocytes are the predominant producers of inflammatory cytokines TNF-α and IL-

1β among monocyte subsets [154, 164-167], via stimulation of TLR 2, 5 and 9. Notably, administration of a TLR2 antagonist just five minutes before reperfusion has been shown to reduce inflammation and infarct size, and improve cardiac function following MI [76]. In addition to this, the co-stimulatory molecules HLA-DR, CD80, and CD86 are expressed at high levels by non-classical monocytes, which may facilitate their contribution to inflammation via CD40-mediated T-cell activation [167]. The exact function of non-classical monocytes following cardiac I/R, in addition to their patrolling behaviour, is therefore yet to be defined.

Though much of the evidence describing non-classical monocyte function following MI is derived from mouse models, analysis of the monocyte transcriptome across mouse and human species has shown that human non-classical monocytes are functionally orthologous to their mouse Ly6C^{lo} equivalent. Gene expression profiling showed that 63 genes were more abundant in both human and mouse non-classical monocytes relative to their classical counterpart, including LFA-1, MAC-1, CX3CR1 and TNF [153]. Furthermore, human non-classical monocytes have increased metabolic activities and efficient cytoskeletal dynamics indicative of actively patrolling cells, and demonstrate vasculature patrolling in lipid-deficient mice [168]. This high conservation of the monocyte transcriptome and function between mice and humans following AMI [169] supports the use of mouse models of cardiac I/R to investigate the recruitment of non-classical monocytes to the injured myocardium following myocardial I/R.

1.3.6 Clinical Implications of Monocyte Subset Counts

In clinical studies of STEMI patients, increasing evidence has shown that counts of circulating monocyte subpopulations following reperfusion hold predictive value for cardiovascular events and patient outcome post-cardiac I/R. For example, peak levels of classical ($CD14^{++}CD16^{-}$) monocytes at day 2.6 post-MI were negatively associated with the extent of myocardial salvage at 7 days post-MI and recovery of LVEF during the chronic phase at 6 months post-MI [170]. Such associations were not observed in the case of $CD16^{+}$ monocytes however this study did not differentiate $CD16^{+}$ intermediate from $CD16^{++}$ non-classical monocytes and therefore the exact dynamics of each monocyte subpopulation was not determined. In a similar study, peak levels of classical ($CD14^{++}CD16^{-}$) monocytes at day 2.8 post-MI, but not those of non-classical monocytes, were significantly higher in patients with MVO than in those without MVO [171]. STEMI patient high counts of classical monocytes at ~day 5 have been shown to predict impaired LVEF, larger infarct size, and MVO, while high classical monocyte counts at 4-month follow up were negatively associated with regional systolic LV function [172].

There is also evidence that the intermediate monocyte population independently predicts cardiac outcome in STEMI patients. In a study of 100 STEMI patients, monocytosis of intermediate ($CD14^{++}CD16^{+}$) monocytes during the acute phase after STEMI (day 1-7) was predictive of 2-year post MI major adverse cardiac events following PPCI; [79]. Furthermore, analysis of post-reperfusion monocyte counts at day 1,3 and 7 following PCI showed that STEMI patients had a 60-80% increase in total monocyte counts and a disproportionate increase (3-fold) in intermediate ($CD14^{++}CD16^{+}$) monocytes compared CAD patients and healthy controls. This increase in intermediate monocyte counts was significantly correlated with troponin, plasma cytokines, and convalescent left ventricular function [173]. In a large study of 951 patients referred for angiography, baseline intermediate monocyte counts were strongly associated with acute MI and non-hemorrhagic stroke, and those patients with the highest counts of this monocyte subset had a 40% risk of a cardiovascular event within three years of study enrollment [174]. The non-classical ($CD14^{+}CD16^{++}$) monocyte subpopulation has also been shown to have predictive value, whereby

decreased counts of these cells in the peripheral blood after MI confers an increased risk of ventricular thrombus formation following MI (time point not specified) [175]. The important dynamics of monocyte subpopulations in predicting patient prognosis has also been reported in the context of stroke patients [176-178]. A trend between circulating non-classical monocytes at day 5 post-MI and worse systolic LV function at follow up has also been reported [245]. Monocytosis of the intermediate monocyte population at day 1-7 post-MI is reported to predict 2 year major adverse cardiac events post-PCI [246]. Peak levels of classical monocytes post-MI are negatively associated with the extent of myocardial salvage at day 7 post-MI, and the recovery of LVEF at 6 months [247]. A more recent study [244] of 102 STEMI patients at day 1,3, and 7 post-PCI found that classical and intermediate monocyte counts are directly associated with infarct size and inversely with LVEF, while non-classical monocytes were directly correlated with scar border zone mass and the formation of an adverse myocardial scar.

Monocyte subpopulations therefore appear to specifically respond to the extent of cardiac injury, suggesting that manipulation of monocyte heterogeneity could be a novel therapeutic target for salvaging ischemic damage, or may offer reliable biomarkers to prioritise patients for follow up treatments/management. Further studies are however required to determine the precise dynamics of circulating monocyte subpopulations in STEMI patients following reperfusion. In particular, the aforementioned studies have investigated circulating monocyte subpopulation dynamics from the earliest time point of day 1 following cardiac I/R, and therefore classical, intermediate and non-classical monocyte behaviour during the acute 24h post-I/R remains to be studied.

1.4 The Chemokine System and CX3CL1/CX3CR1

1.4.1 The Chemokine System

The directional migration of leukocytes during normal and inflammatory processes is a highly complex process, requiring adhesion to the vascular luminal endothelium, transendothelial migration, and subsequent leukocyte chemotaxis, all of which are tightly regulated by members of the chemotactic cytokine family known as chemokines. Chemokines are a group of small (~8–14 kDa), structurally-related secreted proteins which regulate leukocyte trafficking via their interactions with chemokine receptors, a large family of seven-transmembrane domain, G-protein coupled receptors. They target all types of leukocytes including haematopoietic precursors, mature leukocytes of the innate immune system as well as naive, memory, and effector lymphocytes [179]. Human chemokines are classified into four subfamilies, based on the position of the first two of four highly conserved N-terminal cysteine residues: CXC, CC, and CX3C [6]. The C chemokine sub-family is an exception which has only one N-terminal cysteine residue. Uniquely, the CX3C chemokine family is comprised of only a single chemokine, CX3CL1, also known as Fractalkine (FKN). In addition to their structural classification, chemokines are also defined into two functional subsets; inflammatory and homeostatic chemokines. Inflammatory chemokines are upregulated in response to inflammation, infection, and tissue injury. They often have broad target cell selectivity and act on both innate and adaptive cells of the immune system. In contrast, homoeostatic chemokines are constitutively expressed in specific tissues where they regulate leukocyte homing. This includes haematopoiesis in the bone marrow and thymus, the initiation of adaptive immune responses in the spleen and lymph nodes, and immune surveillance of healthy peripheral tissues. Several chemokines are reported to be ‘dual function’ chemokines, whose properties cannot be assigned to either of the two groups [179].

Binding of endothelium-associated chemokines to leukocyte-expressed chemokine receptors is required for the extravasation of leukocytes, by inducing a rapid increase in integrin affinity/avidity and allowing firm and transient leukocyte adhesion. The repertoire of chemokine receptors constitutes 6 CXCRs, 10 CCRs, 1 CX3CR, and 2

XCRs [180, 181]. Adhered leukocytes subsequently traffic across the endothelium and the underlying basement membrane into the tissue whereby a chemokine gradient directs their migration [182]. Leukocyte adhesion and transmigration is largely determined by the selectively of the chemokine system, whereby only those leukocytes that are responsive to the chemokines present on the local endothelium at the given vascular site are able to transmigrate. Such selectivity ensures specific appropriate tissue distribution of distinct leukocyte subsets under both normal and inflammatory conditions [183]. Another essential component of transendothelial migration is the immobilisation of chemokines on endothelial surfaces through interactions with glycosaminoglycans (GAGs) [184]. Importantly, a breakdown in the control of leukocyte mobilisation contributes to chronic inflammatory diseases, suggesting that therapeutic interference of chemokine function may offer a promising approach for the treatment of inflammatory conditions [179].

1.4.2 The CX3CL1/CX3CR1 Axis

CX3CL1 consists of a chemokine domain linked to a transmembrane domain via an extended mucin-rich stalk of an extracellular domain (Figure 1.4). Unlike most other known chemokines, CX3CL1 exists in two isoforms; transmembrane CX3CL1 and soluble CX3CL1, which results from proteolytic cleavage of membrane-anchored CX3CL1 by the enzymes A Disintegrin and metalloproteinase domain-containing protein 10 (ADAM10) or ADAM17 [185]. These isoform properties are also true for the chemokine CXCL16 [186]. Such isoforms allow for both the chemoattractive and adhesive properties of CX3CL1. The membrane-anchored form of CX3CL1 is expressed on activated endothelial cells, macrophages, dendritic cells, and neurons, and functions as an adhesion molecule. Under normal conditions, endothelial cells express basal levels of CX3CL1, however stimulation with inflammatory stimuli such as TNF-α, IFN-γ, and LPS upregulates the expression of endothelial CX3CL1 [187]. High affinity interactions between endothelial transmembrane-expressed CX3CL1 and its receptor CX3CR1, which is expressed on monocytes, $CD8^+$ effector T-cells, NK-cells, dendritic cells, mast cells, and vascular smooth muscle cells, promotes adhesion and arrest of these leukocytes to endothelial cells under physiological flow conditions

[188]. Notably, this CX3CL1-mediated adhesion can occur independently of other integrin and chemokine interactions.

In response to inflammatory stimuli, the general mechanism of leukocyte adhesion is mediated by selectins (Figure 1.5A). Leukocyte-expressed L-selectin is the most important adhesion molecule to initiate leukocyte tethering and rolling on the vascular endothelium via interaction with endothelial-expressed Glycosylation-dependent Cell-adhesion Molecule-1 (GlyCam-1) [189]. Following this binding, P-selectin interacts with the selectin ligand P-selectin glycoprotein ligand-1 (PSGL-1) expressed by leukocytes. Binding of selectins to their respective ligands is a rapid process which allows fast flowing leukocytes to initially be captured from the bloodstream and bind tentatively to the endothelium as they move along in a process known as rolling. Binding of E-selectin to its ligand E-Selectin Glycoprotein Ligand-1 (ESGL-1) expressed by leukocytes promotes 'slow rolling' due to partial activation of leukocyte integrins. This rolling and slow rolling behaviour brings leukocytes into contact with the endothelium to induce further activation of leukocytes by chemokines and proinflammatory agents expressed by endothelial cells. This leads to activation of leukocyte-expressed integrins including the β1-integrin Very Late Antigen 4 (VLA-4) which binds to endothelial-expressed Vascular Cell Adhesion Protein 1 (VCAM-1) This integrin-ligand interaction allows leukocytes to arrest on the vascular endothelial surface. The β2-integrin LFA-1 (CD11a/CD18) expressed by leukocytes is also involved in the firm adhesion of leukocytes through interaction with endothelial-expressed ICAM-1. This firm adhesion then allows leukocytes to crawl along the vasculature, before extravasating at endothelial cell-cell junctions in a platelet/endothelial cell adhesion molecule 1 (PECAM)-dependent mechanism towards the site of inflammation or injury [190, 191]. PECAM is expressed diffusely on the surfaces of most leukocytes and is concentrated at the borders of endothelial cells where it is implicated in the control of diapedesis. These molecules are not an exhaustive list of those involved in leukocyte adhesion and extravasation, but describe the general scheme of selectin/integrin-mediated events.

Leukocytes expressing CX3CR1, namely $CX3CR1^{+}$ non-classical monocytes, however, can interact with the endothelium using a method that is independent of P-

selectin/Integrin interaction [192, 193] (Figure 1.5B). In this scenario, circulating $CX3CR1^+$ leukocytes are captured and bound by endothelium-expressed CX3CL1 in an interaction that has a higher affinity than VCAM-1 binding to integrins [194]. This CX3CL1/CX3CR1-mediated interaction between leukocytes and vascular endothelium initially occurs independently of other adhesion molecules [195] and facilitates the patrolling behaviour of $CX3CR1^+$ monocytes in the blood [144]. This CX3CL1/CX3CR1 interaction then promotes further adhesion of patrolling non-classical monocytes to vascular endothelium via interaction between LFA-1 and ICAM1/2 on the endothelial cell surface [150]. ICAM1 and ICAM2 behave in a redundant fashion to facilitate LFA-1 dependent monocyte adhesion, and ICAM1/2 knockout mice demonstrate a dramatically reduced frequency of non-classical monocyte adhesion to the vasculature [125]. In vivo inhibition of LFA-1 using anti-CD11a/CD18 antibodies leads to the prolonged dissociation of non-classical monocytes from the endothelium and abolishes patrolling behaviour [152]. Expression of CX3CR1 and LFA-1 by non-classical monocytes is therefore crucial to their patrolling behaviour. Under flow conditions, a high frequency of $CD16^+$ intermediate and non-classical monocytes have been shown to arrest on membrane-expressed CX3CL1 [196]. This patrolling behaviour occurs continuously during basal conditions as $CX3CR1^+$ cells act on 'stand-by' for inflammatory stimuli. This method of surveillance therefore prepares the immune system for the timely detection and resolution of damage. In $CX3CR1^+$ monocytes, this patrolling behaviour is known to be slower than rolling, and occurs independently of blood flow [149]. The response following MI is discussed in section 1.4.3.

The soluble form of CX3CL1 is released following constitutive shedding of transmembrane endothelial CX3CL1 which is mediated by ADAM10, while shedding under inflammatory conditions is mediated primarily by ADAM17 [197, 198]. CX3CL1 functions as a conventional chemokine, demonstrating efficient recruitment of CX3CR1-expressing monocytes, NK cells, T cells, and dendritic cells to specific tissues. Importantly, this chemotactic function of the CX3CL1/CX3CR1 axis in regulating leukocyte recruitment has been associated with the pathophysiology of numerous inflammatory disorders, infections, neurological, and tumorigenesis

processes [185, 198]. As such, the CX3CL1/CX3CR1 axis has recently received significant attention as an attractive candidate to target therapeutically.

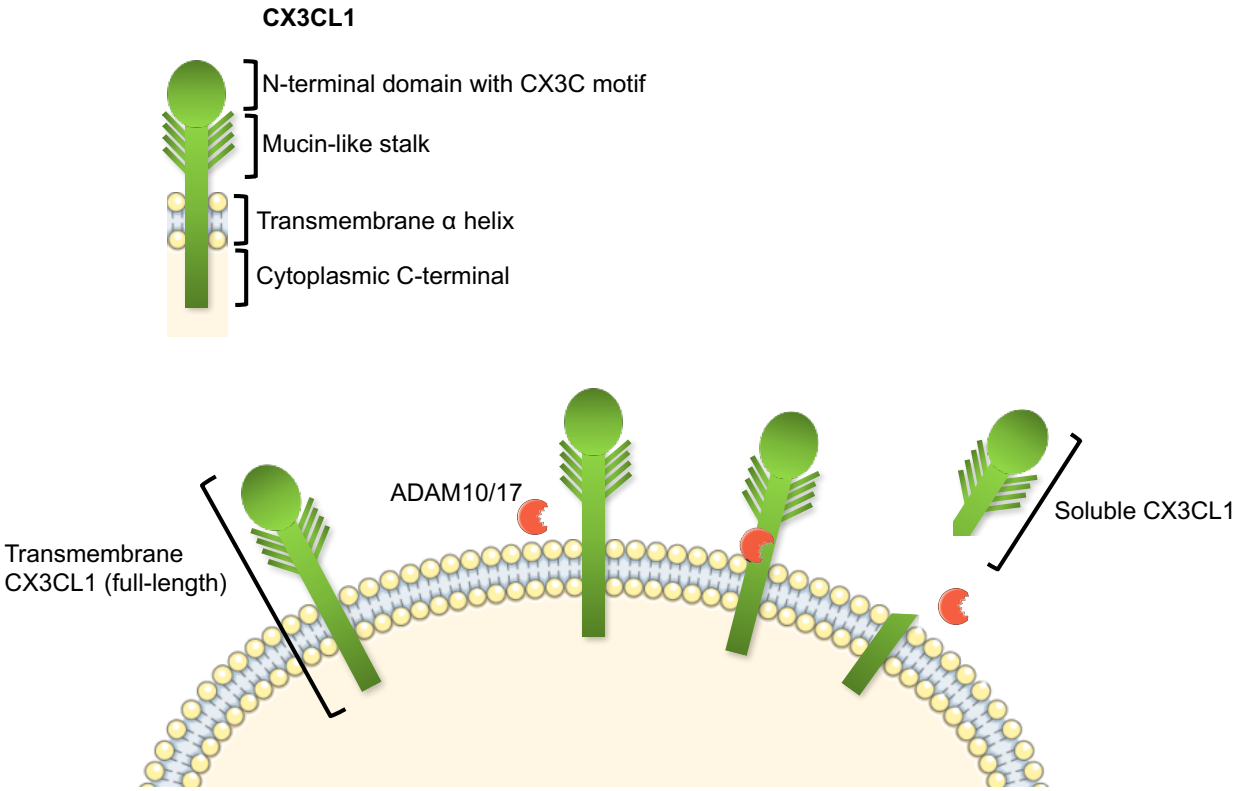

Figure 1. 3. The Molecular Structure of CX3CL1 (Fractalkine).

The structure of the membrane-bound isoform of CX3CL1, showing the specific 4 domains of the molecule: N-terminal CX3C domain, mucin-like stalk, transmembrane α-helix, and cytoplasmic C terminal. The soluble form of CX3CL1 is produced from the membrane-bound form by the cleaving action of the metalloproteinases ADAM10 or ADAM17; normal constitutive shedding is mediated by ADAM10, while shedding under inflammatory conditions is mediated primarily by ADAM17.

1.4.3 The CX3CL1/CX3CR1 Axis Following MI

In response to myocardial damage following cardiac I/R, necrotic cardiomyocytes release alarmins which activate innate immune cells and thereby increase the production of pro-inflammatory cytokines IFN-γ, IL-1, TNF-α, IL-10, and IL-6. Stimulation of vascular endothelial cells by these pro-inflammatory cytokines upregulates the expression of CX3CL1 by the endothelium. This increased expression of endothelium membrane-anchored CX3CL1 strengthens the interaction between circulating $CX3CR1^+$ leukocytes and the vasculature luminal endothelium described earlier in section 1.4.2. This process ensures the firm adhesion and arrest of $CX3CR1^+$ leukocytes, namely non-classical monocytes, from the rapidly flowing bloodstream to the endothelium to permit their extravasation into the injured myocardial tissue.

During this process, CX3CL1-CX3CR1 interaction promotes further monocyte adhesion via interactions between lymphocyte function-associated antigen 1 (LFA-1) comprising CD11a and CD18 integrins, with ICAM1 and ICAM2 on the endothelial surface [144, 199] (Figure 1.5B). Membrane-bound CX3CL1 expressed on vascular endothelial cells also induces changes in the cell shape of firmly adherent monocytes [200, 201]. The inflammatory cascade that ensues following cardiac I/R also leads to the cleavage of endothelial-expressed membrane-anchored CX3CL1 into soluble CX3CL1. This process is mediated by the enzyme ADAM17, and leads to the increased release of CX3CL1 into the circulation which creates a chemotactic gradient for the recruitment of $CX3CR1^+$ leukocytes, in particular non-classical monocytes. This CX3CL1 concentration gradient stimulates the directional migration of peripheral non-classical monocytes to the site of myocardial injury, where they can extravasate into the injured tissue via CX3CL1/CX3CR1-mediated adhesion and extravasation through the vessel wall.

A. General Scheme of Leukocyte Extravasation (Selectin-Mediated)

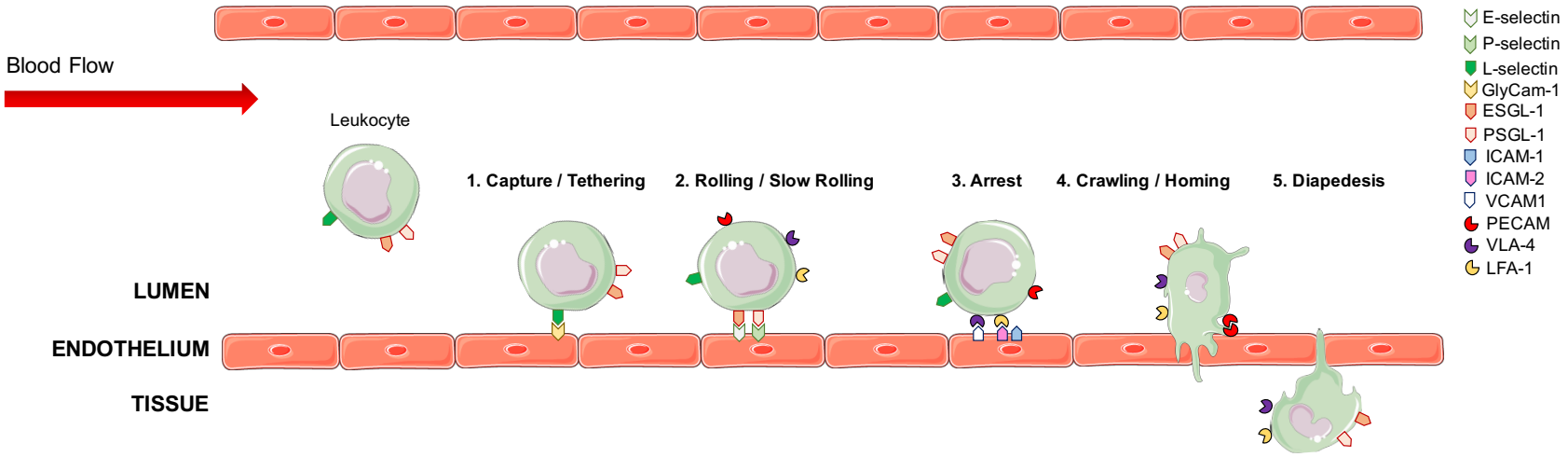

B. Patrolling Non-Classical Monocyte Extravasation (CX3CL1/CX3CR1-Mediated)

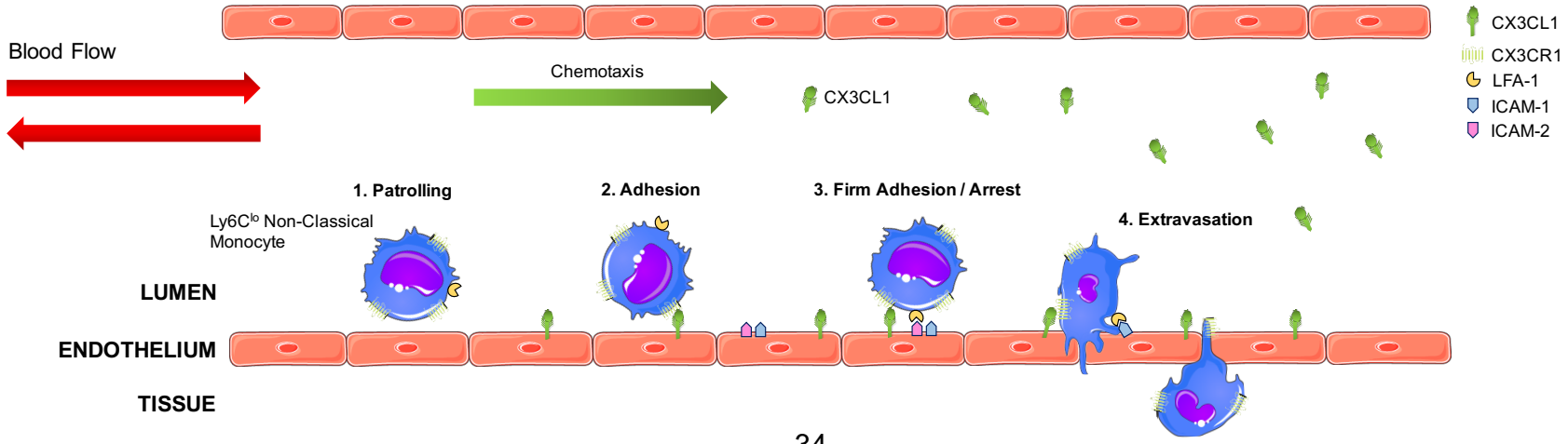

Figure 1. 4. **The different steps of cell interaction with vascular endothelial cells during adhesion and transmigration between leukocytes and CX3CR1^{+} patrolling non-classical monocytes.**

A. The general scheme of leukocyte adhesion is firstly mediated by interaction of leukocyte-expressed L-selectin with endothelial expressed GlyCam-1. This leukocyte tethering then promotes interaction between endothelial P-selectin and E-selectin with their respective leukocyte ligands PSGL-1 and ESGL-1. Binding of selectins to their respective ligands allows fast flowing leukocytes to initially be captured from the bloodstream and 'roll' along the vasculature. This rolling behaviour brings leukocytes into contact with the endothelium to induce further activation of leukocytes by chemokines and proinflammatory agents expressed by endothelial cells, leading to activation of leukocyte-expressed integrins including the β1-integrin VLA-4 which binds to endothelial-expressed VCAM-1. This integrin-ligand interaction allows leukocytes to arrest on the vascular endothelial surface. The β2-integrin LFA-1 (CD11a/CD18) expressed by leukocytes is also involved in the firm adhesion of leukocytes through interaction with endothelial-expressed ICAM-1. This firm adhesion then allows leukocytes to crawl along the vasculature, before extravasating at endothelial cell-cell junctions in PECAM-dependent mechanism towards the site of inflammation or injury. **B.** Leukocytes expressing CX3CR1, namely CX3CR1^{+} non-classical monocytes, can interact with the endothelium using a method that is independent of P-selectin/Integrin interaction. Circulating CX3CR1^{+} leukocytes are captured and bound by endothelium-expressed CX3CL1 in an interaction that initially occurs independently of other adhesion molecules and facilitates the patrolling behaviour of CX3CR1^{+} monocytes in the blood. This interaction promotes further adhesion of patrolling non-classical monocytes to vascular endothelium via interaction between LFA-1 and ICAM1/2 on the endothelial cells surface. ICAM1 and ICAM2 behave in a redundant fashion to facilitate LFA-1 dependent monocyte adhesion. This patrolling behaviour occurs continuously during basal conditions as CX3CR1^{+} cells act on 'stand-by' for inflammatory stimuli, providing a method of immune surveillance for the timely detection and resolution of damage. This patrolling behaviour of CX3CR1^{+} monocytes is known to be slower than rolling, and occurs independently of blood flow.

1.4.4 Clinical Implications of the CX3CL1/CX3CR1 Axis after MI

The chemotactic function of the CX3CL1/CX3CR1 axis in regulating leukocyte recruitment has been associated with the pathophysiology of an extensive range of diseases, including numerous inflammatory disorders, infections, neurological, and tumorigenesis processes [185, 202]. Among these diseases, the CX3CL1/CX3CR1 axis has been frequently implicated in determining the extent of myocardial damage following cardiac I/R. Accumulative evidence from in vitro studies, mouse models of cardiac I/R, and STEMI patients suggests that the CX3CL1/CX3CR1 system is detrimental to myocardial repair following cardiac I/R. In vitro evidence has shown that exposure of cultured rat cardiomyocytes to CX3CL1 increases cardiomyocyte expression of natriuretic peptide A (NT-proBNP), a marker of left ventricular dysfunction [203]. Mouse models of permanent MI have demonstrated that CX3CL1 gene and protein expression are enhanced in the failing heart [204], and that neutralization of CX3CL1 using anti-CX3CL1 antibody reduces macrophage recruitment to the injured myocardium, diminishes infarct size, and improves MI-induced heart failure. Other reports have demonstrated that anti-CX3CL1 (TP233) reduces cardiac remodelling after trans-aortic constriction and MI, improves cardiac function, and decreases infarct size (2-3 weeks) after permanent MI [203]. In a porcine model of cardiac I/R injury, PCI stents coated with a CX3CR1 antagonist (AZ12201182), led to a decrease in monocyte recruitment and reduced stenosis without affecting re-endothelialisation [205]. Based on these studies it therefore appears that the action of CX3CL1/CX3CR1 in response to cardiac I/R is detrimental to infarct healing. Since inhibition of the CX3CL1/CX3CR1 axis has proven successful in improving cardiac outcome following myocardial I/R, therapeutic targeting of CX3CL1 or its receptor CX3CR1 may be a useful intervention to improve outcome and prevent progression to heart failure following I/R.

This association between the CX3CL1/CX3CR1 axis and cardiac function has also been observed in STEMI patient and heart failure patients. Notably, the time course of myocardial CX3CL1 gene expression in mice has a pattern similar to the soluble CX3CL1 change in AMI patients [206]. Research has also shown that STEMI patients have significantly elevated levels of circulating CX3CL1 at 3 hours and 12 hours post-

PCI compared to stable angina pectoris (AP) patients, which was positively correlated with NT-proBNP levels at 1 month post-MI and therefore worse cardiac function [207]. In addition to this, circulating levels of CX3CL1 were found to be increased in patients with chronic heart failure in accordance with disease severity, in both cardiomyocytes and fibrous tissue [208]. Boag et al describe that STEMI patients with fewer circulating $CX3CR1^+$ lymphocytes following reperfusion have a poorer prognosis than those with increased circulating $CX3CR1^+$ lymphocytes, possibly due to an increase in recruitment of cytotoxic T cells to the injured heart tissue [209]. This study established that STEMI patient concentration of circulating CX3CL1 peaked at 90 minutes following reperfusion by PCI. Other studies have demonstrated that higher levels of STEMI patient circulating CX3CL1 at 24h post-reperfusion were predictive of MACE and reduced myocardial salvage [210].

In addition to its apparent role in compromising cardiac repair and promoting myocardial damage, the CX3CL1/CX3CR1 axis has also been shown to hold predictive value for those at risk of cardiovascular disease. It has been reported that the CX3CR1 I249 allele markedly reduces the risk of acute coronary events independent of established coronary risk factors, and is therefore an independent genetic risk factor for CAD [211]. A direct correlation between CX3CR1 V249I and T280M polymorphisms with the occurrence of acute fatal MI has also been reported [212]. These alleles were found to code for CX3CR1 that is overexpressed by activated inflammatory cells, with a higher binding affinity for CX3CL1. It has also been shown that homozygosity for the rare CX3CR1 alleles I249 and M280 is associated with an increased risk of brain infarction [213]. This study also showed that heterozygosity for the CX3CR1 I249 allele increases adhesion of monocytes to immobilised CX3CL1.

The CX3CL1/CX3CR1 axis has also been held partly accountable for the development and progression of atherosclerotic plaques. In mouse models, deletion of CX3CR1 decreases plaque size by reducing macrophage recruitment and adhesion, while an antagonist of CX3CR1 reduced the levels of inflammatory monocytes which in turn decreased the size of atherosclerotic lesions [214, 215]. Plaque size was also improved by a vaccine targeting CX3CR1, which led to the production of anti-CX3CR1

antibodies leading to reduced macrophage infiltration and diminished lipid deposition [216]. Injection of a long-acting CX3CL1 into mice was also found to attenuate atherosclerosis, by reducing monocyte adhesion to endothelial cells [217]. Such evidence suggests that CX3CL1 contributes to atherosclerotic plaque burden, through mechanisms including monocyte survival, recruitment, and extravasation into plaque lesions, which in turn potentiate the immune response. While the exact contribution of each mechanism is not completely clear, there is considerable evidence that inhibition of CX3CL1 may be successful at reducing atherosclerotic lesions by impairing the monocyte response.

Based on this evidence from both experimental models of MI and STEMI patients, the CX3CL1/CX3CR1 axis appears to have a direct and critical role in the extent of repair and therefore function of the heart following cardiac I/R. Inhibition or neutralization of CX3CL1 or inhibition of its receptor CX3CR1 may therefore offer an effective therapeutic target to improve long term outcome in STEMI patients.

1.4.5 CX3CL1/CX3CR1 Signalling

The precise downstream signalling pathways that are activated following binding of CX3CL1 to its receptor CX3CR1 are not clearly defined to date. Reported pathways that have been shown to be activated downstream of CX3CL1/CX3CR1 include Raf-1/MEK1/2-ERK1/2, phosphoinositide 3-kinase (PI3K)/Akt, and NFκB signalling. One of the most well-established functions downstream of CX3CR1 signalling is an anti-apoptotic pathway. A key study by Landsman et al showed that interaction of CX3CL1 with CX3CR1 is required for the survival of $CX3CR1^{+}$ non-classical monocytes [218]; CX3CR1 activation induces upregulation of the anti-apoptotic genes Bcl-2 and B-cell lymphoma-extra large (Bcl-XL). In the absence of CX3CL1 in homeostatic conditions, counts of circulating non-classical monocytes decreased and introduction of the Bcl-2 transgene into $CX3CR1^{-/-}$ mice rescued levels of non-classical monocytes in the blood [218]. Furthermore, addition of CX3CL1 to cultured human monocytes showed that treatment with the ligand reduced serum-induced and oxysterol-induced monocyte death. White et al report that CX3CL1-induced pro-survival signals in monocytes is also dependent on oxidative stress; an increase in the survival of cells following serum-

starvation correlated with reduced levels of intracellular ROS. Finally, treatment with CX3CL1 increased levels of hypoxia-inducible factor-1α (Hif1α), which is known to regulate the expression of genes regulating both apoptosis and angiogenesis [219]. Interestingly, recombinant soluble CX3CL1 (full length without transmembrane anchor, aa 1-337) has been shown to protect primary human monocytes from apoptosis [218], in contrast to mice whereby this effect is mediated by full-length transmembrane–, but not soluble CX3CL1 [220].

This pro-survival function of CX3CL1/CX3CR1 signalling has also been documented in brain microglial cells, via tight regulation of Bcl-XL [221]. Furthermore, activation of the PI3K-Akt pathway by CX3CL1 stimulation has shown to promote the survival of vascular SMCs [222, 223], neuronal cells [224], T-helper cells, and endothelial cells during angiogenesis [225]. Interestingly the two isoforms of CX3CL1 confer different effects on $CX3CR1^{+}$ cell survival; in a $CX3CL1^{-/-}$ mouse model, transgenic introduction of CX3CL1 did not recover the depleted population of circulating non-classical monocytes [226]. The CX3CL1/CX3CR1 axis also functions to reduce apoptosis in pancreatic tumour cells [227]; CX3CL1 induced activation of the Akt/NFκB/p65 signalling cascade to increase the expression of Bcl-XL and Bcl-2, and inhibited caspase-3 cleavage, thereby inhibiting apoptosis in pancreatic cells and promoting tumour development. This effect was blocked by inhibition of the NFκB pathway. Activation of the NFκB pathway by CX3CL1 also markedly enhanced cell cycle transition from the G1 to the S phase, thus promoting the proliferation and growth of pancreatic cancer cells.

In addition to this pro-survival function of the CX3CL1/CX3CR1 axis, studies have also demonstrated the importance of CX3CL1/CX3CR1 signalling in the adhesion and migration of $CX3CR1^{+}$ cells, predominantly monocytes. CX3CL1-induced activation of downstream SAPKs (via Src activation), ERKs (via Syk activation), and PI3K pathways are reported to work in conjunction to mediate CX3CL1-dependent adhesion of human monocytes [228]. Inhibitors of all such kinases are successful in reducing monocyte adhesion, indicating that a complex, integrated array of signal transduction pathways is necessary to complete full CX3CL1-dependent monocyte adherence. Liu et al [229] demonstrated that monocyte/macrophage-specific deletion of Ras homolog

gene family member A (RhoA) downregulates CX3CR1 and reduces monocyte/macrophage recruitment to inhibit chronic rejection of mouse cardiac allografts, suggesting a role for the RhoA/ROCK pathway in CX3CR1-mediated monocyte function. In mouse models, monocytes have been shown to rely on MAPK-independent activation of Syk by CX3CL1 for proper reorganization of the actin cytoskeleton and thus monocyte chemotaxis to CX3CL1 [230]. The chemokine CCL2, which is heavily involved in classical monocyte recruitment from the bone marrow and spleen, has been shown to regulate CX3CR1-dependent monocyte adhesion; CCL2 induces a rapid increase in CX3CR1 surface density on human monocytes and significantly increases monocyte adhesion to immobilized CX3CL1 via activation of the p38 MAPK pathway [231]. CX3CL1 stimulation has also been shown to activate the epidermal growth factor receptor (EGFR) to regulate cell proliferation in human vSMCs [222]; activation of CX3CR1 leads to the release epiregulin, which activates its receptor EGFR leading to PI3K activation and subsequent Akt phosphorylation. Notably, PI3K activation via EGFR, but not ERK, is essential for the anti-apoptotic effect of CX3CL1. PI3K activation is also required for proliferation, and without dual activation of both ERK and PI3K pathways, proliferation will not proceed. Finally, CX3CL1 stimulation has been shown to mediate intracellular Ca^{++} signalling; CX3CL1 increased the transient amplitude of Ca^{++} and decreased phosphorylation of cardiac troponin I, suggesting that CX3CL1 depresses myocyte contractility by mechanisms downstream of intracellular calcium [232].

The CX3CL1/CX3CR1 axis is known to positively regulate itself, as activation of endothelial-expressed CX3CR1 by CX3CL1 leads to upregulated expression of the receptor by the endothelium [223]. In this way, the CX3CL1/CX3CR1 axis acts in a positive feedback loop to upregulate its downstream signalling pathways.

While research has implicated a detrimental role for CX3CL1/CX3CR1 signalling in the pathophysiology of myocardial I/R, no treatments specific for the CX3CL1/CX3CR1 axis have been translated into clinical use due to the inadequate understanding of its physiological mechanism. Further studies are therefore highly desired to evaluate the role and molecular mechanisms regulating CX3CR1-mediated non-classical monocyte function following cardiac I/R.

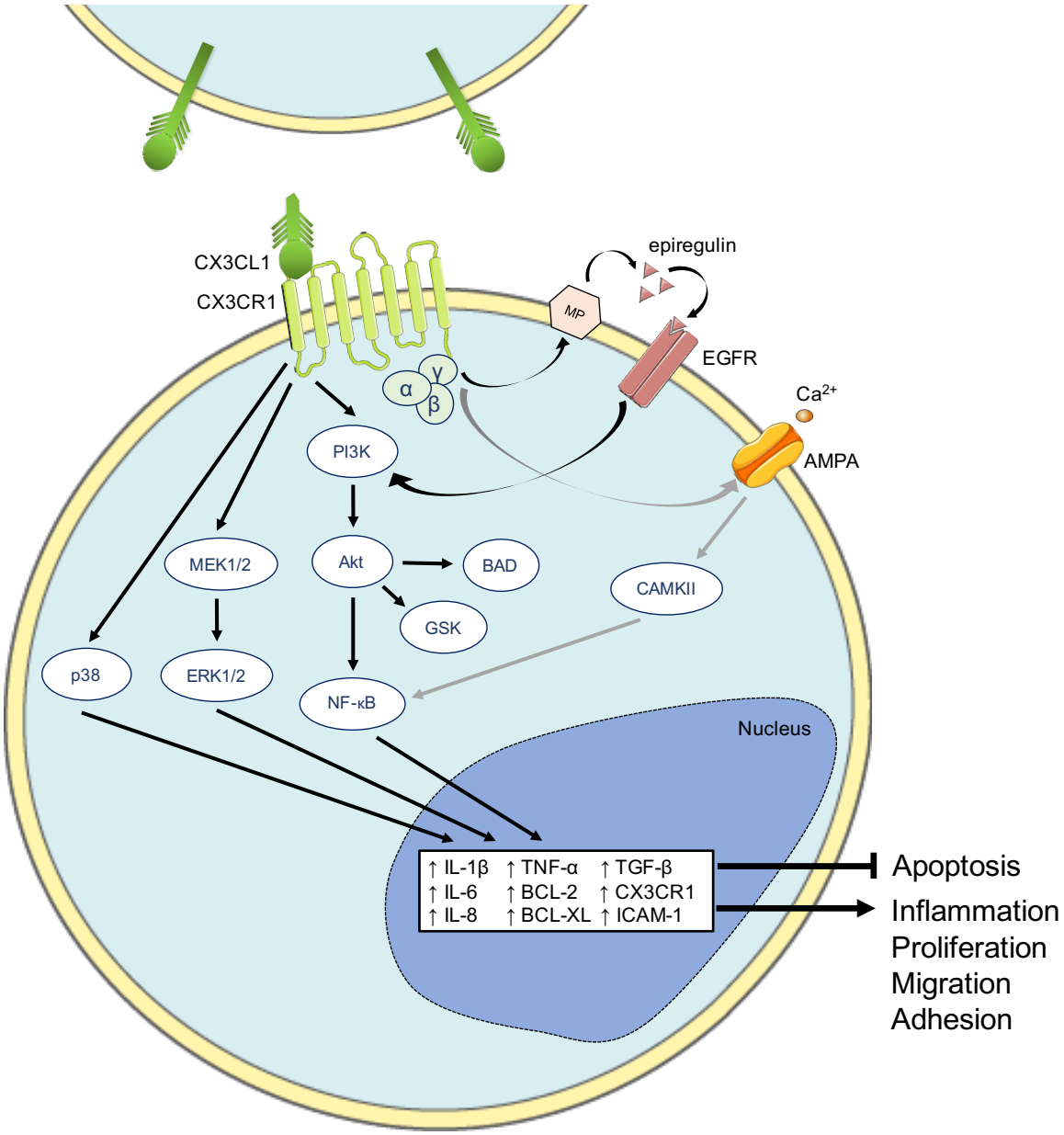
CX3CL1
CX3CR1
epiregulin
MP
EGFR
Ca2+
AMPA
γ
α
β
PI3K
MEK1/2
Akt
BAD
GSK
CAMKII
p38
ERK1/2
NF-κB
Nucleus
↑ IL-1β ↑ TNF-α ↑ TGF-β
↑ IL-6 ↑ BCL-2 ↑ CX3CR1
↑ IL-8 ↑ BCL-XL ↑ ICAM-1
Apoptosis
Inflammation
Proliferation
Migration
Adhesion

Figure 1. 5. CX3CL1/CX3CR1 Signalling Pathways.

The signalling pathways that are activated downstream of CX3CR1 are poorly understood, however a range of pathways have been shown to be activated in response to CX3CL1. Inhibition of apoptosis is the most established function downstream of CX3CL1/CX3CR1 signalling, occurring in a range of cell types including monocytes. MAPK (ERK) and PI3K pathways are reported to be involved in CX3CL1-dependent adhesion of human monocytes. CX3CR1 activation can lead to the release of epiregulin which activates its receptor EGFR leading to PI3K activation. Intracellular Ca^{++} signalling is mediated by CX3CR1 activation which can subsequently induce the NFκB pathway. CX3CL1/CX3CR1 signalling therefore represents a complex, complicated array of downstream signalling pathways which govern the function of different $CX3CR1^{+}$ leukocytes.

1.5. The NFκB Signalling Pathway

1.5.1 NFκB Pathway Stimuli and Target Genes

The NFκB Signalling pathway is divided into two main pathways known as the i) canonical (classical) pathway and ii) non-canonical (alternative) pathway. These two pathways have different mechanisms of signalling, however are both crucial for regulating immune and inflammatory responses [233-235]. A diverse range of soluble and membrane-bound extracellular ligands activate the NFκB canonical pathway, including ligands of various cytokine receptors, PRRs [236, 237] , TNF receptor superfamily members, T-cell receptor (TCR) and B-cell receptor (BCR)s [25, 238, 239]. Other stimuli including chemical agents, environmental stresses, ischemia/hypoxia, and reoxygenation are also inducers of the NFκB pathway [240-242]. In line with its broad repertoire of stimuli, the NFκB pathway regulates the expression of an equally diverse array of immunomodulatory cellular genes, including cytokines, chemokines, adhesion molecules, antimicrobial factors, cell cycle regulators, and cell survival factors. This NFκB regulation of gene expression occurs in a stimulus- and cell type-specific manner, leading to the finely tuned regulation of only a subset of NFκB-responsive genes.

The non-canonical 'alternative' NFκB pathway is activated by immunomodulatory factors including the TNF-family cytokines, lymphotoxin β (TNFSF3) [243, 244], CD40 ligand (CD40L and TNFSF5) [243], B cell activating factor (BAFF and TNFSF13B) [245], and receptor activator of NFκB ligand (RANKL and TNFSF11) [246], but not TNF-α [247-249]. Activation of this canonical pathway leads to induction of a different signalling pathway to that of the canonical pathway [245], and thus induces regulation of different sets of NFκB-responsive genes.

In addition to its primary function as an inducible transcription factor, NFκB also controls the expression of other transcription factors, highlighting its importance in the activation of other pathways and the indirect control of expression of other sets of genes [43]. Studies have also demonstrated that NFκB activation can have contrasting roles in same-cell lineage, depending on the physiological context [250].

One of the most well-recognized functions of NFκB is its regulation of inflammation. While NFκB can engage in direct transcriptional induction of pro-inflammatory cytokines, chemokines, and inflammatory mediators in a range of different innate immune cells, its activation can also induce inflammation through indirect mechanisms such as promoting the activation, differentiation, and effector function of inflammatory T-cells [251-253], and promoting M1 inflammatory macrophage polarization [254]. NFκB also has a role in regulating the activation of inflammasomes [255]. NFκB therefore represents a complex, tightly regulated signalling pathway whose aberrant activation underlines a wide range of chronic inflammatory diseases [25, 250, 256]. The specific role of NFκB pathway induction in driving cardiovascular disease is discussed in section 1.5.3.

1.5.2 The Canonical NFκB Signalling Pathway

The work described in this thesis focuses on activation of the canonical, classical pathway of NFκB signalling, therefore the details of this pathway are described herein. Activation of the canonical pathway is dependent on the phosphorylation and inactivation of a protein known as the inhibitor of κB (IκB), which inhibits activation of the NFκB complex [257]. In the absence of an appropriate stimulus, the NFκB subunits p65 (RelA), p50 (RelB) and c-Rel are sequestered in the cytoplasm by the IκB family of inhibitors. This sequestration specifically blocks the nuclear localization signals on the NFκB subunits thus preventing its transfer to the nucleus. In this classical canonical signalling pathway, a specific stimulus transduces a signal to a protein kinase, namely transforming growth factor beta-activated kinase 1 (TAK1), which subsequently induces phosphorylation of the downstream IKK complex. The IKK complex is composed of two catalytic subunits, IKKα and IKKβ, and a regulatory subunit known as NFκB essential modulator (NEMO) (or IKKγ) [258]. TAK1-induced phosphorylation of the IKK complex typically occurs on the IKKβ subunit, which subsequently stimulates phosphorylation of IκB. IKK phosphorylates the IκBα subunit at two N-terminal serine residues which triggers ubiquitin-dependent degradation of IκBα in the proteasome, and therefore results in Its dissociation from the NFκB subunits p65, p50 and c-Rel [259, 260]. As NFκB is no longer held in the cytoplasm

by its IκB inhibitors it can then rapidly translocate into the nucleus to regulate transcription of its target genes. The NFκB subunits p65, p50 and c-Rel all have transactivation domains (TAD)s at their C-terminus which governs their ability to regulate the expression of target genes.

A range of different stimuli can activate this canonical NFκB pathway, including cytokines, growth factors, mitogens, stress mediators, and bacterial components. Each stimulus has its own specific NFκB signalling specificities, highlighting the complexity of the NFκB system, however the majority of signals converge on the IKK complex [261, 262].

Canonical NFκB Pathway

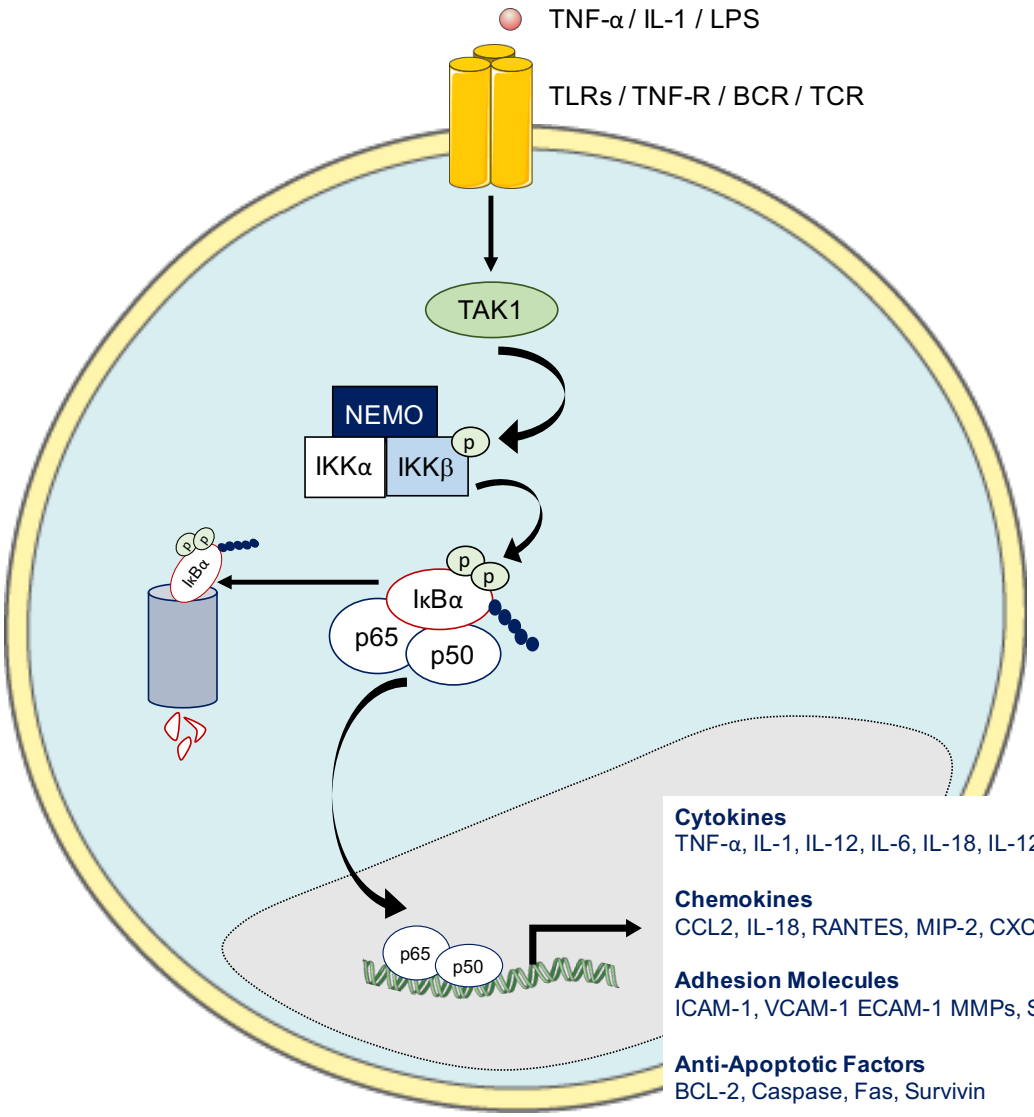

Figure 1. 6. The Canonical NFκB Signalling Pathway.

Activation of the canonical 'classical' NFκB pathway controls the transcription of a plethora of genes in response to a diverse range of stimuli. The NFκB subunit dimers p65 and p50 are sequestered in the cytoplasm by the inhibitor IκBα during resting state. In the presence of a stimulus such as TNF-α, a signal is transduced to the tyrosine kinase TAK1 which subsequently induces phosphorylation of the IKKβ subunit of the IKK complex. Activated IKKβ phosphorylates IκBα leading to its ubiquitin-dependent degradation by the proteasome and resulting dissociation from NFκB p65/p50. These liberated subunits can then rapidly and transiently translocate into the nucleus to regulate genes involved in the response to inflammation and infection such as cytokines and chemokines as well as antigens and immunoreceptors. Other target genes are linked with response to stress and apoptosis as well as growth factors, ligands and enzymes.

1.5.3 The NFκB Signalling Pathway in Cardiovascular Disease

Activation of NFκB constitutes the central part of many cardiovascular inflammatory diseases, and has proven to have a key role in cardiac I/R [263]. NFκB targets inflammation not only directly by increasing the production of inflammatory cytokines, chemokines and adhesion molecules, but also by regulating cell proliferation, apoptosis, morphogenesis and differentiation, therefore it is not surprising that deregulated NFκB signalling has been linked with the development of cardiovascular disease. A number of studies in mouse models of cardiac I/R have demonstrated that inhibition of the NFκB pathway is beneficial to myocardial repair following I/R. Cardiac I/R has shown to increase the DNA binding activity of the NFκB subunits p50 and p65, which leads to an increase in IL-18 expression. Pharmalogical neutralization of IL-18 significantly reduced infarct size, therefore suggesting that NFκB activation may potentiate injury following I/R [264]. Inhibition of IKKβ by Bay 65-1942 in a mouse model of I/R reduced infarct size and preserved cardiac function when administered intraperitoneally either prior to ischemia, at reperfusion, or at 2h following reperfusion, through attenuated inflammation as measured by decreased serum levels of TNFα and interleukin-6 (IL-6) [265]. Chronic inhibition of NFκB signalling in mice has also shown to reduce mortality from heart failure, decrease inflammatory cytokine secretion (IL-1β, IL-6, and TNFα), and diminish levels of apoptosis [235]. Deletion of the NFκB subunit p50 has shown to reduce the extent of I/R injury in vivo, through a mechanism that is associated with decreased neutrophil infiltration into the infarct [266]. A number of other studies have also reported that the extent of I/R injury, which contributes up to 50% of the total infarct size, can be improved by inhibition of the NFκB pathway [267, 268]. Other agents that inhibit NFκB signalling including sulfasalazine and acetylsalicylic acid have also shown a beneficial effect on patient cardiac function following MI [269].

1.5.4 CX3CL1 and NFκB Signalling

A number of studies have provided evidence for a relationship between the CX3CL1/CX3CR1 axis and the NFκB signalling pathway. In a recent study, Ganga et al showed that CX3CL1 induces activation of the NFκB pro-inflammatory signalling pathway through MSK1 in microglial cells [270]. Knockdown of MSK1 with siRNA decreased MSK1 protein levels by ~50%, which was enough to decrease CX3CL1-induced mRNA levels of IL-1β, TNF-α and iNOS. The absence of CX3CR1 also impaired the mRNA levels of NFκB p65 genes regulated by this transcription factor. In a mouse model of sepsis, Raspe et al demonstrated that NFκB can reverse-regulate CX3CL1 and CX3CR1 during cecal ligation and puncture-induced sepsis (CLP)-induced sepsis; CLP stimulated upregulation of CX3CL1 and downregulation of CX3CR1, in a mechanism that is mediated by NFκB, likely via reduced liberation of proinflammatory cytokines [271]. In rat aortic SMCs, TNF-α induces the expression of CX3CL1 and CX3CR1 in a mechanism mediate by NFκB activation. This study also found that CX3CL1 induces its own expression, which is also mediated by the PI3K/Akt/NFκB signalling pathway [272]. In hippocampal neurons, CX3CL1 induces translocation of the NFκB subunit p65 into the nucleus. This process is abrogated by a specific inhibitor of PI3K, suggesting that CX3CL1 activates NFκB through the PI3K/Akt pathway in hippocampal neuronal cells [273]. In intestinal epithelial cells, CX3CL1 activates NFκB and which results in IL-8 and CX3CL1 mRNA expression [274]. Activation of NFκB has also been shown to be involved in TNF-α stimulated CX3CL1 production in vascular SMCs. Downregulation of p65/NFκB signals by pertussis toxin (PTX) may provide an explanation for the anti-CX3CL1 effect of PTX [275]. The shedding and release of soluble astrocytic CX3CL1 has also shown to potentially involve the NFκB pathway alongside ADAM10 protease [276]. Such studies provide preliminary evidence for the involvement of the NFκB pathway in CX3CL1/CX3CR1 signalling. Further research connecting CX3CL1 to the NFκB pathway is therefore necessary to confirm and build upon this existing knowledge. Therapeutic modulation of NFκB activity via manipulation of the CX3CL1/CX3CR1 axis in the heart temporally and spatially may therefore offer a key target to prevent a

chronic or prolonged inflammatory state following cardiac I/R, and in turn improve myocardial repair.

Chapter 2.0. Hypotheses & Aims

While the monocyte response to MI has been investigated previously in mouse models of the disease, there have been discrepancies in both the temporal dynamics and function of non-classical monocytes in the response to cardiac I/R. Such differences may be due to variation in the method of defining these cells, or the study of permanent MI models versus models of cardiac I/R which are known to have a different pathophysiology. This is in contrast to the function of classical monocytes whose role in the immune response to MI is well described. The unclear function of non-classical monocytes may be linked to their high expression of the fractalkine receptor, CX3CR1, though the signalling pathways downstream of this unique receptor are poorly defined. The CX3CL1/CX3CR1 axis has been strongly linked to the extent of myocardial damage following cardiac I/R, and points to the involvement of $CX3CR1^{+}$ non-classical monocytes in potentiating injury in the acute post-reperfusion period.

The principle hypotheses of this thesis are:

i. STEMI patient circulating non-classical monocytes have distinct temporal dynamics in the acute post-reperfusion period, which are associated with subsequent myocardial outcomes. Pre-clinical mouse models show a similar pattern of non-classical monocyte dynamics following cardiac I/R.

ii. Genetic knockout of the fractalkine receptor CX3CR1 in a mouse model of cardiac I/R compromises monocyte adhesion and infiltration into the injured myocardium which influences repair and myocardial function following MI.

iii. Activation of monocyte-expressed CX3CR1 by CX3CL1 binding induces downstream activation of the NFκB pathway which promotes the pro-inflammatory function of non-classical monocytes.

These hypotheses were addressed in the corresponding aims:

i. Determine the precise dynamics of circulating monocyte subpopulations in STEMI and NSTEMI patients at time points from ischemia to 24h post-PCI by FACS analysis, and investigate their relationship with STEMI infarct size and LVEF. Quantify mouse monocyte subpopulations at similar time points following cardiac I/R to identify inter-species similarity in monocyte dynamics.

ii. Investigate adhesion and recruitment of monocyte subpopulations into the injured myocardium following cardiac I/R by using immunofluorescent staining to quantify myocardial post-capillary venule endothelial monocyte adhesion and monocyte infiltration in the infarct region at 2h, 24h, and day 3 post-I/R. Determine the effect of CX3CR1 knockout by comparing $CX3CR1^{+/+}$, $CX3CR1^{+/GFP}$, and $CX3CR1^{GFP/GFP}$ phenotypes.

iii. Examine activation of the NFκB pathway in human monocytes in response to CX3CL1 stimulation by investigating phosphorylation of the NFκB subunit p65 and regulation of downstream target genes IL-1β, IL-6, IL-8 and IκBα.

Together this information will shed light on the exact dynamics of non-classical monocytes following reperfusion, the role of CX3CR1 expression in this response and its relation to cardiac function after MI. A greater understanding of the behaviour of $CX3CR1^{+}$ non-classical is critical to understand the process of repair following I/R, and therefore develop therapeutic strategies to optimise healing.

Chapter 3.0 Materials & Methods

3.1 Retrospective STEMI Patient Study

Analysis of previously obtained FACS data (courtesy of Dr. Stephen Boag and Professor Ioakim Spyridopoulos) was used to quantify monocyte subpopulations in the blood of 53 STEMI patients presenting with acute STEMI to the Freeman Hospital, Newcastle upon Tyne, at the time of PPCI for acute MI, and at 15, 30, 90 minutes (arterial blood) and 24 hours (venous blood) post-reperfusion. In a subset of 23 patients, a follow up venous blood sample was collected at 3-6months. The original study was designed to analyse lymphocyte responses in STEMI patients (Boag et al JCI 2015), however the FACS data obtained allowed additional interrogation of monocyte subset responses post-MI (used here in this retrospective study). Inclusion criteria for STEMI patients included onset of chest pain within 6 hours and new ST segment elevation on ECG of 0.1mV in at least two contiguous leads. A detailed list of inclusion and exclusion criteria is described in Table 3.1. A group of 15 NSTEMI patients undergoing non-emergency angiography with PPCI were also recruited as a control group for the study, in order to investigate whether any changes in the STEMI group were related to I/R rather than a procedure-related outcome of PPCI. STEMI patient infarct size and MVO were assessed using cardiac MRI 1-8 days post-reperfusion. Each blood sample was analyzed using BD FACS FlowJo acquisition software.

3.1.1 Clinical Database of STEMI Patients

A clinical database of STEMI and NSTEMI patients enrolled in the retrospective STEMI patient analysis is listed in Chapter 4, Table 4.1.

Inclusion Criteria	Exclusion Criteria
Onset of chest pain within 6 hours with new ST segment elevation of 0.1mV in at least two contiguous leads	Cardiogenic shock
	Previous myocardial infarction or coronary artery bypass grafting (CABG)
	A known active malignant process
	Active infection
	Chronic inflammatory conditions requiring treatment with immunosuppressive agents
	Pre-existing contraindications to cardiac MRI scanning e.g. pacemaker, severe claustrophobia, breathlessness or frailty likely to limit tolerability of scan
	Patent arterial flow (Thrombolysis in Myocardial Infarction (TIMI) grade 2 or 3 flow) in infarct related artery on initial angiography
	Presence of visible collateral circulation supplying infarct region
	Inability or unwillingness to give informed consent

Table 3. 1. List of inclusion and exclusion criteria for retrospective and prospective STEMI patient studies.

3.1.2 Monocyte Subpopulation Flow Cytometry Analysis

Total monocytes were first gated based on their characteristic forward and side scatter properties. Any T-cells and NK-cells confounding this total monocyte population were then removed using CD3-FITC (clone UCH-T1, #555332, BD Biosciences), and CD56–PerCP-eFluor710 (clone CMSSB, #42-0567-42, eBioscience), respectively. Monocyte subsets were then defined using CD16-PE (clone B73.1, #561313, BD Biosciences), to quantify classical ($CD16^-$), intermediate ($CD16^+$) and non-classical ($CD16^{++}$) monocytes (see Figure 4.1). This analysis generated relative numbers of monocyte subsets for all patient samples. The absolute cell counts of each monocyte subset were then calculated using these relative values in conjunction with previously determined absolute counts for the parent monocyte population in the TruCount assay, as described in the following formula:

$$\text{Absolute count} = \left(\frac{\text{subset events}}{\text{parent events}}\right) \text{x parent absolute count (TruCount)}$$

3.2 Prospective STEMI Patient Flow Cytometry Analysis

3.2.1 Patient Recruitment/Populations, Primary Percutaneous Coronary Intervention, and Blood Sampling

A cohort of 13 STEMI patients were prospectively recruited to the Freeman Hospital, Newcastle-upon Tyne. Inclusion criteria was onset of chest pain within 6 hours with new ST segment elevation. Exclusion criteria were as described for the retrospective study (Table 3.1). Coronary angiography and PPCI were performed, and arterial blood was acquired at the start of the procedure, then at 90 and 180 minutes following reperfusion (Figure 3.1). Arterial blood was collected from the aorta, right coronary artery (RCA) and left coronary artery (LCA) to compare monocyte dynamics between pre-reperfusion vasculatures. Venous blood was obtained at 24 hours. Ethical approval for this prospective study was obtained from the National Research Ethics Service (NRES) North East Ethics Committee and NHS permissions granted by Newcastle University Hospitals NHS Trust (REC reference: 16/NE/0405).

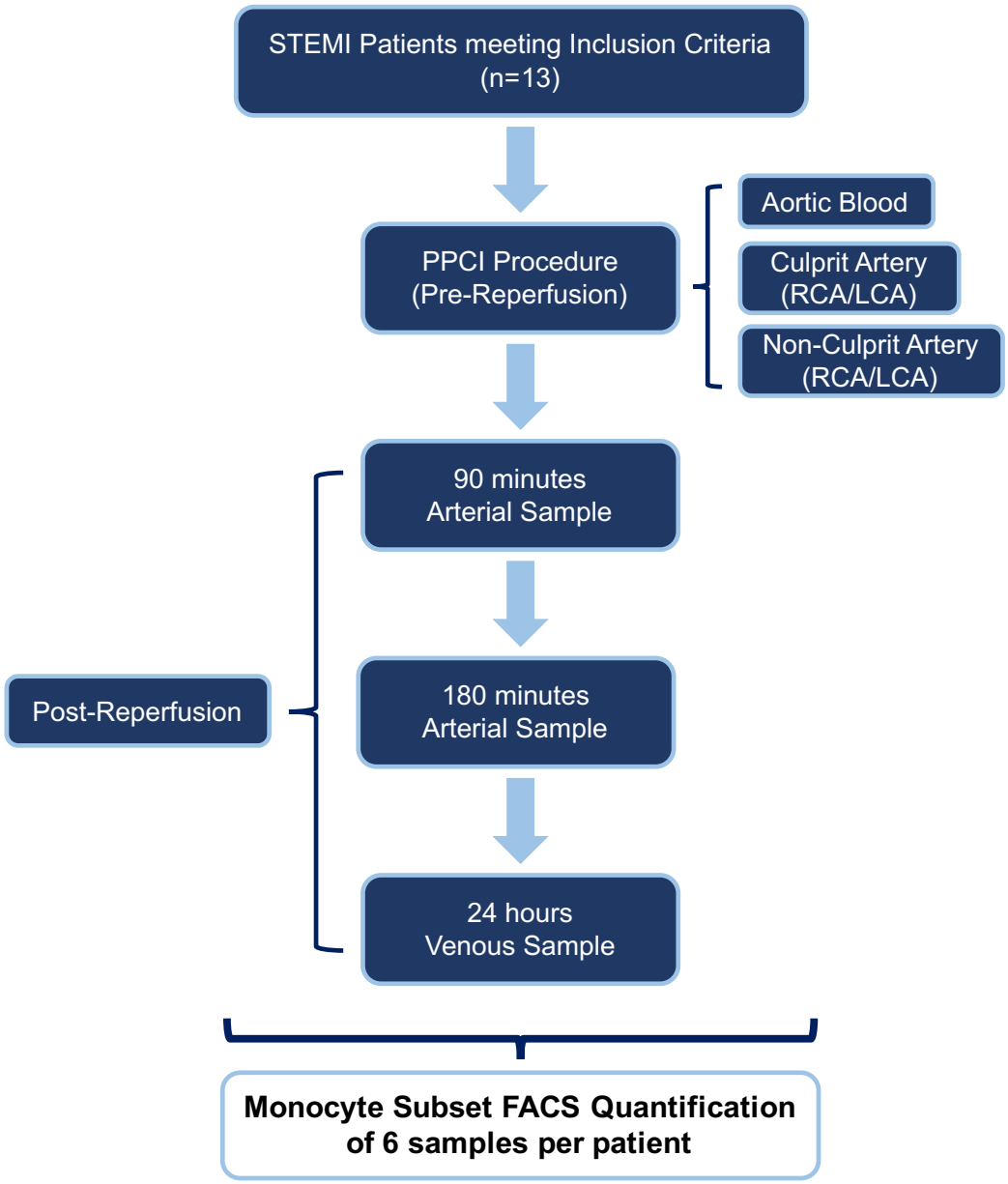

Figure 3. 1. Prospective STEMI Patient study design. Blood was taken at the indicated time points for subsequent FACS analysis of monocyte subpopulations.

3.2.2 Total Monocyte TruCount Assay

Blood was obtained as above in 4 ml EDTA tubes (BD Biosciences). Absolute counts of total monocytes were determined by the clear forward/side scatter gate of monocytes and TruCount beads (BD Biosciences, #340334).

3.2.3 Eight-Colour Flow Cytometric Assay: Quantification of Monocyte Subpopulations

Absolute counts of monocyte subpopulations were determined using an eight-colour flow cytometric assay, in conjunction with the total monocyte counts obtained in the TruCount assay. Per patient time point, 50µl of whole blood was stained with a cocktail of the following antibodies (5µl of each antibody): CD14-BV510 (clone M5E2, #301842), CD16-APC-H7 (clone 3G8, #560715, BD Biosciences), HLA-DR-BV421 (clone L243, #307636), CD3-FITC (clone UCHT1, #300406), CD19-FITC (clone HIB19, #302206), CD56-FITC (clone HCD56, #318304), CCR2-PE-Cy7 (clone K036C2, #357212), CX3CR1-APC (clone 2A9-1, #341610). All antibodies were supplied from BioLegend unless stated otherwise (Table 3.6). Samples were then lysed using Pharm Lyse solution (BD Biosciences) diluted 1/10 in dH_2O for 15 minutes at RT, followed by two wash steps using a BD Lyse Wash Assistant machine (BD Biosciences). Analysis was performed using a BD LSRFortessa machine with FCS Express 6/7 De Novo Software. Manual compensation was performed using compensation beads (UltraComp eBeads, #01-2222-41, Invitrogen). One drop of eBeads was added to a 3µl sample of each individual antibody. Unstained whole blood was used as a universal negative control to set up compensation. Compensation control samples were acquired on a BD LSRFortessa machine and analysed using FCS Express 6/7 De Novo Software to set up a compensation matrix which could then be applied to patient blood samples. A thorough and reproducible method of classical, intermediate, and non-classical monocyte subset classification was performed as illustrated in Figure 4.8. The cell count for each subset was calculated as the count of the parent population (derived from TruCount assay above) multiplied by the percentage of the parent cells within the subset gate, as previously described.

3.3 Mouse Lines and Genotyping

All animal procedures were performed under a UK Home Office license.

3.3.1 Mouse Lines

The care and use of animals were in accordance with the UK Government Animals (Scientific Procedures) Act 1986 and were approved by Newcastle University's Animal Welfare and Ethical Review Body. Wild type C57BL/6 male mice were purchased from Charles River UK. $CX3CR1^{EGFP}$ mice on the C57BL/6J background were provided by Dr. David Grainger (University of Manchester), with permission from Steffen Jung [277]. In this mouse line, the EGFP gene replaces the first 390bp of the second CX3CR1 exon encoding the N terminus of the seven-transmembrane receptor shown to be crucial for interaction with CX3CL1. Heterozygous $CX3CR1^{+/EGFP}$ mice have reduced fractalkine receptor expression and also serve as a reporter line, while $CX3CR1^{EGFP/EGFP}$ mice have a complete CX3CR1 knockout and report only an EGFP signal.

3.3.2 Genotyping: DNA Extraction

Tissue was obtained from mice ear clips for DNA extraction and the subsequent genotyping of each mouse. Ear clips were first incubated in 100µl lysis buffer 1 (section 3.3.5) for 1 hour in a thermomixer set at 95°C at 350rpm. After a brief vortex of the tubes, 100µl of lysis buffer 2 (section 3.3.5) was added to the clips. The tubes were then vortexed and centrifuged at 13,000 rpm for 5min to pellet any undigested tissue or debris. The resulting supernatant contained extracted DNA which was then stored at -20.C until required.

3.3.3 Genotyping: Polymerase Chain Reaction (PCR)

Each PCR reaction was made up to a total volume of 10ul in PCR tubes. Individual PCR reaction mixtures were calculated and made up for the appropriate number of animals to be genotyped. This consisted of 5µl 25mM MgCl2, 2.5µl 10x Reaction

Buffer IV, 0.2µl Red Hot Taq DNA Polymerase (all purchased from ABgene, Thermo Scientific), 0.25µl of each forward and reverse primer (20µM), 0.5µl 10mM dNTPs (New England Biolabs), 2µl template DNA and dH_2O made up to a final volume of 10µl. All primers used for genotyping are listed in Table 3.2. For each PCR, a negative (dH_2O) and positive control (animal confirmed positive) was included. PCR reactions were performed using the conditions detailed in Table 3.3 using a C1000 thermal cycler (Bio-Rad).

3.3.4 Genotyping: Agarose Gel Electrophoresis

For the visualization of PCR products, 2% agarose gels were prepared by dissolving 2g of DNA agar (Seakem LE Agarose for gel electrophoresis) in 100ml of 1xTAE buffer (section 3.3.5) and boiling in a microwave for 5-10 minutes until the agar was completely dissolved. Gel solution was topped up with 1xTAE to the original 100ml volume. The gel solution was then allowed to cool before adding 0.001% of Ethidium Bromide solution (10µl per 100ml) for later visualization of DNA bands. The gel was then carefully poured into a horizontal gel tray and well combs inserted and left to set for 45 minutes. Once set, the well comb was carefully removed and the gel was placed in an electrophoresis tank and fully immersed in 1xTAE buffer (section 3.3.5). A volume of 9µl of each PCR product was then loaded into the wells. A 1kb DNA ladder (Invitrogen) was also loaded alongside the samples to allow assessment of PCR product size. The loaded gel was left to run at approximately 80volts for 60 minutes. The DNA bands were finally visualised by exposure to UV light and image capture using a GeneGnome System and GeneSnap Software (Syngene Bio Imaging).

Primer		No. Bases	SEQUENCE	Product Size
CX3CR1	Trans	19	CTCCCCCTGAACCTGAAAC	CX3CR1 Transgenic ≈ 500bp CX3CR1 WT = 410bp
	WT	20	GTCTTCACGTTCGGTCTGGT	
	Common	19	CCCAGACACTCGTTGTCCT	

Table 3. 2. List of primers used for genotyping.

Total Rxn Vol	PROG	Cycle Details	Cycle. No.
10µl	GT-Cre	5 minutes at 95°C 30 seconds at 95°C 30 seconds at 62°C 90 seconds at 72°C 5 minutes 72°C 15°C forever	X 35

Table 3. 3. PCR reaction conditions used for genotyping.

3.3.5 Reagents, Solutions and Buffers

GoTaq G2 Hot Start Green Master Mix
Promega. Cat no. M7421, M7422, M7423.

Lysis buffer 1

(25mM NaOH and 0.2 mM EDTA) 2.5ml of 0.5M NaOH + 0.02ml of 0.5M EDTA in 50ml of milli-Q H_2O, adjust to pH12 with NaOH.

Lysis buffer 2

(40mM Tris-HCl) 4ml of 0.5M Tris-HCl in 50ml milli-Q H_2O, adjust to pH5 with HCl.

1X TAE Buffer

40mM tris base-acetate and 1mM EDTA

3.4 Mouse Model of Myocardial Ischemia-Reperfusion

Acute myocardial infarction was induced in adult male C57BL/6 mice, *Cx3cr1*$^{+/+}$, *Cx3cr1*$^{+/GFP}$ and *Cx3cr1*$^{GFP/GFP}$ mice (12-14 weeks of age) by an experienced microsurgeon (Dr. Rachael Redgrave). Mice were anaesthetised using isoflurane (3% isoflurane/97% oxygen) and general anaesthesia was maintained throughout the surgery using mechanical ventilation following endotracheal intubation. Under sterile conditions, left-side thoracotomy was performed through the fourth intercostal space and the left anterior descending coronary artery (LAD) was identified running from beneath the left atria towards the apex of the heart. To generate MI, a 7-0 prolene suture was placed under the LAD, (approximately 1-2mm distal to the left atria), and loosely tied in a double knot. A 1-2mm piece of PE-10 tubing was inserted into the suture loop and the knot was tightened and secured, causing occlusion of the LAD to create a transient infarction. Myocardial ischemia was verified by visible immediate blanching of the left ventricular myocardium. The chest wall was then temporarily closed and reopened after 60 minutes of ischaemia, followed by removal of PE tubing from the suture to allow reperfusion of the LAD. Sham-operated mice underwent thoracotomy and pericardial opening but no LAD ligation. After completion of the procedure, the chest was closed and anaesthesia was discontinued. In addition, the mice were administered 0.05mg/kg buprenophrine subcutaneously to alleviate post-operative pain. Mice were subsequently placed in a 33°C incubator and given soaked diet to facilitate recovery. At either 2h, 24h, 3 days, or 6 weeks following reperfusion, mice were humanely culled and heart tissue harvested.

3.5 Preparation of Tissue for Immunostaining

Hearts were dissected, washed in PBS to remove blood clots from the ventricle chambers and subsequently placed in a light fixative of 0.2% or 1% paraformaldehyde overnight at 4°C. Following fixation, hearts were transferred into a 30% sucrose solution and left at 4°C overnight. Hearts were then embedded in Optimal Cutting Temperature compound (OCT) for 30 minutes on dry ice and stored at -80°C until required. Tissue blocks were equilibrated to approximately -20°C for 30mins prior to sectioning. Transverse sections of 10μm thickness were cut from base to apex

following a sister section methodology (Figure 3.3) using a Lecia cryostat. Sections were collected apical to the ligature (Figure 3.2) and mounted on Superfrost (ThermoFisher Scientific) slides. Slides were then air dried for 30mins at RT prior to their storage at -80°C.

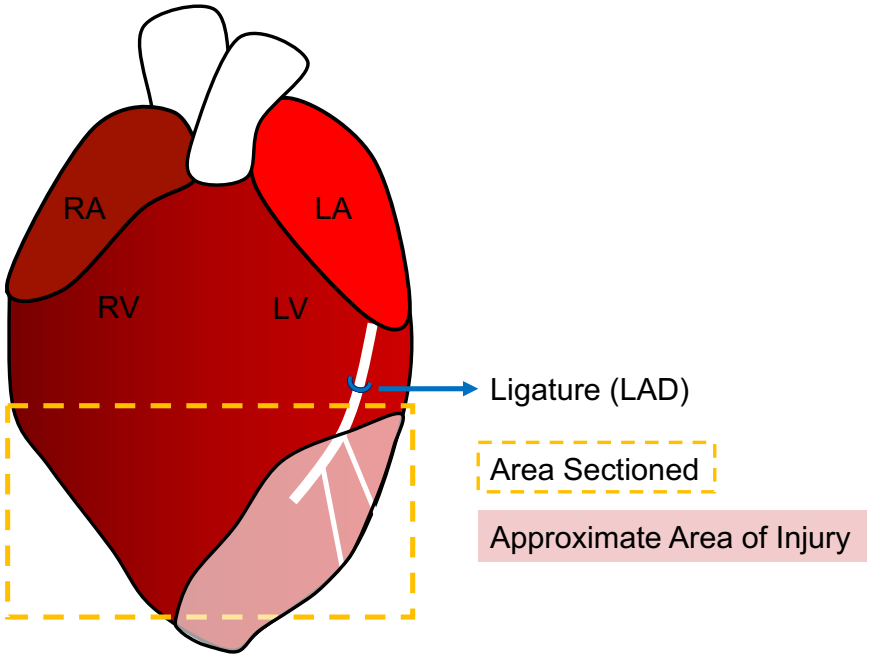

Figure 3. 2. Processing of mouse heart tissue.

Tissue was sectioned and collected from the ischaemic heart region, identified as the area between the LAD ligature and the apex of the heart. Naïve and sham heart sections were collected at approximately the same point in the heart.

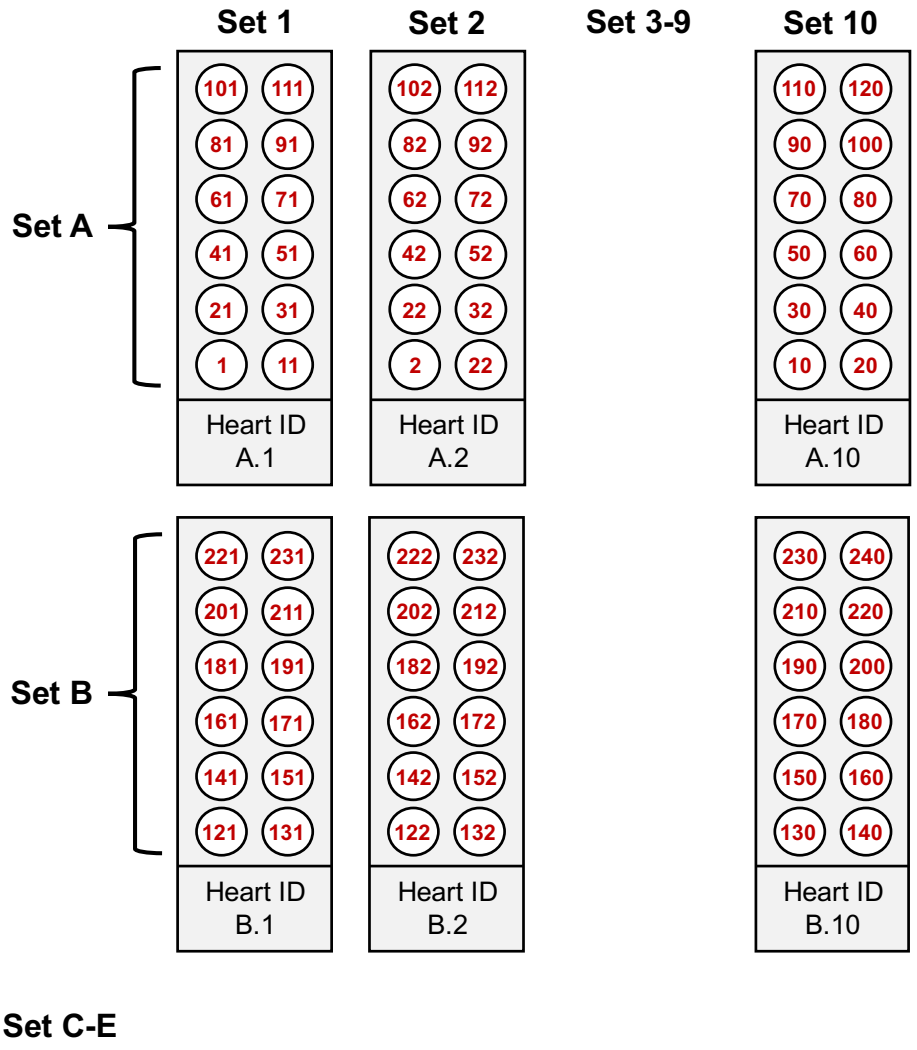

Figure 3. 3. Method of sister sectioning of mouse heart tissue.

Sister sectioning of tissue following a 10-sister set method ensured 10 sets of slides were created with each neighbouring 10µm section on any one slide separated by approximately 100µm of heart tissue. The numbers on the slides correspond to the order in which the sections were cut. Dependent on the size of the heart the number of sets per heart varied, generating up to 5 sets (from A-E) with 10-14 sections per slide. This method permits 10 different staining runs and allows analysis of similar heart regions between different experiments.

3.6 Immunofluorescence Staining of Leukocytes and Monocytes

3.6.1 Single CD45 Leukocyte Staining

Heart sections were air dried and fixed in 4% paraformaldehyde (PFA) for 10 minutes at room temperature (RT). Sections were washed for 5 minutes 3 times in PBS and subsequently permeabilised using 0.3% Triton-100 in PBS for 30 minutes at RT. Following permeablisiation, sections were blocked in 1% BSA for 30 minutes at RT. Appropriate concentrations of primary antibody (Table 3.8) were then added and left in a levelled, humidified staining chamber overnight at 4°C. On day 2, slides were washed three times in PBS to remove excess primary antibody. Secondary antibody staining was then performed for 2 hours at RT in the dark. After three 5 minute PBS washes, coverslips were mounted using Prolong Gold antifade reagent with DAPI (ThermoFisher Scientific) and left at 4°C overnight in the dark. Data was acquired using M2 Axio Imager (Zeiss). Images were taken at x5, x20 and x40 magnification and analysed using ZEN 2.3 software (Zeiss).

3.6.2 Multiplex CD11b CCR2 GFP Monocyte and Neutrophil Staining

Heart sections were air dried and briefly washed in PBS before being blocked in a solution of 5% goat serum, 1% BSA and 0.5% Tween20 for 2h at RT. Appropriate concentrations of primary antibody (Table 3.8) diluted in block solution were then added and left in a levelled, humidified staining chamber overnight at 4°C. On day 2, slides were washed three times in PBS to remove excess primary antibody. Tissue was then stained with appropriate secondary antibodies diluted in block solution for 2 hours at RT in the dark. After three 5 minute PBS washes, coverslips were mounted using Prolong Gold antifade reagent with DAPI and left at 4°C overnight. Data was acquired and analysed as previously stated.

3.6.3 Multiplex F4/80 GFP Macrophage Staining

Staining of heart tissue macrophages was performed as described in section 3.6.2 but using an Alexa Fluor 647 anti-mouse F4/80 Antibody (Table 3.8).

3.7 Imaging and Analysis

To calculate the density of leukocyte ($CD45^+$), monocyte ($CD11b^+GFP^+$), or macrophage ($F4/80^+$) infiltrate, 8 representative fields of view (FOV) were taken at x40 magnification within the infarct region (Figure 3.4). The number of positively stained cells of interest per FOV were then manually counted using the event function of Zen 2.3 software. Three sections per heart were used to calculate an average density per heart.

For the definition of $CD11b^+GFP^{mid}$ classical monocytes and $CD11b^+GFP^{hi}$ non-classical monocytes, the GFP MFI of randomly selected classical and non-classical monocyte cells in 40x images from three individual *Cx3cr1*$^{+/GFP}$ hearts was analysed. This was performed by manually drawing a line across the width of a given cell of interest which would then generate a Zen-automated value for the GFP MFI. This was performed for n=50 cells of each monocyte subpopulation.

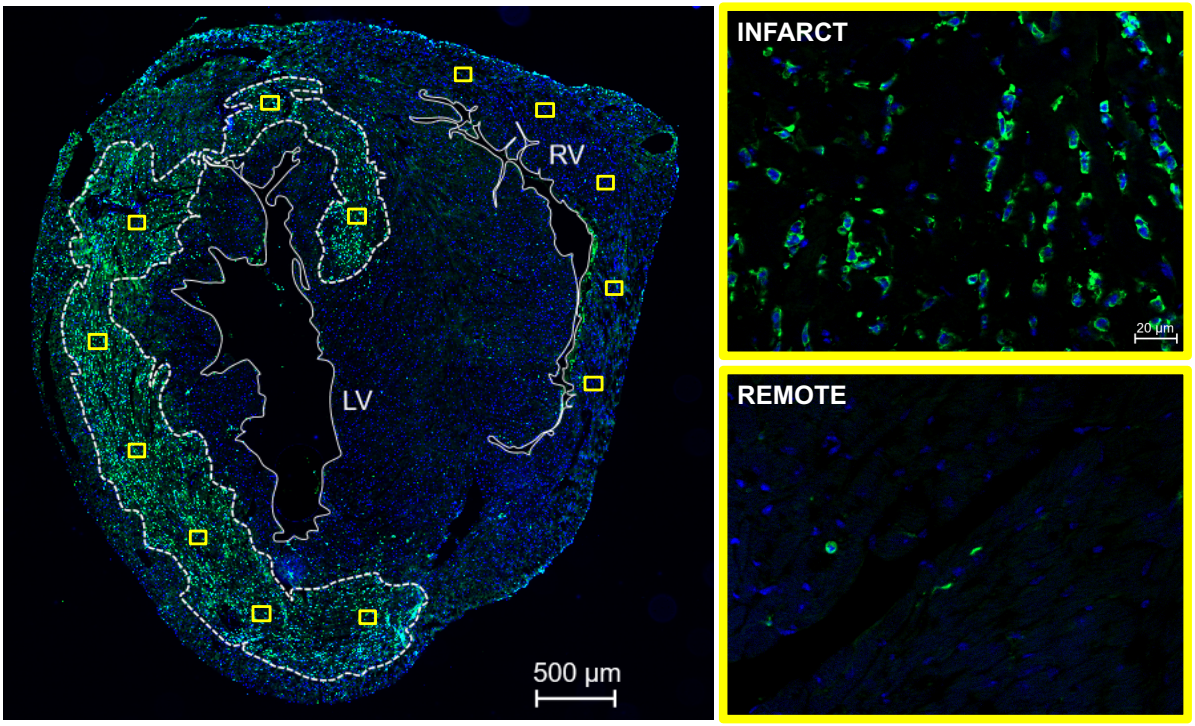

Figure 3. 4. Technique used to quantify cell counts of interest in mouse heart tissue.

Representative image of CD45 staining to quantify the density of leukocyte infiltrate in the injured mouse myocardium. Eight fields of views (yellow boxes) within the infarct region (dotted white line) that were considered representative of the infarct were imaged per section. For each FOV, an image was taken at x40 magnification and $CD45^+$ DAPI (nucleated) cells were manually counted on Zen 2.3 software. Three sections per heart were analysed and used to calculate an average number of leukocytes within the infarcted and remote regions. The same technique was applied to monocyte ($CD11b^+GFP^+$), neutrophil ($CD11b^+GFP^-$) and macrophage ($F4/80^+$) quantification.

3.8 Mouse Blood Sampling and Flow Cytometry Analysis

20-40µl tail-vein murine peripheral blood was collected into EDTA tubes (Teklab, #K100PP). Samples were incubated with Fc block (1/10 dilution) for 10 minutes at RT. Samples were incubated with antibodies against CD11b, CD115, Ly6G, LY6C, CCR2, and CX3CR1 (Table 3.7) for 30 minutes at RT in the dark. 1ml of BD Pharmlyse solution (1/10 in dH_2O) was added to each sample, briefly vortexed, and left for 15 minutes in the dark at RT to allow red blood cell lysis to occur. 1.5ml FACS buffer (PBS + 1% BSA) was then added to each sample to neutralize the lysis buffer and centrifuged at 400g at 4°C for 5 minutes. Supernatants were discarded and samples were centrifuged again. Samples were then re-suspended in 300µl FACS buffer and kept on ice until data acquisition. Immediately before acquisition on BD LSRFortessa, 30µl DAPI (BD Pharmingen, #564907) was added to each sample. To determine the absolute counts of cells per µl of blood, samples were transferred to TruCount bead tubes (BD Biosciences, #340334). Absolute counts of the cell population of interest were calculated by dividing the number of positive cell events by the number of bead events, and then multiplying by the BD TruCount bead concentration (beads per test/test volume).

3.9 Preparation of Mouse Tissue for Flow Cytometry Analysis

3.9.1 Mouse Splenocyte Isolation and FACS Staining

Spleens were dissected from sacrificed mice. Spleens were gently ground with a 2ml syringe plunger through a 70µm filter pre-wet with 2ml PBS. Samples were centrifuged at 300g for 5 minutes at 4°C and supernatants discarded. Pellets were then re-suspended in 3ml 1x Pharm Lyse solution for 5 minutes at RT. 10ml of FACS buffer (PBS + 1% BSA) was then added to the samples to neutralise the RBC lysis buffer, and centrifuged again at 300g for 5 minutes before suspending in fresh FACS buffer. Cell suspensions were then filtered through a 30µm filter. 100µl of cell suspension was used per FACS sample. Fc block (1/50) was added to each sample and incubated for 10 minutes at RT. A mix of antibodies (CD11b, Ly6C, Ly6G, NK.1, CD11c, CD4, CD8, CD19, CCR2, CX3CR1 (Table 3.7) was added to each sample and incubated on ice for 30 minutes in the dark. Samples were then washed in 2ml FACS buffer, centrifuged at 300g for 5 minutes and re-suspended in 300µl FACS buffer before acquisition on BD LSRFortessa. 30µl of DAPI was added to samples immediately before acquisition.

3.9.2 Bone Marrow Isolation and FACS Staining

Bone marrow was obtained from the femur and tibia of humanely killed mice. Bone with the head removed was inserted into an appropriate size pipette tip within an eppendorf and centrifuged at 1000g for 60 seconds to obtain a pellet of bone marrow cells. Bone marrow pellets were re-suspended in 50µl of 1x Pharm Lyse solution to break up the pellet and remove RBCs, and incubated for one minute at RT. Samples were then washed in 200µl FACS buffer and centrifuged at 1000g for 60 seconds. Supernatant was discarded and samples were re-suspended in 200µl FACS buffer. Cells were then filtered using 30 µm CellTrics filters. 100µl of cell suspension was used per sample. Samples were incubated in 50µl Fc block (BioLegend, #101302) for 10 minutes at RT followed by incubation in a cocktail of antibodies (CD11b CD45 Ly6C Ly6G CCR2 CX3CR1) (Table 3.7) for 30 minutes at 4°C in the dark. Cells were washed in 2ml FACS buffer and centrifuged at 800g for 5 minutes. Samples were then

re-suspended in 300µl FACS buffer prior to acquisition on BD LSRFortessa. DAPI was added to samples immediately before acquisition.

3.9.3 Mouse Cardiac Digest and FACS Staining

Isolation of the Mouse Heart

Mice were euthanized by either CO_2 asphyxiation or cervical dislocation, and placed in the supine position and immobilised by pinning the paws and feet to the dissection surface. The heart was removed and the left and right atria were trimmed away to ensure only the intact myocardium (left and right ventricular tissues) was isolated. The isolated heart was then placed in ice cold HBSS in a 50ml falcon.

Mechanical and Enzymatic Digestion of the Mouse Heart

The isolated heart was placed on tissue culture dish on ice containing 5 ml HBSS. The heart was chopped into three or four pieces to expose interior surfaces of ventricles and rinse out any blood (if any) that may remain in ventricular cavities. Heart pieces were then transferred to a fresh tissue culture dish, minimizing the amount of transferred buffer. Next the heart tissue was finely minced and then transferred to a previously prepared 50ml tube containing 10ml Collagenase solution. The tissue and solution were gently mixed and suspended before incubating in a 37°C water bath for 30 min with gentle agitation. The mixture was agitated every 5-10 minutes to ensure that large tissue aggregates were minimized. After incubation, the digestion mixture was mixed by pipetting.

The digestion mixture was then centrifuged at 400g for 5min at 4°C. The supernatant was removed and the pellet was resuspended in 5ml pre-chilled collagenase solution until there were no large tissue aggregates visible. The solution was then incubated in a 37°C water bath for 20min with gentle agitation. The digestion reaction was then terminated by adding 5ml ice cold 1xHBSS, and placed on ice. The digestion mixture was resuspended briefly and transferred into a 15ml tube through a 50µm ficon filter membrane. The solution was then centrifuged at 400g for 10min at 4°C, the

supernatant removed and the pellet re-suspended in 1 ml 2% FBS/PBS solution. This was repeated, followed by the addition of 150µl 2% FBS/PBS solution and kept on ice for subsequent antibody staining.

Cardiac Digest Cell Suspension FACS Staining

Fc block was first added (1µl per sample) to 50µl of cell suspension, mixed, and kept on ice for 5min. A cocktail of antibodies (CD45, CD11b, Ly6C, CX3CR1, CCR2) (Table 3.7) diluted in 2% FBS/PBS was added and mixed by pipetting and left for 15min on ice. The samples were then washed in 200µl 2% FBS/PBS and centrifuged at 400g for 5min. The pellet was then resuspended in 200µl 2% FBS/PBS, and transferred to a 5ml flow cytometry tube through a 50µm falcon, and analysed by a BD LSRFortessa Flow Cytometer.

3.10 Cell Lines & Cell Culture

The THP-1 human monocytic cell line is an immortalized-monocyte-like cell line derived from the peripheral blood of a childhood case of acute monocytic leukemia (M5 subtype) [278]. THP-1 cells represent a valuable tool for researching monocyte function in both health and disease. All procedures were carried out under sterile conditions in a tissue culture hood. THP-1 monocytes were cultured at a density of 1-5x10^5cells/ml in RPMI 1640 Dulbecco's modified Eagle's medium (DMEM) supplemented with 5% heat inactivated fetal calf serum (FCS) and 0.5% Penicillin-Streptomycin (P/S), at 37^{o}C. The medium was replaced every 2-3 days. The Mono Mac 6 (MM6) cell line is established from the peripheral blood of a patient with monoblastic leukemia [279]. MM6 monocytes were cultured at the same density and in the same conditions as THP-1 cells and the medium was replaced every 2-3 days. U937 is a pro-monocytic, human myeloid leukaemia cell line isolated from the histiocytic lymphoma of a 37-year-old male [280]. U937 cells metabolize faster than THP-1 and MM6 monocytes and therefore required a higher frequency of media changes every ~2 days.

3.11 THP-1 Stimulation with CX3CL1

Cultured THP-1 cells were serum starved for 48h prior to stimulation with CX3CL1 (Recombinant Human CX3CL1/Fractalkine (Full Length) Protein, R&D Systems #365-FR-025) or TNF-α (Recombinant Human TNF-alpha Protein, R&D Systems, #210-TA-005). THP-1 cells were pre-treated with the inhibitors (BI605906, #5300, Tocris and AZD8797 CX3CR1 antagonist compound 18a) where appropriate for 30 minutes prior to CX3CL1 or TNF-α stimulation. Cells were subsequently processed for either protein extraction (section 3.14.1) or RNA extraction (3.13.1).

3.12 Real-Time PCR

3.12.1 RNA Extraction

Total RNA from cell lysates (approximately $5x10^5$ cells per sample) was isolated using the RNeasy Mini Kit (Qiagen) followed by the RNeasy Micro Kit (Qiagen) to purify and concentrate the final yield. Protocols were followed according to manufacturers' recommendations including the on column DNase digestion step. RNA is vulnerable to degradation therefore prior to doing any practical work the laboratory bench was cleaned with RNase Zap wipes (Invitrogen), gloves were worn and barrier filter tips were used. RNA concentration (in ng/µl) was measured using the Nanodrop ND-1000 spectrophotometer (Thermo Scientific) at an absorbance of 260nm (A260). Purity of obtained RNA was also assessed; RNA was considered pure when the A260/A280 ratio was above 1.9 and the A260/A230 was between 1.8-2.2 (if either ratio is appreciably lower than these values this suggests the presence of contaminating protein or co-purified contaminants respectively). RNA was stored at -80^oC in RNase free water until required.

3.12.2 Reverse Transcription and cDNA Synthesis

cDNA was prepared from extracted RNA using a High Capacity cDNA Reverse Transcription kit (Applied Biosystems). Briefly, 1µg RNA in 10µl DEPC-treated dH_2O was added to a reaction mix consisting of 2µl 10X reverse transcription buffer, 0.8µl

25X dNTP mix, 2µl 10X random primers, 2µl Multiscribe Reverse Transcriptase and made up to a final volume of 20µl with 4.2µl with DEPC-treated dH_2O. The mixture was incubated at 25°C for 10minutes (to allow primer extension), 37°C for 120 minutes, 85°C for 5 minutes and cooled down swiftly to 4°C degrees and stored at -20°C until required.

3.12.3 RT-PCR

RT-PCR reaction mixtures were made up to a total volume of 50µl in 0.2 ml thin walled PCR tubes and consisted of 5µl MgCl2 (25mM), 5µl 10X Buffer IV, 0.4µl Taq red hot polymerase (Applied Biosystems), 1µl 20mM dNTPs (New England Biolabs), 1µl forward primer (20µM), 1µl reverse primer (20µM), 33.6µl dH_2O, and 2µl sample cDNA. Reactions were carried out using a C1000 thermal cycler (Bio-Rad).

Gene	Assay ID	Cat no.	Company
GAPDH	Hs02786624	4331182	Applied Biosystems
RPL13A	Hs03043885_g1	4331182	Applied Biosystems
IL-6	Hs00174131_m1	4331182	Applied Biosystems
IL-8	Hs00174103_m1	4331182	Applied Biosystems
IκBα	Hs00153283_m1	4331182	Applied Biosystems
IL-1β	Hs01555410_m1	4331182	Applied Biosystems

Table 3. 4. List of primers used in Real-Time PCR.

qPCR details	Hold Stage	PCR Stage
QuantStudio 7 Flex System 384-well Comparative CT (DDCT) Taqman Reagents Standard Run	2 minutes at 50°C 10 minutes at 95°C	15 seconds at 95°C 1 minute at 60°C X 40 Cycles

Table 3. 5. Real-Time PCR reaction conditions and cycles.

3.13 Protein Analysis

3.13.1 Protein Extraction, BCA Assay and SDS-PAGE

Protein Extraction

For the extraction of protein, approximately $5x10^5$ cells were washed in PBS, pelleted and stored in 400µl lysis buffer (section 3.13.4) at -80°C. Protein samples were then denatured at 95°C for 5 minutes in a thermomixer, centrifuged for 5 minutes at 10,000g, and briefly sonicated 5x. The bicinchoninic acid assay (BCA assay) was then used to determine protein concentration to allow subsequent calculation of sample volume required for 30µg protein. Prior to separation via SDS-PAGE, samples were diluted in dH_2O, Laemmli buffer (containing 1/10 β-mercaptoethanol), to a concentration of 30µg protein per sample.

SDS-PAGE

For the separation of proteins, 40µl of whole cell lysate was loaded per well of a pre-cast 10% Tris-HCl polyacrylamide mini-gel (Bio-Rad). The gels were run in 1X SDS running buffer initially for 10 minutes at 150 volts, followed by 1 hour at 100 volts. Molecular weights of the proteins were determined using a pre-stained protein marker (New England Biolabs). Equal loading of protein was assessed by using α-tubulin as a loading control.

3.13.2 Western Blotting

Protein Transfer to Membrane

Following protein separation by SDS-PAGE, the separated proteins were transferred in a wet transfer apparatus (Bio-Rad) to polyvinylidene fluoride (PVDF) membrane (GE healthcare) at 4^oC in cold transfer buffer for 1 hour 30 minutes at 20 volts. Prior to transfer, the PVDF membrane was activated in methanol for 15 seconds followed by equilibration in cold transfer buffer for 20 minutes. Where necessary, successful

transfer and equivalence of protein loading was confirmed using Ponceau S stain (Sigma). Briefly, membranes were incubated with Ponceau S solution for 5 minutes at room temperature then rinsed in dH_2O to remove background staining and allow clear visualization of the transferred protein bands. To de-stain, membranes were washed 2 x 5 minutes in TBST wash buffer.

Immunoblotting

Membranes were incubated in blocking buffer (4% Marvel dry milk/TBST) for 1 hour at room temperature to avoid non-specific antibody binding. This was followed by incubating membranes overnight at 4^oC with primary antibodies diluted to a specific concentration (Table 3.9) in primary antibody diluent (2% BSA/TBST). The following day, membranes were briefly rinsed in TBST before being washed 3 x 5 minutes in 4% Marvel/TBST. The membranes were then incubated with the appropriate secondary antibody directed against the primary antibody's species of origin (Table 3.9). Secondary antibodies were diluted to a 1/10,000 concentration in 4% Marvel/TBST and left to incubate for 1 hour at room temperature. Membranes were again briefly rinsed in TBST before being washed 3 x 5 minutes in TBST.

3.13.3 Densitometry Analysis

Successful antibody binding was visualized by Odyssey CLx Imager. Densitometry analysis was performed using ImageQuant TL image analysis software (GE Healthcare) which allows fully automatic lane and band detection and quantitation. Results were expressed as the densitometry ratio of target gene bands to the α-tubulin bands.

3.13.4 Solutions & Buffers

Lysis Buffer

10mM Tris-HCl pH 7.4, 1% Triton X-100, 1/100 dilution of protease inhibitors (Sigma), 1/10 dilution pf 10X phosphatase inhibitor (PhosSTOP tablets, Roche)

2X SDS Loading Buffer

12.5ml 0.5M Tris-base pH 6.8, 10ml glycerol, 20ml 10% Sodium Dodecyl Sulphate (SDS), 7ml dH_2O, 0.5ml β-mercaptoethanol, 20mg Bromphenol Blue

1X SDS Running Buffer

14.4g Glycine, 3g Tris-base and 10ml of 10X SDS dissolved in 1 litre of dH_2O

1X Transfer Buffer

14.4 g Glycine, 3g Tris-base dissolved in 1 litre dH_2O

10X TBS

24.2g Tris-base, 88g NaCl dissolved in 1 litre of dH_2O. PH adjusted to 7.6 with HCl

TBST

150mM NaCl, 50mM Tris-HCl, 0.1% Tween-20

3.14 Isolation of Human Peripheral Blood Monocytes

EDTA anti-coagulated blood was obtained from healthy volunteers after informed consent and in accordance with the ethical guidelines of the institution. PBMCs were firstly removed by centrifugation of whole blood over Histopaque (Sigma Aldrich, #10771), followed by erythrocyte lysis using Lysing Buffer (BD Pharm Lyse, #555899). PBMCs were then subject to monocyte negative selection using the Monocyte Isolation Kit II and manual columns (Miltenyi Biotec, #130-042-201), strictly according to the manufacturer's protocol. The isolation of viable monocytes was evaluated by trypan blue staining and manual counting using a haemocytometer. The purity of human monocytes was evaluated by fluorescent staining with the previously established human monocyte marker antibody panel (CD14, CD16, HLA-DR, CD3, CD9, CD56, CCR2, CX3CR1) and FACS analysis.

3.15 FACS Analysis of Phosphorylated p65 in MM6 Monocytes

In CX3CR1 inhibitor treated cells, MonoMac6 (MM6) monocytes were treated with KAN567 for 30 minutes prior to stimulation with CX3CL1. CX3CL1 was then added for 60 minutes, or TNF-α for 15 minutes as a positive control. Following stimulation, cells were pelleted, washed once in cold PBS, and resuspended in 100µl PBS. MM6 cells were then incubated with monocyte marker antibody-fluors CD14 and CD16 (5µl of each antibody per sample) for 30 minutes in the dark at RT (Table 3.6). Cells were then washed with excess PBS, centrifuged at 400g and supernatant removed. To fix the cells, they were resuspended in 500µl 4% PFA in the dark for 15 minutes at RT. Following fixation, cells were washed in excess PBS, centrifuged at 400g for 5 minutes and supernatant removed. Cell samples were then transferred to 15ml falcon tubes, followed by the addition of 3.6ml of ice cold methanol dropwise while vortexing. Cells were then left on ice for 30 minutes in the dark to allow cell permeablisiation. Cells were then washed in excess PBS, centrifuged at 400g for 5 minutes, resuspended in 1ml PBS and transferred to an Eppendorf tube. Cells were again pelleted and then resuspended in 100µl of anti-phospho-p65 primary antibody diluted in PBS + 1% BSA and incubated for 1h in the dark at RT (Table 3.9). Cells were then washed in excess PBS (1% BSA), centrifuged, supernatant removed, resuspended in 1/100 secondary

antibody (Anti-rabbit IgG PE Conjugate, #8885, Cell Signalling), diluted in PBS + 1% BSA and incubated for 30 minutes in the dark at RT. Following secondary antibody incubation, cells were washed twice in PBS, resuspended in 500µl PBS and transferred to FACS tubes for subsequent acquisition using a BD LSRFortessa cell analyzer.

3.16 Statistical Analyses

All statistical analysis was performed using SPSS or GraphPad Prism and all graphs were produced in GraphPad Prism. Where multiple comparisons were made, reported values are those corrected for multiple tests. Correlations between parameters were assessed using Spearman correlation coefficient. Data are expressed as mean ± standard error of the mean (SEM) except where otherwise stated. A p value of less than 0.05 was considered significant. Statistical analyses of patient data were reviewed and approved by a chartered senior statistician (Dr. Kim Pearce).

3.17 Study Approval

The prospective STEMI patient study was approved by the local ethics committee (REC reference: 16/NE/0405), and was conducted according to the principles set out in the Declaration of Helsinki. Written informed consent was obtained from all prospective patients.

Ethical approval for volunteer human blood samples from the Newcastle University Medical School as part of the study ‘The role of inflammation in human immunity’. Samples were arranged and collected by Dr. Marie-Helene Ruchaud-Sparaganoa and Jonathon Scott.

Anti-Human Antibody	Fluorochrome	Clone	Company	Cat No.
CD16	APC-H7	3G8	BD Biosciences	560715
CD14	BV510	M5E2	BioLegend	301842
CCR2	PE-Cy7	K036C2	BioLegend	357212
CX3CR1	APC	2A9-1	BioLegend	341609
HLA-DR	BV421	L243	BioLegend	307635
CD3	FITC	UCHT1	BioLegend	300406
CD19	FITC	HIB19	BioLegend	302206
CD56	FITC	HCD56	BioLegend	318304

Table 3. 6. List of antibodies used in human blood FACS.

Anti-Mouse Antibody	Fluorochrome	Clone	Company	Cat#
CD11b	APC	M1/70	BioLegend	101211
Ly6C	PE	HK1.4	BioLegend	128007
CX3CR1	BV421	SA011F11	BioLegend	149023
CCR2	PE-Cy7	SA203G11	BioLegend	150611
LY6G	PerCP-Cy5.5	1A8	BioLegend	127615
CD115	BV711	AFS98	BioLegend	135515
F4/80	BV605	BM8	BioLegend	123133
CD45	BV785	30-F11	BioLegend	103149
CD4	BV711	RM4-5	BioLegend	100549
CD8a	BV711	53-6.7	BioLegend	100747
CD19	BV711	6D5	BioLegend	115555
NK1.1	BV605	PK136	BioLegend	108739
CD11c	BV785	N418	BioLegend	117335
Brilliant Stain Buffer			BD	563794
Fc Block - CD16/32	-	93	BioLegend	101302

Table 3. 7. List of antibodies used in mouse blood, spleen, bone marrow, and cardiac digest tissue FACS.

Antibody	Species raised in	Concentration	Vendor	Cat No.
Primary Antibodies				
Anti-mouse CD45	Rat	1/100	BioLegend	103102
Anti-mouse CD11b	Rat	1/100	BD Pharminogen	553308
Anti-mouse GFP	Chicken	1/300	Abcam	ab13970
Anti-mouse CCR2	Rabbit	1/50	Abcam	ab203128
Alexa Fluor 647 Anti-mouse F4/80 Antibody	Rat	1/100	BioLegend	123121
Anti-mouse CD68	Rat	1/100	ABD Serotec	MCA1957GA
Secondary Antibodies				
Anti-rat Alexa-488	Goat	1/200	Life Technologies	A11006
Anti-chicken Alexa-568	Goat	1/200	Life Technologies	A11041
Anti-rabbit Alexa-647	Goat	1/200	Abcam	ab150079

Table 3. 8. List of antibodies used in Immunofluorescent Staining of mouse heart tissue.

Primary Antibody	Species	Blocking Solution	Working Dilution	Size (kDa)	Vendor	Cat. No	Secondary Antibody	Working Dilution	Cat. No
RelA/NFkB p65 Antibody	Sheep	4% Marvel/TBST	1µg/ml	65	Biotechne	AF5078	IRDye 800CW Donkey anti-Goat IgG Secondary Antibody	1:10000	92632214
Phospho-NF-κB p65 (Ser536) (93H1)	Rabbit	4% Marvel/TBST	1:1000	65	Cell Signalling	3033	IRDye 800CW Donkey anti-Rabbit IgG Secondary Antibody	1:10000	92632213
Phospho-IκBα (Ser32/36) (5A5)	Mouse	4% Marvel/TBST	1:1000	40	Cell Signalling	9246	IRDye 680RD Donkey anti-Mouse IgG Secondary Antibody	1:10000	92668072
IκBα Antibody	Rabbit	4% Marvel/TBST	1:1000	40	Cell Signalling	9242	IRDye 800CW Donkey anti-Rabbit IgG Secondary Antibody	1:10000	92632213
Tubulin (Sigma)	Mouse	4% Marvel/TBST	1:1000	50	Sigma	T6074	IRDye 680RD Donkey anti-Mouse IgG Secondary Antibody	1:10000	92668072

Table 3. 9. List of antibodies used in THP-1 western blot protein expression analysis.

All secondary antibodies supplied from LICOR.

Chapter 4.0. STEMI Patient Monocyte Subpopulation Counts and Prognostic Significance

4.1 Introduction

The central role of monocytes in the innate immune response to MI was initially discovered in mouse models, which established that monocytes and macrophages dominate the myocardial cellular infiltrate during the first 2 weeks following MI, and participate significantly in infarct repair (section 1.3.5). This work lead to the prevailing concept that MI leads to an acute inflammatory response, which is mediated by classical monocytes from day 1-4 post-MI, and is subsequently followed by a pro-fibrotic reparative response dominated by non-classical monocytes from day 5-9 post-MI [158, 281] (see section 1.3.5). Importantly, a perturbation of either phase during the biphasic monocyte response has been shown to severely compromise cardiac repair in a parabolic manner; if inflammatory classical monocytes persist too long in the infarct, the reparative functions of non-classical monocytes, myofibroblasts and endothelial cells are impaired, however if the infarct recruits insufficient classical monocytes, wound healing is delayed since debris cannot be cleared efficiently and therefore cannot be replaced with granulation tissue and collagen matrix [282]. Evidence documenting the monocyte response to human MI is however sparse due to the low availability of tissue specimens for obvious ethical reasons. Clinical studies of STEMI patients have therefore been largely restricted to investigating the dynamics of circulating monocyte subpopulations (classical, intermediate, non-classical) in the blood following reperfusion by PPCI. Such access to blood samples is clinically very feasible since STEMI patients require vascular access as part of their routine clinical care during reperfusion by PPCI following STEMI. This scenario is different from many traditional preclinical models of MI which study the monocyte response following unreperfused MI, in contrast to post-ischemia reperfusion. Although, more contemporary studies use mouse models of cardiac I/R which physiologically resemble that of the clinical setting more closely. Nevertheless, preclinical models are usually surgical models that require invasive procedures such as thoracotomy drive a systemic inflammatory response even in the sham situation.

Among the small number of studies published to date, there has been a focus on monocyte subpopulation dynamics following MI at time points ranging from day 1 to 7 following reperfusion [170-175, 283]. Monocyte subpopulations in the blood have been shown to specifically respond to the extent of cardiac injury following MI, and may therefore offer reliable biomarkers to prioritize patients for follow up treatments/management. However, the reported associations are varied and in some cases contradictory (see Chapter 1 section 1.3.6). The precise link between blood levels of monocyte subpopulations and STEMI patient cardiac outcome is therefore yet to be determined. Moreover, the earliest time point studied among those published is day 1 post-reperfusion. As such, current literature has not addressed monocyte subset dynamics within the first immediate 24h following reperfusion, which represents a critical time point to intervene, and is prior to patient discharge. In this study, I therefore investigated monocyte dynamics at time points within the first 24h following by PPCI, during the very immediate acute phase following reperfusion. To achieve this, a database of 53 STEMI patient blood samples from pre-reperfusion, 15min, 30min, 90min, and 24h following reperfusion by PPCI were retrospectively analysed. All patients were admitted to the Freeman Hospital, Newcastle upon Tyne, between September 2012 and March 2015 (see Table 4.1 for patient database). All STEMI patients received a cardiac MRI therefore monocyte dynamics could be assessed against markers of myocardial injury (infarct size; IS and microvascular obstruction; MVO) or myocardial function (left ventricular ejection fraction; LVEF). In a subset of STEMI patients (n=20), 3-month follow up samples were also collected. NSTEMI patients (n=15) were recruited as a control population in this study, as this allows the study of MI without the sudden ischemia and intense inflammatory cascade that characterises STEMI following vessel opening; NSTEMI patients still undergo the same PCI procedure (urgent, though non-emergency), however have only a partially narrowed artery and therefore do not have significant myocardial tissue damage, and therefore demonstrate a differential inflammatory pattern which is evidenced by an absence of significant correlations between inflammatory indexes and myocardial infarction at admission (t0), 12h after symptoms [284]. NSTEMI blood samples were collected at pre-reperfusion, 15min, 30min, and 90min post-PCI. By comparing STEMI and NSTEMI patient populations in this study, it was therefore possible to distinguish monocyte subpopulation dynamics that are specific to cardiac-ischemia-reperfusion

[STEMI]. In particular, this study focussed on the non-classical monocyte population, which represent 5-10% of total human blood monocytes [141, 285, 286]. This focus was due to their known high expression of CX3CR1, compared to classical and intermediate monocytes which express low and medium levels of the fractalkine receptor, respectively. In both mouse and human, numerous studies have now linked the CX3CL1/CX3CR1 axis to post-reperfusion cardiac repair [210, 287-291]. In this chapter, I therefore hypothesised that circulating CX3CR1^{hi} non-classical monocyte dynamics in STEMI patient blood post-PCI are associated with long term cardiac function.

4.2 Results

4.2.1 Monocyte Subpopulation Dynamics in Retrospective STEMI and NSTEMI Patient Cohort

Human circulating classical, intermediate, and non-classical monocyte populations were defined by FACS analysis as shown in Figure 4.1 (details in section 3.1). A database of patient clinical parameters is described in Table 4.1. Retrospective analysis of STEMI and NSTEMI patient blood samples at time points from pre-reperfusion to 24h post-PCI revealed distinct temporal dynamics of monocyte subpopulations following PPCI (Figure 4.2A). STEMI patient circulating $CD16^-$ classical monocyte counts dropped in the circulation from baseline to 90 minutes post-reperfusion by 16% ($p=0.023$). This was followed by a sharp recovery in $CD16^-$ classical monocytes at 24h post-PCI ($p<0.0001$) from 90min by 46%, increasing to and surpassing pre-reperfusion baseline counts. When comparing $CD16^-$ classical monocyte dynamics between ACS, there were no significant differences in classical monocyte counts between STEMI and NSTEMI patients at any of the time points studied (Table 4.2). The dynamics of intermediate monocytes following reperfusion followed a similar pattern to that of classical monocytes; $CD16^+$ intermediate monocyte counts decreased in the circulation from pre-PCI to 90 minutes post-reperfusion by 24% ($p=0.044$), followed by an increase at 24h post-reperfusion ($p<0.0001$) from 90min by 100% to beyond baseline levels. Again, no significant differences in $CD16^+$ intermediate monocyte counts were observed between STEMI and NSTEMI patients throughout the time course studied (Table 4.2).

While classical and intermediate monocyte populations showed a modest drop in the circulation from pre-reperfusion to 90min, the extent of non-classical monocyte depletion was much greater; STEMI patients showed an acute 46% fall in circulating $CD16^{++}$ non-classical monocytes from pre-PCI to 90 minutes post-reperfusion (39 ± 5 to 21 ± 4 cells/μl, $p<0.0001$). By 24h, $CD16^{++}$ non-classical monocytes increased from 90min by 133%, and returned to but did not surpass pre-perfusion counts ($p=0.015$). In contrast to classical and intermediate monocyte counts which did not significantly vary between ACS groups, non-classical monocyte counts were significantly different

between STEMI and NSTEMI patients. STEMI patients had significantly lower counts of circulating non-classical monocytes than their NSTEMI counterparts at 15min ($p<0.05$), 30min ($p<0.01$), and 90 minutes' ($p<0.05$) post-reperfusion. Follow up blood samples in a subgroup (n=20) of STEMI patients at 3 months following reperfusion revealed that all monocyte subset counts returned to baseline levels (Figure 4.2B). Absolute monocyte subpopulation cell counts are stated in Table 4.2.

Baseline data for STEMI and NSTEMI patients in a retrospective and prospective study of blood monocyte subpopulations post-PCI.				
	Retrospective			Prospective
	STEMI (n=53)	NSTEMI (n=15)	P value	STEMI (n=13)
Age	59.3 ± 10.7	61.1 ± 11.8	0.742	58.9 ± 10.5
Male (%)	44 (74.6)	11 (73.3)	1.000	10 (76.9)
BMI	26.8 ± 4.6	30.9 ± 6.0	0.006	28.9 ± 6.6
Diabetes (%)	6 (10.2)	0 (0)	0.337	1 (7.7)
Active smoker (%)	31 (52.5)	4 (26.7)	0.089	6 (46.2)
Hypertension (%)	19 (32.2)	10 (66.7)	0.020	6 (46.2)
Anterior MI (%)	28 (47.5)	N/A	N/A	10 (76.9)
Peak troponin T (ng/l)	4899 ± 3385	207 ± 214	<0.001	3173 ± 2838
Procedural characteristics				
Door-to-balloon time (minutes)	26.8 ± 14.3	N/A	N/A	27.4 ± 13.7
Onset-to-reperfusion time (minutes)	164.6 ± 81.3	N/A	N/A	151.9 ± 81.4
Pre-PCI flow (TIMI 0/1/2/3)	55/4/0/0	2/1/0/12	<0.001	13/0/0/0/
Post PCI flow (TIMI 0/1/2/3)	0/0/0/59	1/0/0/14	0.203	1/1/1/10
Vascular access (radial/femoral)	56/3	13/2	0.265	13/0
Continuous variables expressed as mean ± SD; categorical variables expressed as n (%)				

Table 4. 1. Baseline data for STEMI and NSTEMI patients in a retrospective and prospective study of blood monocyte subpopulations post-reperfusion.

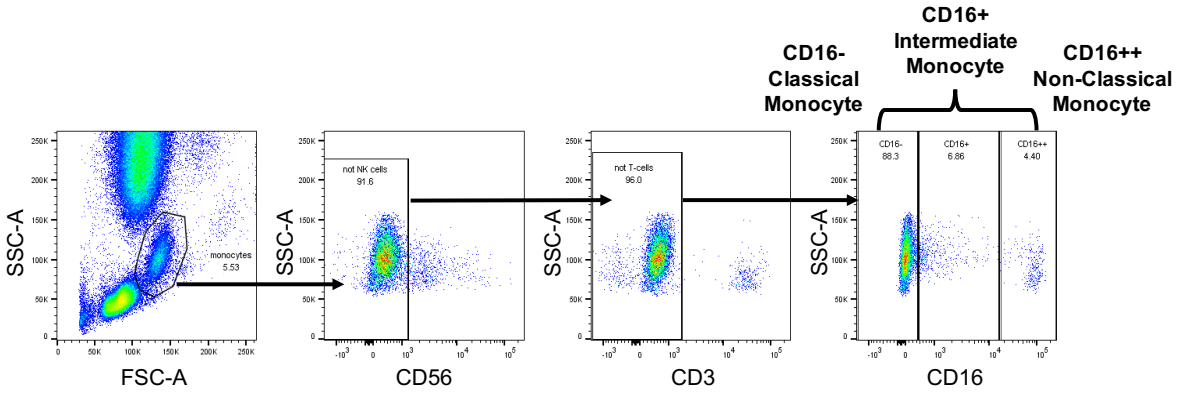

Figure 4. 1. Flow Cytometry gating strategy for retrospective monocyte subset analysis in STEMI and NSTEMI patient blood.

Quantification of monocytes was achieved using the scatter properties of monocytes, excluding T-cells and NK-cells on the basis of CD3 and CD56 expression respectively, followed by CD16 expression to define each monocyte subset ($CD16^-$ classical, $CD16^+$ intermediate, $CD16^{++}$ non-classical monocytes). Data was analysed using FlowJo Software.

A

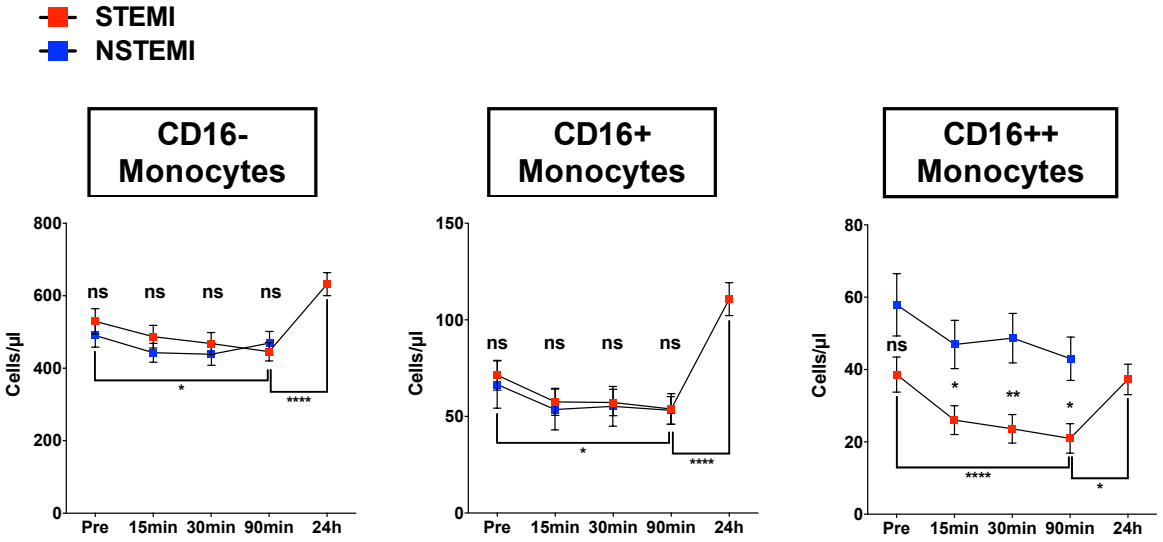
STEMI
NSTEMI
CD16- Monocytes
CD16+ Monocytes
CD16++ Monocytes
Cells/µl
Pre
15min
30min
90min
24h
ns
*
****
**

B

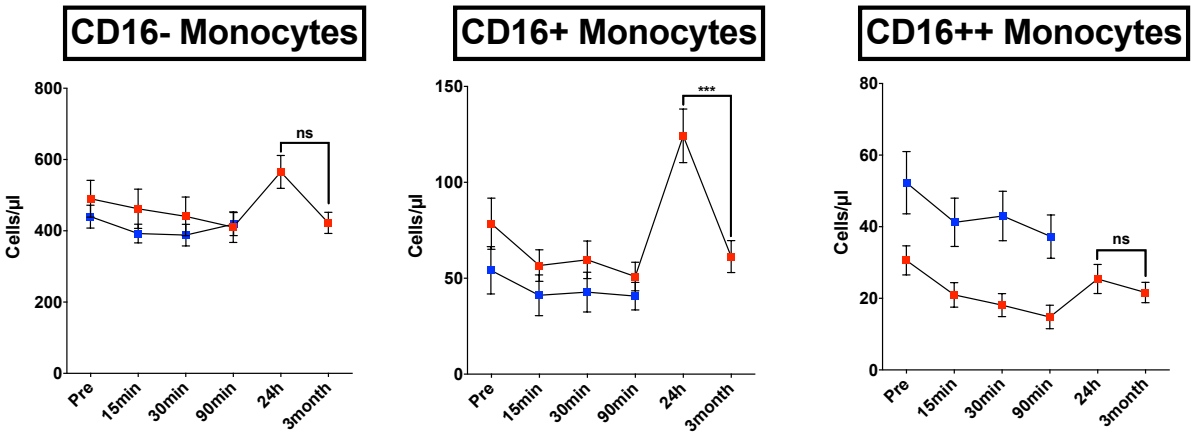
CD16- Monocytes
CD16+ Monocytes
CD16++ Monocytes
Cells/µl
Pre
15min
30min
90min
24h
3month
ns
***

Figure 4. 2. Retrospective STEMI patient monocyte subpopulation dynamics during the acute post-reperfusion period.

A. Changes in circulating monocyte subset counts in STEMI and NSTEMI patients immediately following reperfusion to 24h post-PCI. STEMI patient classical $CD16^{-}$, intermediate $CD16^{+}$, and non-classical $CD16^{++}$ monocyte subpopulations show acute changes in cell counts over time. The most dramatic change is the drop in $CD16^{++}$ non-classical monocytes from pre-reperfusion to 90min post reperfusion ($p<0.0001$). Lower asterisks indicate statistical differences in counts between indicated time points in STEMI patients (One-way Anova with Bonferroni's adjustment for multiple comparisons); upper asterisks indicate statistical differences between STEMI and NSTEMI counts at indicated time points (Repeated measure paired analysis with Bonferroni adjustment for multiple comparisons as a full factorial model). STEMI n=53, NSTEMI n=15. B. Follow-up samples were collected in a subset of STEMI patients (n=20) at 3-6 months. Data at each time point is shown for this subset (n=20) of STEMI patients. Data refers to mean ± SEM. *$p<0.05$, **$p<0.01$, ***$p<0.001$, ****$p<0.0001$.

Mean Cell Count (cells/μl ± SEM) NSTEMI (n=15) / STEMI (n=53)							
Time Point	Total Monocytes	Classical Monocytes	Intermediate Monocytes	Non-Classical Monocytes	NSTEMI vs STEMI p value		
					Classical Monocytes	Intermediate Monocytes	Non-Classical Monocytes
Pre-PPCI	614±39	489±32	67±12	58±9	ns (0.512)	ns (0.751)	ns (0.76)
	639±47	529±35	71±8	39±5			
15min	542±32	442±26	54±11	47±7	ns (0.451)	ns (0.796)	* (0.014)
	571±42	487±31	58±7	26±4			
30min	541±35	437±30	55±10	49±7	ns (0.567)	ns (0.861)	** (0.004)
	549±41	468±30	57±7	24±4			
90min	564±34	468±32	53±7	43±6	ns (0.704)	ns (0.935)	* (0.013)
	520±37	446±25	54±8	21±4			
24hr	N/A				N/A		
	780±44	632±32	111±9	37±4			
3-6 month	N/A				N/A		
(n=20)	505±41	422±30	61±8	22±3			

Table 4. 2. STEMI and NSTEMI patient monocyte subpopulation cell counts pre-reperfusion and at various time points post-reperfusion.

Data expressed as mean ± SEM. STEMI and NSTEMI patient groups were compared using repeated measure paired analysis with Bonferroni adjustment for multiple comparisons as a full factorial model. *p<0.05, **p<0.01.

4.2.2 Preferential Depletion in Non-Classical Monocytes from Pre-Reperfusion to 90 minutes Post-PCI is Predictive of STEMI Patient Infarct Size

After observing that STEMI patients show a transient 46±4% depletion in circulating $CD16^{++}$ non-classical monocytes at 90 minutes following reperfusion, I subsequently investigated whether these dynamics correlated with markers of myocardial injury (infarct size; IS and microvascular obstruction; MVO) or myocardial function (left ventricular ejection fraction; LVEF), as assessed by cardiac MRI. Within the STEMI patient group, 45 patients received a cardiac MRI 1-8 days (on average 3.2 days) after primary PCI. Patients were divided into tertiles based on infarct size, expressed as the percentage of damaged tissue out of the left ventricle (small: <13.3%, medium: 13.3-23.8%, large: >23.8%) (Table 4.3). These groups were then compared with regard to the monocyte subset dynamics quantified during the total acute post-reperfusion (pre-90min) and early post-reperfusion (15-30min) period.

Interestingly this analysis revealed that STEMI patients with larger infarcts had a greater depletion of circulating $CD16^{++}$ non-classical monocytes during the total acute post-reperfusion period (pre-90min), than those patients with small infarcts (p=0.039) (Figure 4.3A). Specifically, large infarct patients showed approximately a 60% (±5) drop in non-classical monocytes from pre-PCI to 90minutes, while small and medium infarct STEMI patients showed a 36% (±8) and 49% (±4) depletion, respectively. This significant correlation between non-classical monocyte dynamics and infarct size was only observed between pre-reperfusion and 90 min, and not between other time periods such as 15-30min post-PCI (Figure 4.3B). Classical and intermediate monocyte dynamics between pre-reperfusion and 90min post-PCI showed no association with infarct size (Figure 4.3A). These monocyte subpopulations also showed no significant association with STEMI patient infarct size during the early post-reperfusion (15-30min) period (Figure 4.3B).

.

Infarct Size		
Small	Medium	Large
<13.3%	13.3-23.8%	>23.8%
MVO		
Zero	Low	High
0g	0.1-2.7g	>2.7g

Table 4. 3. STEMI patient tertiles of infarct size and MVO as assessed by cardiac MRI.

STEMI patients received cardiac MRI between day 1-8 following primary PCI. Short axis LGE images were used to quantify infarct size and MVO, all of which were taken at end diastole. Epicardial and endocardial borders were then traced on each heart slice and a reference region of normal myocardium identified using an automated method with manual correction where necessary. Areas of enhancement (infarction) were then identified and quantified automatically using a signal intensity threshold of 5 SD above normal remote myocardium Infarct size was expressed as the percentage of left ventricle. Regions of hypoenhancement within the enhanced zone (MVO) were identified and quantified using semiautomatic thresholding following manual border delineation of areas of interest, and graded as none, low or high MVO.

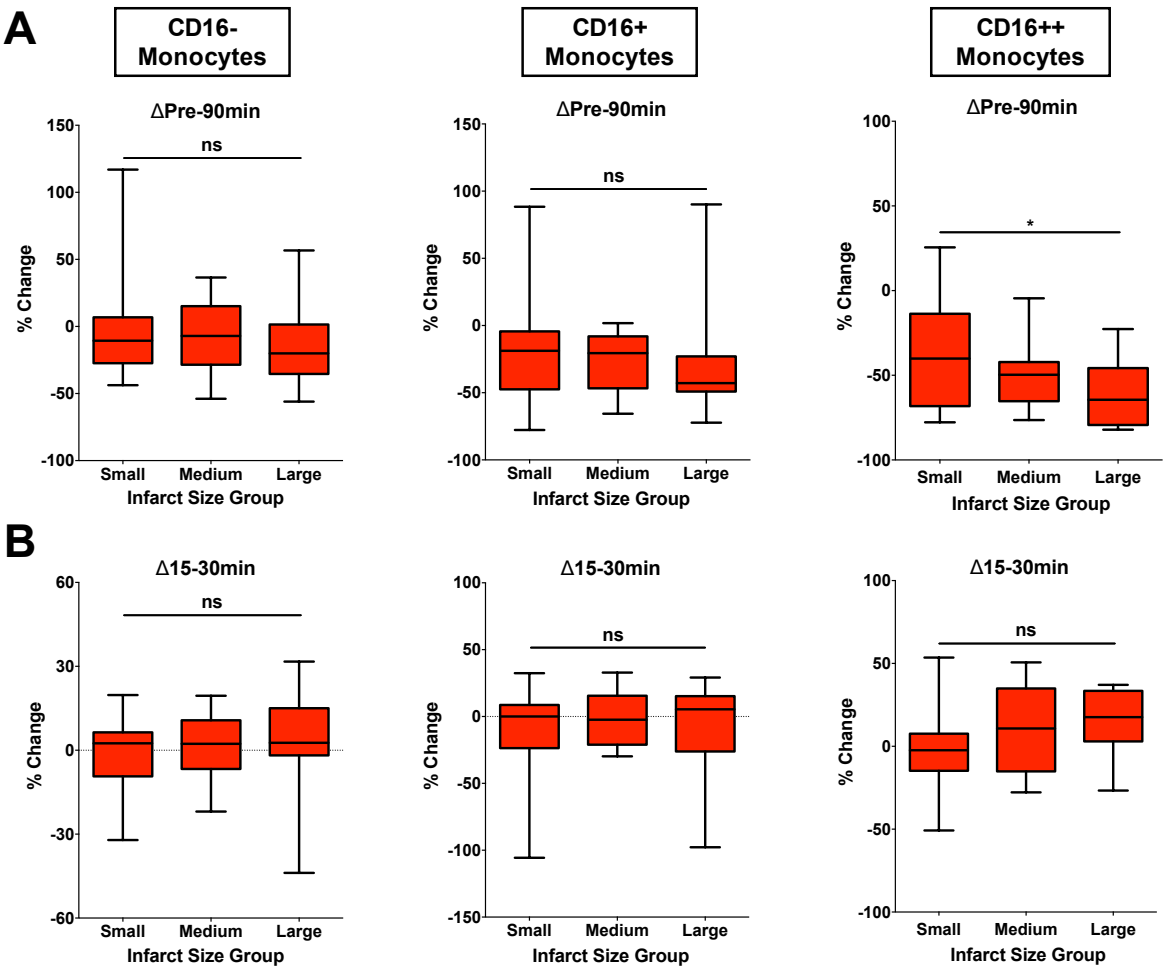

Figure 4. 3. Association between STEMI patient post-reperfusion monocyte subpopulation dynamics with infarct size.

Relationship between infarct size and A. total acute post-reperfusion period (Pre-90min) and B. early post-reperfusion changes (15-30min) in classical $CD16^{-}$, intermediate $CD16^{+}$, and non-classical monocytes $CD16^{++}$ in STEMI patients. STEMI patients underwent cardiac MRI to detect and quantify infarct size. STEMI patients received cardiac MRI between day 1-8 following primary PCI and short axis LGE images were used to quantify infarct size, all of which were taken at end diastole. Infarct size was expressed as the percentage of left ventricle. STEMI patients were categorized into tertiles based on infarct size (n=15 small (<13.3%); n=17 medium (13.3-23.8%); n=13 large (>23.8%). Box plots display median (central line), 25^{th} and 75^{th} percentiles (limits of box), and 5^{th} and 95^{th} percentiles (error bars). Data analysed using Kruskal-Wallis test with Dunn's multiple comparisons test. *$p<0.05$.

4.2.3 STEMI Patient Monocyte Subpopulation Dynamics Show No Association with Microvascular Obstruction

In addition to infarct size, microvascular obstruction was also measured as a marker of myocardial injury following STEMI. Dynamic changes in STEMI patient circulating monocyte subset counts were compared between tertiles of MVO as described in Table 4.3. STEMI patients were divided into three MVO groups defined as either zero MVO (0g = no MVO), low MVO (0.1-2.7g), or high MVO (>2.7g). These comparisons were conducted for the changes in monocyte subpopulation counts occurring over the total acute post-reperfusion period (pre-90min) and the early post reperfusion period (15-30min).

Analysis of classical and intermediate monocyte subpopulation dynamics against the presence of MVO during the total acute post-reperfusion period (pre-90min) revealed no predictive value of classical or intermediate blood counts on this marker of myocardial injury (Figure 4.4A). No significant correlation was observed during the early post-reperfusion period (15-30min) between these monocyte subsets and MVO either (Figure 4.4B).

Non-classical monocyte dynamics also showed no significant association with MVO during the total acute post-reperfusion period (pre-90min) (Figure 4.4A) or early post-reperfusion period (15-30min) (Figure 4.4B). However, a closer look at the percentage drop in non-classical monocytes from pre-reperfusion to 90 minutes across the three MVO groups identified a trend towards a higher MVO status in STEMI patients with a greater depletion of non-classical monocytes at 90 minutes post-reperfusion; patients with zero and low MVO showed a 44%(±5) and 45%(±8) decrease in non-classical monocytes from pre-90min, while high MVO patients had a 57%(±6) depletion in this monocyte subset. Although this association was not significant, a larger sample size of STEMI patients would provide more statistical power to repeat this analysis.

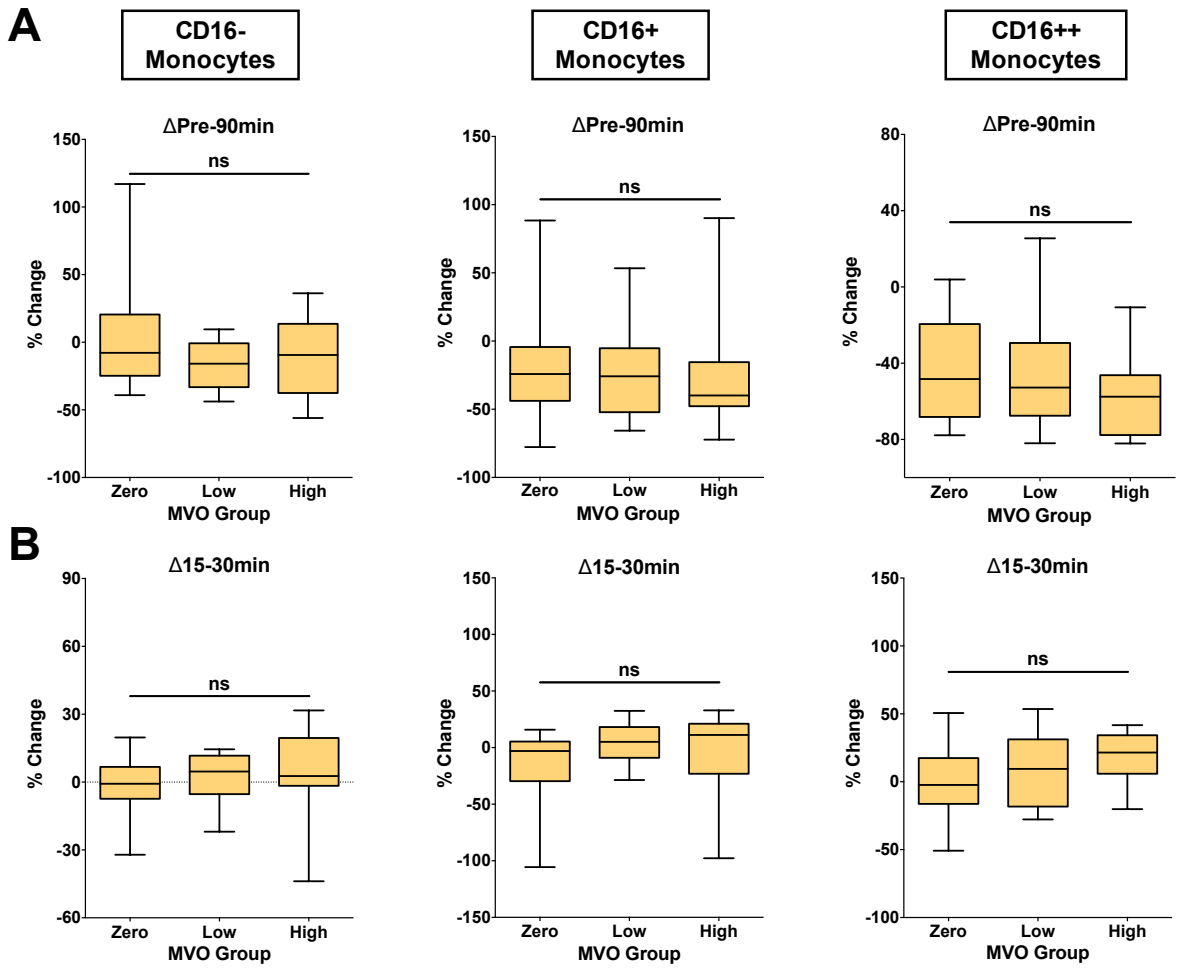

Figure 4. 4. Association between STEMI patient post-reperfusion monocyte subpopulation dynamics with MVO.

Relationship between microvascular obstruction (MVO) and A. total acute reperfusion period (Pre-90min) and B. early acute post-reperfusion changes (15-30min) in classical $CD16^{-}$, intermediate $CD16^{+}$, and non-classical $CD16^{++}$ monocytes in STEMI patients. STEMI patients received cardiac MRI between day 1-8 following primary PCI to detect and quantify MVO. CMR short axis LGE images were used to quantify MVO, all of which were taken at end diastole. Regions of hypoenhancement within the enhanced zone (MVO) were identified and quantified using semiautomatic thresholding following manual border delineation of areas of interest. STEMI patients were categorized into tertiles based on MVO (n=15 none (0g); n=17 low (0.1-2.7g); n=13 high (<2.7g). Box plots display median (central line), 25^{th} and 75^{th} percentiles (limits of box), and 5^{th} and 95^{th} percentiles (error bars). Data analysed using Kruskal-Wallis test with Dunn's multiple comparisons test.

4.2.4 Non-Classical Monocyte Dynamics (Pre-90min) and Classical Monocyte Dynamics (15-30m) following Reperfusion are Predictive of STEMI Patient Left Ventricular Ejection Fraction

Following the observation that non-classical monocyte depletion in the circulation from pre-reperfusion to 90min was predictive of a larger infarct size in STEMI patients, subsequent analysis was performed to determine if these non-classical monocyte dynamics were also associated with left ventricular systolic function post-reperfusion, as measured by LVEF. This analysis was restricted to anterior STEMI patients (n=23), for the reason that left ventricular function correlates much better to infarct size if the anterior, but not posterior wall, is involved.

During the total acute pre-reperfusion period (pre-90min), STEMI patient non-classical monocyte counts show a significant correlation with LVEF ($p=0.043$, $r=0.407$) (Figure 4.5A). Here, the greater the depletion of non-classical monocytes in the circulation, the lower the LVEF, thus suggesting poorer left ventricular systolic function. The counts of classical and intermediate monocyte subsets during this time period had no significant association with STEMI patient LVEF. There was however a trend towards lower LVEF in patients with a greater depletion of classical monocytes from pre-90min ($p=0.075$).

Analysis of the early acute reperfusion period (15-30min) identified a significant association between classical monocyte blood counts and LVEF (Figure 4.5B). During this immediate time frame following reperfusion, a greater depletion of classical monocytes in the circulation was significantly correlated with a lower LVEF and therefore worsened systolic function in these patients ($p=0.017$, $r=0.481$). In contrast to this, non-classical monocytes and intermediate monocytes show no association with LVEF at this earlier time point.

The relationship between non-classical monocytes during the total acute reperfusion period (pre-90min) and classical monocytes during the early acute reperfusion period (15-30min) with LVEF suggests that these monocyte subsets may respond to cardiac

I/R at different time points immediately following reperfusion and in turn govern distinct functions of these different monocyte populations.

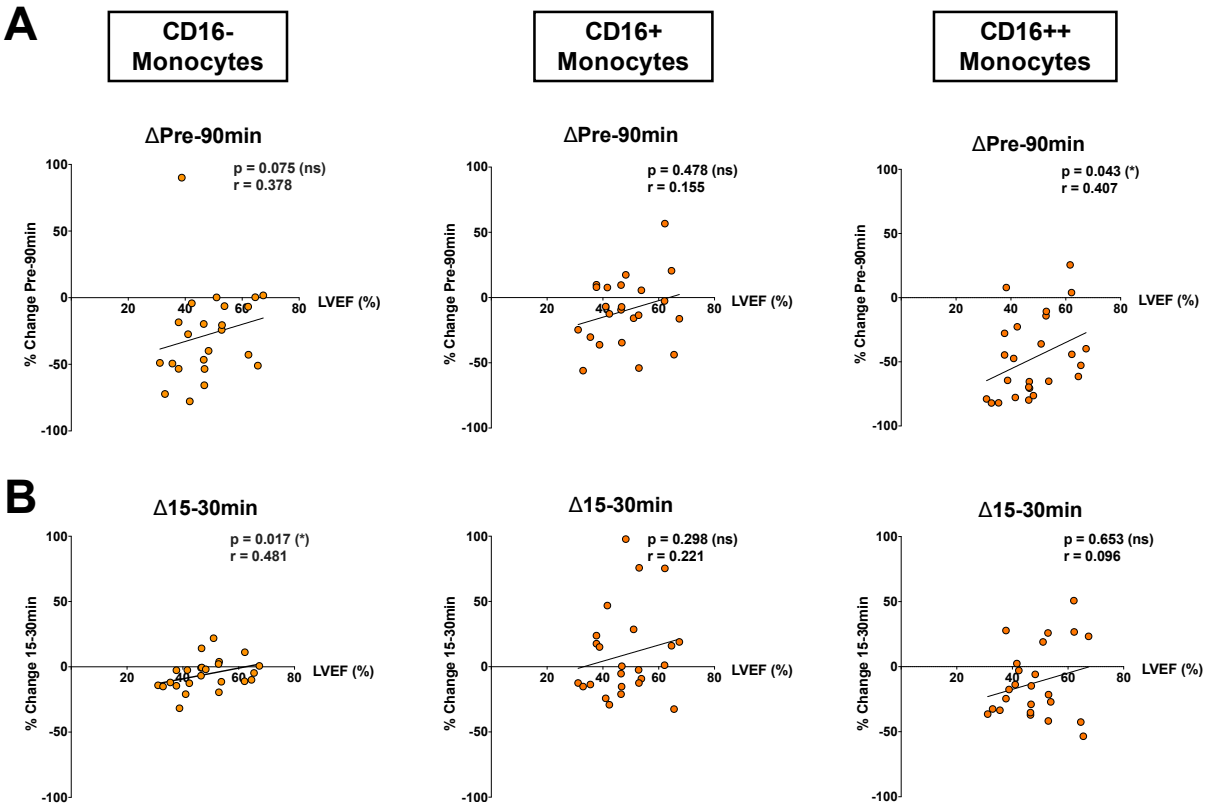

Figure 4. 5. Association between STEMI patient post-reperfusion monocyte subpopulation dynamics with LVEF.

Relationship between LVEF and A. total acute post-reperfusion changes (pre-90min) and B. early acute post-reperfusion changes (15-30m) in classical $CD16^{-}$, intermediate $CD16^{+}$, and non-classical $CD16^{++}$ monocytes in anterior STEMI patients (n=23). Using an MRI sequence technique known as steady-state free precession (SSFP), internal and external dimensions of the LV were measured on each short axis heart slice by planimetry around the endocardial and epicardial borders, allowing calculation of chamber volumes at end-systole and end-diastole which were used to calculate LVEF. A greater depletion in anterior STEMI patient non-classical monocytes during the acute post-reperfusion period (Pre-90min) correlated significantly with lower LVEF. r = Spearman correlation coefficient. *p<0.05.

4.2.5 Preferential Depletion in Non-Classical Monocytes at Pre-Reperfusion-90minutes Post-Reperfusion is not associated with STEMI patient Troponin

Following STEMI, measurement of patient troponin T levels is routinely performed to confirm the diagnosis of an MI and approximate the extent of myocardial damage. Troponin T levels are a biomarker indicative of myocardial necrosis, and therefore typically rise 2-4 hours following the event of an MI [292]. Peak troponin T levels therefore expectedly increase with STEMI patient infarct size, which we observe in this study ($p<0.0001$) (Figure 4.6).

As I previously discovered that the acute post-reperfusion dynamics (pre-90min) of non-classical monocytes were significantly correlated with STEMI patient infarct size, I subsequently analysed the association between monocyte subset kinetics at this time point with peak levels of Troponin T, as a measure of myocardial injury, to identify the existence of a similar relationship.

When analysing the full cohort of STEMI patients, there was no significant correlation between peak troponin T levels and classical, intermediate, or non-classical monocyte dynamics between pre-reperfusion and 90 minutes' post-reperfusion (Figure 4.7A). Categorisation of STEMI patients into tertiles of infarct size (small, medium, large), also revealed no significant relationship between the pre-90min dynamics of monocyte subpopulations in small (Figure 4.7B), medium (Figure 4.7C) or large (Figure 4.7D) infarcts, with peak troponin T levels.

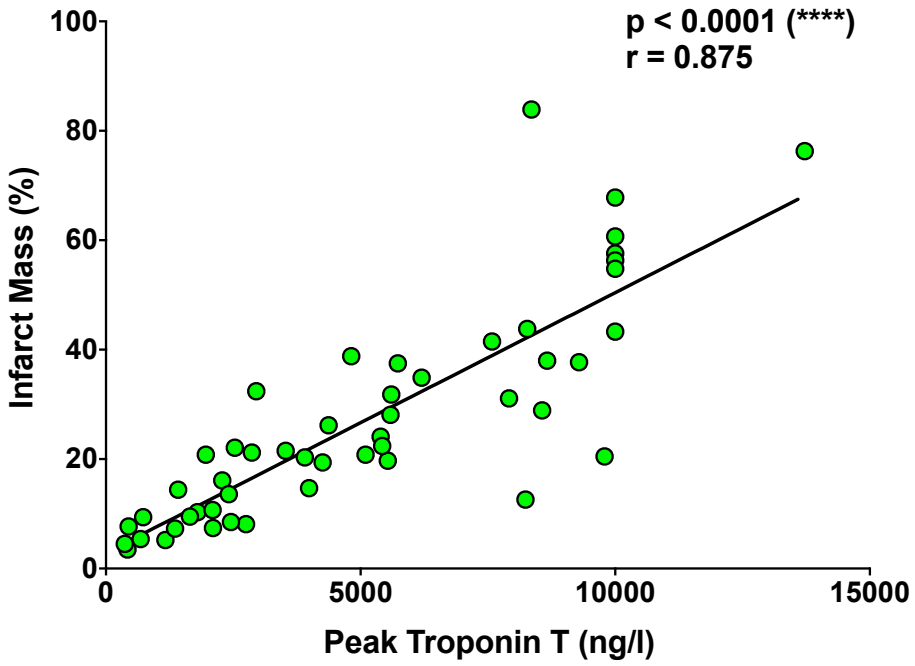

Figure 4. 6. Relationship between STEMI Patient Peak Troponin T levels (ng/l) with infarct mass (% of LV).

STEMI patient peak troponin T levels were measured as part of routine clinical care to confirm the diagnosis of an MI and approximate the extent of myocardial damage. Infarct mass was determined using the same short axis LGE images used for measuring infarct size and MVO; regions of hypoenhancement within the enhanced zone (MVO) were included in the calculated infarct mass. r = Spearman correlation coefficient. n=53 STEMI patients. ****p<0.0001.

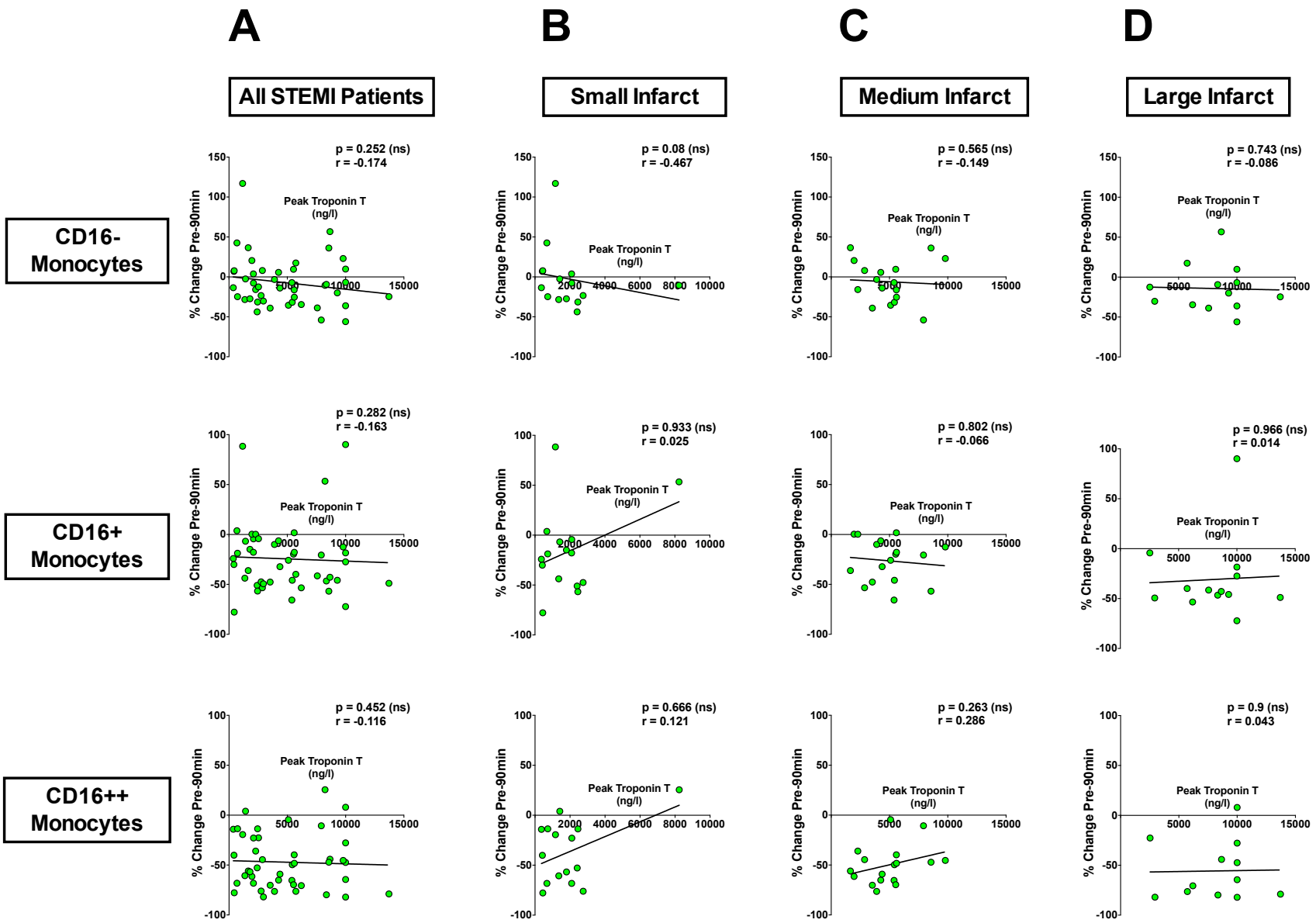
A
B
C
D
All STEMI Patients
Small Infarct
Medium Infarct
Large Infarct
CD16- Monocytes
CD16+ Monocytes
CD16++ Monocytes
% Change Pre-90min
Peak Troponin T (ng/l)
p = 0.252 (ns)
r = -0.174
p = 0.08 (ns)
r = -0.467
p = 0.565 (ns)
r = -0.149
p = 0.743 (ns)
r = -0.086
p = 0.282 (ns)
r = -0.163
p = 0.933 (ns)
r = 0.025
p = 0.802 (ns)
r = -0.066
p = 0.966 (ns)
r = 0.014
p = 0.452 (ns)
r = -0.116
p = 0.666 (ns)
r = 0.121
p = 0.263 (ns)
r = 0.286
p = 0.9 (ns)
r = 0.043

Figure 4. 7. Correlation between STEMI patient peak troponin levels and total acute post-reperfusion changes (pre-90min) in classical, intermediate, and non-classical monocytes.

Acute post-reperfusion changes (pre-90min) in classical $CD16^{-}$, intermediate $CD16^{+}$, and non-classical $CD16^{++}$ monocytes in A. all STEMI patients. B. small infarct patients C. medium infarct patients and D. large infarct patients. Statistics refer to the
r = Spearman correlation coefficient. n=53 STEMI patients.

4.2.6 Enhanced monocyte subset quantification in a prospective STEMI patient study confirms acute post-reperfusion changes (pre-90min) in circulating non-classical monocytes.

In the retrospective STEMI patient study, the analysis of circulating classical, intermediate, and non-classical monocyte populations relied on using scatter properties to define the total monocyte population and CD16 expression to define each monocyte subset. While this method adequately quantified each monocyte subpopulation, a more accurate approach would include a comprehensive panel of leukocyte markers to ensure interpretation of pure monocyte subpopulations.

This strategy was therefore employed in a subsequent smaller prospective STEMI patient study (n=13) (Table 4.1), whereby monocytes were defined as $CD3^{-}$ $CD19^{-}$ $CD56^{-}$ HLA-DR^{+}. Monocyte subpopulations were then further refined as classical ($CD14^{++}$ $CD16^{-}$ $CCR2^{hi}$ $CX3CR1^{low}$), intermediate ($CD14^{++}$ $CD16^{+}$ $CCR2^{mid}$ $CX3CR1^{hi}$) and non-classical ($CD14^{+}$ $CD16^{++}$ $CCR2^{low}$ $CX3CR1^{hi}$) monocytes. This method of monocyte FACS gating is shown in Figure 4.8. Expression of each marker expressed as MFI by each monocyte subset is shown in Figure 4.9. Importantly, the marker expression profile of each blood monocyte subset analysed in this study correspond to current nomenclature [293] [294]. Through the use of this detailed panel of leukocyte markers, this gating strategy also allowed phenotyping of CX3CR1 expression by T-cells, B-cells, and NK-cells (Figure 4.10).

The aim of this prospective study was to confirm the circulating monocyte subpopulation kinetics previously observed in the retrospective STEMI cohort following reperfusion, with a more refined method of polychromatic FACS analysis. The key objective was to identify whether the same ~46% depletion of non-classical monocytes from pre-reperfusion to 90min post-reperfusion seen in the retrospective study also occurred with a refined FACS method. An additional time point of 180 minutes post-reperfusion was included in this prospective study to investigate whether non-classical monocyte counts continue to decline, or plateau in the circulation after 90 minutes.

In concordance with the retrospective STEMI patient study, circulating non-classical monocyte counts significantly decreased during the acute post-reperfusion period (pre-90min) by 52% (±6) (81±11 to 36±5 cells/μl, p=0.0008) (Figure 4.11). At the additional time point of 180 minutes' post-reperfusion, non-classical monocyte counts do not continue to fall but remain depleted at similar levels to 90 minutes' post-reperfusion.

Classical and intermediate monocytes show a 9% and 24% reduction in the blood from pre-reperfusion to 90 minutes' post-reperfusion, respectively (Figure 4.11). These dynamics are comparable with the retrospectively observed 7% and 21% decline in these subsets during this time period. It must however be noted that these changes are not significant in the prospective study, unlike the retrospective analyses, which may be a reflection of the smaller sample size in the prospective cohort. At 24 hours' post-reperfusion, classical and intermediate monocyte counts recover to and beyond pre-reperfusion levels, as witnessed in the retrospective study.

In this prospective analysis, I also sought to determine whether monocyte subset counts differed between arterial locations, specifically between aortic, right coronary artery (RCA), and left coronary artery (LCA) blood samples. For a subset of STEMI patients (n=6), RCA and LCA were identified as either the culprit or non-culprit artery. Pre-reperfusion classical, intermediate, and non-classical monocyte subset counts all showed no significant distinction between aortic, culprit, and non-culprit artery samples (Figure 4.12). Such samples were discontinued after 6 patients due to the absence of a significant difference.

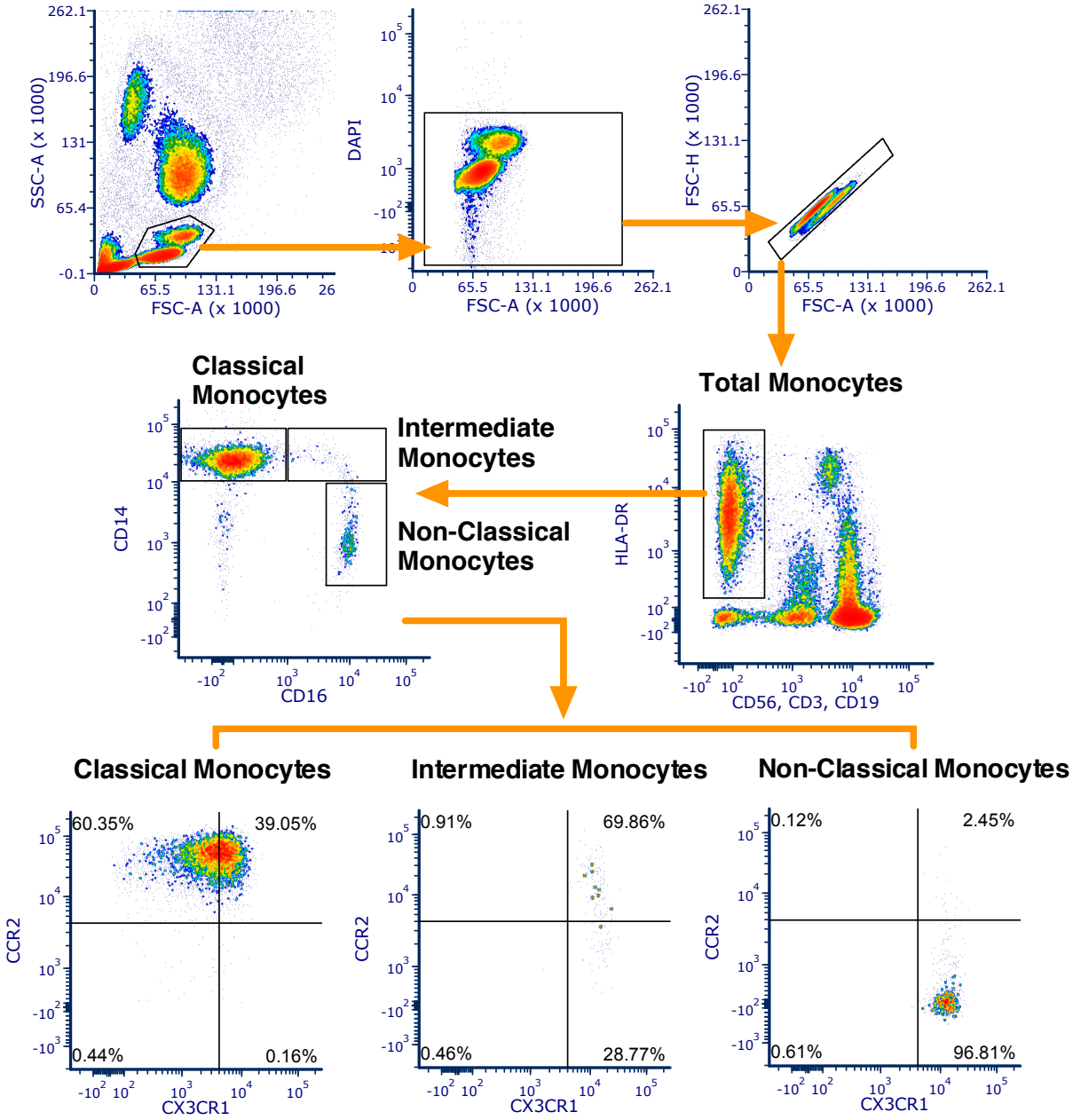
SSC-A (x 1000)
FSC-A (x 1000)
DAPI
FSC-A (x 1000)
FSC-H (x 1000)
FSC-A (x 1000)
Total Monocytes
HLA-DR
CD56, CD3, CD19
Classical Monocytes
Intermediate Monocytes
Non-Classical Monocytes
CD14
CD16
Classical Monocytes
Intermediate Monocytes
Non-Classical Monocytes
CCR2
CX3CR1
60.35%
39.05%
0.44%
0.16%
0.91%
69.86%
0.46%
28.77%
0.12%
2.45%
0.61%
96.81%

Figure 4. 8. Prospective STEMI patient polychromatic (multi-parameter) FACS gating of human blood monocytes.

Gating of whole blood lymphocytes and monocytes was first performed based on the forward (FSC-A) and side (SCA-A) scatter properties of these cell populations. Live cells were then selected as $DAPI^-$, and single cells were selected based on FSC-H and FSC-A to exclude cell doublets. T-cells, B-cells and NK-cells were excluded on the basis of CD3, CD19 and CD56 expression, respectively (Lin^+). HLA-DR^+ non-monocytes such as dendritic cells were excluded as $CD14^-$ $CD16^-$ cells. Expression of monocyte markers CD14, CD16, CCR2 and CX3CR1 by each monocyte subset defined each population as classical monocytes [$CD14^{++}$ $CD16^-$ $CCR2^{high}$ $CX3CR1^{low/mid}$], intermediate monocytes [$CD14^{++}$ $CD16^+$ $CCR2^{inter}$ $CX3CR1^{mid}$], non-classical monocytes [$CD14^+$ $CD16^{++}$ $CCR2^{low}$ $CX3CR1^{high}$].

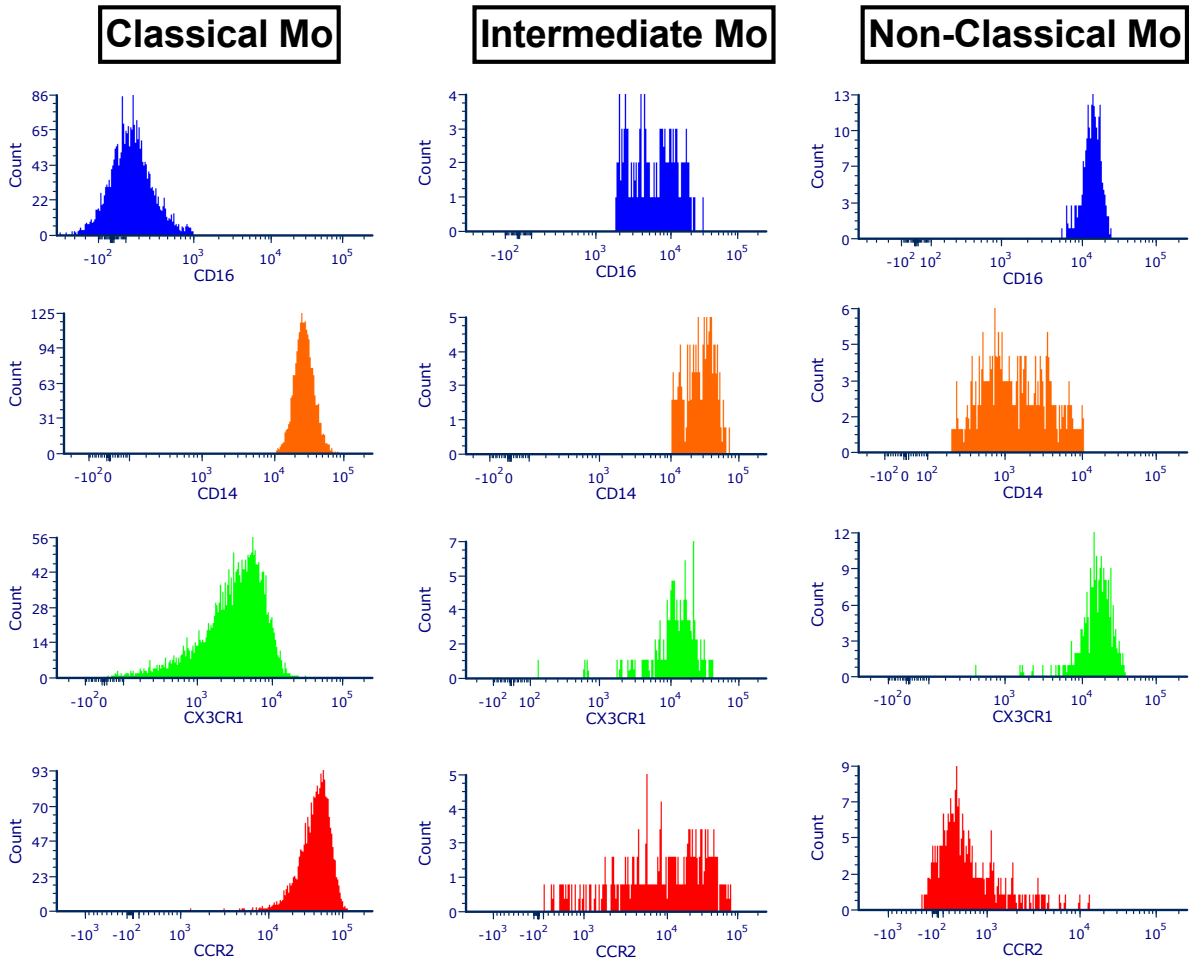

Figure 4. 9. Histograms showing the relative expression of CD16, CD14, CX3CR1, and CCR2 by human blood classical, intermediate, and non-classical monocyte subpopulations.

Expression was quantified using the mean fluorescence intensity (MFI) on the relevant channel for each monocyte subset (CD16-APC-H7, CD14-BV510, CX3CR1-APC, CCR2-PE-Cy7). Mo = monocytes.

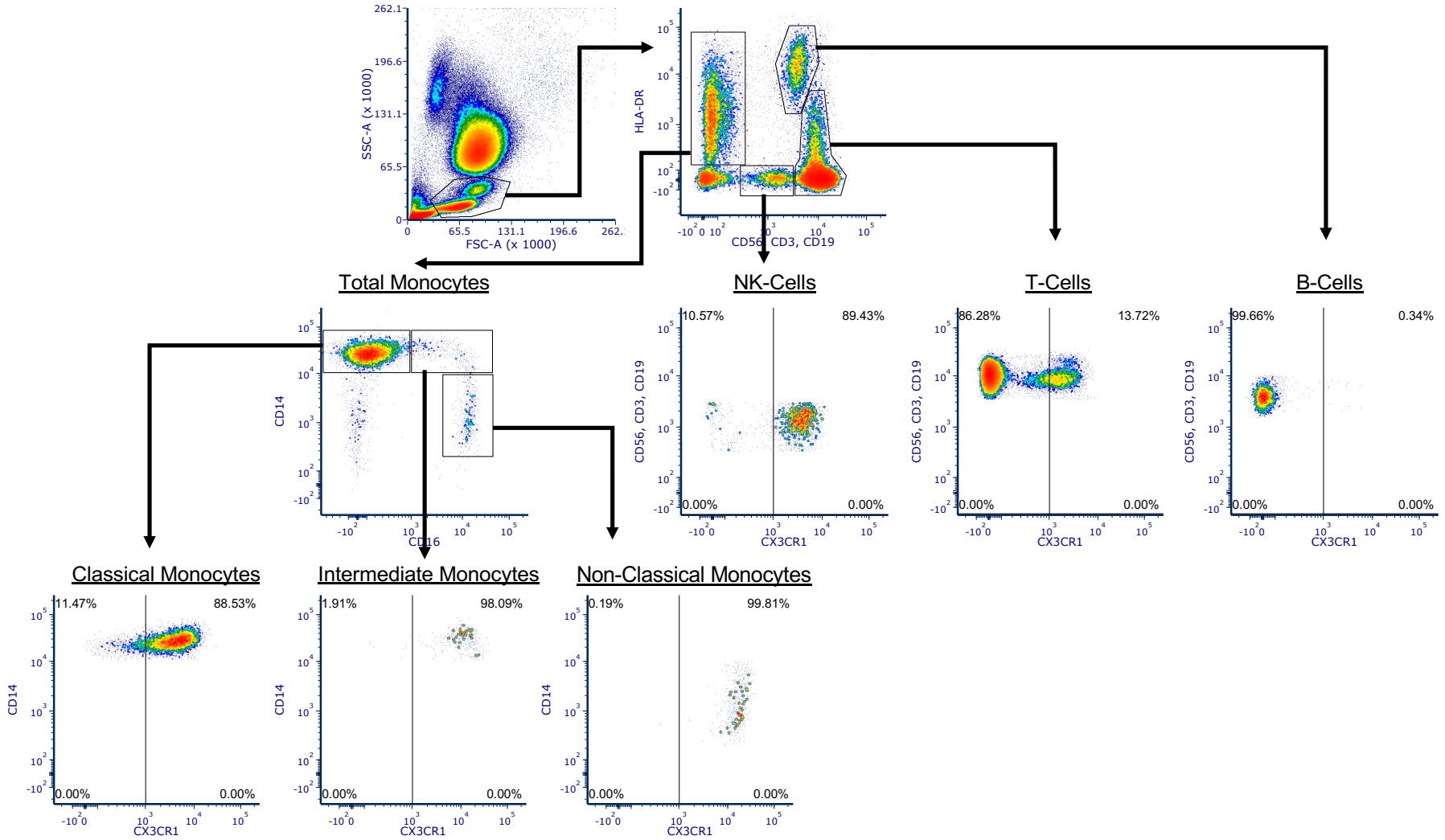
SSC-A (x 1000)
FSC-A (x 1000)
HLA-DR
CD56, CD3, CD19
Total Monocytes
NK-Cells
T-Cells
B-Cells
CD14
CD16
CD56, CD3, CD19
CX3CR1
10.57%
89.43%
0.00%
0.00%
86.28%
13.72%
99.66%
0.34%
Classical Monocytes
Intermediate Monocytes
Non-Classical Monocytes
11.47%
88.53%
1.91%
98.09%
0.19%
99.81%

Figure 4. 10. FACS gating strategy for delineation of monocyte subsets, NK-cells, T-cells, B-cells, and phenotyping of CX3CR1 by each leukocyte population.

Classical monocytes ($CX3CR1^{low}$), intermediate monocytes ($CX3CR1^{med}$), non-classical monocytes ($CX3CR1^{high}$). NK cells and a subset of T-cells express CX3CR1, while B-cells are $CX3CR1^{-}$.

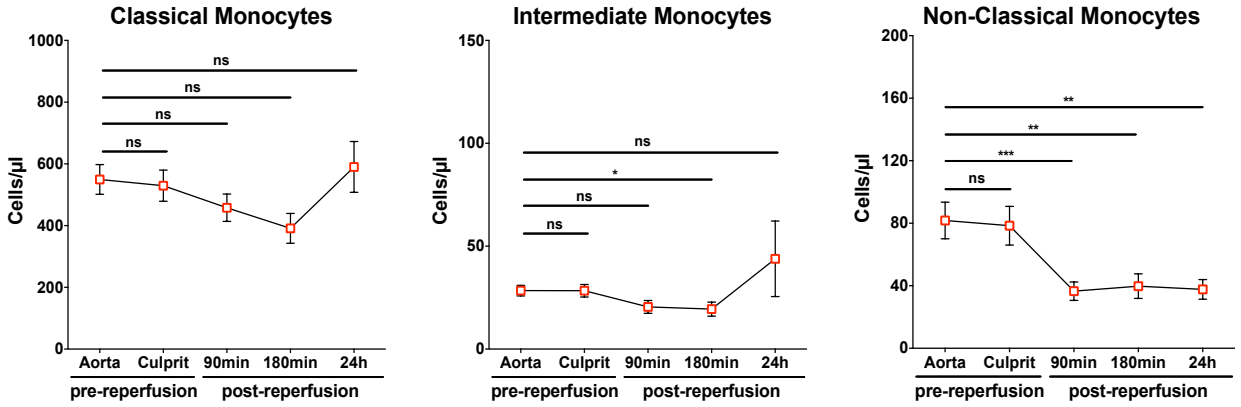

Figure 4. 11. Prospective STEMI patient study confirms the depletion of circulating non-classical monocytes at 90 minutes' post-reperfusion.

Classical, intermediate, and non-classical monocyte cell counts were measured from pre-reperfusion and at 90min, 180min and 24h post-PCI. Statistical analysis of the difference in counts between indicated time points was performed using repeated measure paired analysis with Bonferroni adjustment for multiple comparisons (n=13). *p<0.05, **p<0.01, *** p<0.001.

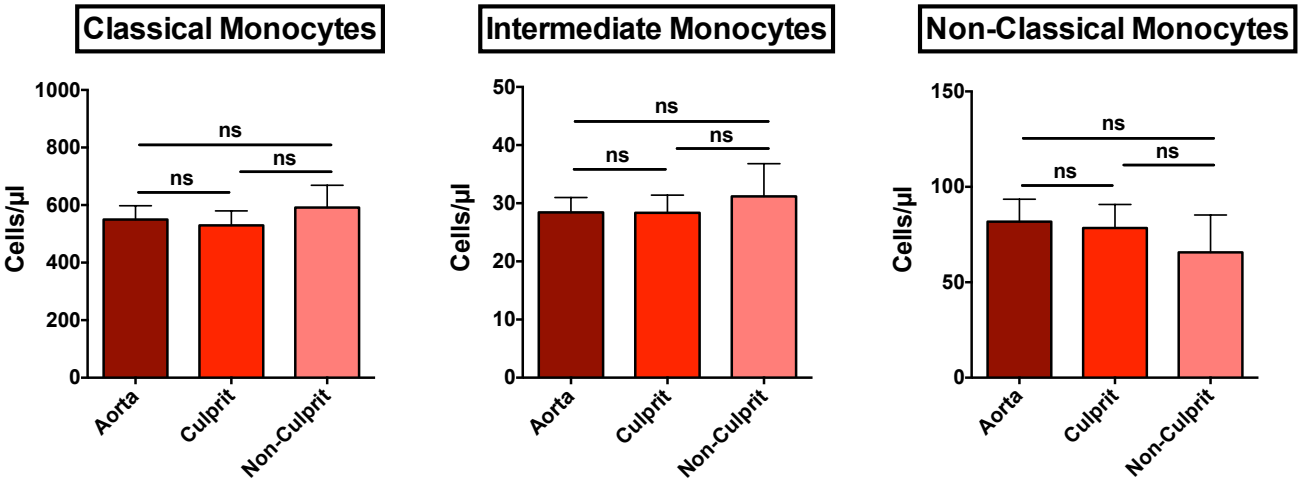

Figure 4. 12. Comparison of prospective STEMI patient monocyte subset counts between aortic, culprit and non-culprit vessels (RCA or LCA).

The culprit and non-culprit vessel was identified as either the RCA or LCA. Statistical analysis of the difference in counts between indicated blood samples was performed using one-way Anova with Tukey's multiple comparison test (n=6).

4.2.7 Comparison of Retrospective and Prospective STEMI Patient Non-Classical Monocyte Dynamics at 24h post-PCI

Comparison between this prospective study and the previously described retrospective STEMI patient study showed that there is a similar fall in circulating non-classical monocytes between pre-reperfusion (baseline) and 90 minutes' post reperfusion (Figure 4.13A). Specifically, non-classical monocytes are depleted from baseline to 90 min post-reperfusion in the retrospective study by 46% which is not significantly different from the 52% drop observed in the prospective study. Classical and intermediate monocytes also show comparable dynamics (from baseline to 90min) between studies. Classical monocytes fall in the circulation by 9% and 7% in retrospective and prospective studies, respectively (Figure 4.13B). Intermediate monocytes show a comparable 24% and 21% decline between studies (Figure 4.13C). At 24h post-reperfusion, classical and intermediate monocyte populations recover in the circulation, returning to baseline levels in both studies. However, a fundamental difference that was observed between the two studies was that non-classical monocyte counts recover at 24 hours post-reperfusion in the retrospective study (Figure 4.2A), while prospective STEMI patients' non-classical monocyte counts remain depleted in the circulation at 24 hours (Figure 4.11). Notably, this discrepancy between studies was specific to $CD16^{++}$ non-classical monocytes. To examine this difference, the retrospective method of monocyte gating was applied to the prospective STEMI patient data (Figure 4.14A). This analysis revealed that there was a population of $CD16^{++}$ cells within the $CD16^{++}$ non-classical monocyte gate that were HLA-DR^{-} and distinct from $CD16^{++}$ HLA-DR^{+} non-classical monocytes. In the human immune system, CD16 is expressed by monocytes, NK-cells and neutrophils [295-297]. Since NK-cells were removed by CD56, it was deduced that these cells may be neutrophils. Further profiling of this confounding cell population revealed that these cells had higher side scatter than monocytes, which also supported the neutrophil identity of these cells since neutrophils are known to have increased side scatter than that of monocytes. Further analysis showed that these cells did not express CX3CR1, and expressed low levels of CD14 and CCR2. Such a cell marker profile was also consistent with a neutrophil identity. Analysis of the dynamics of $CD16^{++}$ HLA-DR^{+} non-classical monocytes following reperfusion compared to the assumed $CD16^{++}$

HLA-DR$^-$ neutrophil population then revealed that non-classical monocytes remain depleted in the circulation at 24h, whilst the suspected neutrophil population increased at 24h post-PCI (Figure 4.14B). These cells are known to increase dramatically in the peripheral blood of STEMI patients at 24h post infarction, most likely due to a shift from the bone marrow following emergency granulopoiesis [298-300].

This analysis concluded that the retrospective analysis of non-classical monocytes at 24h post-reperfusion was confounded by a small population of neutrophils. Despite this limitation at the 24h time point, non-classical monocyte dynamics observed between pre-reperfusion and 90 minutes post-PCI were concordant between studies (Figure 4.13), and therefore it is likely that the associations reported in this thesis between pre-90min non-classical monocytes with infarct size and LVEF are indeed valid.

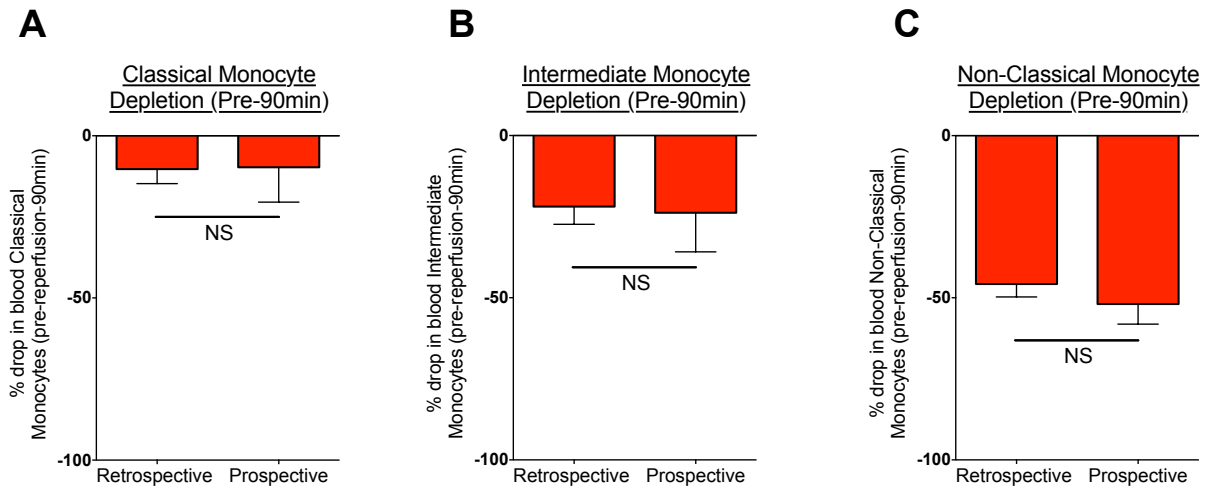

Figure 4. 13. Percentage drop in monocyte subpopulations in STEMI patients from pre-reperfusion to 90 minutes post-PCI.

Retrospective and prospective STEMI patient studies concur, in that there is a significant depletion in non-classical monocytes in the circulation from pre-PCI to 90min post-reperfusion, by 46% and 52% respectively, which is not significantly different between studies.

A

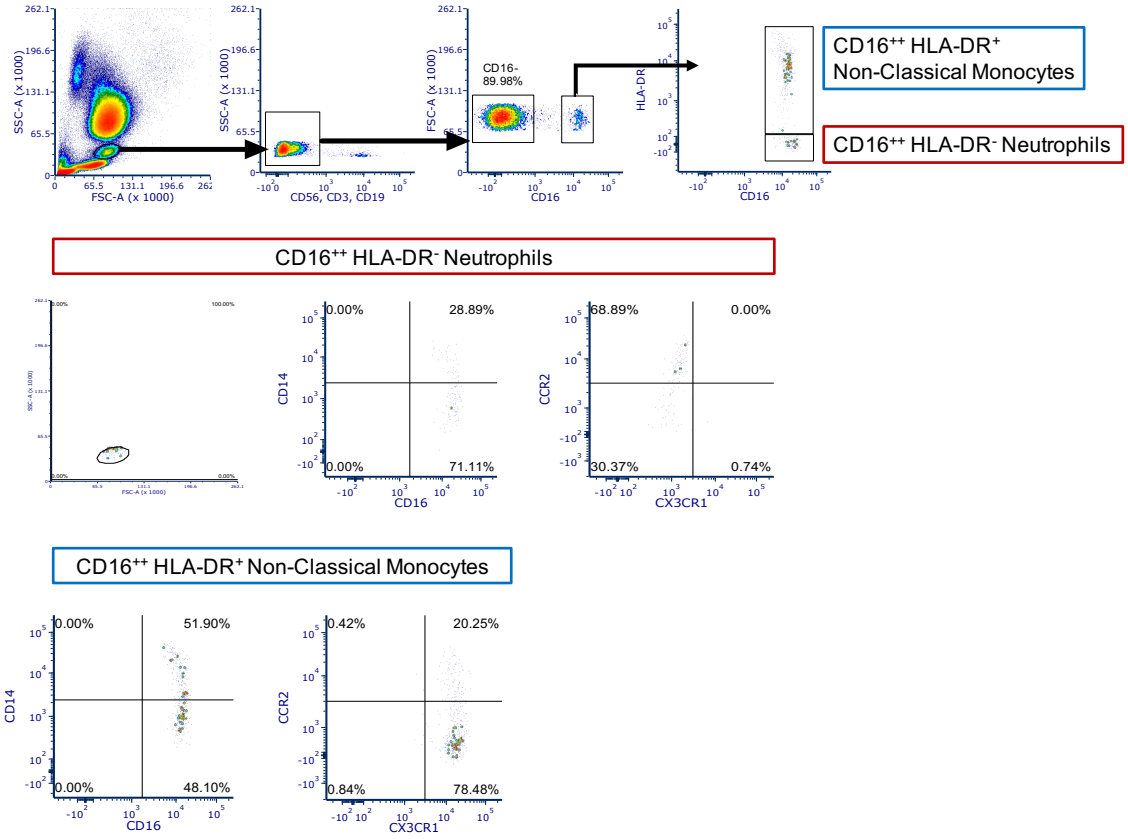
CD16++ HLA-DR+
Non-Classical Monocytes
CD16++ HLA-DR- Neutrophils
SSC-A (x 1000)
FSC-A (x 1000)
CD56, CD3, CD19
CD16-
89.98%
HLA-DR
CD16
CD16++ HLA-DR- Neutrophils
0.00%
28.89%
0.00%
71.11%
CD14
CD16
68.89%
0.00%
30.37%
0.74%
CCR2
CX3CR1
CD16++ HLA-DR+ Non-Classical Monocytes
0.00%
51.90%
0.00%
48.10%
CD14
CD16
0.42%
20.25%
0.84%
78.48%
CCR2
CX3CR1

B

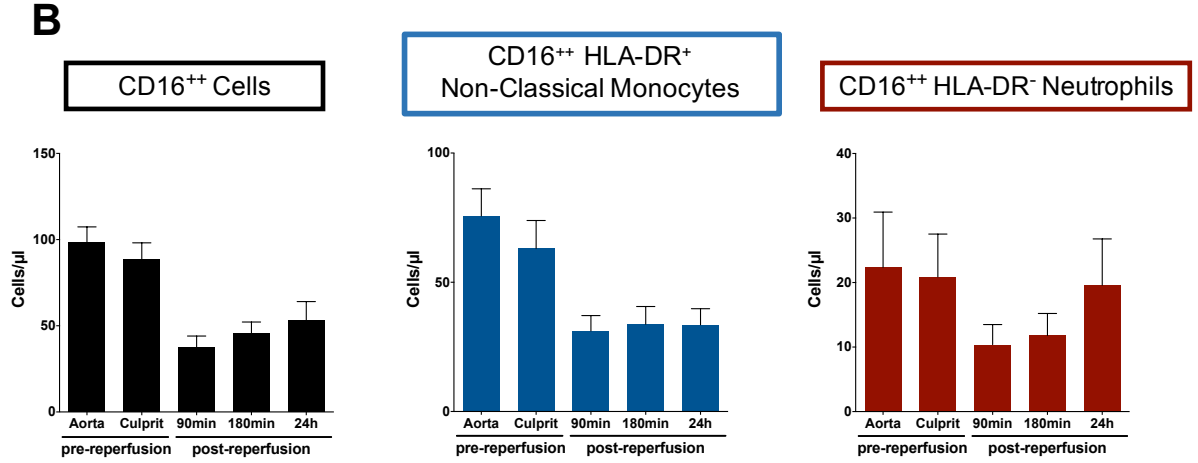
CD16++ Cells
CD16++ HLA-DR+
Non-Classical Monocytes
CD16++ HLA-DR- Neutrophils
Cells/µl
Aorta
Culprit
90min
180min
24h
pre-reperfusion
post-reperfusion

Figure 4. 14. Comparative analyses between retrospective and prospective STEMI patient studies.

A. Representative example of the retrospective monocyte gating method applied to the prospective data, with the subsequent use of HLA-DR, CD14 and CCR2 to interrogate any observed differences. A small population of HLA-DR^{-} CD16^{++} neutrophils are present within the CD16^{++} non-classical monocyte gate which are responsible for the increase in CD16^{++} population counts at 24h post-PCI in the retrospective study. B. Comparison of dynamics between CD16^{++} HLA-DR^{+} non-classical monocytes and CD16^{++} HLA-DR^{-} neutrophils shows that a small population of neutrophils contaminating the CD16^{++} non-classical monocyte gate is responsible for the increased counts of these cells observed at 24h post-I/R. When this neutrophil population is excluded, non-classical monocyte counts do not increase at 24h but remain depleted.

4.2.8 Comparison of Retrospective and Prospective STEMI Patient Non-Classical Monocyte Dynamics at Pre-Reperfusion

In addition to the discrepancy in non-classical monocyte counts at 24h post-cardiac I/R between studies, it was also important to address the difference in non-classical monocyte counts observed at the time of pre-reperfusion between retrospective and prospective STEMI patient cohorts. At this time point, retrospective STEMI patients had noticeably lower counts of non-classical monocytes than those in the prospective analysis (Figure 4.15). Such a difference in non-classical monocyte counts specifically at pre-reperfusion was investigated as both a technical and biological discrepancy.

When comparing the gating strategies for monocyte quantification between studies, a fundamental difference was that the retrospective total monocyte gate was defined on the forward and side scatter of total monocytes (Figure 4.1), in contrast to the prospective method which included both the lymphocyte and monocyte populations (Figure 4.8). Examination of classical, intermediate, and non-classical monocyte subpopulations within the prospective total monocyte and lymphocyte scatter gate revealed that the non-classical monocytes have lower side scatter than the other monocyte subsets, and therefore are situated closer to the lymphocyte border of the monocyte scatter population (Figure 4.16). Based on this observation it was speculated that the retrospective gating method may have led to the exclusion of a small proportion of non-classical monocytes due to the gating cut off at the monocyte/lymphocyte border. This technical difference between retrospective and prospective gating methods may in part account for the reduced counts of pre-reperfusion non-classical monocytes in the retrospective cohort compared to the prospective cohort.

It is also plausible that such variation may be due to a biological difference between patient cohorts; it is well published that leukocyte counts fall in the circulation in response to ischemia following MI, the extent of which is related to the extent of myocardial injury. It therefore follows that a larger infarct would induce a stronger depletion of circulating leukocytes. To investigate the existence of a difference in infarct size and therefore the extent of myocardial injury between retrospective and

prospective STEMI patients, peak troponin T levels were compared between studies. Interestingly, the retrospective STEMI patient cohort was found to have a higher average level of peak troponin T (4895±530) than prospective patients (3173±786) (Figure 4.17A). Although this difference was not significant, it demonstrated a similar trend to the non-significantly higher counts of pre-reperfusion non-classical monocytes in prospective patients. Peak troponin T levels were then correlated against pre-reperfusion non-classical monocyte counts in each study. This analysis showed that retrospective STEMI patient pre-reperfusion non-classical monocyte counts correlated significantly with peak troponin T levels (Figure 4.17B), whereby a lower non-classical monocyte count at pre-reperfusion was significantly associated with a greater infarct size as determined by higher peak troponin T. It therefore appeared that the retrospective cohort had a larger average infarct size than prospective patients, as determined by high Troponin T levels, which induced an earlier depletion of non-classical monocytes in the circulation. Patients in the retrospective cohort may have suffered from larger infarct due to the longer ischemia period observed in this cohort; the mean onset-to-balloon time was 10% longer in the retrospective population (161min) than in the prospective cohort (151min). On a final note, it is also important to keep in mind the natural variation in the individual response to cardiac I/R between patients, which is inevitable in any study.

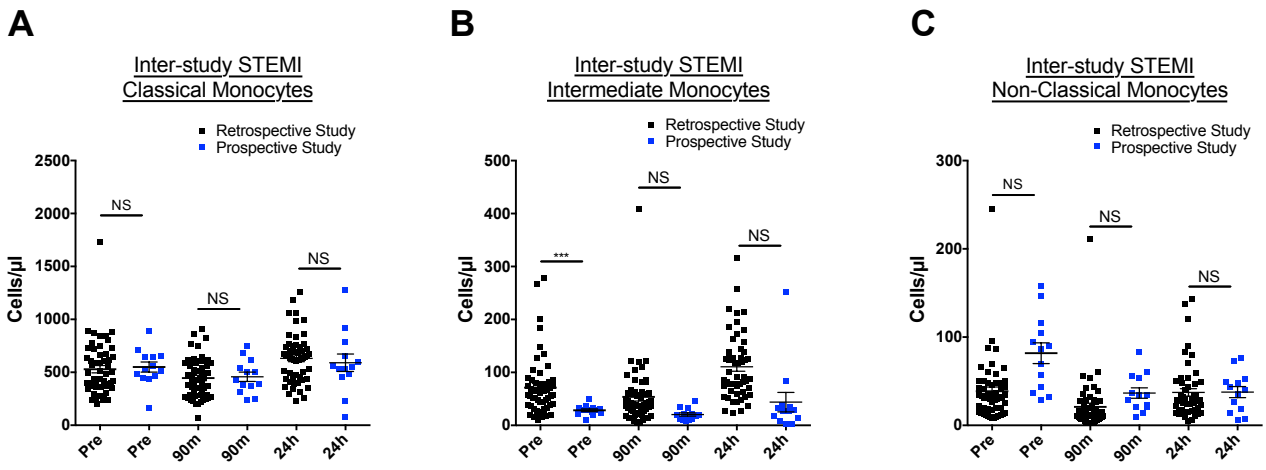

Figure 4. 15. Comparison of monocyte subpopulation counts between retrospective and prospective STEMI patient cohorts at pre-reperfusion, 90 minutes and 24 hours following PCI.

Comparative data shows no significant difference in non-classical monocyte counts between studies at any of the time points studied, though there is a trend towards reduced non-classical monocyte counts at pre-reperfusion and 90 minutes' post-reperfusion in the retrospective study compared to the prospective study. Intermediate monocyte counts are significantly reduced in the prospective study at pre-reperfusion. At 90 minutes and 24 hours intermediate monocyte counts appear to be reduced in the prospective study, though this is not significant. Data analysed by one-way Anova with Tukey's multiple comparison test. ***$p<0.001$.

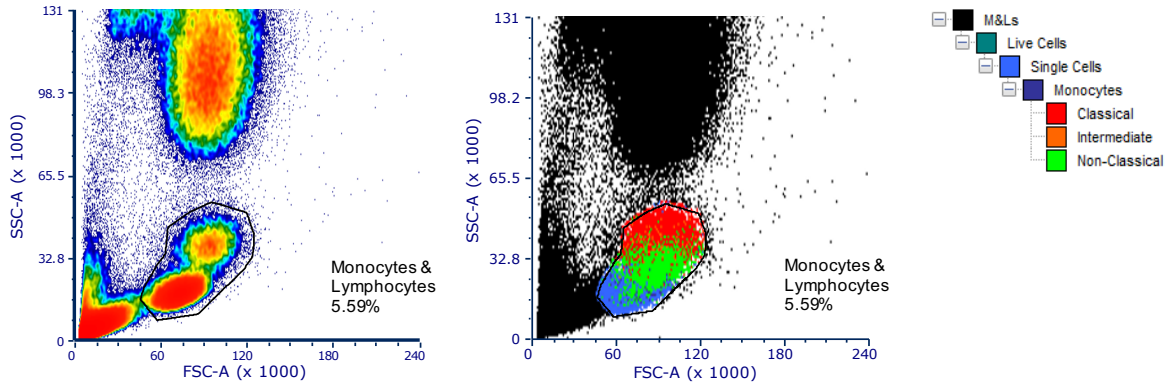

Figure 4. 16. Analysis of blood monocyte subpopulation scatter properties in the prospective STEMI patient study.

Interrogation of human blood monocyte subpopulation side scatter showed that non-classical monocytes have lower side scatter than classical and intermediate monocytes, and overlap with the lymphocyte population. Total monocyte and lymphocyte populations should therefore be gated on to ensure inclusion of all non-classical monocytes in their quantification by FACS.

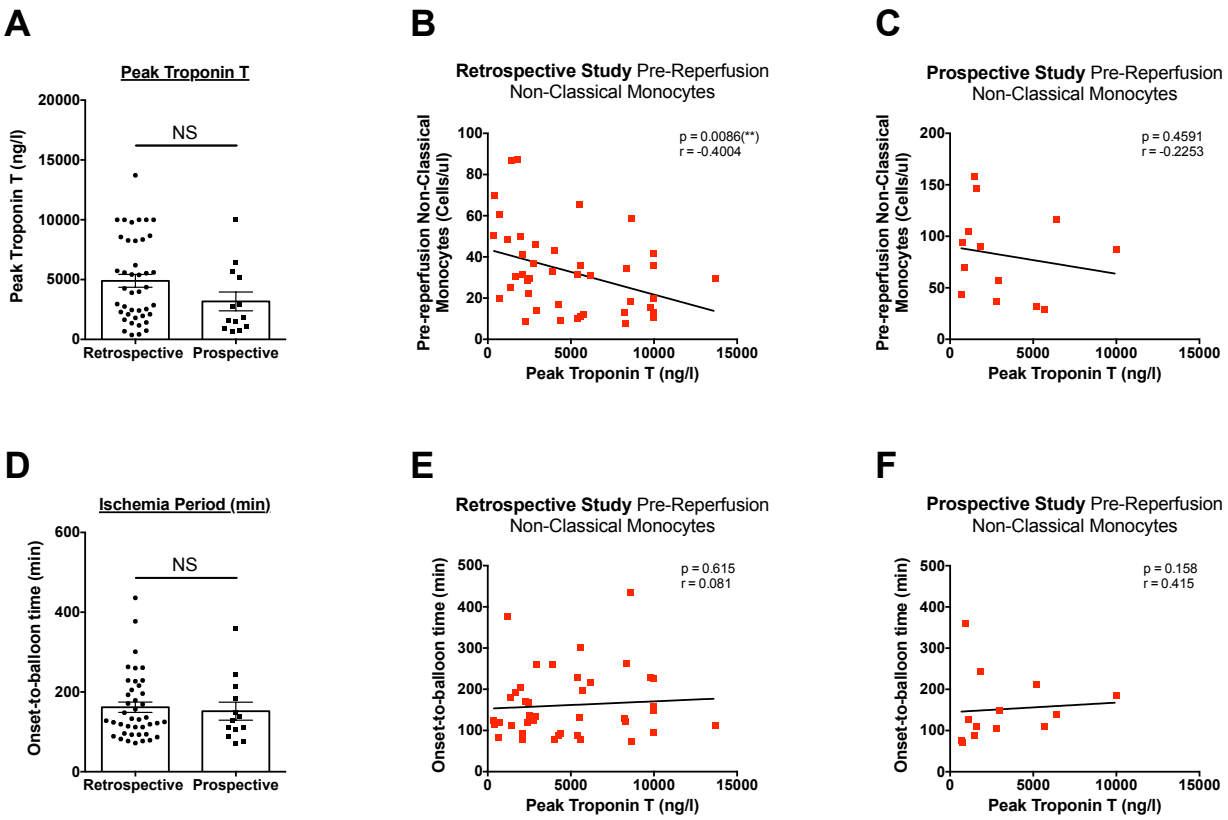
A
Peak Troponin T
Peak Troponin T (ng/l)
20000
15000
10000
5000
0
NS
Retrospective
Prospective
B
Retrospective Study Pre-Reperfusion
Non-Classical Monocytes
Pre-reperfusion Non-Classical Monocytes (Cells/ul)
p = 0.0086(**)
r = -0.4004
Peak Troponin T (ng/l)
C
Prospective Study Pre-Reperfusion
Non-Classical Monocytes
Pre-reperfusion Non-Classical Monocytes (Cells/ul)
p = 0.4591
r = -0.2253
Peak Troponin T (ng/l)
D
Ischemia Period (min)
Onset-to-balloon time (min)
NS
Retrospective
Prospective
E
Retrospective Study Pre-Reperfusion
Non-Classical Monocytes
Onset-to-balloon time (min)
p = 0.615
r = 0.081
Peak Troponin T (ng/l)
F
Prospective Study Pre-Reperfusion
Non-Classical Monocytes
Onset-to-balloon time (min)
p = 0.158
r = 0.415
Peak Troponin T (ng/l)

Figure 4. 17. Comparison of troponin T levels and onset-to-balloon times between retrospective and prospective STEMI patient studies with relation to acute post-reperfusion (Pre-90min) non-classical monocyte dynamics.

A, D. Comparison of peak troponin T levels and onset-to-balloon times between retrospective (n=53) and prospective studies (n=13), respectively. B. Relationship between pre-reperfusion non-classical monocyte counts and peak troponin T levels in the retrospective study; a lower count of non-classical monocytes prior to reperfusion is significantly associated with higher peak troponin T levels ($p = 0.0086$), which may explain the lower pre-reperfusion non-classical monocyte count in the retrospective study compared to the prospective study. C. No significant relationship between pre-reperfusion non-classical monocyte counts and peak troponin T levels in the prospective study, though this analysis may be underpowered (n=13). E, F. Relationship between onset-to-balloon time (ischemic period) and peak troponin T levels in the E. retrospective study and F. prospective study. In both studies, there was no significant correlation between onset-to-balloon time and peak troponin T levels. A, D. Data analysed by Mann-Whitney U Test. B, C, E, F. r = Spearman correlation coefficient. **$p<0.01$.

4.3 Discussion

4.3.1. Generation of a Reproducible and Accurate Human Monocyte Subset FACS Gating Strategy

The study of human monocyte subsets until recent years has been hampered by the use of inconsistent methods of monocyte subset definition. Research has traditionally relied on the markers CD16 and CD14 for monocyte subset definition, though populations of intermediate and non-classical monocytes defined using this approach are frequently contaminated [301]. For example, one limitation of the conventional CD16 / CD14 gating strategy is the confounding of the non-classical monocyte population by NK-cells which have low CD14 and high CD16 expression. One way to avoid inclusion of NK-cells in the non-classical monocyte gate is to exclude $CD14^{very\ low\text{-}neg}$ cells, however this can result in up to 50% loss of the non-classical monocyte population [302]. As employed in this study, a specific NK-cell marker (CD56) should therefore be included. The results of such studies using CD16 and CD14 therefore frequently misclassify monocyte subsets and are not directly comparable to accurately determine monocyte subpopulation dynamics in disease [303]. One approach to minimize the inconsistencies that arise from the arbitrary gate placement using CD14 and CD16 is to combine multiple informative cell surface markers. In this study, I therefore designed a polychromatic (8 antibodies) panel consisting of CD3, CD19, CD56 and HLA-DR, in addition to the baseline markers of CD14 and CD16. These markers permitted exclusion of T-cells, B-cells, NK-cells, and granulocyte populations. This approach alone however does not address the issue of inter-monocyte subset contamination. To address this and increase the specificity of monocyte subset identification, the chemokine markers CCR2 and CX3CR1 were included and used in combination to confirm monocyte subset definition; classical monocytes $CCR2^{hi}$ $CX3CR1^{lo}$, intermediate monocytes $CCR2^{mid}$ $CX3CR1^{mid}$, non-classical monocytes $CCR2^{lo}$ $CX3CR1^{hi}$. This method was reproducible throughout the STEMI patient prospective study and therefore provides a robust, accurate, and sensitive protocol for human blood monocyte subset quantification by flow cytometry. More recent studies have used a similar approach and reported high monocyte subset purity [286].

4.3.2. Circulating Non-Classical Monocytes Are Preferentially Depleted in STEMI Patients at 90 minutes post-PCI

The retrospective and prospective studies of STEMI patient monocyte dynamics following reperfusion reported in this chapter show for the first time, that non-classical monocytes are preferentially depleted in the circulation at 90 minutes following PCI, compared to pre-reperfusion (baseline). This drop was dramatic, with a loss of 46% and 52% circulating non-classical monocytes in the retrospective and prospective study, respectively. This finding cannot be directly compared with existing literature to date, since all clinical studies of monocyte subset dynamics following MI have focused on time points from day 1 onwards following reperfusion. As such, the immediate 24h changes in monocyte kinetics following PCI have not been addressed. Moreover, I observed that NSTEMI control group levels of non-classical monocytes were consistently higher than that of STEMI patients, at 15, 30, and 90 minutes' post-reperfusion, and NSTEMI patients did not demonstrate a significant depletion of non-classical monocytes. Given that NSTEMI patients did not experience cardiac I/R, however did receive the same PCI procedure, it is therefore reasonable to conclude that the characteristic changes in circulating non-classical monocyte counts were not procedurally induced, but rather were in response to cardiac I/R injury. In this respect, the NSTEMI group of patients was a particularly important control group for the study of monocyte behaviour following myocardial I/R. The striking dynamics of non-classical monocytes during the acute post-reperfusion period are largely confined to this subset, and are not observed to the same extent in the case of classical and intermediate monocyte populations; classical and intermediate monocytes fall in the circulation by an average of 8% and 22% between studies, respectively. Based on this observation it is reasonable to suspect that the specificity of response by non-classical monocytes may be related to their high expression of CX3CR1, which is expressed at lower levels by classical and intermediate monocytes. The expression of CX3CR1 therefore increases incrementally with the extent of monocyte subset depletion in the circulation following reperfusion. In support of this idea, Boag et al [209] have shown that STEMI patient serum CX3CL1 levels peak at 90 minutes following reperfusion, and is therefore synchronous with the peak depletion of non-classical monocytes.

The vast loss of non-classical monocytes from the circulation following cardiac I/R could indicate a number of responses by these cells in response to myocardial injury. It is possible that following reperfusion, these cells are marginated to the coronary endothelium, prior to their extravasation into the myocardial tissue to facilitate repair, leading to a decrease in circulating counts. As previously described in Chapter 1, this process is largely mediated by the CX3CL1/CX3CR1 axis; the release of CX3CL1 following myocardial injury governs the chemoattraction of non-classical monocytes to the injured myocardial tissue, while upregulation of vascular endothelium-expressed CX3CL1 in response to inflammatory signals mediates interaction with CX3CR1 to permit extravasation of non-classical monocytes. This process could occur within the myocardial vasculature and at sites of endothelial activation.

4.3.3. Acute Post-Reperfusion (Pre-90min) Non-Classical Monocyte Dynamics in STEMI Patients are Predictive of Infarct Size and LVEF, but not MVO

It is possible to speculate that infiltration of large numbers of non-classical monocytes into the heart that are lost from the circulation during the acute-reperfusion period, may contribute to inflammation and potentially tissue damage at their destination in the myocardium following cardiac I/R. Assuming the occurrence of this scenario, the dynamics of non-classical monocytes should correlate with parameters of patient myocardial function. Indeed, in this study, it was found that patients with a larger infarct size also showed a stronger depletion of circulating non-classical monocytes during the acute post-reperfusion period (pre-90min). The exact mechanistic link between non-classical monocyte depletion and infarct size is unclear from this study, however may be related to the inflammatory potential of non-classical monocytes. Recent reports have described that upon activation, non-classical monocytes are the dominant inflammatory subset over classical monocytes, and produce high levels of inflammatory cytokines TNF- and IL-1 in response to a range of stimuli predominantly via TLR signalling [154, 164-166]. Furthermore, non-classical monocytes have recently been shown to express high levels of costimulatory molecules HLA-DR, CD80, CD86, and may therefore contribute to inflammation via CD40-mediated T-cell activation [167]. Through these potential mechanisms, it is possible to postulate that a greater depletion of non-classical monocytes following

reperfusion could lead to exaggerated infiltration of these cells into the injured myocardium which may in turn exacerbate the inflammatory response to cardiac I/R and compromise heart tissue repair. In support of this idea, treatment with anti-CX3CL1 antibody in a mouse model of cardiac I/R mice lead to smaller infarct size, potentially due to reduced Ly6C^{lo} non-classical monocyte infiltration into the myocardium [203]. It is however necessary to consider the correlational nature of the association between non-classical monocyte dynamics and infarct size, and acknowledge that this does not prove causation. It may conversely be the case that a large infarct size leads to greater loss of non-classical monocytes from the circulation as opposed to the other way around. This relationship is however specific to the non-classical monocyte subset; classical and intermediate monocytes dynamics from pre-90min do not show a significant correlation with infarct size. Studies of classical and intermediate monocyte dynamics at day 1, 3 and 7 following reperfusion however showed that reduced counts of these cells directly correlated with increased infarct size [283].

In addition to infarct size, I also looked at the presence and extent of MVO in relation to (pre-90min) non-classical monocyte dynamics, since MVO is known to be a powerful predictor of prognosis in terms of mortality [304] and major adverse cardiac events (MACE) [305, 306]. At the time intervals studied (pre-90min, 15-30min), there was no significant association between non-classical monocyte counts and MVO. No correlation was observed for the other subsets, classical or intermediate. This cannot be directly compared with contemporary research as there are no studies to date that have investigated the association of post-reperfusion monocyte dynamics with MVO during the immediate 24h. Outside of this time period, a study by Tsujioka et al found that the peak levels of classical monocytes (~day 3), but not those of non-classical monocytes (~day 5), were significantly higher in patients with MVO than in those without MVO [307].

A final parameter, LVEF, was assessed in STEMI patients against non-classical monocyte post-reperfusion dynamics. LVEF is a central measure of left ventricular systolic function, and therefore has prognostic value in predicting adverse outcomes in patients following STEMI. In this study, I show that the non-classical monocyte

dynamics during the acute post-reperfusion period (pre-90min) are predictive of LVEF (in addition to infarct size). The mechanistic link behind this association may be related to the same reasons described for infarct size; excessive recruitment of non-classical monocytes to the infarct and thus exacerbated inflammation and repair. When considering this relationship, it is important to note that there is a degree of uncertainty regarding the lack of standardization of the time of cardiac MRI scan (day 1-8 post-PCI) in relation to reperfusion. While there was found to be no significant correlation between scan timing with infarct size or MVO in the retrospective study, there was a positive association between scan timing and LVEF ($r=0.36$, $p<0.01$); as the time to scan increased, there was a trend towards higher LVEF. This variable may therefore be a potential source of error for the association observed between non-classical monocyte dynamics with LVEF, but not infarct size. A study of monocyte dynamics at day 1, 3 and 7 post-reperfusion has however demonstrated that a progressive decrease in classical and intermediate monocytes correlates inversely with LVEF, while non-classical monocytes gradually increase over day 1, 3 and 7, which is not correlated with LVEF [283].

4.3.4 Comparison between Retrospective and Prospective STEMI Patient Studies

The discrepancies in non-classical monocyte counts observed between retrospective and prospective cohorts described in this thesis were investigated by addressing technical and biological differences between the two studies. Application of the retrospective gating strategy to prospective data concluded that a small population of $CD16^{++}$ HLA-DR^{-} $CD14^{lo}$ $CCR2^{mid}$ neutrophils was present in the $CD16^{++}$ non-classical monocyte gate; neutrophils do not constitutively express HLA-DR, though expression can be upregulated by IFN-γ stimulation [308], CD14 is weakly expressed by neutrophils [309], and chronic inflammation can induce the expression of CCR2 by neutrophils [310, 311]. The increased count of non-classical monocytes at pre-reperfusion in the prospective study compared with the retrospective study was explained by both potential technical and biological factors; exclusion of the lymphocyte population in the retrospective gating method may have underestimated the count of non-classical monocytes which may sit at the lymphocyte/monocyte

border, while a longer ischemic/onset-to-balloon time in the retrospective cohort may have induced an earlier depletion of non-classical monocytes from the circulation.

The overall the results reported from the retrospective and prospective studies in this chapter support the emerging concept that circulating monocyte subset dynamics in STEMI patients following reperfusion are associated in some way, with long term cardiac function and patient prognosis. Direct intervention to modify the monocyte response early after STEMI may therefore have favourable effects on the inflammatory and reparative phases of infarct healing. The distinct CX3CL1/CX3CR1-dependent recruitment mechanism of non-classical monocytes offers a reasonable target to control the number of non-classical monocytes to the infarct. Currently there remains no approved targeted therapy to reduce cardiac I/R injury in STEMI patients. This potential intervention however would offer the opportunity to therapeutically intervene while acute MI patients are still hospitalized, and therefore represents a clinically feasible scenario.

4.4 Conclusions

In conclusion, this prospective STEMI study supports the study's hypothesis that non-classical, but not classical and intermediate monocytes, have distinct acute post-reperfusion dynamics (pre-90min) in STEMI patients. The accuracy and reproducibility of the prospective monocyte quantification method used herein provides confidence in these dynamics. The significant association with infarct size and LVEF suggests the potential existence of a mechanistic link between early non-classical monocyte dynamics (acute 24h) following reperfusion and cardiac repair. Additional investigations are therefore needed to determine how these non-classical monocyte responses in the blood are related to those in the injured heart tissue. For this, I used a mouse model of cardiac I/R to study monocyte infiltration into the myocardium post cardiac I/R, as described in the next chapter (Chapter 5). Post-reperfusion changes may not only occur in the counts of non-classical monocytes, but also in their functional characteristics. Functional assay experiments to investigate the effect of CX3CL1 stimulation on human monocytes are described later in Chapter 6.

Chapter 5.0. Monocyte Subpopulations in a Mouse Model of Cardiac I/R and the Effect of Genetic CX3CR1 Knockout

5.1 Introduction

In the previous chapter, I demonstrated that STEMI patient CX3CR1^{hi} non-classical monocytes are preferentially depleted in the circulation during the acute pre-reperfusion period (pre-90min post-PCI). The extent of this depletion was associated with patient infarct size and LVEF, whereby a greater drop in circulating non-classical monocytes was predictive of larger infarct size and lower LVEF. Human non-classical monocytes are distinct from their classical and intermediate monocyte subset counterparts partly through their high expression of CX3CR1, which raises the question; is the depletion of this cell type from the circulation following cardiac I/R related to extent of CX3CR1 expression and in turn CX3CL1/CX3CR1 signalling? It is also unclear whether the depletion of circulating non-classical monocytes is indicative of their recruitment to the injured myocardium. Mouse models of cardiac I/R originally described that non-classical monocytes arrive in the injured myocardium at approximately day 5 following I/R and peak at day 7 [281], however this theory has since been disproved as it has been shown that classical monocytes undergo a phenotypic shift into non-classical monocytes rather than a subsequent second influx of these cells. Yan et al demonstrated that reperfusion 45 minutes after MI changes the timing of immune cell influx into the infarct myocardium to an earlier time point compared with permanent MI, whereby the macrophage infiltration shifts from day 7 to day 3 (M1 macrophages dominating day 1-3 with a gradual increase in M2 macrophages peaking at day 5 post-MI) [312]. Furthermore, monocyte recruitment has been shown to outpace neutrophils within the first 30 minutes after onset of ischemia. It has been suggested that these are patrolling Ly6C^{lo} monocytes that amplify the initial inflammatory signal [313]. More refined gating strategies and lineage tracing experiments have identified these Ly6C^{lo} monocytes as Ly-6C^{lo} macrophages, which are derived from Ly-6C^{high} monocytes [314]. Evidence describing the temporal evolution of non-classical monocytes in response to cardiac I/R is therefore somewhat

contradictory to date, and there may be a more acute earlier role of non-classical monocytes following cardiac I/R than originally anticipated.

It is likely that the acute depletion of circulating non-classical monocytes observed in STEMI patients signifies their recruitment to the myocardium based on the fact that vascular endothelium-expressed transmembrane CX3CL1 is cleaved into soluble CX3CL1 in response to myocardial damage and inflammatory stimuli [197]. As a result, non-classical monocytes will no longer demonstrate patrolling behaviour as witnessed in the resting state [125], but can migrate more readily to the heart tissue. In order to investigate monocyte recruitment to the injured heart tissue in this study, a mouse model of cardiac ischemia-reperfusion (I/R) was used (described in section 3.4). This model permits the study of immune cell infiltration into the injured myocardium at specified time points following cardiac I/R, using two methodological approaches; 1) immunofluorescence staining of the heart tissue (section 3.5, 3.6), and 2), enzymatic digestion of the heart tissue and FACS analysis (section 3.9.3). Monocyte subpopulations were also studied in the circulation, spleen, and bone marrow following myocardial I/R. These compartments are known to host large reservoirs of monocyte populations and therefore must also be studied to understand the complete physiological monocyte response to cardiac I/R [147, 315-317].

To investigate the importance of monocyte-expressed CX3CR1 in monocyte recruitment, adhesion, and infiltration into the injured heart tissue post-cardiac I/R, a transgenic CX3CR1-GFP mouse line was used (section 3.3.1), in which an essential part of the *Cx3cr1* gene is replaced by EGFP [277]. These mice express EGFP in monocytes, dendritic cells, NK cells, and brain microglia under control of the endogenous *Cx3cr1* locus. This line was used to compare the post-cardiac I/R monocyte response between *Cx3cr1*$^{+/+}$, *Cx3cr1*$^{+/GFP}$, and complete knockout *Cx3cr1*$^{GFP/GFP}$ mice.

The first aim of this work was to investigate mouse classical and non-classical monocyte dynamics in the peripheral circulation at 2h and 24h post-cardiac I/R to ask whether there was a similar depletion to that observed in STEMI patients post-PCI. Mouse monocyte subpopulations are defined by different markers to that in human;

Ly6C^{hi} monocytes resemble CD14^{++}CD16^{-} classical monocytes, while Ly6C^{lo} monocytes resemble CD14^{+}CD16^{++} non-classical monocytes [318-321]. An intermediate population also exists in mice, as in humans. The effect of genetic CX3CR1 ablation on Ly6C^{lo} non-classical monocyte dynamics post-I/R was evaluated by comparing *Cx3cr1*$^{+/+}$, *Cx3cr1*$^{+/GFP}$ and *Cx3cr1*$^{GFP/GFP}$ mice circulating monocyte populations. Complete knockout of CX3CR1 in this mouse model was first validated as described in section 5.2.1

5.2 Results

5.2.1 Validation of *Cx3cr1*$^{GFP/GFP}$ Mouse Model

Validation experiments were performed on mouse splenocytes to confirm the loss of CX3CR1 gene and protein expression in *Cx3cr1*$^{+/GFP}$ and *Cx3cr1*$^{GFP/GFP}$ mice. qPCR analysis showed a ~50% loss of CX3CR1 gene expression in *Cx3cr1*$^{+/GFP}$ mice compared to WT animals, and 100% loss of CX3CR1 gene expression in *Cx3cr1*$^{GFP/GFP}$ mice (Figure 5.1A). Analysis of mouse splenocyte CX3CR1 protein expression by FACS showed co-expression of CX3CR1 and GFP in *Cx3cr1*$^{+/GFP}$ mice, and practically a complete loss of CX3CR1 protein expression in *Cx3cr1*$^{GFP/GFP}$ mice coinciding with increased GFP expression (Figure 5.1B).

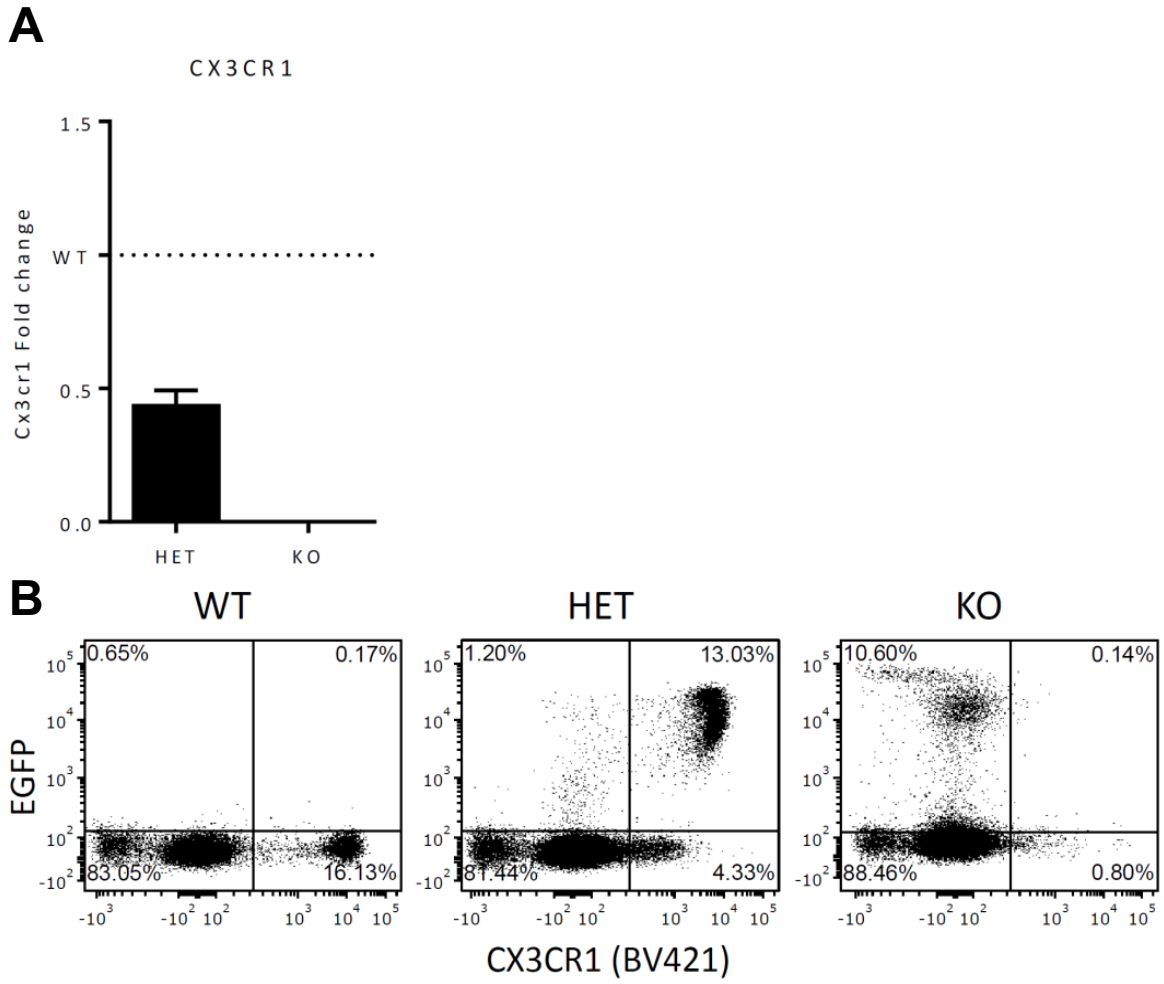

Figure 5. 1. Validation of *Cx3cr1*$^{GFP/GFP}$ Mouse Model

A. qPCR data of mouse splenocytes showing loss of CX3CR1 transcripts; *Cx3cr1*$^{+/GFP}$ mice show 50% CX3CR1 transcript compared with WT, and practically 0% in *Cx3cr1*$^{GFP/GFP}$ mice. B. FACS data of mouse splenocytes showing reduction of CX3CR1 protein and increased eGFP expression in *Cx3cr1*$^{+/GFP}$ and *Cx3cr1*$^{GFP/GFP}$ mice. Data courtesy of Lilia Draganova.

5.2.2 Mouse Baseline Circulating Classical, Intermediate and Non-Classical Monocyte Subpopulation Dynamics and the Effect of Genetic CX3CR1 Knockout.

Baseline peripheral blood Ly6C^{hi} classical, Ly6C^{inter} intermediate, and Ly6C^{lo} non-classical monocyte counts were first quantified across *Cx3cr1*$^{+/+}$, *Cx3cr1*$^{+/GFP}$ and *Cx3cr1*$^{GFP/GFP}$ mice to determine any pre-existing differences in monocyte subpopulations due to genetic depletion of CX3CR1. Peripheral blood samples were collected from mouse tail vein and analysed by FACS as described in section 3.8. Monocyte subpopulations were defined as classical [CD11b^{+} CD115^{+} LY6G^{-} LY6C^{hi} CCR2^{hi} CX3CR1^{mid-hi}], intermediate [CD11b^{+} CD115^{+} LY6G^{-} LY6C^{inter} CCR2^{mid} CX3CR1^{mid-hi}], and non-classical [CD11b^{+} CD115^{+} LY6G^{-} LY6C^{lo} CCR2^{lo} CX3CR1^{hi}] monocytes as shown in Figure 5.1. Absolute counts of each monocyte subpopulation per µl of blood were determined using Trucount beads.

This initial analysis showed that baseline counts of the Ly6C^{hi} classical monocyte population were not significantly different between *Cx3cr1*$^{+/+}$, *Cx3cr1*$^{+/GFP}$ and *Cx3cr1*$^{GFP/GFP}$ mice, with counts of 303(±94)/µl, 294(±33)/µl, and 277(±84)/µl, respectively (Figure 5.2). There was also no significant change in the absolute counts of intermediate monocytes between *Cx3cr1*$^{+/+}$ (77(±18)/µl), *Cx3cr1*$^{+/GFP}$ (129(±25)/µl), and *Cx3cr1*$^{GFP/GFP}$ mice (81(±20)/µl). In contrast, circulating non-classical monocyte counts were significantly reduced in *Cx3cr1*$^{GFP/GFP}$ mice (96(±17)/µl), being 47.5% lower than in *Cx3cr1*$^{+/+}$ mice (183(±33)/µl) ($p = 0.047$), and 48.4% lower than in *Cx3cr1*$^{+/GFP}$ mice (186(±23)/µl) ($p = 0.024$). These findings are in line with published data demonstrating that CX3CR1 expression is required for the survival of circulating CX3CR1^{+} non-classical monocytes [218, 322].

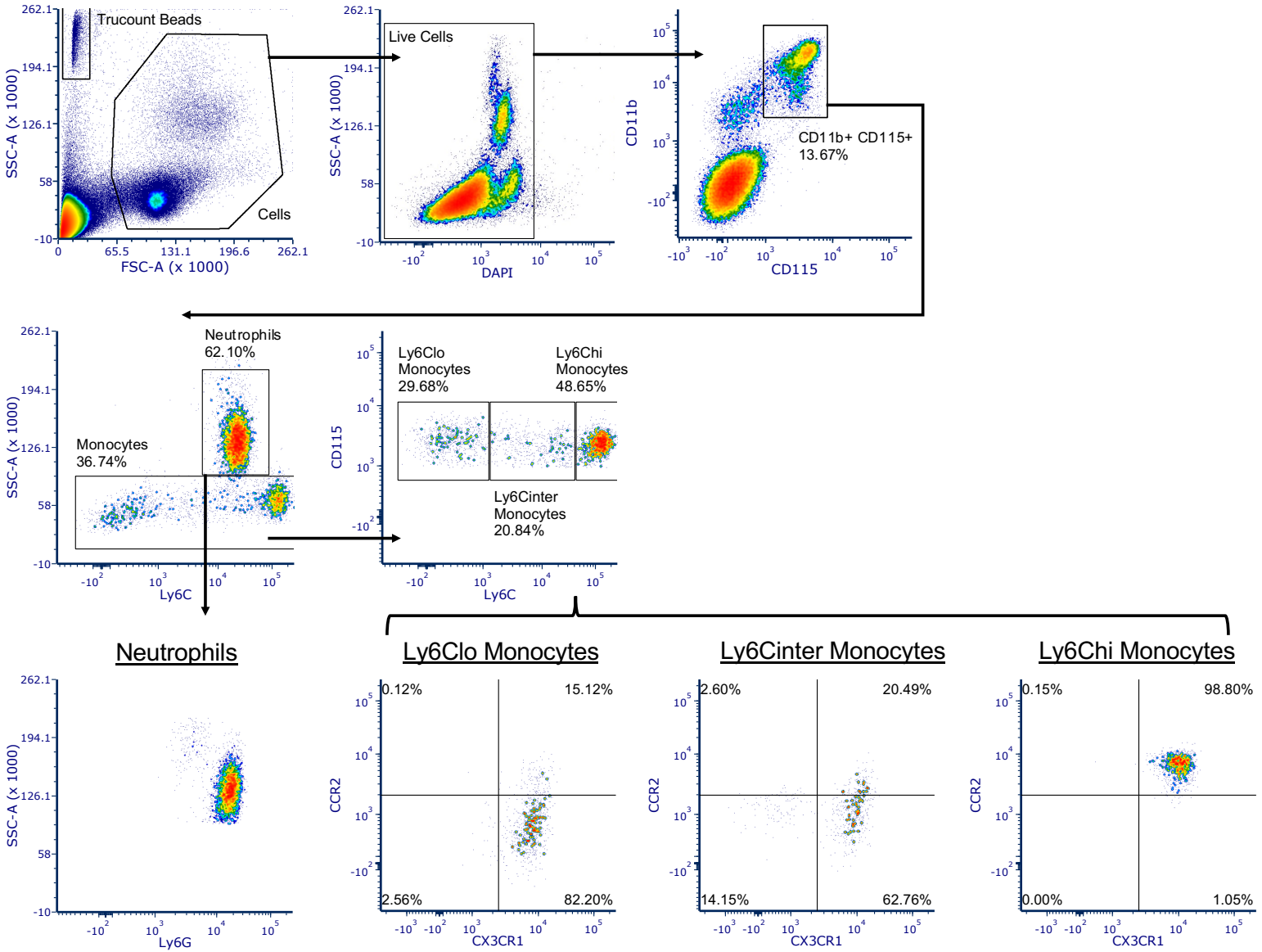
Trucount Beads
Cells
SSC-A (x 1000)
FSC-A (x 1000)
Live Cells
DAPI
CD11b
CD115
CD11b+ CD115+
13.67%
Neutrophils
62.10%
Monocytes
36.74%
Ly6C
Ly6Clo
Monocytes
29.68%
Ly6Chi
Monocytes
48.65%
Ly6Cinter
Monocytes
20.84%
Neutrophils
Ly6Clo Monocytes
Ly6Cinter Monocytes
Ly6Chi Monocytes
Ly6G
CCR2
CX3CR1
0.12%
15.12%
2.56%
82.20%
2.60%
20.49%
14.15%
62.76%
0.15%
98.80%
0.00%
1.05%

Figure 5. 2. FACS gating strategy for defining mouse blood monocyte subpopulations.

Mouse peripheral blood samples (<50µl) were collected from tail vein. Mouse blood myeloid cells were defined as $CD11b^{+}$ $CD115^{+}$ cells and neutrophils were excluded based on high side scatter and $Ly6G^{+}$ expression. Monocytes were then classified as classical [$LY6C^{hi}$ $CCR2^{hi}$ $CX3CR1^{mid\text{-}hi}$], intermediate [$LY6C^{inter}$ $CCR2^{mid}$ $CX3CR1^{mid\text{-}hi}$] and non-classical [$LY6C^{lo}$ $CCR2^{lo}$ $CX3CR1^{hi}$] monocytes. Absolute counts of blood monocyte subpopulations were quantified using TruCount beads.

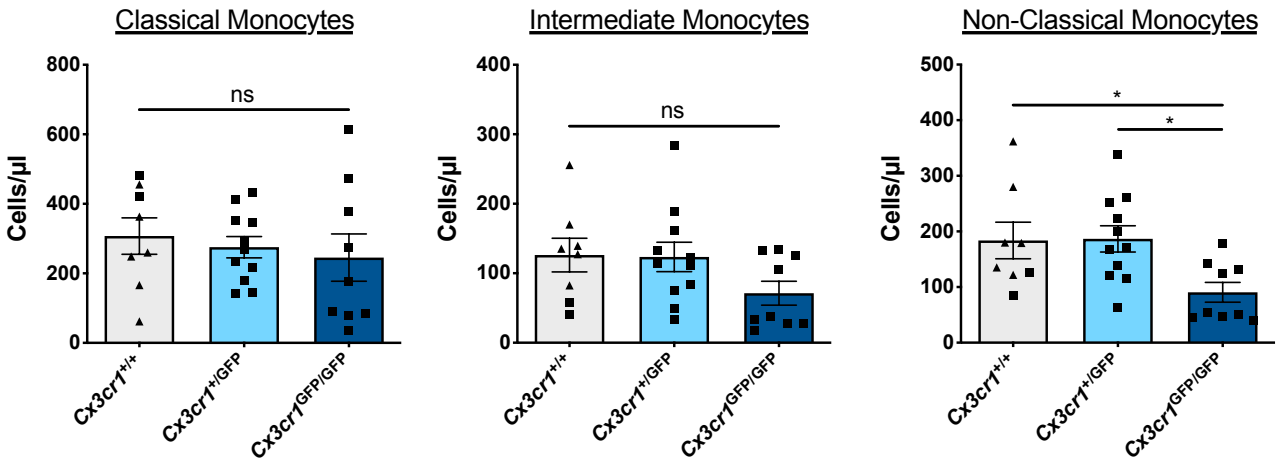

Figure 5. 3. Comparison of mouse baseline circulating monocyte subpopulation counts between *Cx3cr1*$^{+/+}$, *Cx3cr*1$^{+/GFP}$ and *Cx3cr1*$^{GFP/GFP}$ mice. Baseline TruCount of circulating classical [CD11b^{+}CD115^{+}LY6G^{-}LY6C^{hi} CCR2^{hi}CX3CR1$^{mid\text{-}hi}$], intermediate [CD11b^{+}CD115^{+}LY6G^{-}LY6C^{inter} CCR2^{mid}CX3CR1$^{mid\text{-}hi}$], and non-classical [CD11b^{+}CD115^{+}LY6G^{-}LY6C^{lo}CCR2^{lo} CX3CR1^{hi}] monocytes. In the wild type group, both *Cx3cr1*$^{+/+}$ littermates (square symbols) and C57BL/6 mice (triangles) were used. Data refers to mean ± SEM. Data was analysed by One-way Anova with Tukey's multiple comparison test. *p<0.05. ns, non-significant. n=5 C57BL6, n=2 *Cx3cr1*$^{+/+}$, n=11 *Cx3cr*1$^{+/GFP}$, n=9 *Cx3cr1*$^{GFP/GFP}$.

5.2.3 Mouse Circulating Classical, Intermediate and Non-Classical Monocyte Dynamics at 2h and 24h Post-Cardiac I/R and the Effect of Genetic CX3CR1 Knockout

In order to investigate whether mouse Ly6C^{lo} non-classical monocytes show a depletion in the circulation following myocardial I/R which mirrors that of STEMI patient non-classical monocytes, mice underwent 60 minutes' ischemia followed by either 2h or 24h reperfusion to mimic PCI in the clinical setting. The impact of genetic CX3CR1 depletion on monocyte subpopulation dynamics following cardiac I/R was evaluated in *Cx3cr1*$^{+/+}$, *Cx3cr1*$^{+/GFP}$ and *Cx3cr1*$^{GFP/GFP}$ mice. This analysis was performed using consecutive bleeds at baseline, 2h and 24h post-cardiac I/R to permit comparison between time points within any one individual. Circulating monocyte subpopulation counts at 2h and 24h following myocardial I/R showed a similar trend in all mice analysed. At 2h, all three monocyte subpopulations decreased in the circulation from baseline, and then at 24h returned to normal. However, these dynamic changes only reached statistical significance for *Cx3cr1*$^{+/GFP}$ mice ($p<0.01$) (Figure 5.3).

When analyzing the acute post-reperfusion (2h) percentage change of each monocyte subpopulation count between genotypes, classical and intermediate monocytes showed no significant difference in the severity of cell depletion between *Cx3cr1*$^{+/+}$, *Cx3cr1*$^{+/GFP}$ and *Cx3cr1*$^{GFP/GFP}$ mice (Figure 5.4). By contrast, the extent of non-classical monocyte depletion was significantly greater in *Cx3cr1*$^{GFP/GFP}$ mice (~75%) compared to that in *Cx3cr1*$^{+/+}$ mice (~25%) ($p = 0.031$).

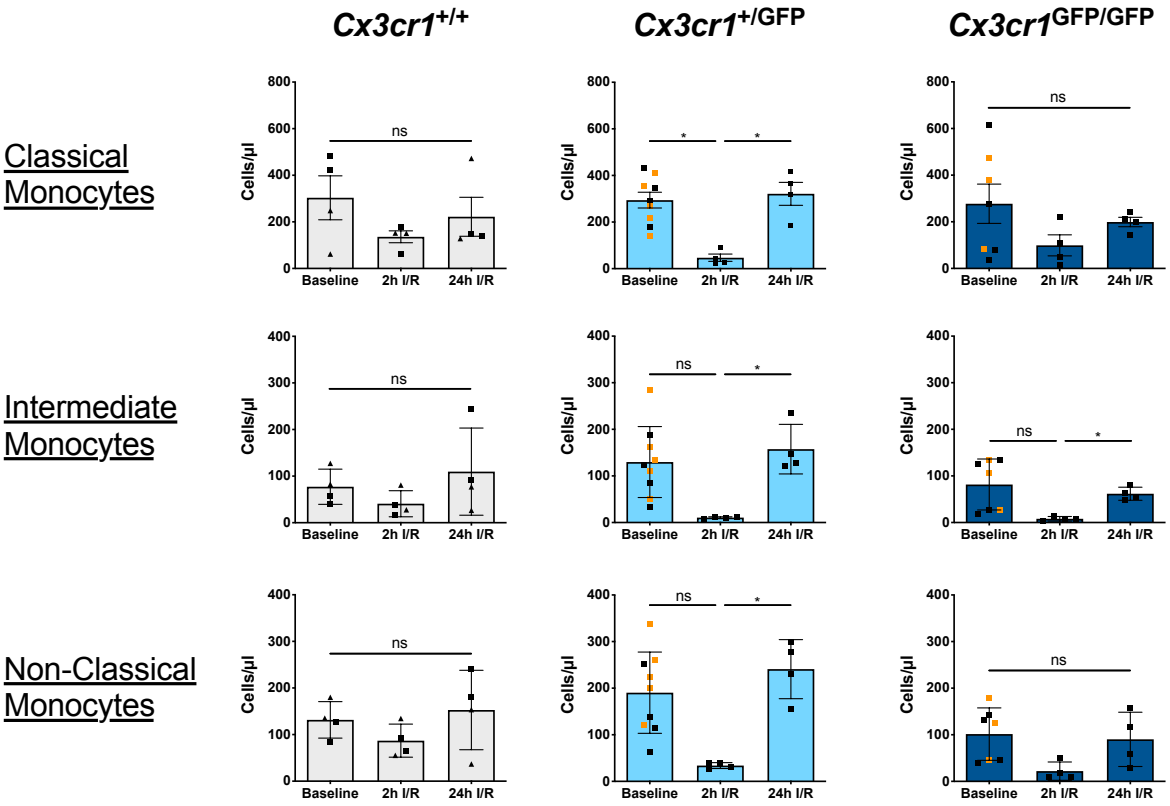

Figure 5. 4. Comparison in mouse circulating monocyte subpopulation counts at 2h and 24h post-cardiac I/R between *Cx3cr1*$^{+/+}$, *Cx3cr1*$^{+/GFP}$ and *Cx3cr1*$^{+/GFP}$ mice.

Absolute Trucount of peripheral circulating classical [CD11b^{+}CD115^{+}LY6G^{-}LY6C^{hi} CCR2^{hi}CX3CR1$^{mid\text{-}hi}$], intermediate [CD11b^{+}CD115^{+}LY6G^{-}LY6C^{inter} CCR2^{mid}CX3CR1$^{mid\text{-}hi}$], and non-classical [CD11b^{+}CD115^{+}LY6G^{-}LY6C^{lo}CCR2^{lo} CX3CR1^{hi}] monocytes at baseline, 2h, and 24h post cardiac I/R, in *Cx3cr1*$^{+/+}$, *Cx3cr1*$^{+/GFP}$, and *Cx3cr1*$^{GFP/GFP}$ mice. Black triangle points = C57BL/6. Orange points = baseline mice without repeated bleeds. Data refers to mean ± SEM. Data was analysed by Repeated Measures One-way Anova with Tukey's multiple comparison test. *p<0.05. n=2 C57BL6, n=2 *Cx3cr1*$^{+/+}$, n=4 *Cx3cr1*$^{+/GFP}$ (repeat bleeds), n=5 *Cx3cr1*$^{+/GFP}$ (baseline only), n=4 *Cx3cr1*$^{GFP/GFP}$ (repeat bleeds), n=3 *Cx3cr1*$^{GFP/GFP}$ (baseline only).

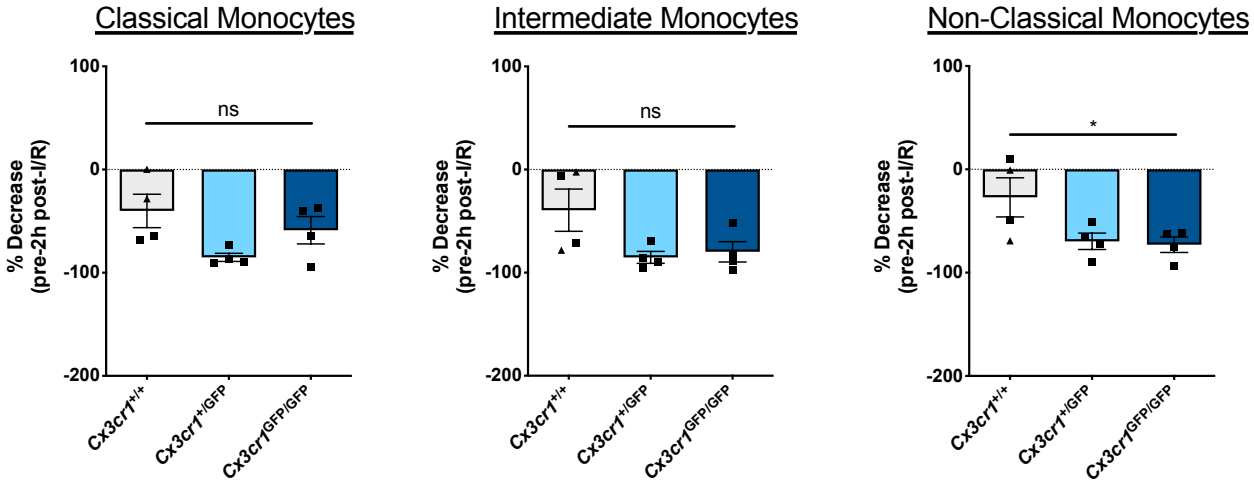

Figure 5. 5. Acute post-reperfusion (2h) percentage change in mouse circulating classical, intermediate, and non-classical monocytes between *Cx3cr1*$^{+/+}$, *Cx3cr1*$^{+/GFP}$, and *Cx3cr1*$^{GFP/GFP}$ mice.

Data were analysed by Repeated Measures One-way Anova with Tukey's multiple comparison test. Data refers to mean ± SEM. *p<0.05. n=2 C57BL6, n=2 *Cx3cr1*$^{+/+}$, n=4 *Cx3cr1*$^{+/GFP}$, n=4 *Cx3cr1*$^{GFP/GFP}$.

5.2.4 Leukocyte Infiltration into the Injured Myocardium at 2h and 24h Post-Cardiac I/R and the Effect of Genetic CX3CR1 Knockout

The next aim of this work was to explain the loss of monocyte subpopulations from the circulation at 2h following cardiac I/R, and the stronger depletion of non-classical monocytes in the *Cx3cr1*$^{GFP/GFP}$ circulation. This was investigated by examining the adherence of monocytes to the coronary endothelium and infiltration of monocytes into the injured myocardial tissue at different times post-cardiac I/R. To determine the effect of genetic CX3CR1 knockout on these immune responses, data was compared between *Cx3cr1*$^{+/+}$, *Cx3cr1*$^{+/GFP}$ and *Cx3cr1*$^{GFP/GFP}$ mice.

Immunostaining of injured heart tissue sections were used for this work. However, the extent of I/R injury varies through the heart. Therefore, in order to establish the optimal tissue sections to use for analysis, hearts at 2h and 24h post-cardiac I/R were first stained for the pan-leukocyte marker CD45 (section 3.6.1 for staining method, 3.7 for imaging and analysis). This experiment also allowed analysis of any major leukocyte response differences following loss of CX3CR1. Naïve and sham-operated mice were included as control groups to quantify myocardial leukocytes in steady state and following thoracotomy surgery without ischemia reperfusion, respectively. The remote, uninjured myocardium (RV) served as an internal control for these experiments (Figure 5.6B). Control-stained heart tissue with no antibody and no primary antibody were clean showing specificity of the immunostaining (Figure 5.5B).

The temporal leukocyte response was firstly evaluated in wild type mice (Figure 5.6A). Representative images of CD45 immunofluorescent staining of *Cx3cr1*$^{+/+}$ hearts at each time point studied are shown in Figure 5.5A. In 2h and 24h sham hearts, there was no significant difference in leukocyte infiltration compared to naïve hearts. This confirmed that thoracotomy surgery does not stimulate a significant immune response in the myocardium (Figure 5.6A). At 24h following I/R, leukocyte infiltration dramatically increased from 2h by approximately 6-fold ($p<0.0001$). This response was specific to the infarcted myocardium as CD45^{+} counts were significantly greater in the LV region compared to the RV remote area ($p<0.0001$) (Figure 5.6B).

To investigate the importance of CX3CR1 expression in this leukocyte response to cardiac I/R, the same analysis was performed on *Cx3cr1*$^{+/GFP}$ and *Cx3cr1*$^{GFP/GFP}$ hearts and compared with wild type (*Cx3cr1*$^{+/+}$ littermates and C57BL/6) mice. Leukocyte counts in naïve hearts were first compared between genotypes to identify any pre-existing differences due to the absence of CX3CR1 expression. This analysis showed a trend towards reduced CD45^{+} cell counts in *Cx3cr1*$^{+/GFP}$ and *Cx3cr1*$^{GFP/GFP}$ naïve hearts compared to that of *Cx3cr1*$^{+/+}$ mice, however cell counts were very low and this difference was not significant (Figure 5.6C). At 2h post-I/R, leukocyte infiltration into the injured myocardium was significantly lower in *Cx3cr1*$^{+/GFP}$ ($p<0.05$) and *Cx3cr1*$^{GFP/GFP}$ ($p<0.01$) hearts compared to *Cx3cr1*$^{+/+}$ mice, by 1.5-fold and 1.6-fold respectively (Figure 5.6D). All genotypes showed lower leukocyte counts in 2h sham hearts compared to 2h I/R hearts, which was significant for the *Cx3cr1*$^{+/+}$ ($p<0.0001$) and *Cx3cr1*$^{+/GFP}$ ($p<0.01$) group but not *Cx3cr1*$^{GFP/GFP}$ mice. By 24h post-I/R, leukocyte infiltration increased from 2h by 5.6-fold, 10.6-fold and 10.7-fold in *Cx3cr1*$^{+/+}$, *Cx3cr1*$^{+/GFP}$, and *Cx3cr1*$^{GFP/GFP}$ mice, respectively (Figure 5.6.E). This leukocyte response at 24h post-I/R was specific to cardiac I/R in all genotypes since leukocyte infiltration was consistently significantly higher in 24h I/R hearts compared to 24h sham hearts ($p<0.0001$) and compared to naïve hearts (Figure 5.6B, $p<0.0001$). Unlike at 2h post-I/R, total leukocyte counts at 24h I/R were not significantly different between genotypes, suggesting a recovery in response by *Cx3cr1*$^{+/GFP}$ and *Cx3cr1*$^{GFP/GFP}$ mice at this later time point.

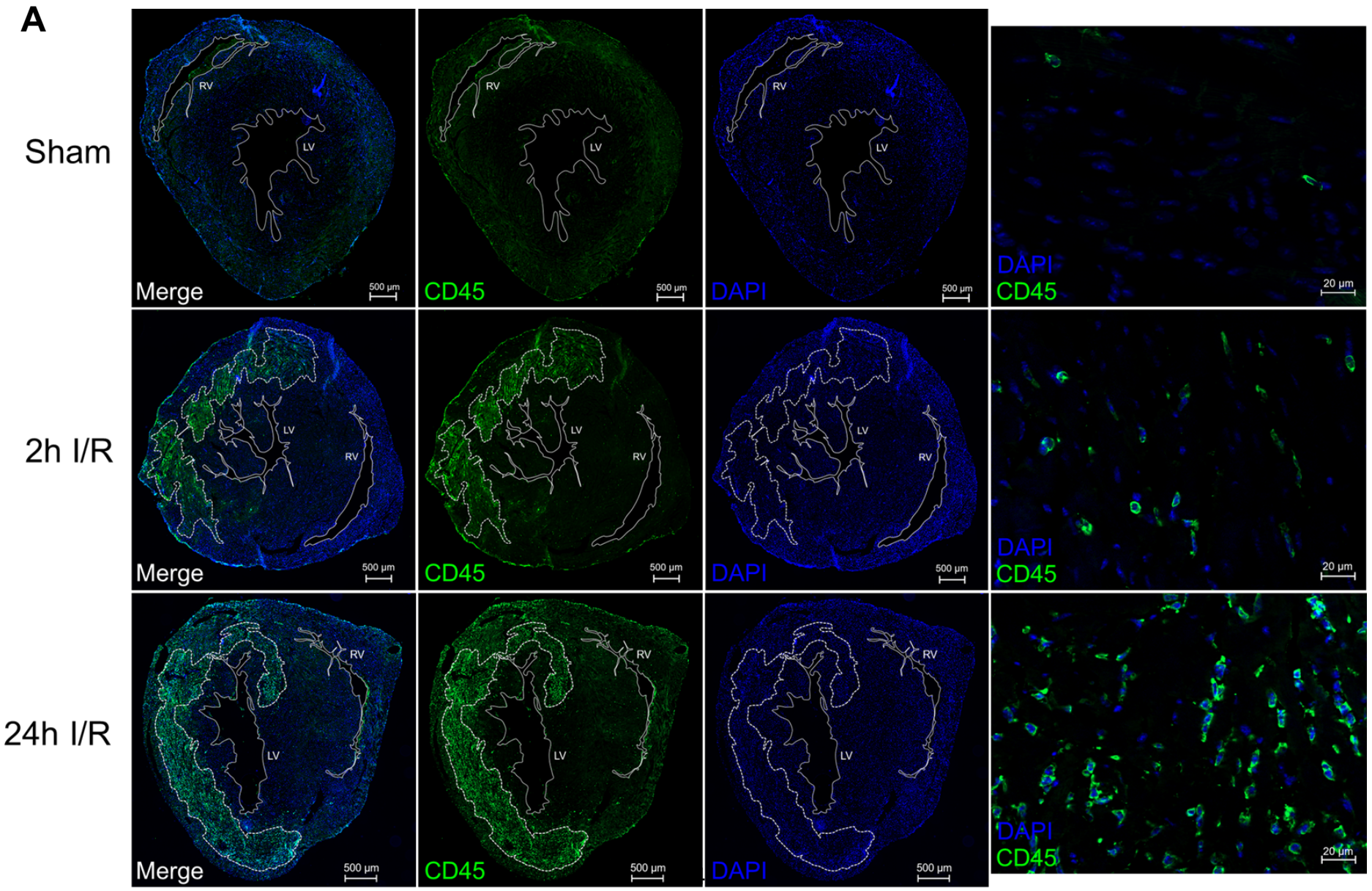
A
Sham
2h I/R
24h I/R
RV
LV
Merge
CD45
DAPI
500 μm
20 μm

B

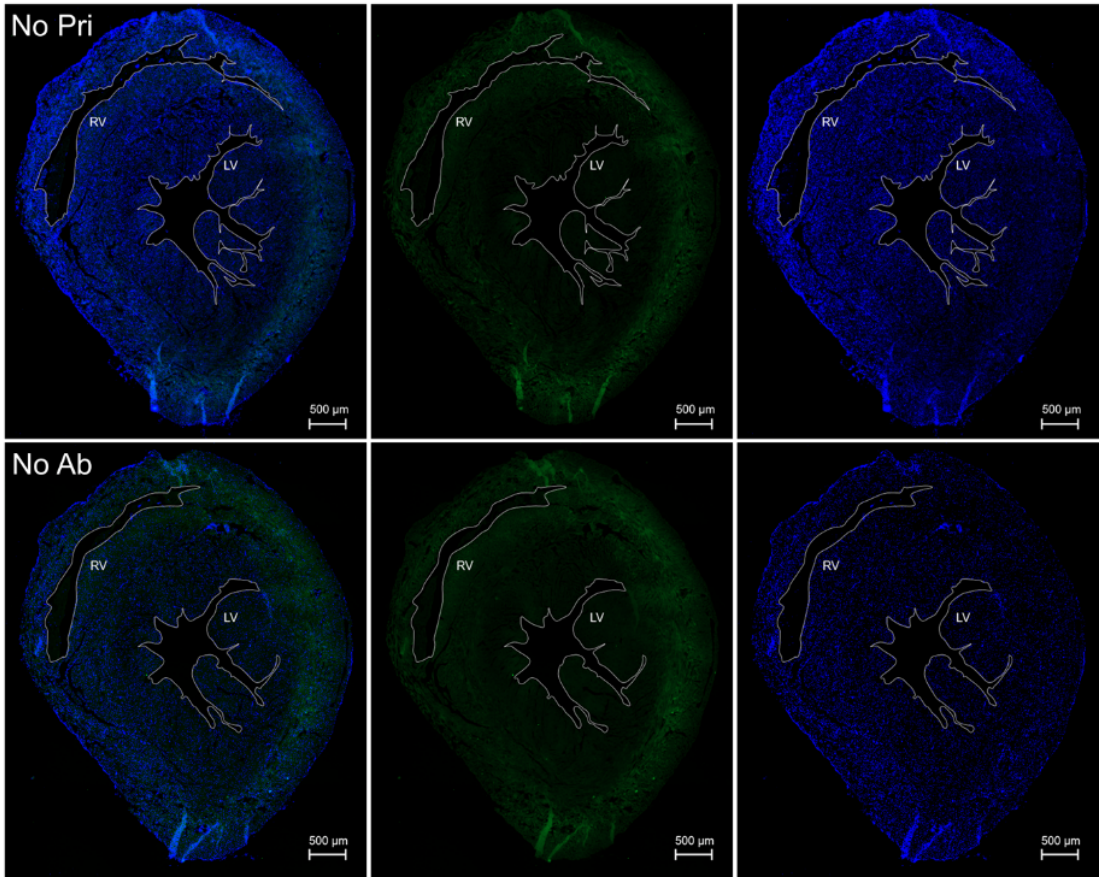

Figure 5. 6. CD45^{+} leukocyte immunofluorescent staining of mouse heart tissue at 2h and 24h following cardiac I/R.

A. Representative 5x tile 40x FOV images of CD45^{+} leukocyte immunofluorescent staining in sham-operated, 2h I/R, and 24h I/R *Cx3cr1*$^{+/+}$ mouse heart cryosections. Mouse anti-Rat CD45 primary antibody was detected with Goat Anti-Rat Alexa-488 secondary antibody. B. Representative 5x tile images of no primary antibody and no antibody control stained mouse heart tissues; both controls were clean. All images were taken and analysed using Zen Software.

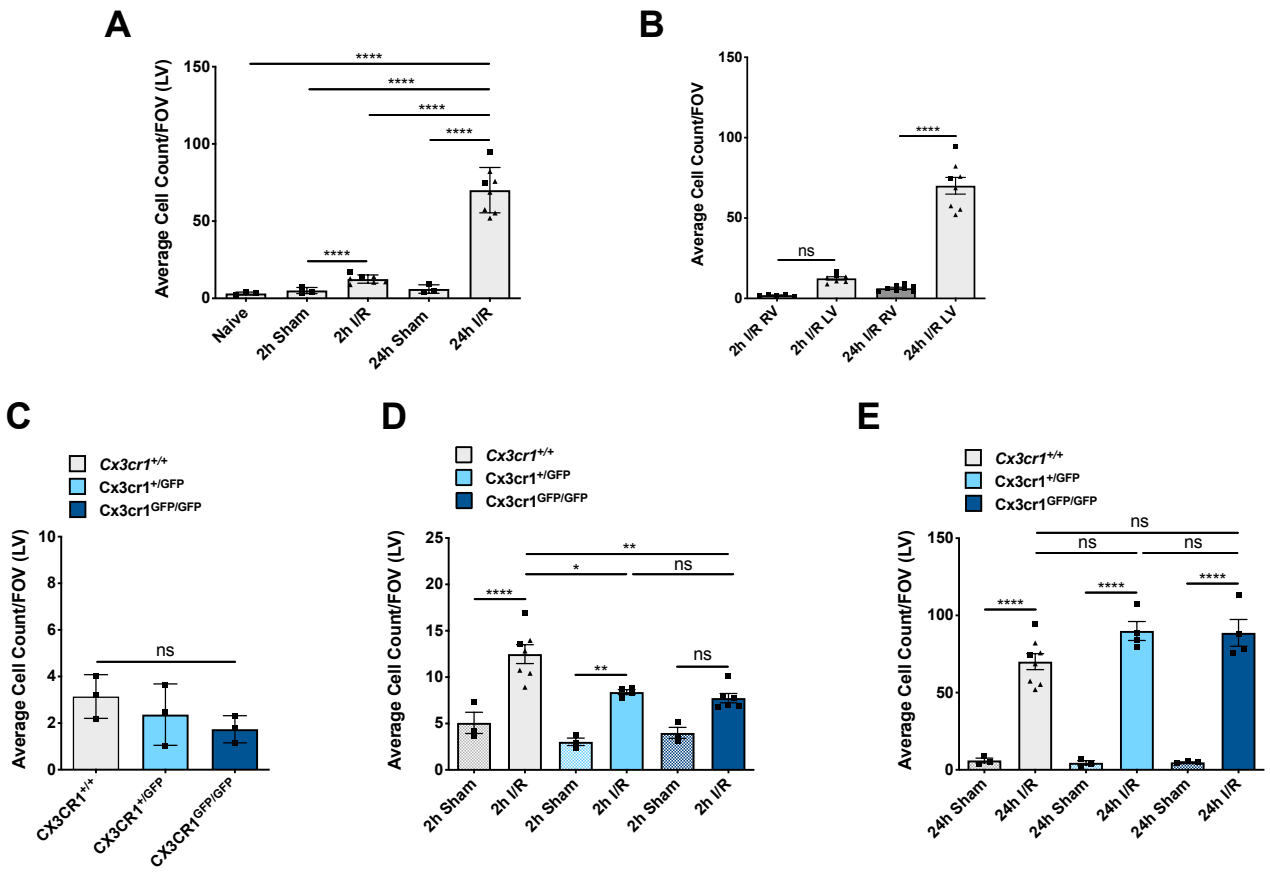
A
Average Cell Count/FOV (LV)
150
100
50
0
****
****
****
****
****
Naive
2h Sham
2h I/R
24h Sham
24h I/R
B
Average Cell Count/FOV
150
100
50
0
ns
****
2h I/R RV
2h I/R LV
24h I/R RV
24h I/R LV
C
Cx3cr1+/+
Cx3cr1+/GFP
Cx3cr1GFP/GFP
Average Cell Count/FOV (LV)
10
8
6
4
2
0
ns
CX3CR1+/+
CX3CR1+/GFP
CX3CR1GFP/GFP
D
Cx3cr1+/+
Cx3cr1+/GFP
Cx3cr1GFP/GFP
Average Cell Count/FOV (LV)
25
20
15
10
5
0
**
*
ns
****
**
ns
2h Sham
2h I/R
2h Sham
2h I/R
2h Sham
2h I/R
E
Cx3cr1+/+
Cx3cr1+/GFP
Cx3cr1GFP/GFP
Average Cell Count/FOV (LV)
150
100
50
0
ns
ns
ns
****
****
****
24h Sham
24h I/R
24h Sham
24h I/R
24h Sham
24h I/R

Figure 5. 7. Leukocyte infiltration into the injured myocardium at 2h and 24h following cardiac I/R in *Cx3cr1*$^{+/+}$, *Cx3cr1*$^{+/GFP}$, and *Cx3cr1*$^{GFP/GFP}$ mice.

A. Infiltration of CD45^{+} leukocytes into the reperfused myocardium at 2h and 24h post-I/R in WT mice (n=3 naïve and sham mice; n=7 for 2h I/R, n=8 for 24h I/R. WT controls included *Cx3cr1*$^{+/+}$ littermates (square points, n=2) and C57BL/6 mice (triangle points, n=5). One-way Anova with Tukey's multiple comparison test. B. Comparison of leukocyte infiltration between injured (LV) and remote (RV) heart regions in *Cx3cr1*$^{+/+}$ mice at 2h and 24h post-I/R. C. Baseline resident leukocytes in *Cx3cr1*$^{+/+}$, *Cx3cr1*$^{+/GFP}$, and *Cx3cr1*$^{GFP/GFP}$ naïve hearts. n=3 mice/genotype. One-way Anova with Tukey's multiple comparison test. D. Leukocyte infiltration into the LV at 2h post-cardiac I/R in *Cx3cr1*$^{+/+}$, *Cx3cr1*$^{+/GFP}$, and *Cx3cr1*$^{GFP/GFP}$ mice. n=7 *Cx3cr1*$^{+/+}$, n=4 *Cx3cr1*$^{+/GFP}$, n=6 *Cx3cr1*$^{GFP/GFP}$. Two-way Anova with Tukey's multiple comparison test. E. Leukocyte infiltration into the LV at 24h post-cardiac I/R in *Cx3cr1*$^{+/+}$, *Cx3cr1*$^{+/GFP}$, and *Cx3cr1*$^{GFP/GFP}$ mice. n=8 *Cx3cr1*$^{+/+}$, n=4 *Cx3cr1*$^{+/GFP}$, n=4 *Cx3cr1*$^{GFP/GFP}$. All data refers to mean ± SEM Data analysed by Two-way Anova with Tukey's multiple comparison test. *p<0.01, **p<0.05, ****p<0.0001.

5.2.5 Classical Monocyte, Non-Classical Monocyte, and Neutrophil Infiltration into the Injured Myocardium at 2h, 24h, and Day 3 post-Cardiac I/R in *Cx3cr1*$^{+/GFP}$ and *Cx3cr1*$^{GFP/GFP}$ mice.

The findings from the previous section suggest that genetic depletion of CX3CR1 may disturb the leukocyte response to myocardial repair following cardiac I/R, since leukocyte infiltration into the infarct tissue at 2h post-I/R was significantly lower in CX3CR1-depleted hearts compared to that of the wild-type group. The effect of genetic CX3CR1 ablation specifically on the acute monocyte response to cardiac I/R has not been widely investigated to date. There is however reason to believe that depletion of this receptor may influence the CX3CR1^{hi} non-classical monocyte response to cardiac I/R and thereby compromise infarct healing, since a number of recent studies have reported associations between the CX3CR1/CX3CL1 axis and myocardial function following cardiac I/R in both mouse models of myocardial I/R and STEMI patients [203, 209, 210, 288-291]. In this study, it was therefore hypothesised that *Cx3cr1*$^{GFP/GFP}$ mice have an impaired non-classical monocyte response following cardiac I/R, leading to disturbed myocardial repair and impaired long-term cardiac function. To investigate this, sister sets of the same leukocyte-stained hearts (naïve, 2h sham, 2h I/R, 24h sham, 24h I/R), and additional 3-day I/R hearts, were stained for monocytes using the markers CD11b, GFP, and CCR2 (details in section 3.6.2). This staining panel was designed for the quantification of classical monocytes [CD11b^{+} GFP^{mid} CCR2^{hi}], non-classical monocytes [CD11b^{+} GFP^{hi} CCR2^{lo}], and neutrophils [CD11b^{+} GFP^{-} CCR2^{-}]. Definition of these monocyte subpopulations is shown in Figure 5.7. Analysis of GFP MFI using Zen Software (described in section 3.7) showed a significant difference in GFP expression between CD11b^{+}GFP^{mid} classical monocytes and CD11b^{+}GFP^{hi} non-classical monocytes (Figure 5.22). Ly6C was also tested on the basis that it would theoretically distinguish Ly6C^{lo} non-classical monocytes from Ly6C^{hi} classical monocytes, however staining of mouse heart tissue with anti-Ly6C antibody revealed that this marker was also abundantly expressed by endothelial cells in the myocardium (Figure 5.8). Furthermore, staining with anti-CX3CR1 antibody (Abcam, #ab8021) was found to be non-specific since positive staining was found in *Cx3cr1*$^{GFP/GFP}$ heart tissue (Figure 5.9). GFP staining was therefore used for monocyte subset definition rather than CX3CR1 and consequently *Cx3cr1*$^{+/GFP}$ mice were used as the control group for

comparison with *Cx3cr1*$^{GFP/GFP}$ hearts. Neutrophils were quantified as CD11b^{+}GFP^{-} cells and were used as an internal control population as they are known to infiltrate the infarct and dominate repair at 24h post-I/R (Figure 5.10).

Classical monocytes, non-classical monocytes, and neutrophil populations were first quantified in *Cx3cr1*$^{+/GFP}$ mice in naïve, sham, 2h I/R, 24h I/R, and day 3 I/R hearts to investigate the time course of monocyte subpopulation infiltration into the injured myocardium in the control group. At 2h following I/R, *Cx3cr1*$^{+/GFP}$ classical monocyte infiltration was very low and not significantly different from naïve and sham hearts (Figure 5.13A). By 24h, classical monocytes increased slightly from 2h by ~1.5-fold. This was followed by a further increase at day 3, when classical monocyte infiltration increased by a further ~5-fold from 24h ($p<0.001$). Non-classical monocyte counts in naïve and sham-operated hearts were also very low in *Cx3cr1*$^{+/GFP}$ mice, and did not significantly increase at 2h post-I/R. From 2h to 24h post-I/R, the *Cx3cr1*$^{+/GFP}$ non-classical monocyte population in the injured myocardium increased by ~4-fold, and by a further ~2-fold at day 3 post-I/R ($p<0.01$). When considering the neutrophil population, infiltration of these cells was very low at 2h I/R and similar to 2h sham hearts. By 24h however, neutrophil counts increased dramatically by ~6-fold in the injured myocardium ($p<0.0001$), which was subsequently followed by a significant return to just-above baseline counts at day 3 post I/R. Representative images of *Cx3cr1*$^{+/GFP}$ mouse heart tissue at each time point studied are shown in Figure 5.11A and Figure 5.12.

The effect of complete genetic CX3CR1 ablation on these temporal dynamics of monocyte subpopulation infiltration into the injured myocardium at 2h, 24h, and 3 day post-cardiac I/R was assessed by comparing the *Cx3cr1*$^{+/GFP}$ control group with *Cx3cr1*$^{GFP/GFP}$ hearts. At all time points studied, classical monocyte infiltration was similar between *Cx3cr1*$^{+/GFP}$ and *Cx3cr1*$^{GFP/GFP}$ hearts (Figure 5.13C). However, non-classical monocyte counts in *Cx3cr1*$^{GFP/GFP}$ infarcts were ~2-fold lower than in *Cx3cr1*$^{+/GFP}$ hearts at 24h ($p<0.05$), although this difference was not seen at 2h. At day 3, non-classical monocyte infiltration in *Cx3cr1*$^{GFP/GFP}$ mice showed a recovery in response, reaching that seen in *Cx3cr1*$^{+/GFP}$ hearts. Quantification of neutrophils in *Cx3cr1*$^{GFP/GFP}$ mice at 2h, 24h, and day 3 post-I/R compared to *Cx3cr1*$^{+/GFP}$ mice

revealed no significant differences between genotypes at any of the time points studied (Figure 5.13E).

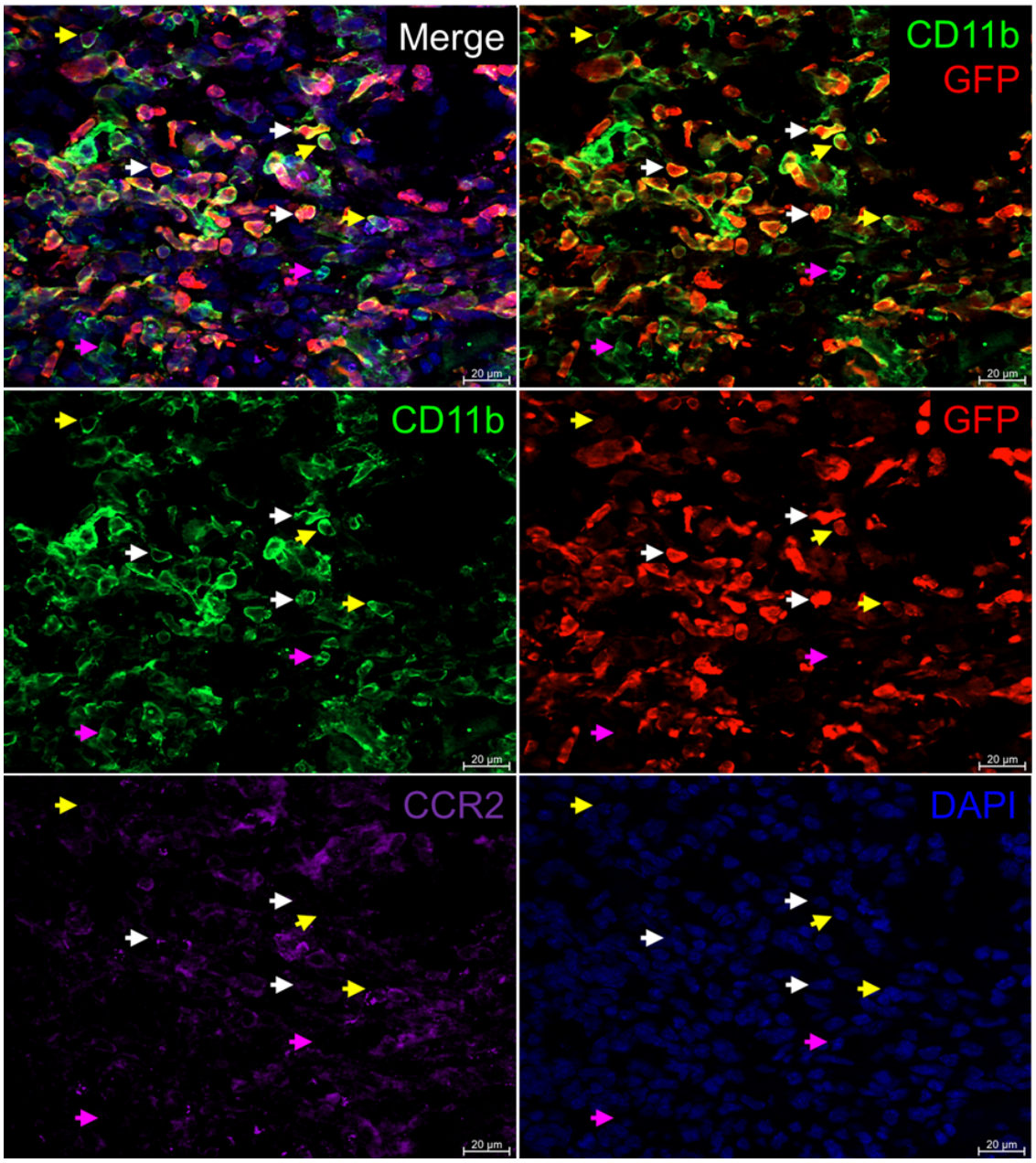

Figure 5. 8. Method for the definition of monocyte subpopulations in mouse heart tissue by immunofluorescence microscopy.

$CD11b^{+}GFP^{hi}$ non-classical monocytes (white arrow), $CD11b^{+}GFP^{mid}$ classical monocytes (yellow arrow), $CD11b^{+}GFP^{-}$ neutrophils (pink arrow). CCR2 staining was weak, despite multiple optimisation attempts, and therefore the number of classical monocytes may have been underestimated. This analysis was performed on 2h and 24h I/R and sham hearts in *Cx3cr1*$^{+/GFP}$ and *Cx3cr1*$^{GFP/GFP}$ mice. 2h I/R: n=4 *Cx3cr1*$^{+/GFP}$, n=5 *Cx3cr1*$^{GFP/GFP}$; 24h I/R: n=4/genotype; day 3 I/R: n=5/genotype; 2h and 24h sham: n=3/genotype.

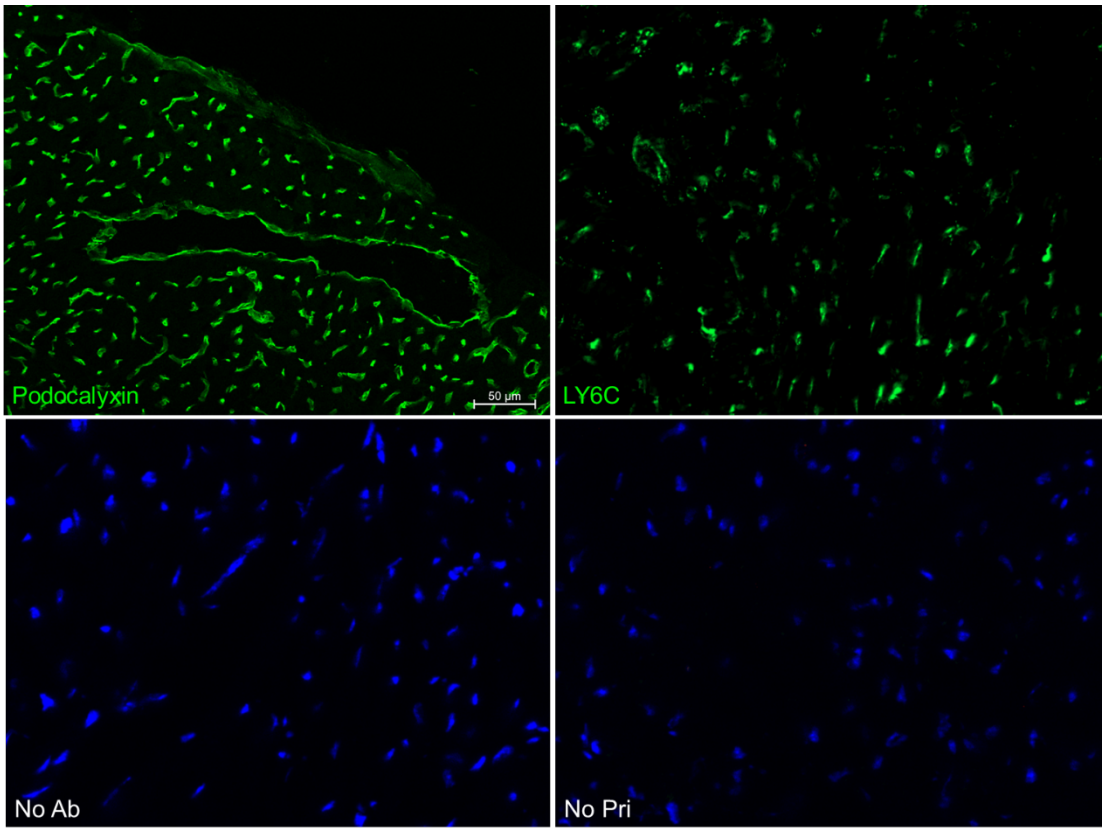

Figure 5. 9. Expression of Ly6C in mouse heart tissue.

Staining of mouse heart tissue cryosections with Ly6C antibody showed expression of this marker by endothelial cells. Comparison with Podocalyxin staining, a well-established marker of endothelial cells, showed a similar pattern to Ly6C staining.

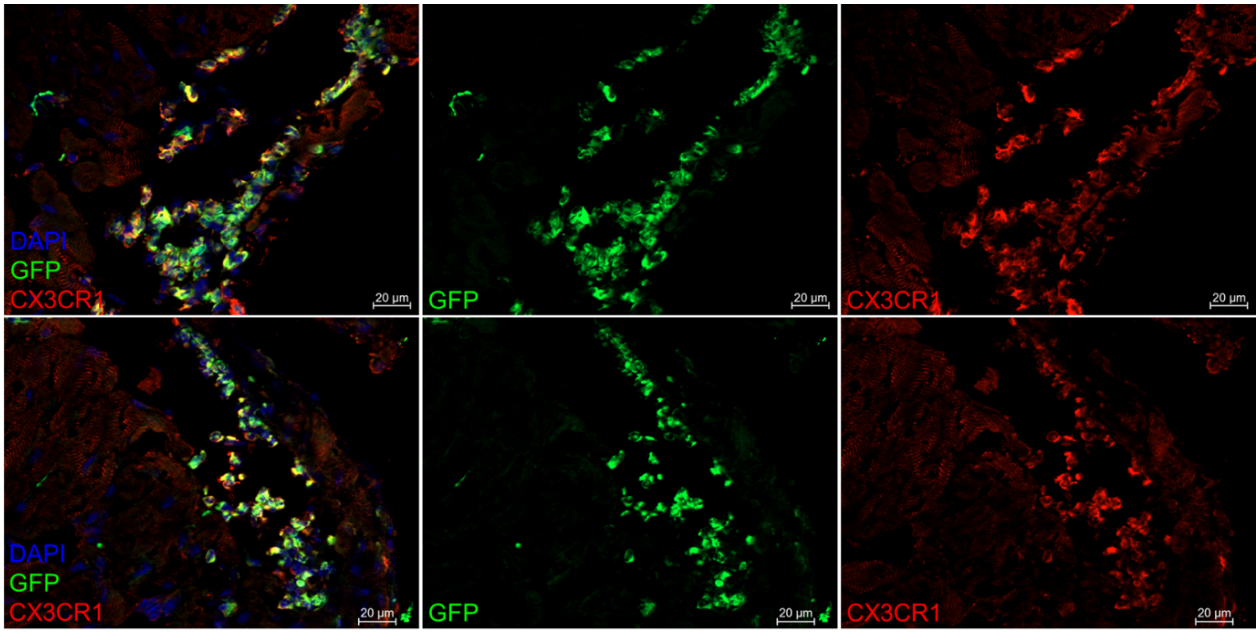

Figure 5. 10. Non-specific CX3CR1 staining in *Cx3cr1*$^{GFP/GFP}$ mouse heart tissue.

Representative images of non-specific staining with anti-CX3CR1 (Abcam, #ab8021) in *Cx3cr1*$^{GFP/GFP}$ hearts. Identification of non-specific CX3CR1 staining in *Cx3cr1*$^{-/-}$ hearts meant that this antibody could not be used in this study. Therefore, GFP staining in *Cx3cr1*$^{+/GFP}$ and *Cx3cr1*$^{GFP/GFP}$ hearts was used for the quantification of infiltrated monocytes in the injured myocardium.

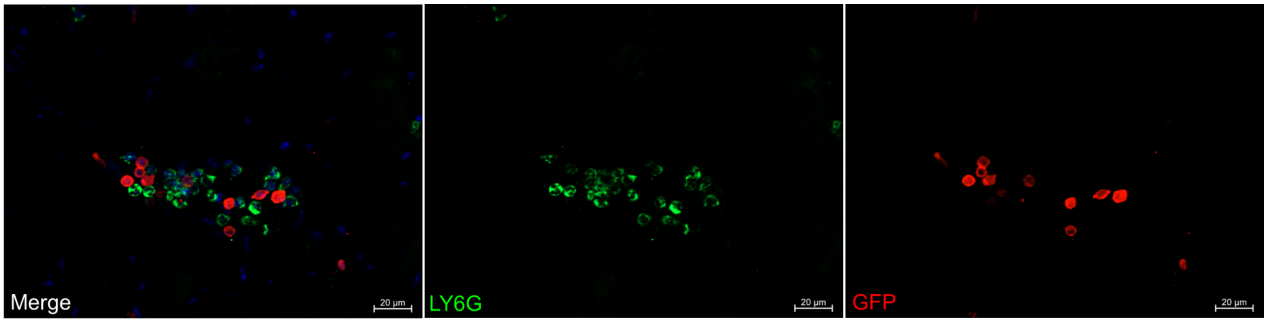

Figure 5. 11. Ly6G staining of neutrophils in mouse heart tissue.

Representative image illustrating the lack of GFP expression by $Ly6G^{+}$ (green) neutrophils in *Cx3cr1*$^{GFP/GFP}$ mouse heart tissue, allowing them to be distinguished from $CD11b^{+}$ GFP^{+} (red) monocytes in *Cx3cr1*$^{+/GFP}$ control hearts and *Cx3cr1*$^{GFP/GFP}$ hearts.

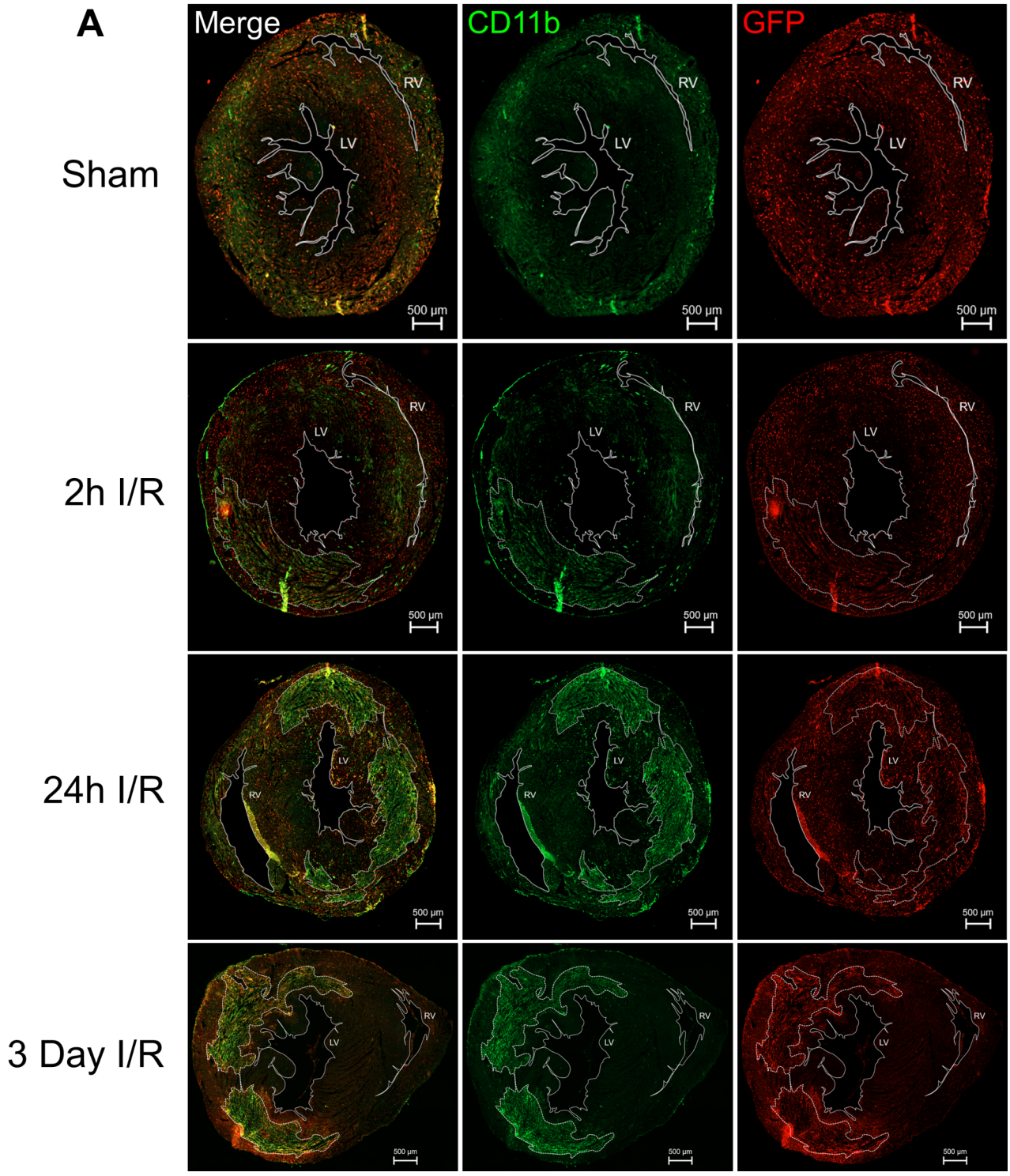
A
Merge
CD11b
GFP
Sham
2h I/R
24h I/R
3 Day I/R
RV
LV
500 µm

B

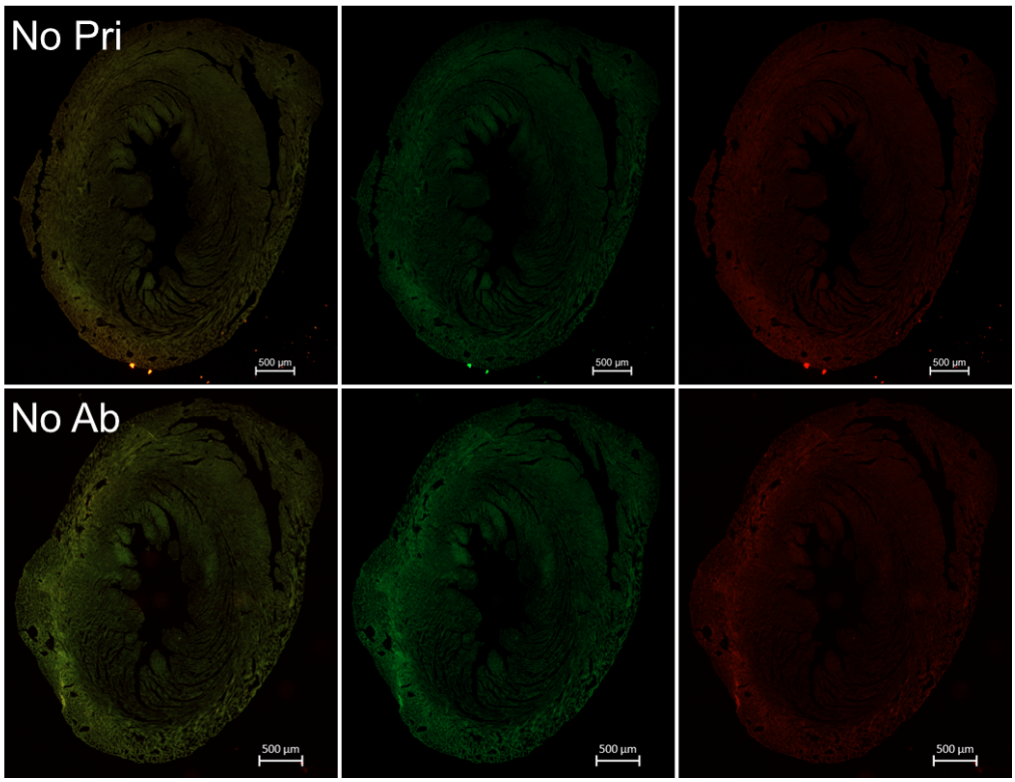

Figure 5. 12. Tile images of CD11b^{+} GFP^{+} monocyte immunofluorescent staining of mouse heart tissue at 2h, 24h and day 3 following cardiac I/R.

A. Representative tile images at 5x magnification of CD11b and GFP immunofluorescent staining of *Cx3cr1*$^{+/GFP}$ mouse heart tissue in sham, 2h I/R, 24h I/R and day 3 I/R heart tissue. Details of antibodies used are described in Table 3.8. B. Representative tile images of no primary antibody and no antibody controls. No primary antibody and no antibody controls were clean.

A

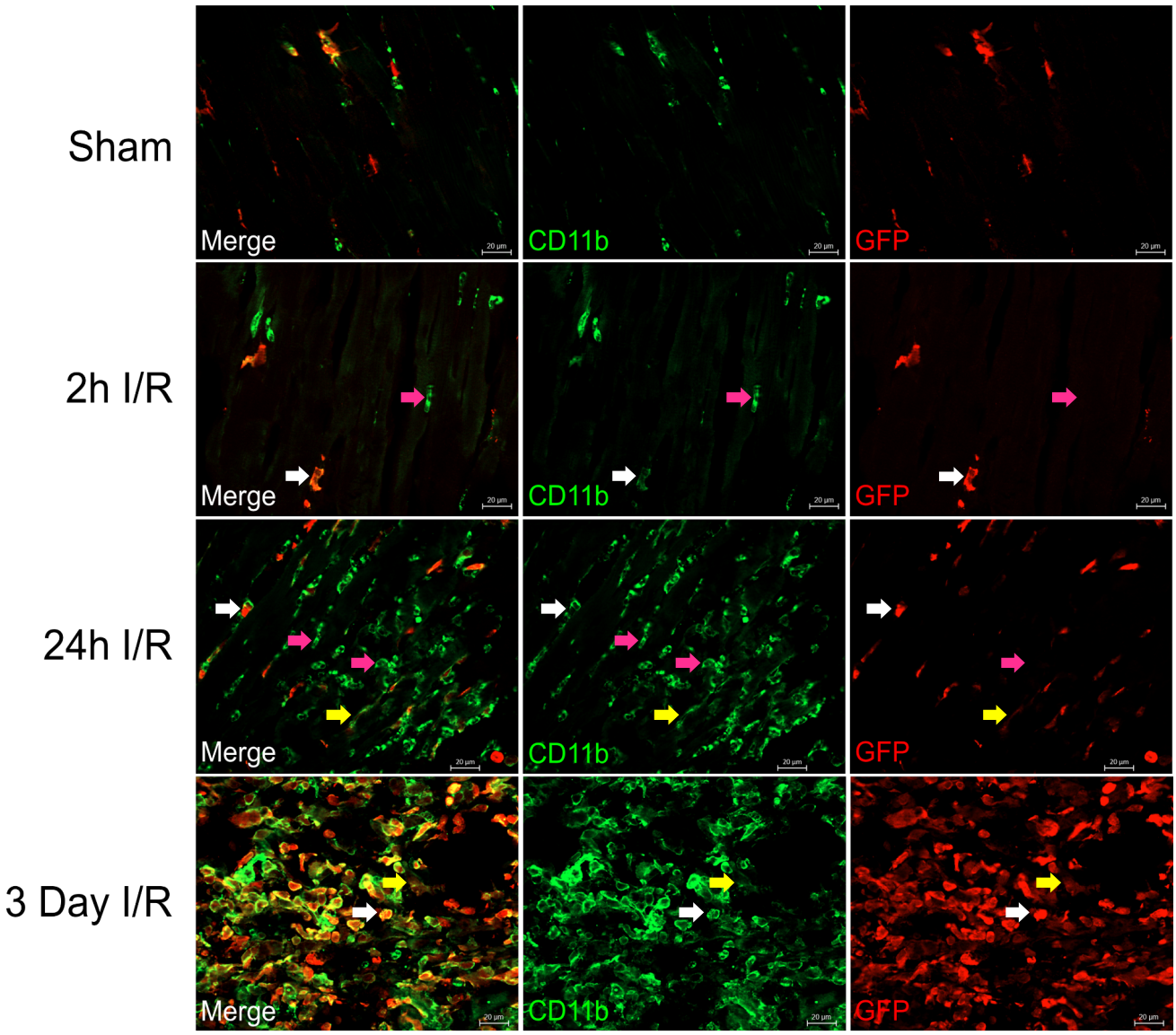

B

3 Day I/R

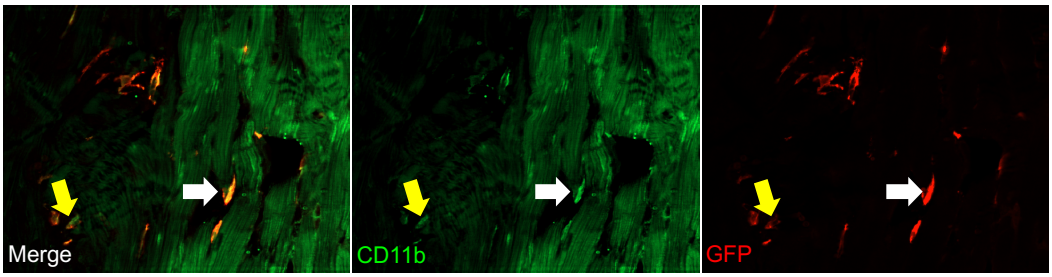

Figure 5. 13. 40x Magnification images of Monocyte CD11b^{+} GFP^{+} immunofluorescent staining of mouse heart tissue at 2h, 24h and day 3 following cardiac I/R.

A. Representative images taken at 40x magnification of CD11b and GFP immunofluorescent stained *Cx3cr1*$^{+/GFP}$ mouse heart tissue, comparing sham, 2h I/R, 24h I/R and day 3 I/R heart tissue. CD11b^{+}GFP^{hi} non-classical monocytes (white arrow), CD11b^{+}GFP^{mid} classical monocytes (yellow arrow), and CD11b^{+}GFP^{-} neutrophils (pink arrow). B. Representative remote region field of view (FOV) images at 40x magnification of CD11b and GFP immunofluorescent staining of day 3 I/R *Cx3cr1*$^{+/GFP}$ mouse heart tissue. CD11b^{+}GFP^{hi} non-classical monocytes (white arrow), CD11b^{+}GFP^{mid} classical monocytes (yellow arrow). All imaging and analysis was performed using Zen Software. 2h I/R: n=4 *Cx3cr1*$^{+/GFP}$, n=5 *Cx3cr1*$^{GFP/GFP}$; 24h I/R: n=4/genotype; day 3 I/R: n=5/genotype. 2h and 24h sham: n=3/genotype.

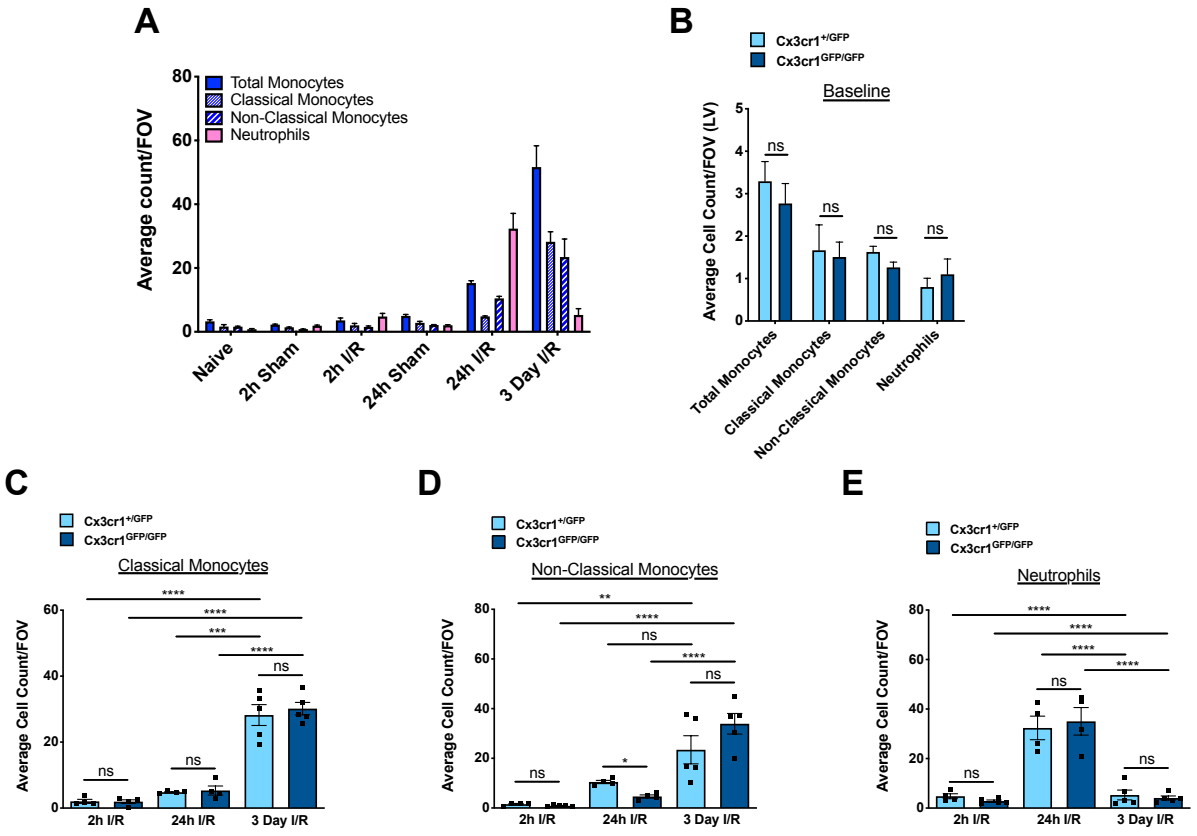

Figure 5. 14. Infiltration of monocyte subpopulations and neutrophils into the reperfused myocardium from peripheral blood at 2h, 24h, and day 3 post-I/R in *Cx3cr1*$^{+/GFP}$ and *Cx3cr1*$^{GFP/GFP}$ mice.

A. Myeloid cell infiltration at 2h, 24h, and day 3 post-I/R in *Cx3cr1*$^{+/GFP}$ control mice. Data are average of n=3 mice/genotype for naïve and sham mice. n=4 2h I/R, n=4 24h I/R. Data analysed by One-way Anova with Tukey's multiple comparison test. B. Comparison of baseline myeloid cell populations in the LV in *Cx3cr1*$^{+/+}$, *Cx3cr1*$^{+/GFP}$, and *Cx3cr1*$^{GFP/GFP}$ naïve hearts, n=3 mice/genotype. Data analysed by Two-way Anova with Sidak's multiple comparison test. C. Classical Monocyte, D. Non-Classical Monocyte, and E. Neutrophil infiltration into the LV at 2h, 24h, and day 3 post-cardiac I/R in *Cx3cr1*$^{+/GFP}$ and *Cx3cr1*$^{GFP/GFP}$ mice. n=4 2h I/R *Cx3cr1*$^{+/GFP}$, n=5 2h I/R *Cx3cr1*$^{GFP/GFP}$. n=4/genotype at 24h I/R. n=5/genotype at day 3 I/R. Two-way Anova with Tukey's multiple comparison test. All data refers to mean ± SEM. **p<0.01, ***p<0.001, ****p<0.0001.

5.2.6 Total Monocyte Infiltration into the Injured Myocardium at 2h, 24h, and Day 3 post Cardiac-I/R in *Cx3cr1*$^{+/GFP}$ and *Cx3cr1*$^{GFP/GFP}$ mice.

The previous section describes the time course of classical and non-classical monocyte infiltration into the injured myocardium at 2h, 24h, and day 3 following cardiac I/R, in *Cx3cr1*$^{+/GFP}$ and *Cx3cr1*$^{GFP/GFP}$ mice. Methodological limitations however meant that discriminating classical and non-classical monocyte subpopulations using this technique proved challenging. The definition of each monocyte subset by microscopy relied on a subjective threshold of GFP and CCR2 expression. This technique was further limited by the poor quality of CCR2 staining potentially leading to an under-estimate of classical monocyte numbers. Due to such uncertainties with the discrimination of classical and non-classical monocyte subsets, monocyte infiltration was re-quantified as a total monocyte population in the same 2h, 24h, and day 3 post-cardiac I/R hearts. Total monocytes were confidently identified and quantified as $CD11b^+$ GFP^+ cells.

From 2h to 24h post-cardiac I/R, the total monocyte counts in the injured myocardium increased by 4.3-fold in *Cx3cr1*$^{+/GFP}$ mice and by 3.5-fold fold in *Cx3cr1*$^{GFP/GFP}$ mice, though neither of these increases were statistically significant (Figure 5.14). By day 3 post-I/R however, the total monocyte infiltrate in the injured myocardium in both *Cx3cr1*$^{+/GFP}$ and *Cx3cr1*$^{GFP/GFP}$ mice increased significantly from 2h to day 3 post-I/R ($p<0.0001$), by 14.8-fold and 22.4-fold, respectively. This was an increase from 24h by 4.3-fold in *Cx3cr1*$^{+/GFP}$ hearts ($p<0.0001$) and 6.4-fold in *Cx3cr1*$^{GFP/GFP}$ hearts ($p<0.0001$). As such, both genotypes showed a similar pattern of total monocyte accumulation into the injured myocardial tissue, across 2h, 24h, and day 3 post-cardiac I/R. At each time point studied, there were no significant differences in total monocyte counts between *Cx3cr1*$^{+/GFP}$ and *Cx3cr1*$^{GFP/GFP}$ mice.

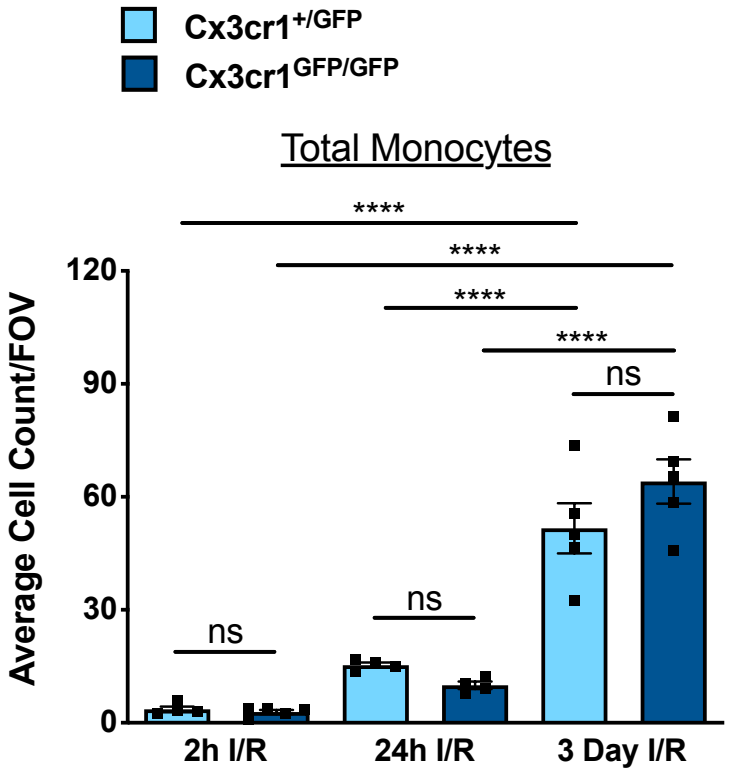

Figure 5. 15. Infiltration of total monocytes into the reperfused myocardium at 2h, 24h, and day 3 post-I/R in *Cx3cr1*$^{+/GFP}$ and *Cx3cr1*$^{GFP/GFP}$ mice.

Total monocytes were defined as CD11b^{+}GFP^{+} cells in the infarcted region. Two-way Anova with Sidak's multiple comparison test. n=4 2h I/R *Cx3cr1*$^{+/GFP}$, n=5 2h I/R *Cx3cr1*$^{GFP/GFP}$. n=4/genotype at 24h I/R. n=5/genotype at day 3 I/R. All data refers to mean ± SEM. ****p<0.0001.

5.2.7 Monocyte Adhesion to Myocardial Vascular Endothelium at 2h and 24h post-Cardiac I/R in *Cx3cr1*$^{+/GFP}$ and *Cx3cr1*$^{GFP/GFP}$ mice.

Although total monocyte infiltration was not affected in *Cx3cr1*$^{GFP/GFP}$ mice compared with *Cx3cr1*$^{+/GFP}$ controls, it is possible that there may have been differences in the adhesion of monocytes to the endothelium. As such, monocyte adhesion to the myocardial vascular endothelium was quantified at 2h and 24h post-I/R. This was performed on the same hearts as the monocyte infiltration analysis. Leukocyte adhesion occurs on venous endothelium prior to extravasation, therefore veins were imaged for monocyte adhesion quantification. Each heart had between 1 and 5 major veins in the infarcted region and were identified on the basis of their known architecture and sub-epicardial position, which is distinct from the intramyocardial position of arteries. To confirm endothelium was present, Podocalyxin staining was used in some cases [323]. These veins were located in the original ischaemic area, but mainly adjacent to the necrotic area. As this is exactly where ischemia reperfusion occurs, it was a key region of interest to study monocyte adhesion in response to cardiac I/R. Smaller veins have the potential to represent a tear in the tissue and therefore were excluded where confirmatory endothelial staining was not available, in order to avoid false-positive results. Classical and non-classical monocyte subpopulations were also analysed for completeness, despite the issues previously mentioned that reduced confidence in discriminating these populations. Adhered cell counts were normalized to the perimeter of the vessel, as vein size is variable within the heart (Figure 5.15).

Monocyte adhesion was first compared between veins in the infarct region (LV) and the remote region (RV), in order to identify any adhesion response that was specific to cardiac I/R. This analysis showed that at 2h post-I/R, *Cx3cr1*$^{+/GFP}$ counts of vein adhered total monocytes were significantly greater in the injured myocardium compared to the remote area ($p<0.01$), however this difference was not seen in *Cx3cr1*$^{GFP/GFP}$ mice (Figure 5.16A). When comparing 2h post-I/R monocyte adhesion in the infarct region between genotypes, there was no significant difference in total monocyte, classical monocyte, or non-classical monocyte adhered counts between *Cx3cr1*$^{+/GFP}$ and *Cx3cr1*$^{GFP/GFP}$ hearts (Figure 5.16A).

At 24h, mean total monocyte and non-classical monocyte adhesion decreased from 2h in *Cx3cr1*$^{+/GFP}$ mice, although this change was not statistically significant (Figure 5.16C). Counts of adhered classical monocytes in the infarct region in *Cx3cr1*$^{+/GFP}$ mice between these time points were not different. In *Cx3cr1*$^{GFP/GFP}$ hearts, total monocyte adhesion significantly decreased from 2h to 24h ($p<0.05$) (Figure 5.16D), however classical and non-classical monocyte adhesion counts did not significantly differ. Comparison of infarct region vein endothelial-adhered counts of total, classical, and non-classical monocytes at 24h between genotypes showed no significant difference (Figure 5.16B).

The findings of this analysis therefore showed that total monocyte adherence to myocardial venous endothelium at 2h post-cardiac I/R was specific to the infarct region in *Cx3cr1*$^{+/GFP}$ hearts, but did not discriminate between the injured and remote regions in *Cx3cr1*$^{GFP/GFP}$ mice.

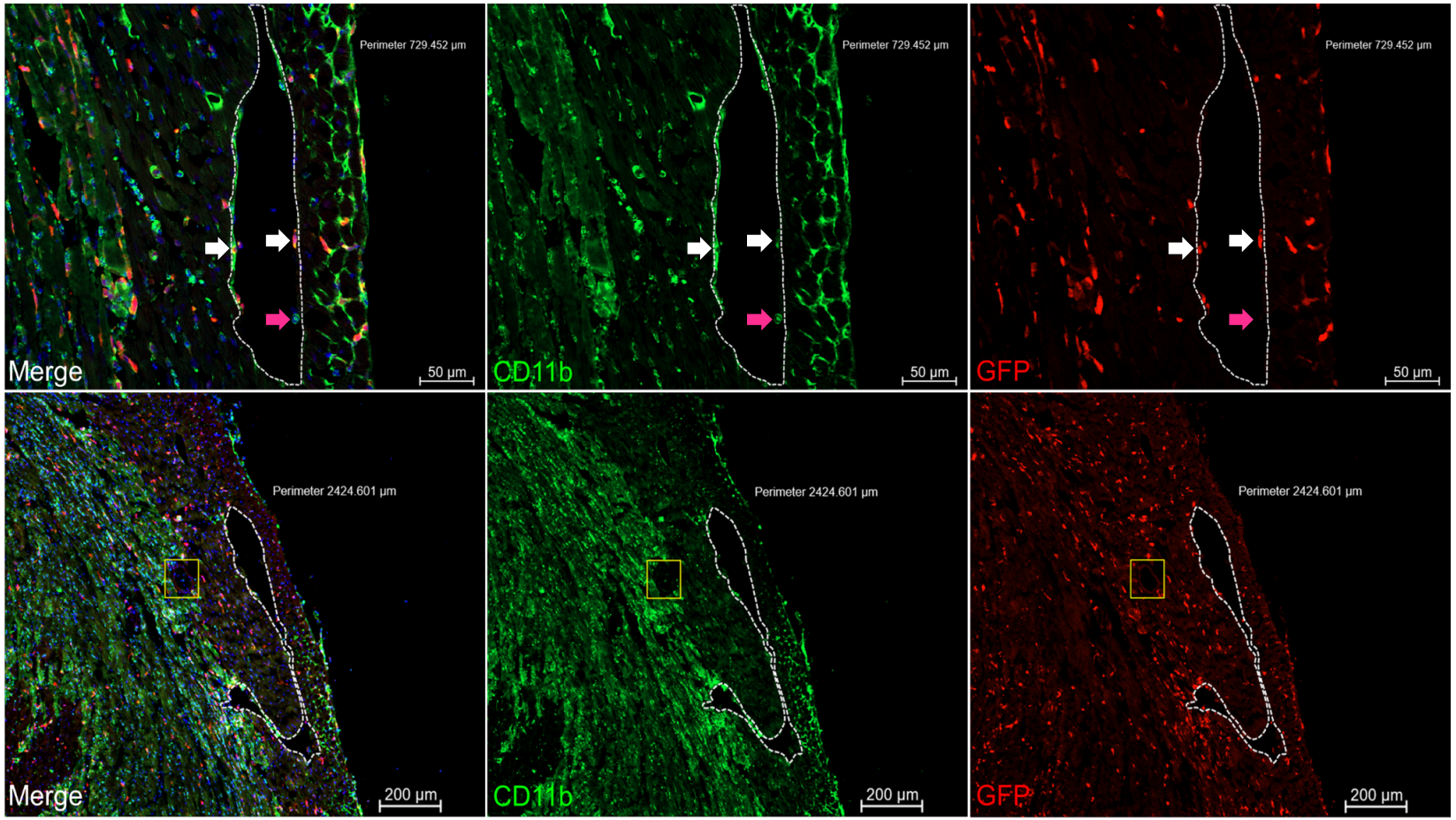
Perimeter 729.452 µm
Merge
50 µm
Perimeter 729.452 µm
CD11b
50 µm
Perimeter 729.452 µm
GFP
50 µm
Perimeter 2424.601 µm
Merge
200 µm
Perimeter 2424.601 µm
CD11b
200 µm
Perimeter 2424.601 µm
GFP
200 µm

Figure 5. 16. Imaging of myocardial veins following cardiac I/R to quantify monocyte adhesion.

Representative 40x and 20x magnification images of myocardial veins (white dashed lines) within the infarcted region at 2h post I/R. Myocardial veins were identified on the basis of their known architecture and sub-epicardial position, which is distinct from the intramyocardial position of arteries. Monocytes were identified as total $CD11b^{+}GFP^{+}$ cells and subdivided into classical $CD11b^{+}GFP^{mid}$ and non-classical $CD11b^{+}GFP^{hi}$ monocyte subpopulations. $CD11b^{+}GFP^{hi}$ non-classical monocytes (white arrow), $CD11b^{+}GFP^{-}$ neutrophils (pink arrow). n=4 2h I/R *Cx3cr1*$^{+/GFP}$, n=5 2h I/R *Cx3cr1*$^{GFP/GFP}$; n=4/genotype at 24h I/R.

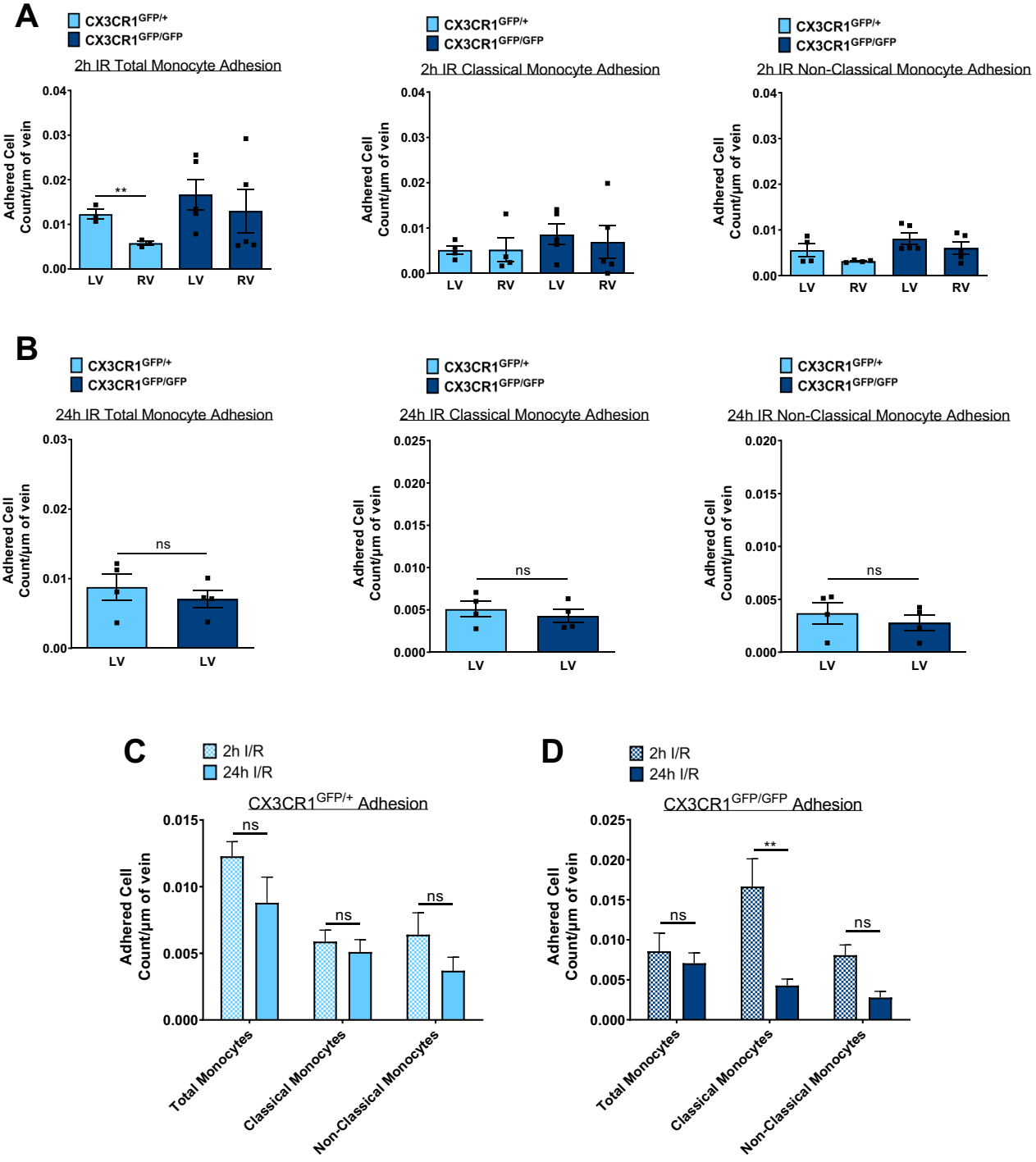
A
CX3CR1GFP/+
CX3CR1GFP/GFP
2h IR Total Monocyte Adhesion
2h IR Classical Monocyte Adhesion
2h IR Non-Classical Monocyte Adhesion
Adhered Cell Count/µm of vein
0.04
0.03
0.02
0.01
0.00
**
LV
RV
LV
RV
B
24h IR Total Monocyte Adhesion
24h IR Classical Monocyte Adhesion
24h IR Non-Classical Monocyte Adhesion
0.03
0.02
0.01
0.00
0.025
0.020
0.015
0.010
0.005
0.000
ns
LV
LV
C
2h I/R
24h I/R
CX3CR1GFP/+ Adhesion
0.015
0.010
0.005
0.000
ns
Total Monocytes
Classical Monocytes
Non-Classical Monocytes
D
CX3CR1GFP/GFP Adhesion
0.025
0.020
0.015
0.010
0.005
0.000
**

Figure 5. 17. Monocyte adhesion to myocardial venous endothelium at 2h and 24h post-cardiac I/R.

Total monocyte ($CD11b^{+}GFP^{+}$), classical monocyte ($CD11b^{+}GFP^{mid}$) and non-classical monocyte ($CD11b^{+}GFP^{hi}$) adhesion to myocardial vein endothelium at 2h post-cardiac I/R (A), and 24h post-cardiac I/R (B). C. Comparison of monocyte adhesion at 2h I/R between *Cx3cr1*$^{+/GFP}$ and *Cx3cr1*$^{GFP/GFP}$ hearts. D. Comparison of monocyte adhesion at 24h I/R between *Cx3cr1*$^{+/GFP}$ and *Cx3cr1*$^{GFP/GFP}$ hearts. Data was analysed by Two-way Anova with Tukey's multiple comparison test. All data refers to mean ± SEM. n=4 2h I/R *Cx3cr1*$^{+/GFP}$, n=5 2h I/R *Cx3cr1*$^{+/GFP}$; n=4/genotype at 24h I/R. *p<0.05, **p<0.01.

5.2.8 Spatial Pattern of GFP$^+$ Cells at Day 3 Post-Cardiac I/R in *Cx3cr1*$^{+/GFP}$ and *Cx3cr1*$^{GFP/GFP}$ Hearts.

At day 3 following cardiac I/R, *Cx3cr1*$^{+/GFP}$ and *Cx3cr1*$^{GFP/GFP}$ hearts appeared to show a difference in GFP$^+$ cell localisation within the infarct. To analyse this behaviour of GFP$^+$ cells, their counts were quantified in the defined areas of i) the total infarct region, ii) the infarct border zone (BZ), and iii) the infarct central zone (CZ). Counts of GFP$^+$ cells were then quantified per mm^2 of heart tissue within the specific infarct area. Within the group of *Cx3cr1*$^{GFP/GFP}$ hearts (n=5), three hearts showed a spatial pattern of GFP$^+$ cell accumulation at the BZ of the infarct (Figure 5.17), which was specific to day 3 I/R and not observed at 2h or 24h. Importantly, this GFP$^+$ expression largely co-localized with CD11b$^+$ expression, indicating that these cells were likely to be monocytes/macrophages. The counts of GFP$^+$ cells at the infarct border zone (BZ) was significantly greater than the GFP$^+$ population within the central zone (CZ) of the infarct in these three *Cx3cr1*$^{GFP/GFP}$ hearts ($p<0.05$) (Figure 5.18). In contrast to this observation in *Cx3cr1*$^{GFP/GFP}$ hearts, *Cx3cr1*$^{+/GFP}$ mice did not demonstrate GFP$^+$ cell marginalisation to the infarct BZ, but rather showed a dispersed population GFP$^+$ cells throughout the injured myocardium. As such, the infarct BZ and CZ could not be accurately identified and defined in *Cx3cr1*$^{+/GFP}$ hearts, therefore GFP$^+$ cells were quantified within the total infarct region. Counts of GFP$^+$ cells within the total infarct area were not significantly different between *Cx3cr1*$^{+/GFP}$ and *Cx3cr1*$^{GFP/GFP}$ hearts groups at this time point of day 3 post-I/R, though there was a trend towards reduced counts in *Cx3cr1*$^{GFP/GFP}$ infarcts. (Figure 5.18).

This possible phenotype observed in *Cx3cr1*$^{GFP/GFP}$ mice at day 3 post-I/R suggests that GFP$^+$ cells at this time point in the injured myocardium may locate and function distinctly from that of *Cx3cr1*$^{+/GFP}$ mice, presumably due to the absence of CX3CR1 expression.

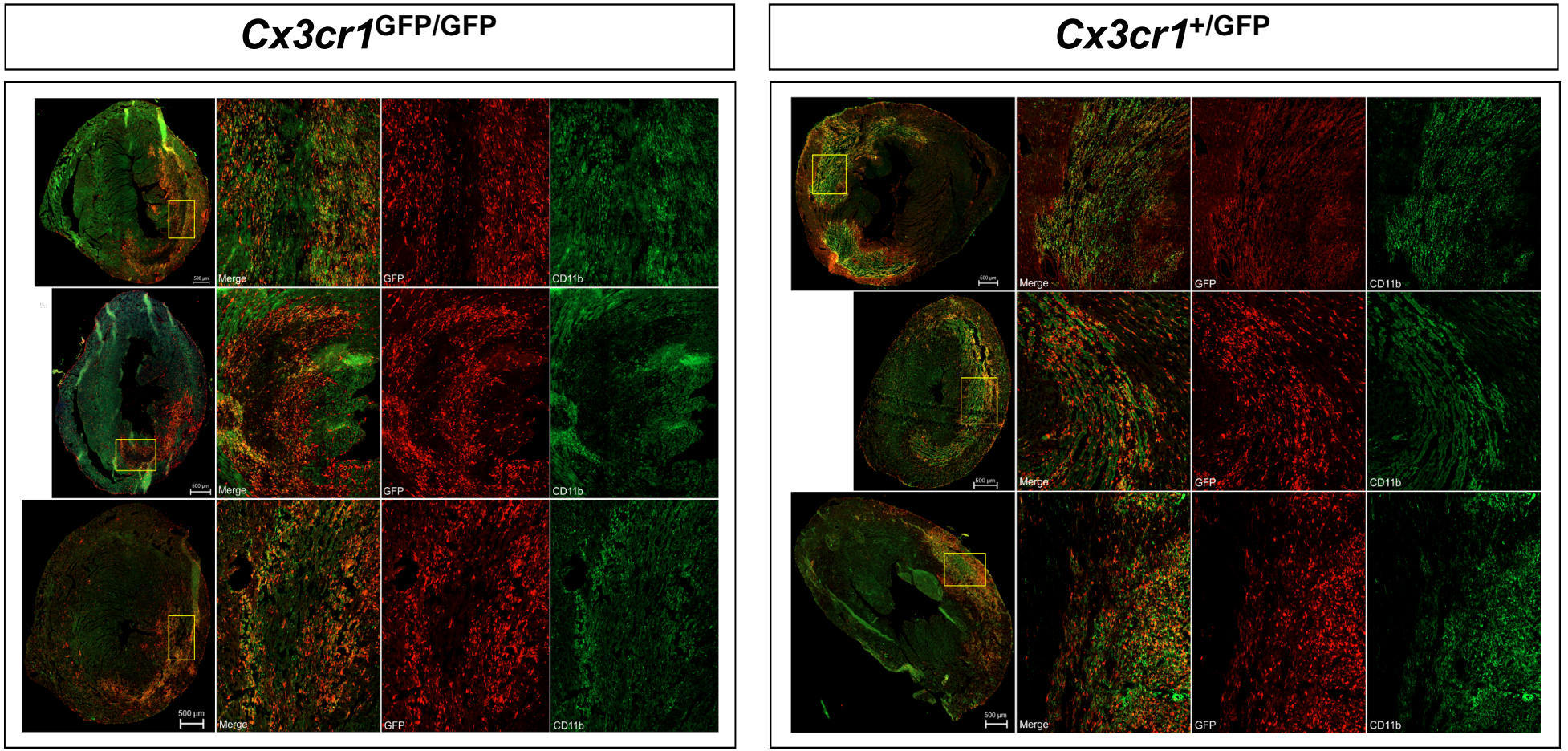
Cx3cr1GFP/GFP
Cx3cr1+/GFP
Merge
GFP
CD11b
500 µm

Figure 5. 18. Tile 5x and 40x Images of the spatial pattern of GFP$^+$ cells in the infarct mouse heart tissue at day 3 post-I/R in *Cx3cr1*$^{+/GFP}$ and *Cx3cr1*$^{GFP/GFP}$ mice.

Day 3 post-I/R 5x and 20x magnification images of CD11b$^+$GFP$^+$ monocytes in the infarcted myocardium in *Cx3cr1*$^{+/GFP}$ and *Cx3cr1*$^{GFP/GFP}$ hearts. n=3 *Cx3cr1*$^{GFP/GFP}$ hearts specifically show GFP$^+$ marginalisation at the infarct border zone, with significantly greater GFP$^+$ cell counts at the infarct border than in the infarct central zone ($p<0.05$). The GFP$^+$ population in *Cx3cr1*$^{+/GFP}$ hearts is dispersed throughout the infarct region and is not specific to the border zone. All images were taken and analysed using Zen software.

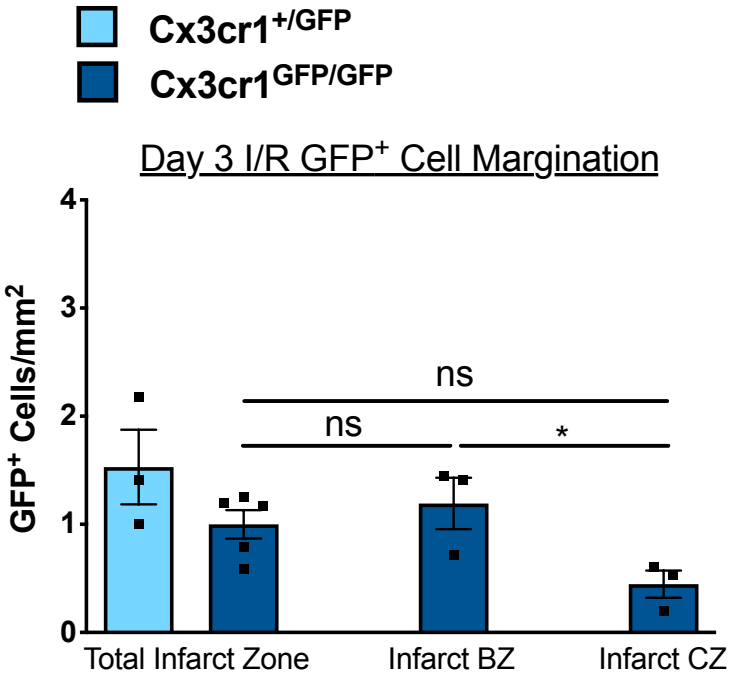

Figure 5. 19. Quantification of the spatial pattern of GFP$^+$ cells in *Cx3cr1*$^{+/GFP}$ and *Cx3cr1*$^{GFP/GFP}$ hearts at day 3 post-I/R.

GFP$^+$ cells were quantified in the total infarct area, infarct border zone (BZ), and infarct central zone (CZ), per mm^2 of myocardial tissue. n=3 *Cx3cr1*$^{+/GFP}$, n=5 *Cx3cr1*$^{GFP/GFP}$. BZ and CZ not clear in *Cx3cr1*$^{+/GFP}$ hearts and in n=2 *Cx3cr1*$^{GFP/GFP}$ hearts, therefore only total infarct GFP$^+$ cells could be quantified in these hearts. One-way Anova with Tukey's multiple comparison test. Data refers to mean ± SEM. *p<0.05.

5.2.9. Macrophage Populations in the Infarcted Heart at Day 3 Post-Cardiac I/R

Following the recruitment of monocyte subpopulations into the injured myocardial tissue following cardiac I/R, monocyte subpopulations perform their own distinct functions contributing to infarct repair. Upon infiltration, pro-inflammatory classical monocytes release inflammatory cytokines such as TNF-α and produce nitric oxide to mediate removal of necrotic tissue. This pro-inflammatory response shifts over the ensuing days to predominantly a reparative phenotype, mediated by non-classical monocytes which release anti-inflammatory mediators, promote angiogenesis and the deposition of scar tissue. In addition to their own direct functions in the innate immune response to cardiac I/R, monocyte subpopulations also undergo differentiation into distinct macrophage populations which perform their own secondary distinct functions [324]. A resident cardiac macrophage population also exists in the myocardium, however murine models of cardiac I/R show a complete loss of this population within the infarct at 24h post-MI [325]. As such, macrophage cells present in the infarct from 24h post-I/R are likely to be derived from infiltrated monocyte subpopulations. Macrophages exist as a heterogeneous population, but can be classified broadly as either M1 or M2 macrophages [326]; M1 'inflammatory' macrophages are proposed to arise predominantly from Ly6C^{hi} classical monocytes, and are present in the heart tissue at day 1-3 following I/R to drive acute inflammation and facilitate the clearance of necrotic material. At day 5-7, it is believed that M1 macrophages adopt a reparative M2-like 'alternative' macrophage phenotype to attenuate inflammation and promote scar formation [327]. Ly6C^{lo} monocytes can also differentiate into M2 macrophages to promote tissue healing and angiogenesis [328].

The importance of non-classical monocyte CX3CR1 expression in this process of differentiation into distinct macrophage populations is not yet fully understood. CX3CR1 expression has however been identified as a key regulator of macrophage function at sites of inflammation [329, 330], and in many tissues, a link between the macrophage CX3CR1 phenotype and cell activation state has been observed [331-333]. With this in mind, it is possible that CX3CR1 is important for the maturation of infiltrated monocytes within the infarcted myocardium, which in turn is linked to the resolution of inflammation following I/R.

In the next part of this work, I therefore investigated the effect of genetic CX3CR1 depletion on macrophage populations present in the injured myocardium at day 3 following I/R. This analysis was performed on the same *Cx3cr1*$^{+/GFP}$ and *Cx3cr1*$^{GFP/GFP}$ mouse hearts that were used for quantifying monocyte subpopulation infiltration at day 3 post I/R. As such, *Cx3cr1*$^{+/GFP}$ mice again served as a control group. Macrophages were defined as F4/80^{+} cells, which is one of the best markers to identify mouse tissue macrophages [334, 335]. Details of the staining protocol are described in section 3.6.3. CD68 was considered but omitted on the basis that it is a marker of both macrophage and monocyte populations. GFP expression was used to define F4/80^{+} GFP^{hi} M2 macrophages and F4/80^{+} GFP^{mid} M1 macrophages, since M2 macrophages are derived from CX3CR1^{hi} non-classical monocytes while M1 macrophages develop from CX3CR1^{mid} classical monocytes [336]. The differentiation between GFP^{hi} and GFP^{lo} macrophage definition was performed as described for CD11b^{+}GFP^{hi} classical and CD11b^{+}GFP^{mid} classical monocytes in section 5.2.4. Macrophage subpopulation quantification was however interpreted with caution as for monocyte subpopulations due to some uncertainty defining GFP^{mid} and GFP^{hi} cells as discussed in section 5.2.5. A representative 40x image of F4/80^{+}GFP^{+} staining in the infarcted tissue at day 3 post-cardiac I/R is shown in Figure 5.19.

When considering macrophages as a total population, *Cx3cr1*$^{GFP/GFP}$ mice had a significantly lower count of F4/80^{+} cells present in the infarct tissue compared to that of *Cx3cr1*$^{+/GFP}$ mice, by approximately 1.4-fold ($p<0.05$) (Figure 5.20). As all F4/80^{+} staining was found to co-localize with positive GFP staining, this reduced infarct macrophage population in *Cx3cr1*$^{GFP/GFP}$ hearts is likely to reflect the spatial localisation of these cells at the infarct border observed at day 3 I/R (section 5.2.7). This difference in day 3 I/R total macrophage counts in the infarct between *Cx3cr1*$^{+/GFP}$ and *Cx3cr1*$^{GFP/GFP}$ groups may therefore not indicate a difference in the numbers of these cells between genotypes, but rather be a result of the significantly lower count of GFP^{+} cells located in the infarct central zone compared to the infarct border in *Cx3cr1*$^{GFP/GFP}$ hearts.

When comparing the ratio of day 3 post-I/R M1 and M2 macrophage subpopulations in *Cx3cr1*$^{+/GFP}$ hearts, counts of F4/80^{+}GFP^{mid} M1 macrophages were significantly

higher than M2 F4/80^{+}GFP^{hi} macrophages ($p<0.01$). In *Cx3cr1*$^{GFP/GFP}$ mice, the difference between macrophage subpopulation counts was not significantly different, though there was a trend towards increased F4/80^{+}GFP^{mid} M1 macrophages. Between genotypes, counts of day 3 post-I/R M1 F4/80^{+}GFP^{mid} macrophages were not significantly different, however there was a trend towards decreased numbers in *Cx3cr1*$^{GFP/GFP}$ hearts. The counts of M2 F4/80^{+} GFP^{hi} macrophages in the infarct region were not different between genotypes.

This analysis of day 3 I/R macrophage populations suggested that i) *Cx3cr1*$^{+/GFP}$ control group M1 macrophages are present in significantly greater numbers than M2 macrophages at day 3 post-I/R, ii) M1 and M2 macrophage subpopulation counts are not significantly affected by genetic CX3CR1 knockout and iii) all F4/80^{+} macrophages present in the infarct at day 3 retain GFP expression.

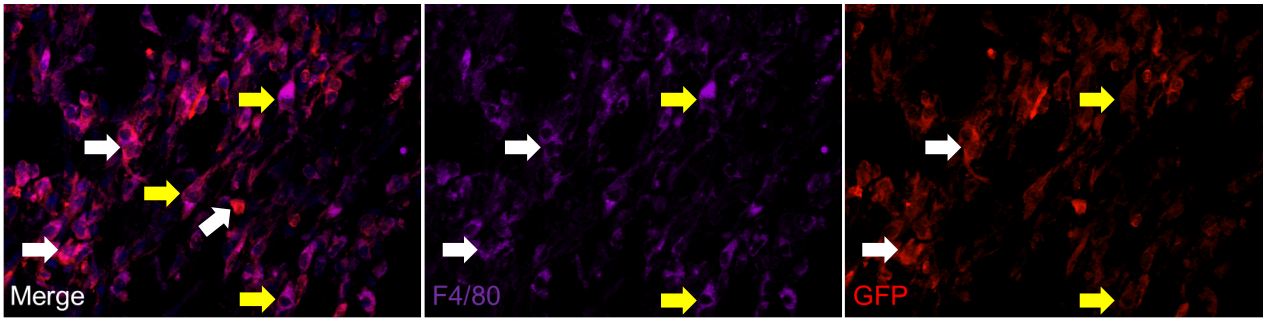

Figure 5. 20. Immunofluorescent staining of F4/80^{+} GFP^{+} macrophages in the mouse infarct myocardium.

Representative infarct region field of view (FOV) images at 40x magnification of F4/80 and GFP immunofluorescent staining of day 3 I/R *Cx3cr1*$^{+/GFP}$ mouse heart tissue in the infarct region to identify macrophages. Macrophages were broadly classified as F4/80^{+}GFP^{hi} M2 macrophages (white arrow), and F4/80^{+}GFP^{med} M1 macrophages (yellow arrow). Images were taken and analysed using Zen software.

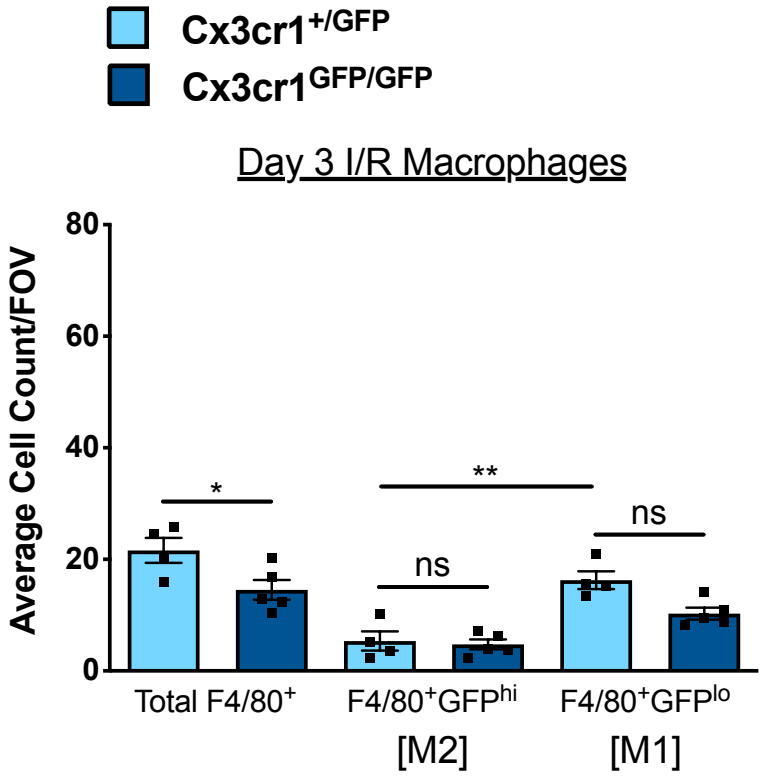

Figure 5. 21. Infarct macrophage populations in the injured myocardium at day 3 post-cardiac I/R in *Cx3cr1*$^{+/GFP}$ and *Cx3cr1*$^{GFP/GFP}$ mice.

Macrophages were defined as F4/80^{+} cells and broadly sub-classified into M1 (GFP^{lo}) and M2 (GFP^{hi}) subsets based on GFP expression. Two-way Anova with Tukey's multiple comparison test. n=4 *Cx3cr1*$^{+/GFP}$, n=5 *Cx3cr1*$^{GFP/GFP}$. Data refers to mean ± SEM. *p<0.05, **p<0.01.

5.2.10 Cardiac Digest

The study of mouse monocyte subpopulations in the infarct heart by immunofluorescence microscopy is limited by both the number and availability of monocyte subset marker detection antibodies. Standard fluorescence microscopy is restricted to the use of four fluorescent markers, including the nuclear marker DAPI, which for identifying a complex population like non-classical monocytes presents a challenge. Other techniques such as advanced confocal allows the use of an increased numbers of fluors, while Hyperion permits further markers using heavy metal-labelled antibodies [337, 338]. To date, there is no exclusive marker defining mouse non-classical monocytes, unlike other leukocyte populations such as B-cells (CD19), T-cells (CD3), neutrophils (Ly6G) etc. Instead, monocytes are defined by their expression of the myeloid cell marker CD11b, in combination with Ly6C, which is also expressed by neutrophils, endothelial cells, and T-cell subsets [339-341]. The distinction between monocytes and other $CD11b^{+}$ $Ly6C^{+}$ leukocytes, predominantly neutrophils, is then based on CCR2 and CX3CR1, which are expressed by monocytes but not neutrophils [336, 342].

To overcome the limitations imposed by immunofluorescent microscopy and to achieve a more accurate level of cell characterization, an alternative method of cardiac digestion and FACS analysis was used to study monocyte subset infiltration into the injured myocardium at 24h post-cardiac I/R. This time point was chosen to further investigate the reduced non-classical monocyte infiltrate in the injured myocardium observed in *Cx3cr1*$^{+/GFP}$ hearts compared to *Cx3cr1*$^{GFP/GFP}$ mice described as in section 5.2.4. This cardiac digest technique compromises a combination of mechanical and enzymatic digestion of the myocardium which generates a suspension of isolated single viable cells that can be analysed by flow cytometry for the identification, phenotyping, and quantification of leukocytes (details in 3.9.3). FACS allowed me to use a more comprehensive panel of markers than microscopy; CD45, CD11b, Ly6C, Ly6G, CCR2, CX3CR1, GFP, and F4/80 (Figure 5.21). These antibodies were chosen on the basis that they would give the greatest accuracy of monocyte subset definition, through their positive and negative selection; CD45 and CD11b defined all myeloid cells, Ly6G defined neutrophils, and Ly6C defined $Ly6C^{hi}$

classical and Ly6C^{lo} non-classical monocytes, while F4/80 allowed identification of macrophages. Expression of CCR2 and GFP by each monocyte subpopulation confirmed their identity. The relative expression of GFP by classical and non-classical monocytes resembled that of monocyte subpopulations in mouse blood and heart tissue analysed by microscopy (Figure 5.22). The LV and RV were processed and analysed independently to compare the injured infarcted myocardial tissue with the remote region.

Using this cardiac digest method, classical and non-classical monocyte infiltration into the infarcted heart tissue at 24h post-cardiac I/R was studied and compared with the findings obtained from immunofluorescent microscopy. It should be mentioned that the heart tissue was not perfused to remove intravascular blood, so these cells cannot be excluded from the data.

LV

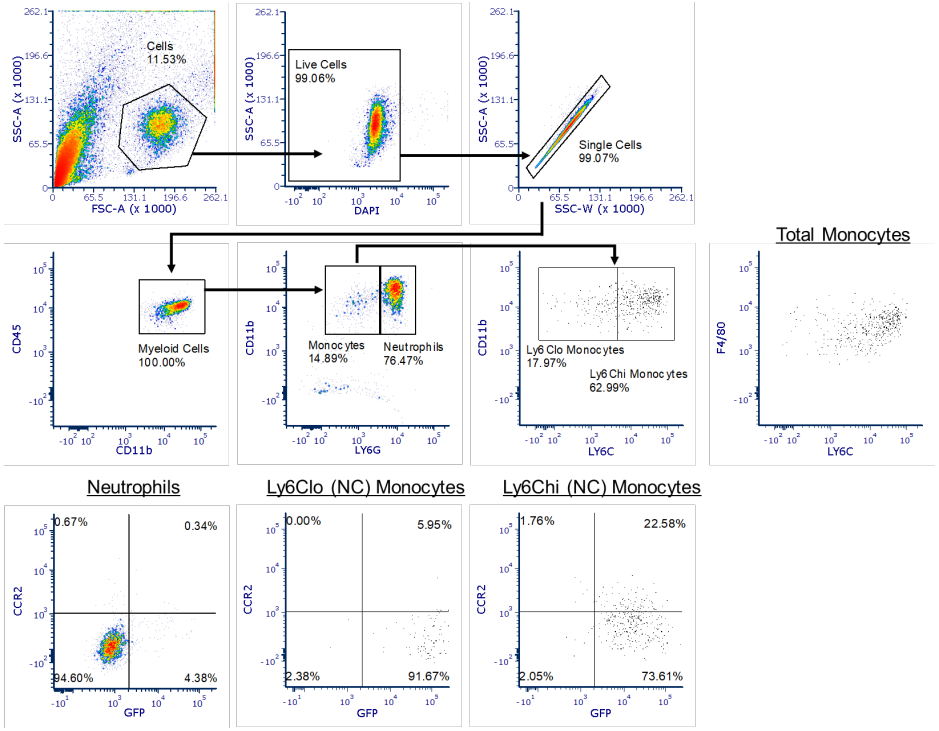
Cells
11.53%
SSC-A (x 1000)
FSC-A (x 1000)
Live Cells
99.06%
DAPI
Single Cells
99.07%
SSC-W (x 1000)
Myeloid Cells
100.00%
CD45
CD11b
Monocytes
14.89%
Neutrophils
76.47%
LY6G
Ly6 Clo Monocytes
17.97%
Ly6 Chi Monocytes
62.99%
LY6C
Total Monocytes
F4/80
Neutrophils
Ly6Clo (NC) Monocytes
Ly6Chi (NC) Monocytes
CCR2
GFP
0.67%
0.34%
94.60%
4.38%
0.00%
5.95%
2.38%
91.67%
1.76%
22.58%
2.05%
73.61%

RV

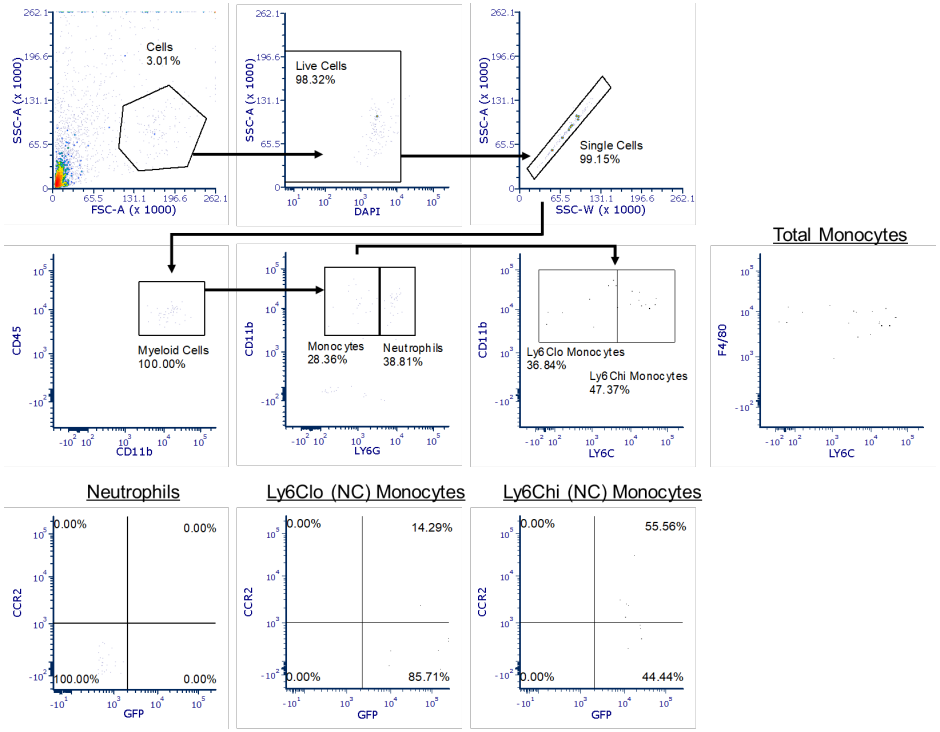
Cells
3.01%
SSC-A (x 1000)
FSC-A (x 1000)
Live Cells
98.32%
DAPI
Single Cells
99.15%
SSC-W (x 1000)
Myeloid Cells
100.00%
CD45
CD11b
Monocytes
28.36%
Neutrophils
38.81%
LY6G
Ly6 Clo Monocytes
36.84%
Ly6 Chi Monocytes
47.37%
LY6C
Total Monocytes
F4/80
Neutrophils
Ly6Clo (NC) Monocytes
Ly6Chi (NC) Monocytes
CCR2
GFP
0.00%
0.00%
100.00%
0.00%
0.00%
14.29%
0.00%
85.71%
0.00%
55.56%
0.00%
44.44%

Figure 5. 22. Example Flow Cytometric gating of *Cx3cr1*$^{GFP/GFP}$ mouse cardiac digest immune cell populations in the LV and RV at 24h post-cardiac I/R.

Total monocytes were defined as CD45^{+}CD11b^{+}Ly6G^{-} cells while neutrophils were defined as CD45^{+}CD11b^{+}Ly6G^{+}. Monocytes were then sub-classified as either classical [LY6C^{hi}CCR2^{hi}CX3CR1/GFP^{mid}] or non-classical [LY6C^{lo}CCR2^{lo}CX3CR1/GFP^{hi}] monocytes. Expression of F4/80 by infarct monocytes at 24h post-I/R indicated that almost all monocytes had begun differentiation into macrophage populations at this time point. Immune cell infiltrate into the myocardium was practically all confined to the LV injured region, with very little infiltrate present in the remote, RV region a 24h post-I/R.

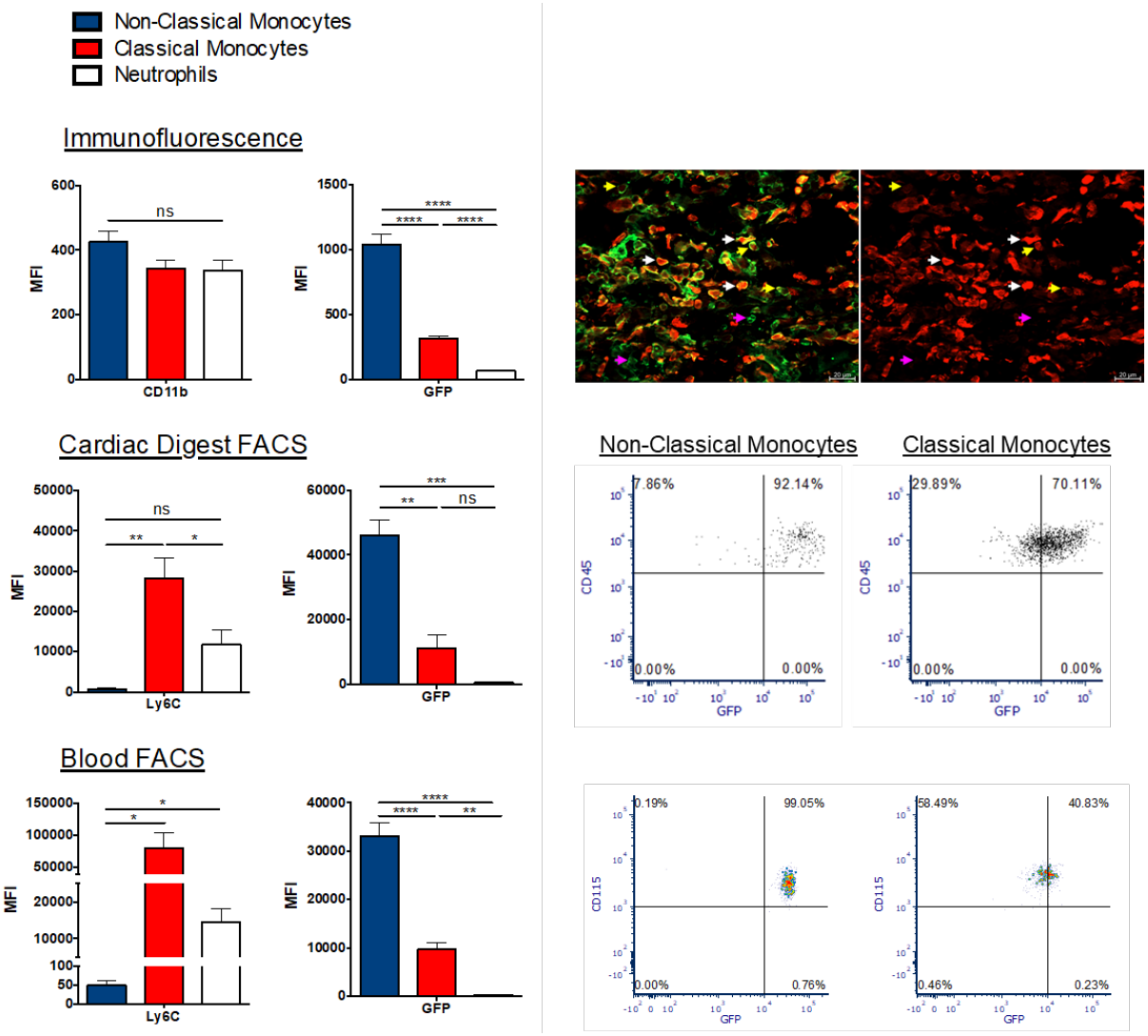
Non-Classical Monocytes
Classical Monocytes
Neutrophils
Immunofluorescence
MFI
CD11b
GFP
ns
****
Cardiac Digest FACS
Ly6C
Blood FACS
Non-Classical Monocytes
Classical Monocytes
CD45
CD115
7.86%
92.14%
0.00%
29.89%
70.11%
0.19%
99.05%
0.76%
58.49%
40.83%
0.46%
0.23%

Figure 5. 23. Analysis of the relative expression of GFP by mouse classical and non-classical monocyte subpopulations in the circulation and in the heart tissue by immunofluorescence microscopy, cardiac digest FACS analysis and peripheral blood FACS analysis.

In immunofluorescence staining, Zen software was used to analyse the GFP MFI of classical monocytes ($CD11b^{+}GFP^{mid}$, yellow arrows) and non-classical monocytes ($CD11b^{+}GFP^{hi}$, white arrows) to facilitate their differentiation, as described in section 3.7. This confirmed negative expression of GFP by neutrophils (pink arrows). Cardiac digest FACS and blood FACS analysis of monocyte subpopulations did not rely on GFP expression as heavily and microscopy, as these methods allowed the use of Ly6C expression to confidently define $Ly6C^{hi}$ classical and $Ly6C^{lo}$ non-classical monocytes. The GFP MFI of $Ly6C^{hi}$ non-classical monocytes in both cardiac digest FACS and blood FACS was significantly greater than $Ly6C^{lo}$ classical monocytes in this FACS analysis, though this difference was marginal on the FACS plots. Zen software was used to analyse the GFP MFI of randomly selected monocyte cells in *Cx3cr1*$^{+/GFP}$ and *Cx3cr1*$^{GFP/GFP}$ heart 40x images which showed that non-classical monocytes expressed significantly greater levels of GFP than classical monocytes, within this analysis. n=7 *Cx3cr1*$^{GFP/GFP}$ mice for blood FACS, n=5 *Cx3cr1*$^{GFP/GFP}$ mice for cardiac digest FACS. Data was analysed by One-way Anova. Data refers to mean ± SEM. *p<0.05, **p<0.01, ***p<0.001, ****p<0.0001.

5.2.11 Cardiac Digest Analysis of Infiltrated Monocyte Subpopulations in the Injured Myocardium at 24h Post-Cardiac I/R

Following cardiac digest, total monocyte and monocyte subpopulations were quantified at 24h post-I/R in the infarct region (LV) and remote myocardium (RV) by FACS analysis. Total monocytes were defined as $CD45^{+}CD11b^{+}Ly6G^{-}$ cells, which were then sub-classified into classical $LY6C^{hi}CCR2^{hi}CX3CR1/GFP^{mid}$, and non-classical $LY6C^{lo}CCR2^{lo}CX3CR1/GFP^{hi}$ monocytes. Neutrophil infiltration at 24h post-cardiac I/R was quantified as an internal biological control as performed in immunofluorescence microscopy. As monocyte subset definition using this cardiac digest technique did not rely on GFP expression, *Cx3cr1*$^{+/+}$ mice could also be studied. To investigate the importance of monocyte CX3CR1 expression on the infiltration of these cells into the injured myocardium at 24h post-I/R, heart digest monocyte populations samples were compared between *Cx3cr1*$^{+/+}$, *Cx3cr1*$^{+/GFP}$, and *Cx3cr1*$^{GFP/GFP}$ mice.

Comparison of $CD45^{+}$ cell infiltration between the injured myocardium (LV) and remote region (RV), expressed as events/ml of digest, initially demonstrated that leukocyte infiltration into the myocardium at 24h post-I/R was specific to the infarct region; LV cardiac digest samples in all genotypes had a much higher count of $CD45^{+}$ cells than the respective RV cell suspension, which contained very low numbers of $CD45^{+}$ cells (Figure 5.21, 5.23A). *Cx3cr1*$^{GFP/GFP}$ hearts showed a significantly greater count of leukocytes than that of the *Cx3cr1*$^{+/+}$ group ($p<0.01$), such that the difference between LV and RV samples was only significant in the *Cx3cr1*$^{GFP/GFP}$ group. This observation however is likely due to variation in the number of $CD45^{+}$ cell events acquired during FACS.

Neutrophil infiltration into the injured myocardium (LV) at 24h post-cardiac I/R as a proportion of total leukocytes was 78%, 82%, and 65% in *Cx3cr1*$^{+/+}$, *Cx3cr1*$^{+/GFP}$, and *Cx3cr1*$^{GFP/GFP}$ mice, respectively, and therefore dominated the immune response at this time point as expected (Figure 5.23C). This proportion of neutrophils was not significantly different across genotypes. Total monocytes occupied approximately 15%, 17%, and 19% of the total leukocyte population present in the infarct tissue in

Cx3cr1$^{+/+}$, *Cx3cr1*$^{+/GFP}$, and *Cx3cr1*$^{GFP/GFP}$ mice, respectively, and therefore was not significantly affected by genetic CX3CR1 knockout. The total monocyte composition of total leukocytes was consistently higher in the RV compared to the LV across genotypes. This is assumed to be due to vast neutrophil population specifically in the injured myocardium, which in turn lowered the relative CD45^{+} proportion of monocytes in the LV. Quantification of classical and non-classical monocyte subpopulations in the injured myocardium revealed that Ly6C^{hi} classical monocytes occupied approximately 10% of total leukocytes in *Cx3cr1*$^{+/+}$ mice, 9% in *Cx3cr1*$^{+/GFP}$, and 6% in *Cx3cr1*$^{GFP/GFP}$ hearts. Ly6C^{lo} non-classical monocytes compromised approximately 2% of total leukocytes in *Cx3cr1*$^{+/+}$ mice, 5% in *Cx3cr1*$^{+/GFP}$, and 4% in *Cx3cr1*$^{GFP/GFP}$ mice. This proportion of classical and non-classical monocytes of total leukocytes in the 24h I/R infarct across genotypes was not significantly different for either monocyte subpopulation. As monocytes and macrophages are known to share cell surface markers it can be difficult to distinguish between these two cell populations, however a further analysis of monocyte F4/80 expression at day 3 I/R showed that the majority of all monocytes positively expressed this marker (Figure 5.21), indicating the activation of monocytes and their differentiation into macrophages at 24h post-cardiac I/R.

Neutrophil and monocyte populations were also analysed as a proportion of total myeloid cells (Figure 5.23D). At 24h post-I/R, the infarct myeloid population was comprised of 78.5%, 81.7% and 79.8% neutrophils in *Cx3cr1*$^{+/+}$, *Cx3cr1*$^{+/GFP}$, and *Cx3cr1*$^{GFP/GFP}$ hearts. Neutrophil infiltration at 24h post-I/R therefore was not significantly different across genotypes. Classical monocytes occupied a similar proportion of myeloid cells across genotypes, as 12.5%, 11.7% and 9.2% of total CD11b^{+} cells in *Cx3cr1*$^{+/+}$, *Cx3cr1*$^{+/GFP}$, and *Cx3cr1*$^{GFP/GFP}$ hearts, respectively. Non-classical monocytes were present in lower numbers at 24h post-I/R compared to their classical counterpart, which made up 0.7%, 3.5%, and 2.8% of total infarct myeloid cells in *Cx3cr1*$^{+/+}$, *Cx3cr1*$^{+/GFP}$, and *Cx3cr1*$^{GFP/GFP}$ mice, respectively. Infiltration of classical and non-classical monocytes at 24h post-I/R was not significantly affected by genetic CX3CR1 knockout. This was also observed when classical and non-classical monocytes were analysed as a proportion of the total monocyte population in the injured myocardium (Figure 5.23E).

Analysis of CX3CR1 expression showed that in wild-type mice, 25.3% of leukocytes were CX3CR1^{+}, compared to 27.91% in *Cx3cr1*$^{+/GFP}$ mice (Figure 5.23F). In *Cx3cr1*$^{+/GFP}$ mice, 27.4% of leukocytes expressed GFP, compared to 28% in *Cx3cr1*$^{GFP/GFP}$ hearts (Figure 5.23G). This analysis of CX3CR1/GFP^{+} expression in all genotypes at 24h post-I/R suggested the presence of other CX3CR1/GFP^{+} cells in the infarct in addition to these monocytes subpopulations; total monocytes represented 15% of total leukocytes in wild-type mice, which all expressed CX3CR1, however the percentage of CX3CR1-expressing leukocytes was 25.3%. Similarly, *Cx3cr1*$^{+/GFP}$ hearts had 17% total monocytes and 27.9% CX3CR1^{+} cells of the total leukocyte population, and *Cx3cr1*$^{GFP/GFP}$ hearts showed 19% monocytes and 28% GFP^{+} cells of total leukocytes. The presence of other CX3CR1/GFP^{+} cells in the injure myocardium at 24h post-cardiac I/R may reflect populations of CD8^{+}CCR7^{-} T-cells, which are known to express CX3CR1 and respond to cardiac injury [209].

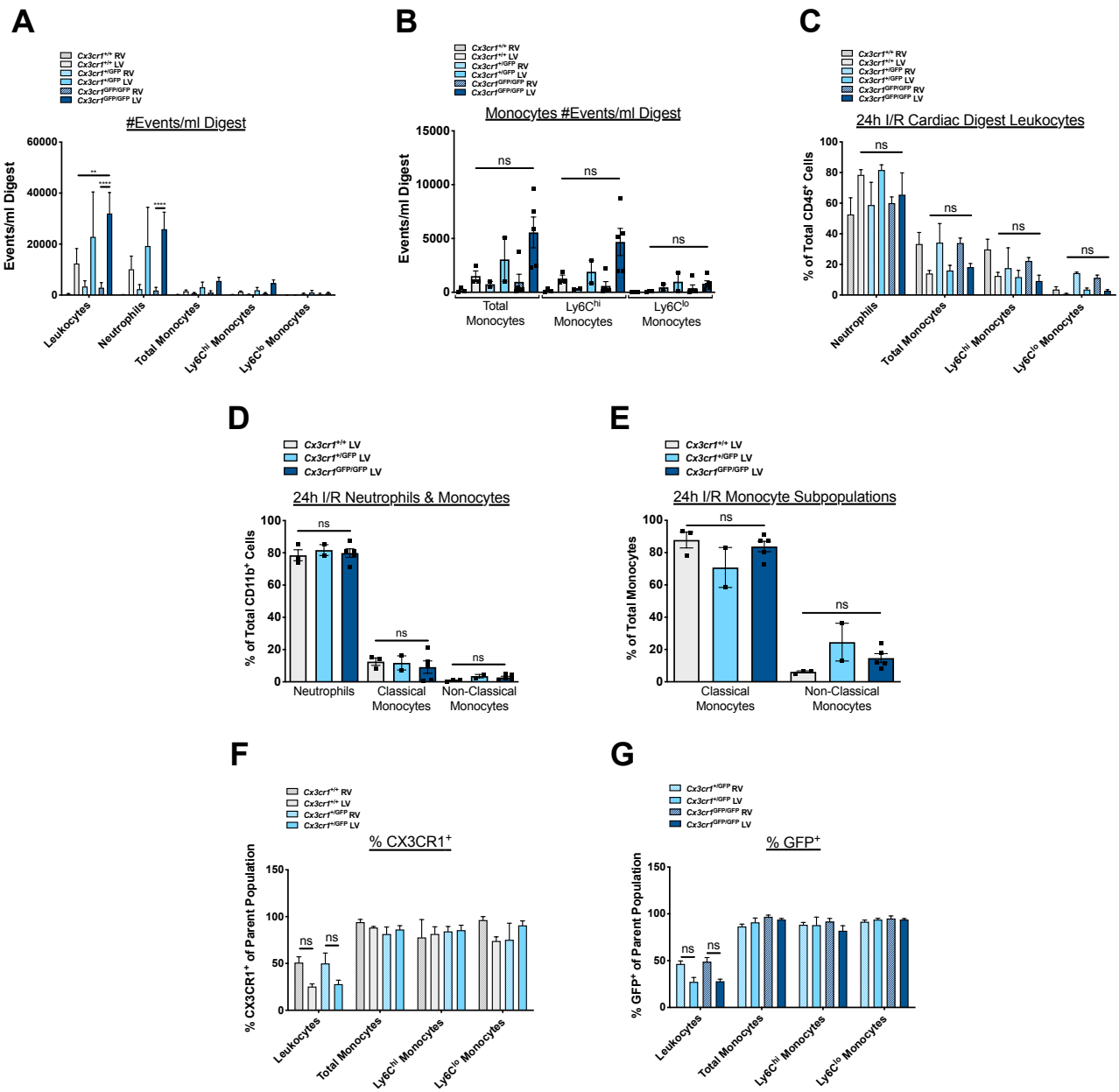
A
Cx3cr1+/+ RV
Cx3cr1+/+ LV
Cx3cr1+/GFP RV
Cx3cr1+/GFP LV
Cx3cr1GFP/GFP RV
Cx3cr1GFP/GFP LV
#Events/ml Digest
Events/ml Digest
60000
40000
20000
0
**
****
****
Leukocytes
Neutrophils
Total Monocytes
Ly6Chi Monocytes
Ly6Clo Monocytes
B
Cx3cr1+/+ RV
Cx3cr1+/+ LV
Cx3cr1+/GFP RV
Cx3cr1+/GFP LV
Cx3cr1GFP/GFP RV
Cx3cr1GFP/GFP LV
Monocytes #Events/ml Digest
Events/ml Digest
15000
10000
5000
0
ns
ns
ns
Total Monocytes
Ly6Chi Monocytes
Ly6Clo Monocytes
C
Cx3cr1+/+ RV
Cx3cr1+/+ LV
Cx3cr1+/GFP RV
Cx3cr1+/GFP LV
Cx3cr1GFP/GFP RV
Cx3cr1GFP/GFP LV
24h I/R Cardiac Digest Leukocytes
% of Total CD45+ Cells
100
80
60
40
20
0
ns
ns
ns
ns
Neutrophils
Total Monocytes
Ly6Chi Monocytes
Ly6Clo Monocytes
D
Cx3cr1+/+ LV
Cx3cr1+/GFP LV
Cx3cr1GFP/GFP LV
24h I/R Neutrophils & Monocytes
% of Total CD11b+ Cells
100
80
60
40
20
0
ns
ns
ns
Neutrophils
Classical Monocytes
Non-Classical Monocytes
E
Cx3cr1+/+ LV
Cx3cr1+/GFP LV
Cx3cr1GFP/GFP LV
24h I/R Monocyte Subpopulations
% of Total Monocytes
100
80
60
40
20
0
ns
ns
Classical Monocytes
Non-Classical Monocytes
F
Cx3cr1+/+ RV
Cx3cr1+/+ LV
Cx3cr1+/GFP RV
Cx3cr1+/GFP LV
% CX3CR1+
% CX3CR1+ of Parent Population
150
100
50
0
ns
ns
Leukocytes
Total Monocytes
Ly6Chi Monocytes
Ly6Clo Monocytes
G
Cx3cr1+/GFP RV
Cx3cr1+/GFP LV
Cx3cr1GFP/GFP RV
Cx3cr1GFP/GFP LV
% GFP+
% GFP+ of Parent Population
150
100
50
0
ns
ns
Leukocytes
Total Monocytes
Ly6Chi Monocytes
Ly6Clo Monocytes

Figure 5. 24. Cardiac Digest analysis monocyte populations at 24h post-cardiac I/R, in the LV and RV in *Cx3cr1*$^{+/+}$, *Cx3cr1*$^{+/GFP}$, *Cx3cr1*$^{GFP/GFP}$ mice.

Total monocytes were defined as $CD45^{+}CD11b^{+}Ly6G^{-}$ cells. Monocytes were then sub-classified as classical [$LY6C^{hi}CCR2^{hi}CX3CR1/GFP^{mid}$] and non-classical [$LY6C^{lo}CCR2^{lo}CX3CR1/GFP^{hi}$] monocytes. A. Leukocytes, total monocytes, classical and non-classical monocyte populations, and neutrophils in the 24h post-cardiac I/R LV region in all genotypes, per ml of digest cell suspension. B. Monocyte subpopulations at 24h post-cardiac I/R expressed as events per ml of digest. C. Total leukocytes, monocyte subpopulations, and neutrophils, expressed as a proportion of total leukocytes across all genotypes. A, B, C. Data was analysed by Two-way Anova with Tukey's multiple comparison test. D. Monocyte subpopulations and neutrophils as a percentage of total myeloid cells, across genotypes. E. Ratio of classical and non-classical monocytes as a proportion of total monocytes across genotypes. D, E. Data was analysed by One-way Anova with Tukey's multiple comparison test. F. Proportion of $CX3CR1^{+}$ cells of parent populations, between LV and RV in *Cx3cr1*$^{+/+}$ and *Cx3cr1*$^{+/GFP}$ mice. G. Proportion of GFP^{+} cells of parent populations, between LV and RV in $CX3CR1^{+/GFP}$ and *Cx3cr1*$^{GFP/GFP}$ mice. Data was analysed by Two-way Anova with Tukey's multiple comparison test. All data refers to mean ± SEM. n=3 *Cx3cr1*$^{+/+}$, n=2 *Cx3cr1*$^{+/GFP}$, n=6 *Cx3cr1*$^{GFP/GFP}$. *p<0.05, **p<0.01, ****p<0.0001.

5.2.12 Comparison of Leukocyte and Monocyte Subpopulations in the Injured Myocardium at 24h Post-Cardiac I/R between Cardiac Digest and Immunofluorescence Microscopy Techniques.

Due to commonality in some of the markers used to study leukocyte and monocyte infiltration into the injured myocardium at 24h I/R between cardiac digest and immunofluorescence microscopy techniques, it was possible to compare analyses between methods. In both approaches, CD45, CD11b and GFP markers were used to define leukocyte and monocyte populations.

A fundamental comparison that was firstly made between these two analyses was leukocyte infiltration at 24h post-I/R into the injured myocardium (LV) compared to the remote area (RV). Since the LV region is the area of tissue that is injured following cardiac I/R, the majority of $CD45^+$ infiltrate was present in the LV area across both techniques. In both cardiac digest and microscopy analysis of leukocyte infiltration, 95% and 92% of total $CD45^+$ cells in *Cx3cr1*$^{+/+}$ hearts were located in the LV respectively (Figure 5.24A), with the remaining 5% and 8% in the remote, non-injured RV (Figure 5.24B). This proportion of LV/RV leukocytes between techniques was not significantly different across *Cx3cr1*$^{+/+}$, *Cx3cr1*$^{+/GFP}$, and *Cx3cr1*$^{GFP/GFP}$ mice (Figure 5.24A, B). This agreement between analyses provides confidence in $CD45^+$ quantification by each technique.

Analysis of myeloid populations in the *Cx3cr1*$^{+/GFP}$ control group across techniques showed that total monocyte and neutrophil infiltration into the injured myocardium (LV) at 24h post-cardiac I/R was also not significantly different between the two approaches (expressed as a % of total $CD11b^+$ myeloid cells) (Figure 5.24C, 5.25A). The LV myeloid population in *Cx3cr1*$^{+/GFP}$ cardiac digest hearts was comprised of 22% monocytes and 78% neutrophils, while *Cx3cr1*$^{+/GFP}$ immunofluorescence microscopy analysis stained for 33% monocytes and 67% neutrophils, expressed as a proportion of total $CD11b^+$ cells. Total monocyte and neutrophil populations in *Cx3cr1*$^{GFP/GFP}$ 24h I/R hearts were also not significantly different between methods; cardiac digest hearts compromised 28% monocytes and 72% neutrophils, while microscopy hearts showed 23% monocytes and 77% neutrophils (Figure 5.24C, Figure 5.25B). These similar

myeloid populations across cardiac digest and microscopy based analyses suggests that $CD11b^+$ cell quantification was accurate in both techniques.

Furthermore, the proportion of GFP^+ cells in *Cx3cr1*$^{+/GFP}$ and *Cx3cr1*$^{GFP/GFP}$ hearts, as a percentage of total $CD11b^+$ myeloid cells, was consistent with the proportions of monocytes and neutrophils (Figure 5.24D). In *Cx3cr1*$^{+/GFP}$ digest hearts, GFP^+ cells represented 23% of $CD11b^+$ cells, which is comparable with the 22% total monocyte proportion of total myeloid cells. In *Cx3cr1*$^{+/GFP}$ microscopy analysed hearts, GFP^+ cells represented 33% of all $CD11b^+$ cells, which was the same as the 33% total monocyte proportion of myeloid cells. This proportion of infarct GFP^+ cells in both genotypes was not significantly different across cardiac digest and microscopy methods, and therefore provides confidence in the method of GFP detection in each approach.

However, variability was noted between methods when analysing specific classical and non-classical monocyte subpopulations. In the 24h post-I/R hearts analysed by cardiac digest and FACS, classical monocytes dominated the total monocyte population. The ratio of classical to non-classical monocytes was approximately 74%:26% in *Cx3cr1*$^{+/GFP}$ hearts and 85%:15% in *Cx3cr1*$^{GFP/GFP}$ hearts (Figure 5.25 A, B). In contrast, the proportion of classical monocytes was lower when cells were analysed using immunofluorescence microscopy and the ratio of classical to non-classical monocytes was 32%:68% in *Cx3cr1*$^{+/GFP}$ hearts and 51%:49% in *Cx3cr1*$^{GFP/GFP}$ hearts.

This discrepancy in classical and non-classical monocyte proportions determined by flow cytometry and immunofluorescence may be attributed to a number of differences between techniques, which are discussed in detail in 5.3.1.

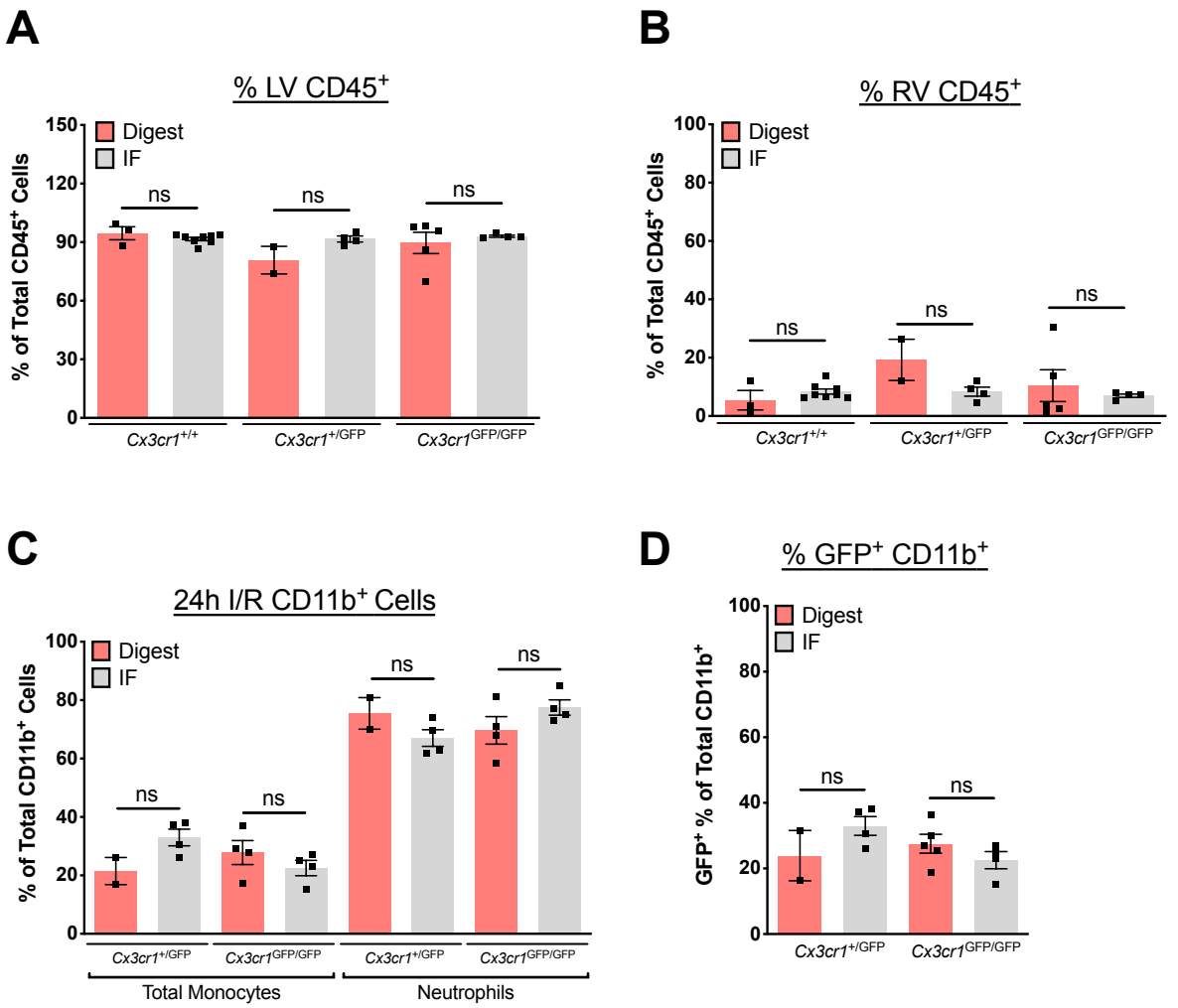

Figure 5. 25. Comparison between 24h post-cardiac I/R leukocyte populations analysed by immunofluorescent staining and cardiac digest techniques.

A. Percentage of 24h post-cardiac I/R total heart leukocytes present in the LV and B. RV, between microscopy and digest techniques. C. Comparison of total LV monocyte and neutrophil populations at 24h post-cardiac I/R between immunofluorescence and cardiac digest techniques, expressed as a proportion of total myeloid cells. D. Percentage GFP^+ cells of total $CD11b^+$ cells in cardiac digest and immunofluorescence staining. Cardiac Digest: n=3 *Cx3cr1*$^{+/+}$, n=2 *Cx3cr1*$^{+/GFP}$, n=5 *Cx3cr1*$^{GFP/GFP}$; Immunofluorescent Staining: n=8 *Cx3cr1*$^{+/+}$, n=4 *Cx3cr1*$^{+/GFP}$, n=4 *Cx3cr1*$^{GFP/GFP}$. Data analysed by One-way Anova with Tukey's multiple comparison test. All data refers to mean ± SEM.

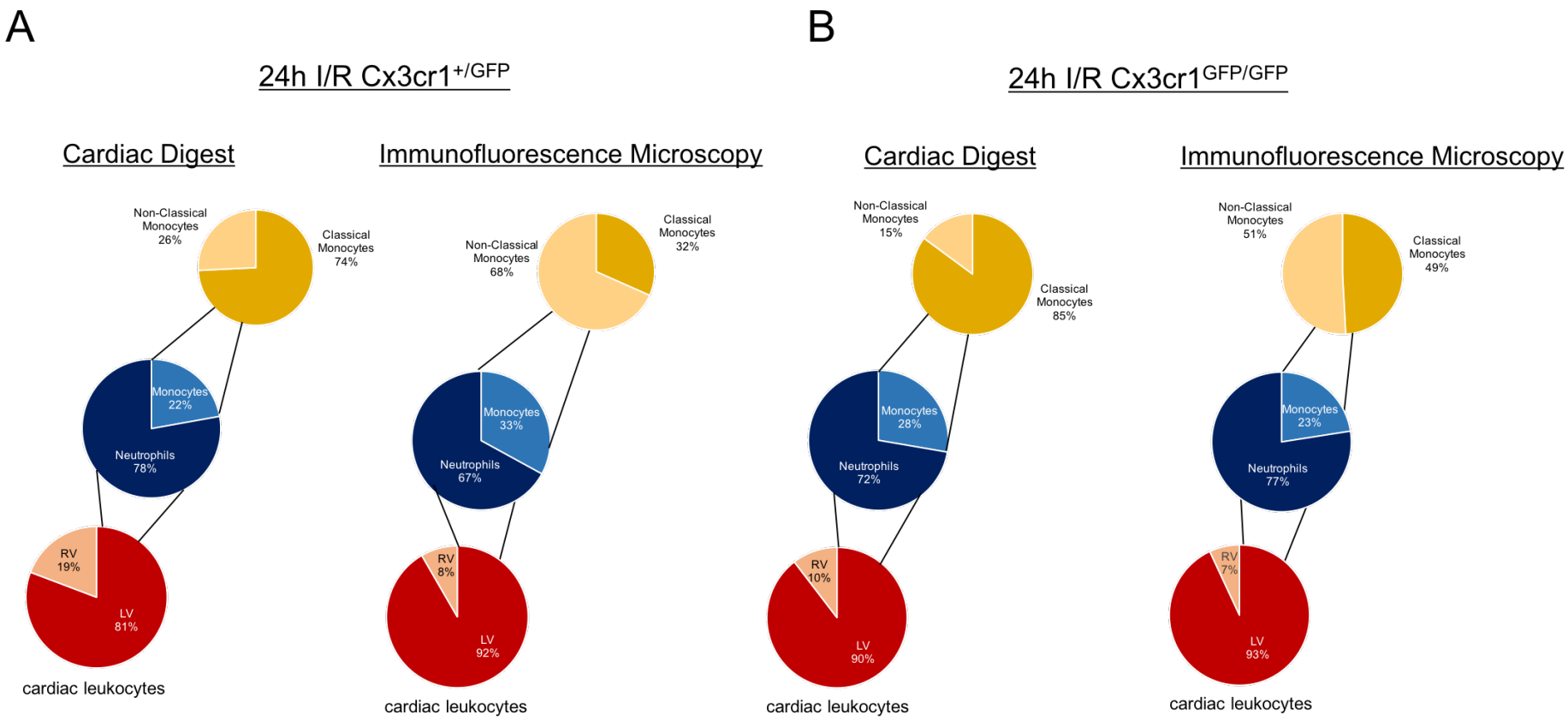

Figure 5. 26. Relative proportions of leukocyte ($CD45^+$), myeloid ($CD11b^+$) and monocyte subpopulations in the injured heart tissue at 24h post-I/R between cardiac digest and immunofluorescent microscopy techniques in *Cx3cr1*$^{+/GFP}$ (A) and *Cx3cr1*$^{GFP/GFP}$ (B) mice.

5.2.13 Analysis of Spleen and Bone Marrow Monocyte Subpopulations at Baseline and 24h Post-Cardiac I/R

The monocyte immune response to cardiac I/R does not solely involve monocyte infiltration from the circulation into the heart tissue, but comprises a complex interplay between numerous compartments of the immune system, including the spleen and bone marrow [316, 343]. These tissues both host significant monocyte populations during baseline conditions, and respond appropriately to the demands of cardiac I/R repair through the release of these cells into the circulation. It was therefore important as part of this study to determine the changes in monocyte subpopulations in both mouse spleen and bone marrow at 24h post-cardiac I/R in addition to the peripheral circulation and injured myocardial tissue.

To address this, spleen and bone marrow tissues from the same animals that were used for 24h post-I/R cardiac digest analyses were isolated, prepared as a suspension of single viable cells, and analysed by flow cytometry for monocyte subset quantification. This was compared with baseline mouse spleen and bone marrow monocyte populations. The effect of genetic CX3CR1 ablation on splenic and bone marrow monocyte subpopulations at baseline and 24h post-I/R was evaluated by comparing *Cx3cr1*$^{+/GFP}$ and *Cx3cr1*$^{GFP/GFP}$ mice.

5.2.14 Splenic Classical and Non-Classical Monocyte Subpopulations at 24h Post-Cardiac I/R

Mouse splenic monocytes were defined as $CD4^{-}CD8^{-}CD19^{-}CD11c^{-/lo}NK1.1^{-}Ly6G^{-}$ cells. This gating strategy ensured exclusion of splenic T-cells (CD4, CD8), B-cells (CD19), dendritic cells (CD11c), NK-cells (NK1.1), and neutrophils (Ly6G). Monocyte subpopulations were then classified as either $Ly6C^{hi}$ classical or $Ly6C^{lo}$ non-classical monocytes (Figure 5.26). This gating strategy was developed based on the recommended markers for defining mouse spleen monocyte subpopulations [344].

At baseline, splenic total monocytes represented up to ~1.6% of total splenocytes in *Cx3cr1*$^{+/GFP}$ mice and ~2% of total splenocytes in *Cx3cr1*$^{GFP/GFP}$ mice, and was not

significantly different between genotypes (Figure 5.27A). This proportion of total monocytes was in the expected baseline range of <5% of all splenocytes [345]. When comparing the total splenic monocyte population at baseline between *Cx3cr1*$^{+/GFP}$ and *Cx3cr1*$^{GFP/GFP}$ mice as a proportion of splenic myeloid cells, there was also no significant difference (Figure 5.27B). At 24h post-I/R, the proportion of total monocytes of myeloid cells in each genotype did not significantly change from that at baseline.

Classical monocyte subpopulations in spleens of *Cx3cr1*$^{+/GFP}$ mice at 24h post-I/R were similar to baseline levels, whether expressed as a proportion of total splenocytes (Figure 5.27C), myeloid cells (Figure 5.27D), or total monocytes (Figure 5.27E). In contrast to this, *Cx3cr1*$^{GFP/GFP}$ mice suggested there was an increase in the proportion of classical monocytes at 24h post-I/R compared to baseline (Figure 5.27E). This increase was synchronous with a decrease in the proportion of splenic non-classical monocytes at 24h post-I/R (Figure 5.27H). Non-classical monocytes in *Cx3cr1*$^{+/GFP}$ spleens however showed no significant change from baseline to 24h post-I/R (Figure 5.27 F, G, H).

The difference in the frequency of monocyte subpopulations between baseline and 24h I/R in *Cx3cr1*$^{GFP/GFP}$ mice are suggestive of two possible scenarios following cardiac I/R; i) genetic CX3CR1 knockout leads to increased efflux of non-classical monocytes from the spleen into the circulation at 24h following cardiac I/R, or ii) genetic CX3CR1 knockout leads to an increased influx of classical monocytes into the spleen.

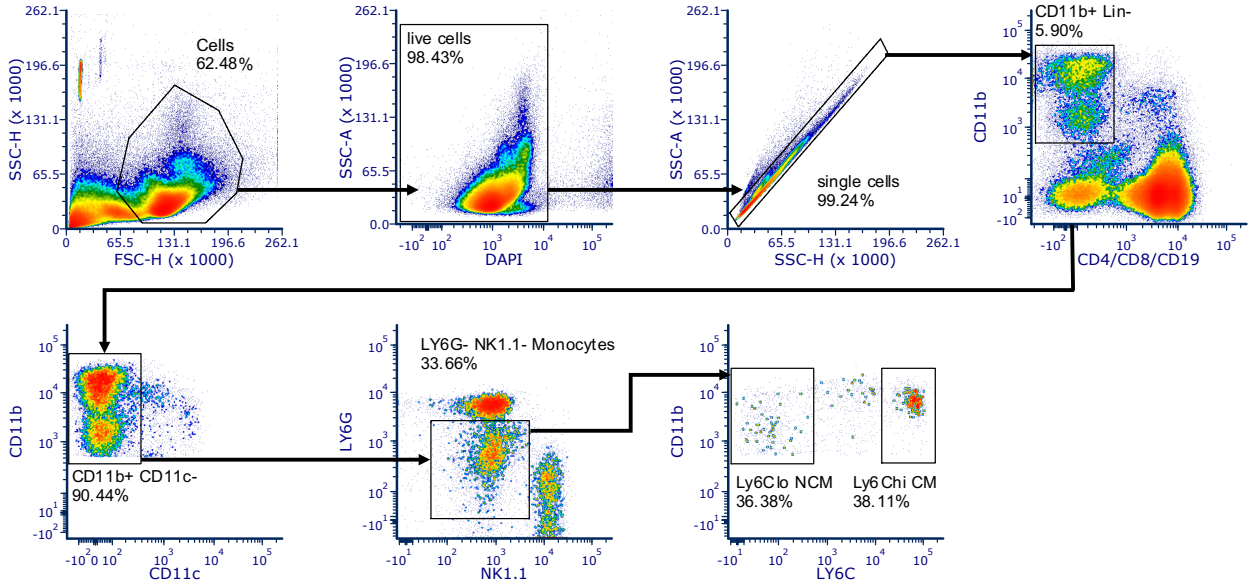

Figure 5. 27. Flow Cytometric gating of murine spleen classical and non-classical monocyte subpopulations in *Cx3cr1*$^{+/GFP}$ and *Cx3cr1*$^{GFP/GFP}$ mice. Total splenic monocytes were defined as CD4^{-}CD8^{-}CD19^{-}CD11c^{-}NK1.1^{-}Ly6G^{-} cells. This panel of markers permitted exclusion of T-cells, B-cells, dendritic cells, NK-cells, and neutrophils from the splenic monocyte population. Total monocytes were then defined as either classical (Ly6C^{hi}) or non-classical (Ly6C^{lo}) monocytes.

Splenic Monocytes 24h-post Cardiac I/R

Total Monocytes

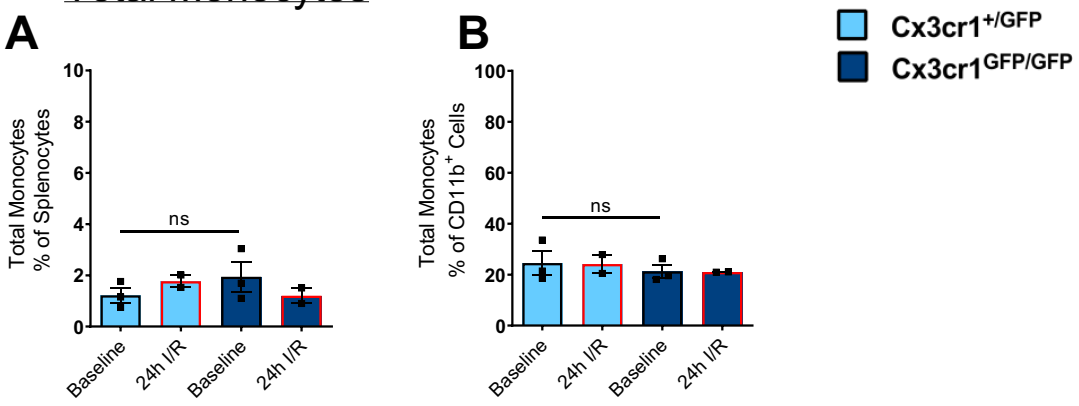

Classical Monocytes

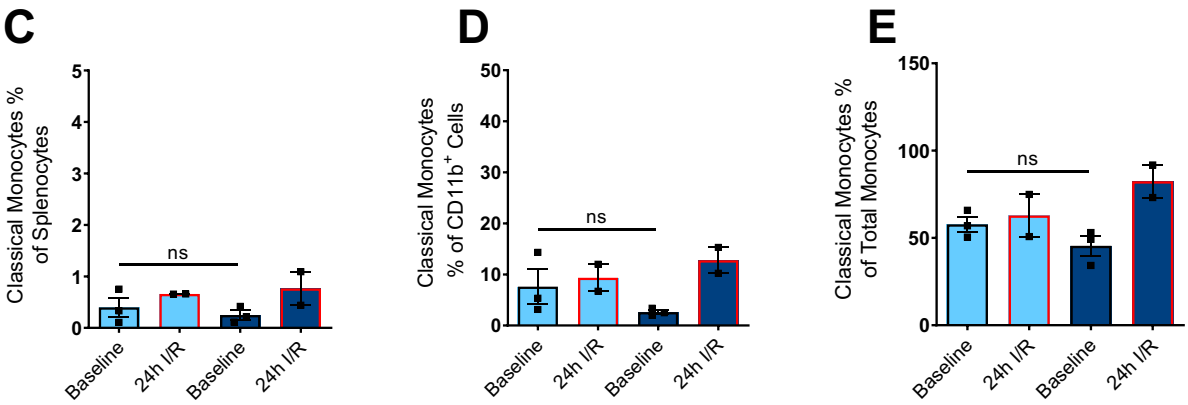

Non-Classical Monocytes

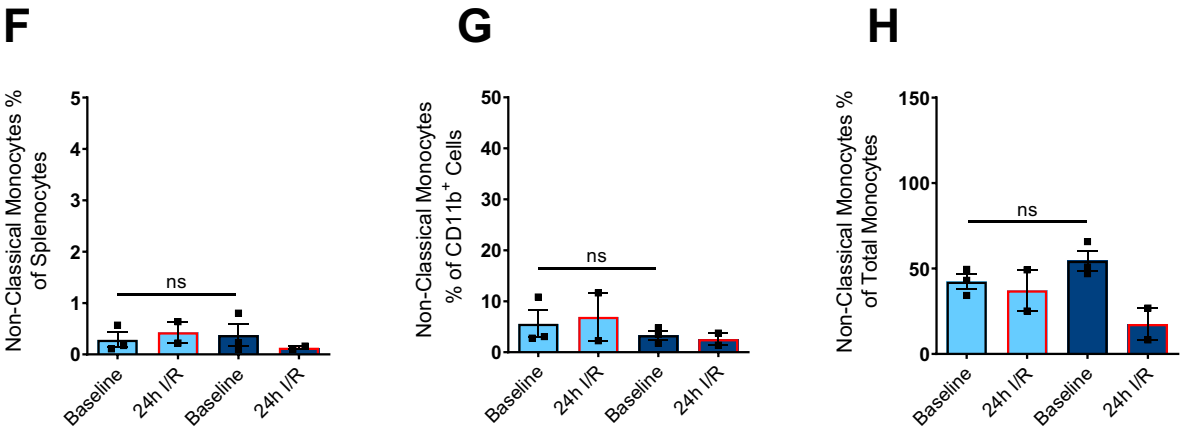

Figure 5. 28. Splenic populations of classical and non-classical monocytes at baseline and 24h post-cardiac I/R in *Cx3cr1*$^{+/GFP}$ and *Cx3cr1*$^{GFP/GFP}$ mice.

Total monocytes (A, B), classical monocytes (C-E) and non-classical monocytes (F-H) were quantified and expressed either a percentage of total splenocytes, myeloid cells, or total monocytes. Data analysed by Two-way Anova with Tukey's multiple comparison test. All data refers to mean ± SEM. n=3/genotype at baseline; n=2/genotype at 24h I/R.

5.2.15 Bone Marrow Classical and Non-Classical Monocyte Populations at Baseline and 24h Post-Cardiac I/R

Monocyte subpopulations in the bone marrow were analysed at baseline and at 24h post-cardiac I/R in *Cx3cr1*$^{+/GFP}$ and *Cx3cr1*$^{GFP/GFP}$ mice. Bone marrow myeloid cells were defined by flow cytometric analysis as CD45^{+}CD11b^{+} cells (Figure 5.28). Neutrophils were excluded on the basis of high SSC and intermediate expression of Ly6C [340]. Total monocytes were then sub-classified as classical Ly6C^{hi} CCR2^{hi} CX3CR1/GFP^{mid-hi}, and non-classical Ly6C^{lo} CCR2^{low} CX3CR1/GFP^{hi} monocytes.

In baseline *Cx3cr1*$^{+/GFP}$ mice, the total monocyte population occupied ~10% of all bone marrow leukocytes and ~20% of all bone marrow myeloid cells, which did not significantly differ at 24h I/R, or in *Cx3cr1*$^{GFP/GFP}$ mice (Figure 5.29A, B). Analysis of monocyte subpopulations showed that baseline classical monocytes represented approximately 5% of bone marrow leukocytes (Figure 5.29C), 15% of bone marrow myeloid cells (Figure 5.29D), and 75% of total bone marrow monocytes (Figure 5.29E), which was not significantly different in *Cx3cr1*$^{GFP/GFP}$ mice or at 24h post-I/R. Non-classical monocytes in the bone marrow at baseline represented approximately 2% of total bone marrow leukocytes (Figure 5.29F), 4% of myeloid cells (Figure 5.29G), and 20% of total bone marrow monocytes (Figure 5.29H), across both genotypes, and did not significantly differ at 24h post-I/R. Genetic knockout of CX3CR1 therefore did not appear to affect monocyte populations in the bone marrow at baseline or at 24h post-I/R, though this data was limited by the low group sizes.

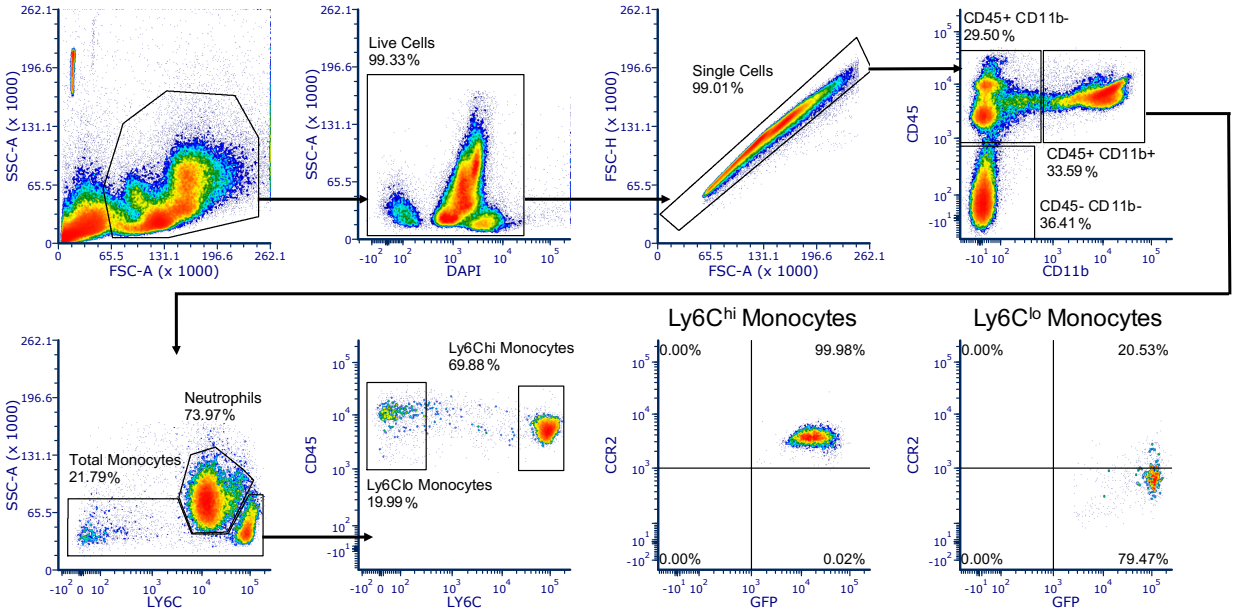

Figure 5. 29. Flow cytometric gating of mouse bone marrow classical and non-classical monocyte subpopulations.

Total monocytes were defined as $CD45^{+}CD11b^{+}Ly6G^{-}SSC^{lo}$ cells. Neutrophils were distinguished from monocytes as SSC^{hi} and $Ly6C^{inter}$. Monocytes were then sub-classified as either classical [$Ly6C^{hi}CCR2^{hi}CX3CR1/GFP^{mid\text{-}hi}$] or non-classical [$Ly6C^{lo}CCR2^{mid}CX3CR1/GFP^{hi}$ monocytes].

Bone Marrow Monocytes 24h-post Cardiac I/R

Total Monocytes

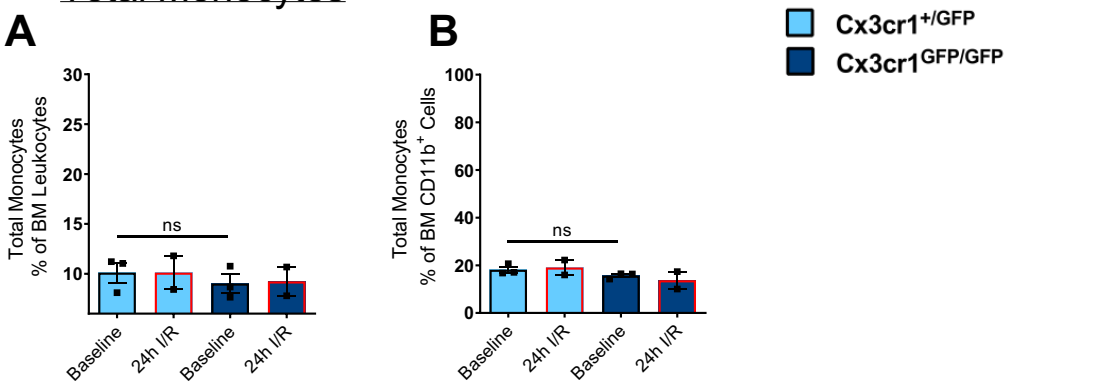

Classical Monocytes

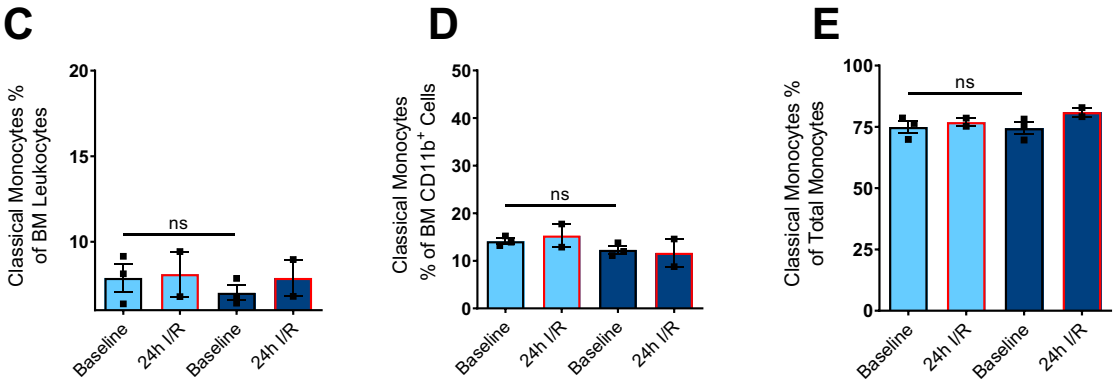

Non-Classical Monocytes

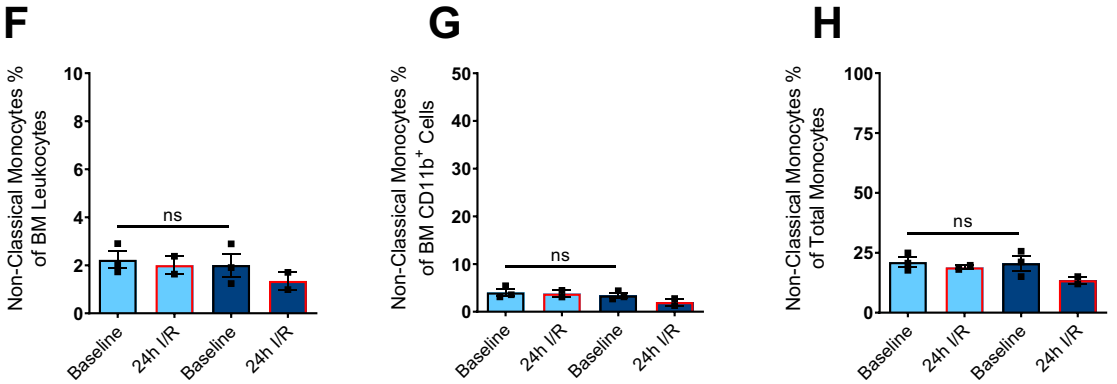

Figure 5. 30. Bone marrow populations of classical and non-classical monocytes at baseline and 24h post-cardiac I/R in *Cx3cr1*$^{+/GFP}$ and *Cx3cr1*$^{GFP/GFP}$ mice.

Bone marrow total monocytes (A, B), classical monocytes (C-E) and non-classical monocytes (F-H) were quantified and expressed either a percentage of total splenocytes, myeloid cells, or total monocytes. Data analysed by Two-way Anova with Tukey's multiple comparison test. All data refers to mean ± SEM. n=3/genotype at baseline; n=2/genotype at 24h I/R.

5.2.16 Analysis of Mouse Cardiac Function at 6 Weeks Post-Myocardial I/R by Cardiac MRI

In addition to investigating the relative monocyte phenotype following myocardial I/R, this study also evaluated the effect of genetic CX3CR1 knockout on cardiac function after cardiac I/R, in *Cx3cr1*$^{+/+}$, *Cx3cr1*$^{+/GFP}$ and *Cx3cr1*$^{GFP/GFP}$ mice. To achieve this, mice underwent cardiac MRI at 6 weeks post cardiac I/R. Mouse myocardial function was assessed by quantifying End Systolic (ESV) and End Diastolic Volumes (EDV), as basic parameters for measuring left ventricular function. LVEF was calculated from these values ((EDV-ESV/EDV) *100), and expressed as a percentage. This data was collected and analysed by Dr. Rachael Redgrave.

Analysis of cardiac function parameters at 6 weeks following myocardial I/R in *Cx3cr1*$^{+/+}$, *Cx3cr1*$^{+/GFP}$ and *Cx3cr1*$^{GFP/GFP}$ mice revealed that genetic knockout of CX3CR1 does not significantly impair myocardial function at this time point following cardiac I/R - ESV and EDV were not significantly different between genotypes. Despite this, there was a noticeable trend towards both increased ESV and EDV in CX3CR1-deficient mice; ESV increased incrementally from *Cx3cr1*$^{+/+}$ (30.1μl), to *Cx3cr1*$^{+/GFP}$ (40.2μl), and *Cx3cr1*$^{GFP/GFP}$ (45.7μl) mice (Figure 5.30A). Similarly, EDV volume increased with the extent of CX3CR1 depletion, whereby *Cx3cr1*$^{+/+}$, *Cx3cr1*$^{+/GFP}$ and *Cx3cr1*$^{GFP/GFP}$ hearts had a EDV of 71.9μl, 77.9μl, and 83.7μl, respectively (Figure 5.30B). Since ejection fraction is calculated based on these ventricular volumes, there was also a trend towards decreased myocardial function as determined by lower ejection fraction, with a greater expression of CX3CR1; *Cx3cr1*$^{+/+}$ had a LVEF of 58.4%, *Cx3cr1*$^{+/GFP}$ of 49.1%, and *Cx3cr1*$^{GFP/GFP}$ of 46.7% (Figure 5.30C). Mean ESV and EDV were greater in C57BL/6 hearts (37.5μl, 85.2μl) compared to the *Cx3cr1*$^{+/+}$ group, (30.1μl, 71.9μl), though these differences were not significant (Figure 5.30A, B).

Such findings suggest that genetic ablation of CX3CR1 does not have a significant effect on cardiac function at six weeks following cardiac I/R. The presence of a slight trend however suggests that a higher number of animals per group may increase statistical power to reveal a significant difference. Furthermore, the absence of an

effect on CX3CR1 deficiency on cardiac function specifically at six weeks post-I/R does not rule out the presence of a phenotype at other time points following I/R.

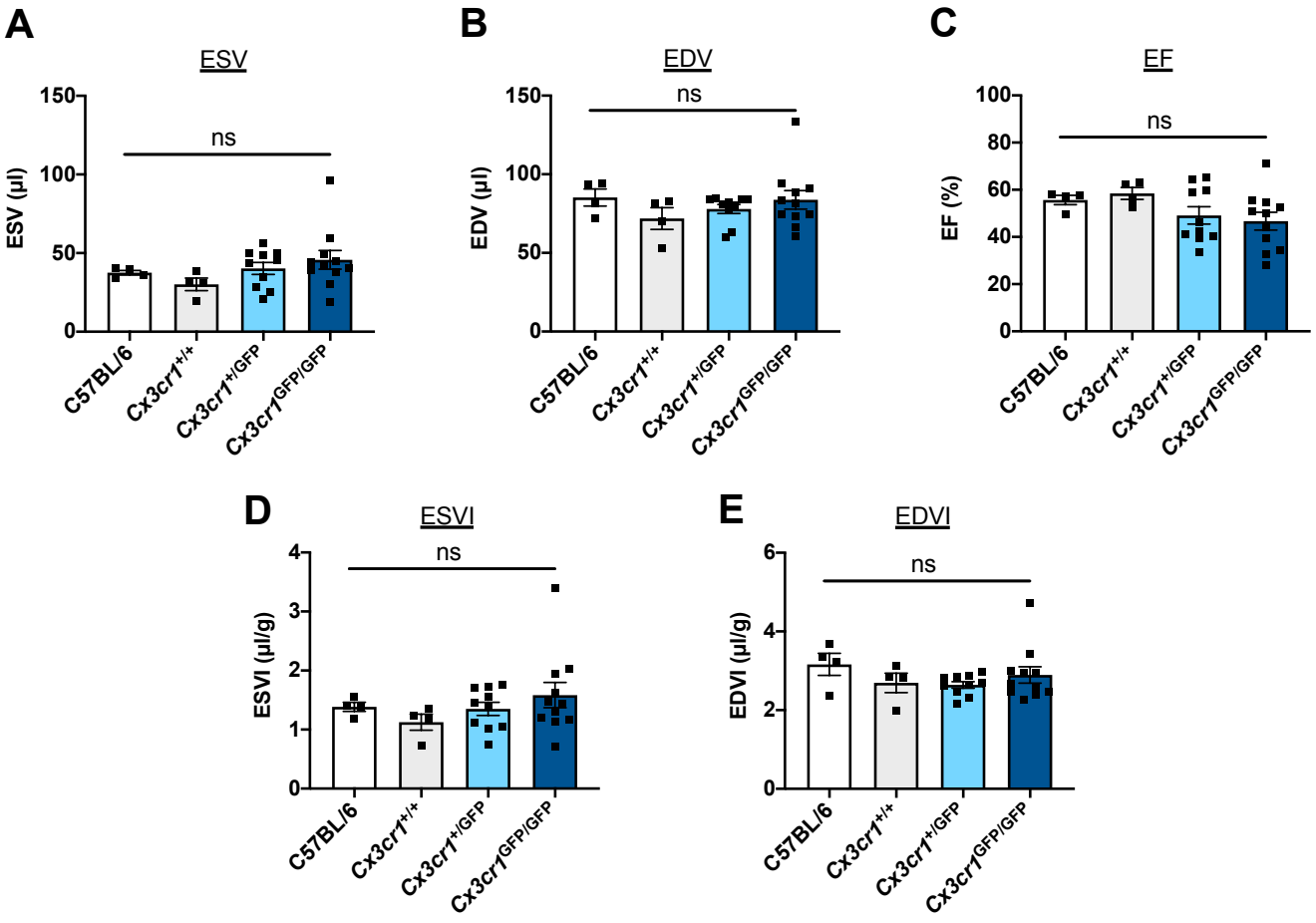

Figure 5. 31. Cardiac MRI assessment of cardiac function at 6 weeks post cardiac I/R in C57BL/6, *Cx3cr1*$^{+/+}$, *Cx3cr1*$^{+/GFP}$, and *Cx3cr1*$^{GFP/GFP}$ mice.

Cardiac function was determined by A. End Systolic Volume (ESV), B. End Diastolic Volume (EDV), and C. Ejection Fraction (EF). D. End Systolic Volume Index (ESVI). E. End Diastolic Volume Index (EDVI). Data was analysed by One-way Anova with Tukey's test for multiple comparisons. All data refers to mean ± SEM. n=4 C57BL/6, n=4 *Cx3cr1*$^{+/+}$, n=10 *Cx3cr1*$^{+/GFP}$, n=11 *Cx3cr1*$^{GFP/GFP}$.

5.2.17 PD-L1 Expression Distinguishes Mouse Blood Ly6C^{lo} Non-Classical Monocytes from Ly6C^{hi} Classical Monocytes

The study of non-classical monocytes throughout this chapter is limited by the lack of an exclusive marker for defining this monocyte subpopulation. While several mouse leukocytes have a clearly defined cell marker for their accurate identification (CD3^{+} T-cells, CD19^{+} B-cells, etc.), the delineation of mouse monocyte subpopulations requires a comprehensive panel of markers. In particular, immunofluorescence quantification of monocyte subsets in the injured myocardium described here relies on the myeloid cell marker CD11b and GFP, with the latter only available when using the CX3CR1-GFP mice. CD11b^{+} neutrophils are GFP^{-} based on their known negative expression of CX3CR1, which was confirmed in this study (section 5.2.1). Immunofluorescent microscopy definition of classical [CD11b^{+} GFP^{mid}] and non-classical [CD11b^{+} GFP^{hi}] monocyte subsets relied on a subjective threshold of GFP expression/intensity. As previously discussed, there is potential for quantitative overlap between monocyte subsets due to this subjective method of quantification. FACS analysis of cardiac digest monocyte populations allowed a more comprehensive panel of markers for the detection of monocyte subsets and therefore more accurately distinguished classical monocytes from non-classical monocytes based on Ly6C expression. When comparing CX3CR1 expression using FACS, this marker did not significantly facilitate the discrimination of classical and non-classical monocytes. A more robust method for studying non-classical monocytes would therefore be greatly beneficial. A recent study by Bianchini et al [346] reported PD-L1 as a promising exclusive marker of mouse non-classical monocytes in the blood and bone marrow compartments. In a pilot study, I therefore investigated the expression of PD-L1 by mouse monocyte subpopulations in the blood, spleen, and bone marrow.

Circulating classical and non-classical monocytes were defined in C57BL/6 mice as previously described with the additional marker of PD-L1 incorporated into the antibody panel; classical monocytes [CD11b^{+}CD115^{+}LY6G^{-}LY6C^{hi}CCR2^{hi} CX3CR1^{mid-hi}], and non-classical monocytes [CD11b^{+}CD115^{+}LY6G^{-}LY6C^{hi}CCR2^{mid} CX3CR1^{hi}]. In the peripheral blood, mouse circulating non-classical monocytes expressed ~2-fold higher levels of PD-L1 than their classical monocyte counterpart

($p<0.0001$) (Figure 5.31A). Importantly, PD-L1 expression was found to be more accurate at quantifying the non-classical monocyte population than CX3CR1 expression, when analysed as a proportion of total leukocytes (Figure 5.31D), or total $CD115^+$ cells (Figure 5.31E). Titration of the PD-L1 antibody in mouse blood was carried out to ensure correct interpretation of relative PD-L1 expression between monocyte subpopulations (Figure 5.30B).

In the spleen, both classical and non-classical monocytes expressed lower levels of PD-L1 than circulating monocytes, with no significant difference in expression between monocyte subpopulations (Figure 5.31A). Monocytes in the bone marrow are known to be primarily classical monocytes (95-100%), with only 1-5% of total monocytes being non-classical monocytes, as conversion from classical $Ly6C^{hi}$ to non-classical $Ly6C^{lo}$ monocytes predominantly occurs in the circulation following their egress from the bone marrow [347]. As a result of this, the non-classical monocyte population quantified in the bone marrow was minimal and therefore PD-L1 expression could not be reliably measured. Classical monocytes however were abundant in number and were found to express high levels of PD-L1, similar to those levels expressed by circulating non-classical monocytes (Figure 5.31A). This is particularly interesting as it may be the case that circulating $Ly6C^{lo}$ non-classical monocytes in the blood express high levels of PD-L1 as they originate from bone marrow $Ly6C^{hi}$ classical monocytes which express high levels of PD-L1.

In humans, to my knowledge there are no published studies investigating the expression of PD-L1 by human circulating monocyte subsets. This may be due to the lack of requirement for an exclusive non-classical marker since CD14, CD16, and CX3CR1 adequately define the three populations of monocytes in humans. In this study, I therefore investigated whether PD-L1 expression was higher on human circulating non-classical monocytes than classical monocytes as observed in the mouse. This analysis showed that while CX3CR1 expression was significantly greater in non-classical and intermediate monocytes compared to classical monocytes ($p<0.001$, $p<0.01$), PD-L1 expression did not significantly differ between monocyte subpopulations (Figure 5.31F).

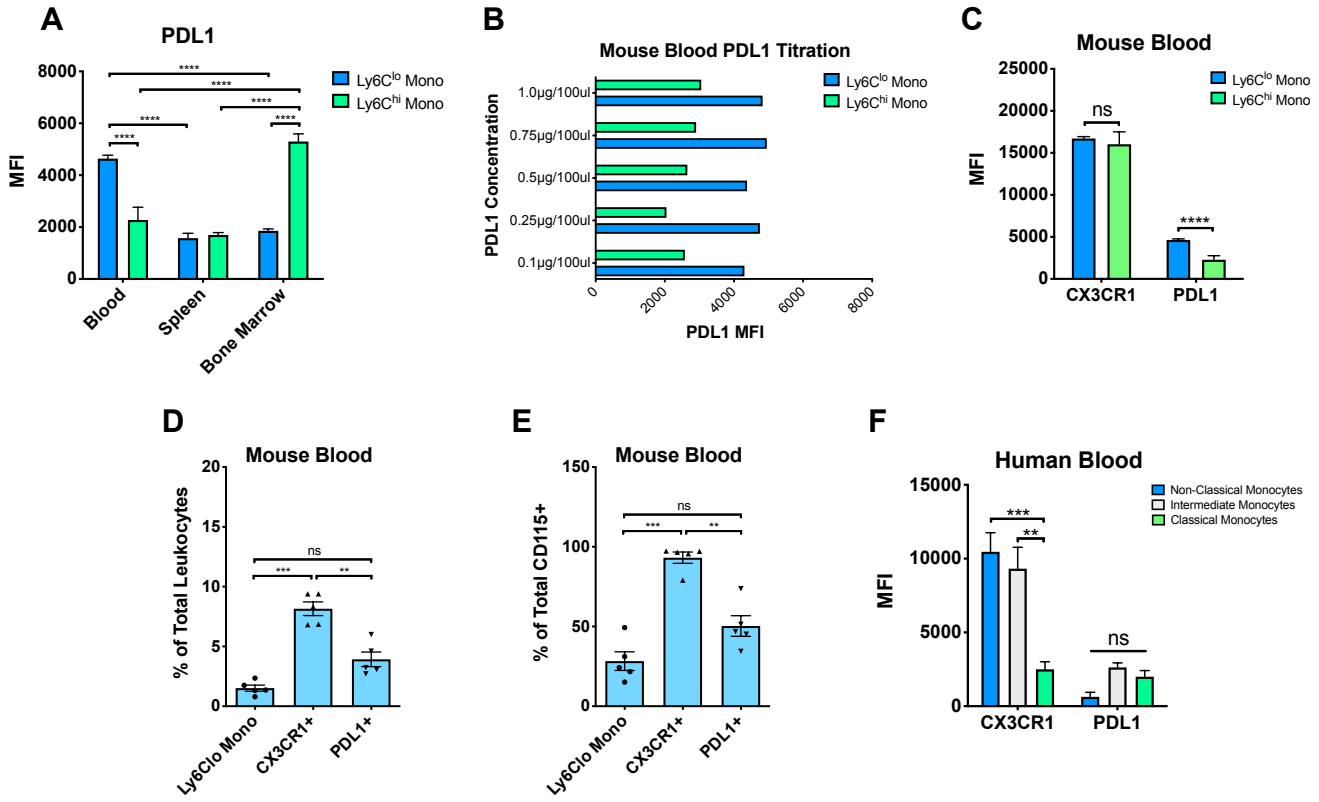

Figure 5. 32. Analysis of PD-L1 expression by monocyte subpopulations in mouse blood, spleen, bone marrow, and human peripheral blood.

A. Mouse PD-L1 expression by Ly6C^{lo} and Ly6C^{hi} monocytes in the blood, spleen and bone marrow of C57BL/6 mice. n=5/blood, n=3 spleen/BM. B. Titration of PD-L1 Antibody on Mouse Blood Monocytes. C. Expression of CX3CR1 compared with PD-L1 to distinguish Ly6C^{lo} and Ly6C^{hi} monocyte populations in mouse blood. A, C. Data analysed by Two-way Anova with Tukey's multiple comparison test. D. Percentage of CX3CR1^{+} and PD-L1^{+} leukocytes compared with the percentage of Ly6C^{lo} non-classical monocytes (n=5). E. Percentage of CX3CR1^{+} and PD-L1^{+} CD115^{+} monocytes compared with the percentage of Ly6C^{lo} non-classical Monocytes (n=5). D, E. One-way Anova with Tukey's multiple comparison test. F. Expression of CX3CR1 compared with PD-L1 to distinguish non-classical, intermediate, and classical monocyte populations in human control blood (n=3 human volunteer blood samples). Two-way Anova with Tukey's multiple comparison test. All data refers to mean ± SEM. **p<0.01, ***p<0.001, ****p<0.0001.

5.3. Discussion

The results from this chapter provide an overview of mouse monocyte subpopulations in the circulation, heart tissue, spleen, and bone marrow, during the acute 24 hours following cardiac I/R, and the effect of genetic CX3CR1 knockout. A summary of monocyte subpopulation changes per tissue investigated in this study is described in Table 5.1.

5.3.1 Circulating Mouse Monocyte Subpopulation Dynamics at 2h and 24h Following Cardiac I/R and the Impact of Genetic CX3CR1 Knockout

The first aim of this work was to analyse mouse circulating monocyte subpopulations at baseline, 2h, and 24h following cardiac I/R, to identify a depletion of mouse non-classical monocytes that was observed in STEMI patients at 90 minutes following PCI. Unlike in humans, the use of mouse models permits investigation into the effect of CX3CR1 knockout on these circulating non-classical monocyte dynamics, by using the *Cx3cr1*^{EGFP} mouse line. *Cx3cr1*$^{GFP/GFP}$ mice showed significantly lower counts of peripheral blood non-classical monocytes than *Cx3cr1*$^{+/+}$ (*p<0.05) and *Cx3cr1*$^{+/GFP}$ mice (*<0.05), while classical and intermediate subpopulations were unaffected. These results are in agreement with those published by Landsman et al [218], who explain that the reduction in circulating non-classical monocytes is due to impaired survival signals in the absence of CX3CR1 expression. Auffray et al also showed that deletion of CX3CR1 reduces the patrolling of non-classical monocytes, which results in overall fewer circulating counts of these cells [150]. Furthermore, Poupel et al demonstrated that pharmacological inhibition of CX3CR1 reduces blood monocyte counts, but does not affect the frequency nor numbers of monocytes in the bone marrow or spleen, and therefore concluded that CX3CR1 antagonism may only act on circulating monocytes [348].

Analysis of post-cardiac I/R monocyte subpopulations in *Cx3cr1*$^{+/+}$ mouse peripheral blood showed that non-classical monocyte counts fell in the circulation at 2h, and therefore mirrored the depletion of STEMI patient non-classical monocytes at 90min post-PCI. When analysing the impact of CX3CR1 depletion, this acute post-

reperfusion depletion of mouse non-classical monocytes at 2h was found to be significantly stronger in *Cx3cr1*$^{GFP/GFP}$ mice compared to *Cx3cr1*$^{+/+}$ mice (*p<0.05). Classical and intermediate monocyte subpopulations also decreased in the circulation at 2h post cardiac-I/R, however the effect of CX3CR1 knockout on the extent of pre-2h depletion was specific to non-classical monocytes. The similarity among mouse monocyte subpopulation dynamics from pre-2h post-I/R may be attributed to their similar expression of CX3CR1; in STEMI patients, there was a greater drop in cells with increased CX3CR1 expression, whereby non-classical monocytes (CX3CR1^{hi}) counts fell incrementally more than intermediate (CX3CR1^{mid}) and classical (CX3CR1^{lo}) monocytes from pre-reperfusion to 90 minutes post-PCI.

The stronger depletion of non-classical monocytes in *Cx3cr1*$^{GFP/GFP}$ peripheral blood compared to that of *Cx3cr1*$^{+/+}$ mice at 2h post-I/R may indicate an increased recruitment of these cells from the peripheral circulation to the injured myocardium in CX3CR1-deficient mice. A possible explanation for this is that circulating non-classical monocytes in *Cx3cr1*$^{+/+}$ mice can firmly adhere to the vascular endothelium via interactions between monocyte-expressed CX3CR1 and endothelial membrane-bound CX3CL1, and as a result may not leave the peripheral circulation as readily. The absence of CX3CR1 expression in *Cx3cr1*$^{+/GFP}$ and *Cx3cr1*$^{GFP/GFP}$ mice hinders this interaction, allowing monocytes to flow more readily through the circulation to the site of injury, leading to their depletion. The greater depletion of non-classical monocytes in *Cx3cr1*$^{-/-}$ mice may also be a reflection of compromised cell survival in the absence of CX3CR1 expression, as previously mentioned.

At 24h post-cardiac I/R, all monocyte subpopulations were replenished in the circulation, which is likely to reflect the release of these cells from the spleen as known to occur following MI [316, 349]. This is also supported by the decrease in the percentage of splenic non-classical monocytes at 24h I/R described in section 5.2.11. Such monocyte subpopulation dynamics at 24h post-I/R were constant across *Cx3cr1*$^{+/+}$, *Cx3cr1*$^{+/GFP}$, and *Cx3cr1*$^{GFP/GFP}$ mice, suggesting that genetic depletion of CX3CR1 does not significantly impair the release of monocytes from other immune cell reservoirs (spleen, bone marrow) following cardiac I/R.

The dynamic profile of circulating monocyte subpopulations following myocardial I/R is not widely documented in mouse models to date, as many studies focus on monocyte infiltration into the heart tissue itself. Monocyte subpopulation dynamics were however reported in a rat model of cardiac I/R at day 1, 3, 5, 7 and 14 post-I/R, [350].

Finally, it is important to address the validity of this data with consideration to the methodological limitations of the techniques used. For ethical reasons, there is a limitation on the volume of mouse tail vein blood that may be obtained for analysis. Within this protocol, blood samples were limited to a small volume of 50μl, which arguably may not be large enough to yield a representative analysis of cell populations in the peripheral blood. Theoretically there should be minimal variation in monocyte subpopulation counts within genotype groups, since these animals are littermates. There was however more variation than expected between subjects, which may be a result of the blood volumes analysed, or mouse health status.

5.3.2 Mouse Monocyte Subpopulations in the Injured Myocardium at 2h, 24h and Day 3 Following Cardiac I/R and the Impact of Genetic CX3CR1 Knockout

The recruitment of monocyte subpopulations into the injured myocardium at 2h and 24h post-cardiac I/R and the effect of genetic CX3CR1 knockout was then assessed by immunofluorescent staining of mouse heart tissue. Leukocyte recruitment dramatically increased at 24h post-I/R compared to control hearts ($p<0.0001$). *Cx3cr1*$^{GFP/GFP}$ hearts showed significantly reduced counts of leukocytes compared to *Cx3cr1*$^{+/+}$ ($p<0.01$) and *Cx3cr1*$^{+/GFP}$ ($p<0.05$) mice at 2h, which subsequently recovered at 24h, indicating a delayed immune response to cardiac I/R in CX3CR1 knockout mice. The recovery in leukocytes at 24h in *Cx3cr1*$^{GFP/GFP}$ hearts suggested that absence of CX3CR1 expression may be compensated for by another biological mechanism to overcome the delayed response at 2h.

The same analysis was performed for monocyte subpopulations in which *Cx3cr1*$^{+/GFP}$ hearts were used as the control group due to the requirement for GFP expression to define monocyte subpopulations (classical CD11b^{+}GFP^{mid}, non-classical

$CD11b^{+}GFP^{hi}$). Monocyte subpopulation infiltration into the injured myocardium was minimal at 2h post-I/R regardless of genotype. Classical and non-classical monocytes then increased in the injured myocardium at 24h post I/R. Classical monocyte recruitment was not significantly affected by genetic CX3CR1 knockout, however non-classical monocyte counts were significantly reduced in *Cx3cr1*$^{GFP/GFP}$ compared to *Cx3cr1*$^{+/GFP}$ hearts ($p<0.05$). Analysis of monocyte subpopulation adhesion to the myocardial vein endothelium at 2h post-I/R showed that *Cx3cr1*$^{GFP/GFP}$ mice did not have reduced adherence of non-classical monocytes compared to *Cx3cr1*$^{+/GFP}$ mice; the reduced non-classical monocyte population in 24h *Cx3cr1*$^{GFP/GFP}$ infarcts was therefore more likely to be due to a migration or extravasation defect than impaired adhesion. Other studies have reported a central role of CX3CR1 in monocyte adhesion, for example Poupel et al have shown that both in vitro and in vivo pharmacological inhibition of CX3CR1 attenuates monocyte adhesion [348], while recent phenotypic studies with mouse models of atherosclerosis have revealed that CX3CR1 deficiency significantly reduces monocyte infiltration into the vessel wall [287]. The similar levels of non-classical monocyte myocardial vein adhesion observed in this study at 2h could be explained by the fact that CX3CR1-expressing cells can also adhere to the endothelium in a mechanism that is independent of CX3CR1 signalling and integrin activation [188, 351]. The lack of difference may also be due to the comparison made between *Cx3cr1*$^{+/GFP}$ and *Cx3cr1*$^{GFP/GFP}$ mice, which does not consider the monocyte adhesion phenotype in $CX3CR1^{+/+}$ mice. It is possible that monoallelic expression of CX3CR1 leads to the same phenotype as complete knockout of CX3CR1, therefore a difference in phenotype would only be observed when comparing normal expression of CX3CR1 in wild-type mice. Furthermore, the precise role of CX3CR1 in monocyte adhesion and the other important factors required in this process such as integrins, selectins, and CCL2, are yet to be confirmed [231]. The delayed infiltration of non-classical monocytes in *Cx3cr1*$^{GFP/GFP}$ hearts at 24h post-I/R subsequently recovered at day 3 following I/R. At this later time point, classical and non-classical monocyte counts dramatically increased from 24h, which was not significantly affected by genetic CX3CR1 knockout. The reduced non-classical monocyte response in CX3CR1 knockout hearts at 24h may therefore indicate a delayed response of these cells rather than complete reduced infiltration in the absence of CX3CR1 expression. Although genetic CX3CR1 knockout did not

significantly affect the counts of monocyte subpopulations at day 3 following I/R, a distinct spatiotemporal pattern of $CD11b^+$ GFP^+ monocytes was observed specifically in *Cx3cr1*$^{GFP/GFP}$ infarcts, whereby counts of GFP^+ cells were significantly greater at the infarct border compared to that of the central zone of the infarct. This phenotype was not observed in *Cx3cr1*$^{+/GFP}$ infarcts, suggesting that complete CX3CR1 knockout may influence the migratory behaviour of infiltrated monocytes in the injured myocardium at day 3 post-I/R. CX3CR1 is known to mediate the migration of $CX3CR1^+$ leukocytes [352], which may explain the difference in the localization of infarct $CD11b^+GFP^+$ cells between *Cx3cr1*$^{+/GFP}$ and *Cx3cr1*$^{GFP/GFP}$ hearts; marginalization of GFP^+ cells at the infarct border specifically in *Cx3cr1*$^{GFP/GFP}$ mice may be reflective of differences in the migratory properties of $CD11b^+CX3CR1^{-/-}$ cells.

Although there did not appear to be a strong phenotype in *Cx3cr1*$^{-/-}$ mice in terms of monocyte infiltration into the injured myocardium, the results of this monocyte subpopulation analysis in the infarct between 2h and day 3 following I/R sheds light on the temporal dynamics of these cells after I/R. The traditional paradigm describes that non-classical monocytes infiltrate the injured myocardium from day 5 post-I/R, peaking at ~day 7, however in this study there appears to be a distinct population of infarct non-classical monocytes at 24h following reperfusion. Other recent studies have also demonstrated an earlier role of non-classical monocytes in response to cardiac injury; endoscopic time lapse imaging of the heart has demonstrated infiltration of GFP^{hi} non-classical monocytes as early 30 minutes [313] and 12h post-cardiac I/R [353]. The conventional idea that non-classical monocytes dominate the second phase of repair following I/R from day 5-9 post-reperfusion therefore overlooks any earlier important role of $CX3CR1^{hi}$ non-classical monocytes.

It is important to address the validity of this immunofluorescence monocyte data with consideration to the methodological limitations of the technique. Definition of monocyte subpopulations in the heart tissue by microscopy described in this chapter relied on the method of manual quantification of $CD11b^+$ GFP^{mid} classical monocytes and $CD11b^+GFP^{hi}$ non-classical monocytes. The distinction between classical and non-classical monocytes relied more heavily on the level of GFP expression due to the poor quality of CCR2 staining. Although this classification of monocyte

subpopulations was based on a subjective threshold of GFP expression, analysis of GFP MFI by $CD11b^{+}GFP^{mid}$ classical monocytes and $CD11b^{+}$ GFP^{hi} non-classical monocytes showed a significant difference in GFP expression between monocyte subpopulations, as observed and defined by eye. The application of automated imaging software to increase the objectivity of the data was considered, however the utility of such software is limited by the natural autofluorescence of mouse heart tissue within the 488nm and 568nm filters used. This is particular prominent in the 488nm laser, which renders automated software unable to distinguish auto-fluorescent cardiomyocytes from positively stained $CD11b^{+}$-Alexa-488 cells. Automated quantification of monocyte subpopulations was therefore not performed to validate the manual counts. An alternative approach to validate the findings was to determine the inter-user variability of manual counts of monocyte subsets. Manual quantification was performed with three independent observers, which showed minimal variability in cell counts, thus providing confidence in the data. The subjectivity involved in this manual method of monocyte subpopulation quantification in the heart tissue was therefore unlikely to have had a significant impact upon the results reported. Furthermore, monocytes were quantified as total population, which could be confidently identified as $CD11b^{+}GFP^{+}$ cells. This analysis demonstrated no effect of genetic CX3CR1 knockout on monocyte infiltration into the injured myocardium at either 2h, 24h or day 3 post-I/R.

To overcome the limitations of monocyte subpopulation analysis by microscopy, this study also used the method of cardiac digest to investigate monocyte subpopulations in the injured heart tissue following cardiac I/R. This analysis concluded that classical and non-classical monocyte subpopulations in the infarct at 24h post-I/R did not significantly differ between *Cx3cr1*$^{+/+}$, *Cx3cr1*$^{+/GFP}$, and *Cx3cr1*$^{GFP/GFP}$ hearts. This method did not identify a decreased population of non-classical monocytes in the infarct of *Cx3cr1*$^{GFP/GFP}$ hearts compared to *Cx3cr1*$^{+/GFP}$ mice that was also observed by microscopy. Furthermore, classical monocytes dominated the proportion of total monocytes over non-classical monocytes, while microscopy showed a more even ratio of monocyte subpopulations. The discrepancy in monocyte subpopulation proportions determined by cardiac digest flow cytometry and immunofluorescence microscopy may be attributed to differences in the definition of classical and non-classical

monocyte populations between techniques. By flow cytometric analyses, monocyte subpopulations were confidently defined using a detailed panel markers as classical [Ly6C^{hi}CCR2^{hi}CX3CR1^{mid-hi}] and non-classical [Ly6C^{lo}CCR2^{mid}CX3CR1^{hi}]. Such differences in monocyte subpopulation proportions determined by cardiac digest flow cytometry and immunofluorescence microscopy may also be due to inefficiencies in antigen detection in fixed tissues. This is likely for mouse heart tissue monocyte staining using anti-CD11b and anti-GFP antibodies, which do not reveal stellate-shaped myeloid cells in fixed mouse tissue. Although heart tissue was only lightly fixed in this study to minimize the loss of antigen, microscopic analyses of monocytes may fail to detect all cells. Variation may also have risen from the nature of the heart digest method; in particular, the small population of non-classical monocytes may be a result of the mechanical and enzymatic digestion step affecting certain cell populations. Furthermore, monocytes do not represent a fixed cell state, but are rather cells transitioning through maturation states. As a result, definition of these cells is further complicated by their maturation state which coincides with changes in the expression of specific surface markers [354].

5.3.3 Mouse Macrophage Subpopulations in the Injured Myocardium at Day 3 Following Cardiac I/R and the Impact of Genetic CX3CR1 Knockout

The effect of genetic CX3CR1 knockout on infarct macrophage populations was also assessed at day 3 following cardiac I/R as monocyte subpopulations are known to differentiate into their respective macrophage populations following their infiltration into myocardial tissue. This study firstly demonstrated that counts of *Cx3cr1*$^{+/GFP}$ control group M1 macrophages were significantly higher than M2 macrophages at day 3 post-I/R. This is in agreement with the established concept that M1 macrophages dominate earlier repair ~day 3 while M2 macrophages mediate the second later phase of repair [355]. There was no significant effect of *Cx3cr1*$^{-/-}$ on M1 and M2 macrophage populations in the infarct at day 3 post-I/R, though there was a noticeable trend towards lower counts of M1 macrophages in *Cx3cr1*$^{GFP/GFP}$ hearts. When macrophages were considered as a total population, complete CX3CR1 knockout hearts had significantly lower counts of macrophages than *Cx3cr1*$^{+/GFP}$ hearts. Based on this data it was concluded that absence of CX3CR1 expression may disrupt the

differentiation of classical monocytes into M1 macrophages following cardiac I/R. Other reports have demonstrated that CX3CR1 plays an important role in the phenotypic conversion and pro-inflammatory functional polarization of monocytes in the liver; macrophages in *Cx3cr1*$^{+/GFP}$ mice have a stronger pro-inflammatory phenotype than in *Cx3cr1*$^{GFP/GFP}$ mice [356]. The observed reduced population of macrophages in *Cx3cr1*$^{GFP/GFP}$ infarcts (Figure 5.20) may also be a result of the impaired survival signals in these *Cx3cr1*-knockout mice which leads to increased apoptosis of CX3CR1-expressing cells [218, 322, 357].

When considering these findings, it also important to acknowledge that the definition of macrophage subpopulations used in this study by microscopy may be an oversimplification of this heterogeneous cell type; currently the M1/M2 classification of macrophages is criticized for not fully covering the total spectrum of macrophage phenotypes. Particularly in a pathological context, macrophages demonstrate high plasticity, modifying their expression and transcription profile along a continuous spectrum, with M1 and M2 phenotypes as the polar extremes [358, 359]. With this in mind it is possible that there is quantitative overlap in the counts of M1 and M2 macrophages at day 3 post I/R described in this study. In addition to this, surface markers can be complicated in several other aspects, including the availability of appropriate antibodies. Functional analysis is therefore arguably a better measure.

5.3.4 Mouse Monocyte Subpopulations in the Spleen and Bone Marrow at 24h Following Cardiac I/R and the Impact of Genetic CX3CR1 Knockout

Investigation of splenic and bone marrow classical and non-classical monocyte subpopulations at 24h post-I/R in a small cohort of *Cx3cr1*$^{+/GFP}$ and *Cx3cr1*$^{GFP/GFP}$ mice showed that the splenic non-classical population decreased from baseline at 24h post-I/R. Bone marrow non-classical monocytes also decreased at this time point though this was not statistically significant. Such findings indicate that complete genetic knockout of CX3CR1 may lead to the release of non-classical monocytes from the spleen and their egress from the bone marrow at 24h following cardiac I/R. This process would explain the increase in mouse non-classical monocytes observed at 24h in the peripheral blood, though this was shown to occur similarly in both

Cx3cr1$^{+/GFP}$ and *Cx3cr1*$^{GFP/GFP}$ mice. It is important to note that this analysis was based on a relative ratio of monocyte subpopulations, and thus it could also conversely be possible that there is an increase in classical monocytes in the spleen and bone marrow, rather than a decrease in their non-classical counterpart. However, the sample size of the 24h I/R group (n=2) limits the analysis. Additional animals and absolute counts would therefore be required to draw valid conclusions.

5.3.5 PD-L1 is a Useful Marker of Mouse Circulating Non-Classical Monocytes

This study confirmed a previous report showing that PD-L1 is a useful marker for defining non-classical monocytes from classical monocytes in mouse blood [360]. Further research is required to determine if this significantly greater expression of PD-L1 by non-classical monocytes compared to classical monocytes is also seen in the heart tissue monocyte populations post-cardiac I/R. Such a tool may facilitate non-classical monocyte definition and improve quantification following myocardial I/R, which would be particularly useful considering the limitations of monocyte identification by microscopy described in this study.

5.3.6. Genetic CX3CR1 Knockout Has No Significant Effect on Cardiac Function at 6 weeks Post-Cardiac I/R

The CX3CL1/CX3CR1 axis has been implicated in myocardial repair following I/R by a number of studies, among which the general consensus suggests that CX3CL1 is detrimental to cardiac repair and therefore worsens long term myocardial function. For example in mouse models, CX3CL1 has been shown to promote myocardial injury, increase infarct size, and accelerate the progress of heart failure [203, 288]. Therapeutic inhibition of CX3CL1/CX3CR1 may therefore confer a cardio-protective role to improve cardiac repair and function following I/R. This has been demonstrated by Gu et al [289] who showed that anti-CX3CL1 therapy reduces infarct size, improves cardiac remodeling and function, and reduces mortality, though this was in a permanent MI model.

Based on these studies, it could be suggested that *Cx3cr1*$^{GFP/GFP}$ mice may be protected from cardiac injury and demonstrate improved cardiac function following I/R, compared to control mice. As such, the effect of genetic CX3CR1 knockout on myocardial function following I/R was examined at 6 weeks following reperfusion in this study. This analysis revealed that there was no significant effect of genetic CX3CR1 ablation on mouse ejection fraction at 6 weeks following I/R. There was however a notable trend towards improved cardiac function with increased CX3CR1 expression, observed as a small incremental decrease in ejection fraction from *Cx3cr1*$^{+/+}$, to *Cx3cr1*$^{+/GFP}$, to *Cx3cr1*$^{GFP/GFP}$ hearts. While this observation contradicts the cardio-protective role of CX3CL1/CX3CR1 neutralization reported by others, it may be explained by the method of inhibition. Furthermore, it is possible that a lack of phenotype observed in this study is due to the modest sample size of the groups used; increased animal numbers may reveal a statistically significant difference cardiac function between genotypes which is underpowered using the group size in this study. Moreover, it is important to consider that the absence of an effect of genetic CX3CR1 deficiency on cardiac function at six weeks post-I/R does not rule out the presence of a phenotype at other time points following I/R. Future work should therefore assess myocardial function in response to different modes of CX3CL11/CX3CR1 inhibition and at different time points following cardiac I/R.

5.3.7 Use of the *Cx3cr1*^{EGFP} line for the Study of the CX3CL1/CX3CR1 Axis in the Post-Cardiac I/R Non-Classical Monocyte Response

To study the effect of CX3CR1 knockout on any biological function in mice, the *Cx3cr1*$^{GFP/GFP}$ mouse is a valuable tool. In this construct, the first 320bp of the CX3CR1 gene is replaced by the EGFP gene [277]. In addition to investigating biological functions in response to genetic CX3CR1 knockout, this tool also acts as a reporter mouse to track GFP^{+} monocytes. This model is not however perfect for the study of CX3CR1^{+} monocytes following cardiac I/R, since this germline mutation also affects other CX3CR1-expressing cells including NK-cells, activated T-cells, dendritic cells, and brain microglia. As such it is difficult to extrapolate the effects of genetic CX3CR1 deficiency on monocyte behaviour from its effects on the immune system more broadly. Indeed, monocyte phenotypes in *Cx3cr1*$^{GFP/GFP}$ mice may be an indirect

consequence of CX3CR1 deficiency on other immune cell types. Furthermore, it is possible that *Cx3cr1*$^{-/-}$ mice may have developed compensatory mechanisms to overcome the lack of CX3CR1 expression, in order to function normally. It is also important to consider that different mechanisms of inhibition of the CX3CL1/CX3CR1 axis from genetic knockout, such as pharmacological inhibition of CX3CL1, or CX3CR1, may elicit different phenotypes; for example, Poupel et al show that long-term pharmacological anti-CX3CR1 treatment in mice resulted in a 30% reduction in inflammatory monocyte numbers, while having no effect on resident monocytes [348]. By contrast, findings in *Cx3cr1*$^{GFP/GFP}$ mice by Landsman et al showed a 3-fold reduction in resident monocyte numbers, with no alteration in the number of inflammatory monocytes [218]. Targeted disruption of the mouse CX3CL1 gene however does not appear to generate any detectable phenotype; *Cx3cl1*$^{-/-}$ mice have no histologic abnormalities in any major organs, and hematopoietic lineages in blood and lymphoid tissue are essentially normal [226]. *Cx3cr1*$^{-/-}$ mice also do not demonstrate differences to wild-type mice with regard to monocyte recruitment, DC differentiation and migration, or microglial responses [277]. The exact mechanism of CX3CL1/CX3CR1 axis inhibition may therefore lead to alternative monocytic phenotypes that affect outcome on cardiac function following I/R. This discrepancy is not unique and may exist for several reasons, one of which is the aforementioned compensatory mechanisms that take place in gene-deleted mice during development. There is also potential for the existence of other sites of action of the CX3CR1 antagonist that have not yet been identified.

5.3.8 Translational Value of Cardiac I/R Mouse Models for the Study of Post-Cardiac I/R Non-Classical Monocytes

A wider consideration of this study is how relevant the study of monocytes in mice is to our knowledge and understanding of monocytes in human. While classical and non-classical subpopulations are broadly conserved across human and mice, the monocyte subpopulations in each species are defined by different markers (Ly6C in mice, CD14 and CD16 in humans), though these markers are unlikely to govern their function. Furthermore, comparison of monocyte gene expression profiles between mouse and human have revealed that a number of molecules are conversely

expressed between species' subsets [361]. For the study of the CX3CL1/CX3CR1 axis, it is also difficult to extrapolate findings from human monocytes, where there is an obvious greater difference in CX3CR1 expression by non-classical monocytes compared to classical monocytes, to mice, where Ly6C^{hi} classical and Ly6C^{lo} non-classical monocytes express similar levels of CX3CR1. It is possible that the clear greater expression of CX3CR1 by human non-classical monocytes may be reflective of a more important/central function of CX3CR1 on human non-classical monocytes. The lack of a striking phenotype observed in *Cx3cr1*$^{GFP/GFP}$ mice in this chapter may therefore not necessarily be true for inhibition of CX3CR1 in the clinical setting.

5.4 Conclusions

This study demonstrates that mouse blood non-classical monocyte counts are significantly reduced in response to genetic depletion of CX3CR1, and therefore supports existing reports of the effect of CX3CR1 expression on monocyte survival. Non-classical monocytes appear in the injured myocardium at 24h post-I/R, contradicting the traditional paradigm that these cells infiltrate the heart ~day 5 post-reperfusion, which has also been challenged by recent research. Genetic CX3CR1 knockout appears to reduce the infiltration of non-classical monocytes at 24h post-I/R but not at day 3 post-I/R, suggesting a delayed response of these cells in the absence of CX3CR1 expression. These findings however need to be confirmed by other methods of studying monocyte infiltration into the myocardium, such as using PD-L1 which is shown in this study to be a useful marker of the non-classical monocyte subset in the blood. Genetic ablation of CX3CR1 in mice does not impair cardiac function at six weeks post-I/R, however inhibition of the CX3CL1/CX3CR1 axis using a different approach such as pharmacological inhibition of the receptor, or a deficiency in the ligand, CX3CL1, may provide new insights.

To help understand the specific role of CX3CR1 in non-classical monocyte function following cardiac I/R, the signalling pathways downstream of this receptor must be characterised. Recent efforts to define these pathways have provided initial insight into the molecular mechanisms regulating non-classical monocyte function, but remain largely inconclusive. The next chapter of this work therefore focuses on potential

pathways downstream of CX3CL1/CX3CR1 signalling to help explain non-classical monocyte function.

Monocyte subpopulation changes per tissue investigated									
	Blood			**Heart**		**Spleen**		**Bone Marrow**	
Genotype	*Cx3cr1*$^{+/+}$	*Cx3cr1*$^{+/GFP}$	*Cx3cr1*$^{GFP/GFP}$	*Cx3cr1*$^{+/GFP}$	*Cx3cr1*$^{GFP/GFP}$	*Cx3cr1*$^{+/GFP}$	*Cx3cr1*$^{GFP/GFP}$	*Cx3cr1*$^{+/GFP}$	*Cx3cr1*$^{GFP/GFP}$
Ly6C^{hi} Classical Monocytes	**2h IR:** counts decreased from baseline (NS) **24h IR:** counts increased and returned to baseline (NS)	**2h IR:** counts decreased from baseline ($p<0.05$) **24h IR:** counts increased and returned to baseline ($p<0.05$)	**Baseline:** counts NS from *Cx3cr1*$^{+/+}$ and *Cx3cr1*$^{+/GFP}$ **2h IR:** counts decreased from baseline (NS) **24h IR:** counts increased and returned to baseline (NS)	**2h IR:** counts similar to naïve and sham hearts (NS) **24h IR (IF):** increase from 2h by ~1.5-fold (NS) **Day 3 IR:** increase from 24h by 5-fold ($p<0.001$)	**2h IR:** NS from *Cx3cr1*$^{+/GFP}$ **24h IR (IF):** NS from *Cx3cr1*$^{+/GFP}$ **24h IR (Digest):** NS from *Cx3cr1*$^{+/GFP}$ **Day 3 IR:** NS from *Cx3cr1*$^{+/GFP}$	**24h IR:** CM population similar to baseline (NS)	**24h IR:** increase in proportion of CM compared to baseline (NS)	**Baseline:** CM ~5% of total BM leukocytes **24h IR:** NS different from baseline	**Baseline:** NS different from *Cx3cr1*$^{+/GFP}$ **24h IR:** NS different from *Cx3cr1*$^{+/GFP}$
Ly6C^{inter} Intermediate Monocytes	**2h IR:** counts decreased from baseline (NS) **24h IR:** counts increased and returned to baseline (NS)	**2h IR:** counts decreased from baseline (NS) **24h IR:** counts increased and returned to baseline ($p<0.05$)	**Baseline:** counts NS from *Cx3cr1*$^{+/+}$ and *Cx3cr1*$^{+/GFP}$ **2h IR:** counts decreased from baseline (NS) **24h IR:** counts increased and returned to baseline ($p<0.05$)						
Ly6C^{lo} Non-Classical Monocytes	**2h IR:** counts decreased from baseline (NS) **24h IR:** counts increased and returned to baseline (NS)	**2h IR:** counts decreased from baseline (NS) **24h IR:** counts increased and returned to baseline ($p<0.05$)	**Baseline:** counts 47.5% lower than *Cx3cr1*$^{+/+}$ ($p=0.047$) and 48.4% lower than *Cx3cr1*$^{+/GFP}$ ($p=0.024$) **2h IR:** counts decreased from baseline (NS) **24h IR:** counts increased and returned to baseline (NS)	**2h IR:** counts similar to naïve and sham hearts (NS) **24h IR:** increase from 2h by ~4-fold (NS) **Day 3 IR:** increase from 24h by 2-fold ($p<0.01$)	**2h IR:** NS from *Cx3cr1*$^{+/GFP}$ **24h IR:** counts 2-fold lower than *Cx3cr1*$^{+/GFP}$ ($p<0.05$) **24h IR (Digest):** NS from *Cx3cr1*$^{+/GFP}$ **Day 3 IR:** NS from *Cx3cr1*$^{+/GFP}$	**24h IR:** NCM population similar to baseline (NS)	**24h IR:** decrease in proportion of NCM compared to baseline (NS)	**Baseline:** CM ~2% of total BM leukocytes **24h IR:** CM ~5% of total BM leukocytes	**Baseline:** NS different from *Cx3cr1*$^{+/GFP}$ **24h IR:** NS different from *Cx3cr1*$^{+/GFP}$

Table 5. 1. Summary of mouse monocyte subpopulation changes (Ly6C^{hi} classical, Ly6C^{inter} intermediate, Ly6C^{lo} non-classical) in the peripheral blood, heart, spleen, and bone marrow during the acute 24h following cardiac I/R.

The effect of CX3CR1 knockout on monocyte subpopulations in each tissue investigated was analysed by comparing *Cx3cr1*$^{+/+}$, *Cx3cr1*$^{+/GFP}$, and *Cx3cr1*$^{GFP/GFP}$ mice.

Chapter 6.0. Activation of the NFκB Pathway by CX3CR1 Signalling in Human Monocytes

6.1. Introduction

In order to understand the specific role of CX3CR1 in non-classical monocyte function following cardiac I/R, the signalling pathways that are activated downstream of this receptor following CX3CL1 binding must be characterised. Recent efforts have demonstrated that a number of different signalling pathways may be induced downstream of CX3CR1, though this evidence is varied and largely inconclusive. Among those studied, the NFκB signalling pathway has most frequently been shown to be a potential downstream target of CX3CR1 signalling. These reports however cover a broad range of immune cells, and the evidence of NFκB activation by CX3CL1/CX3CR1 specifically in monocytes is sparse. Activation of NFκB specifically following myocardial I/R has been documented by a number of studies [362, 363], and importantly its inhibition has been shown to be cardioprotective [364, 365], as determined by reduced I/R injury, attenuated infarct size, and improved cardiac function after MI [366-369]. The aim of this chapter was therefore to investigate activation of this pathway in human non-classical monocytes in response to CX3CL1 stimulation, which may help to explain the function of these cells following reperfusion. The NFκB pathway regulates gene transcription, cytokine production, and cell survival. Such functions downstream of NFκB signalling could be crucial to monocyte function following CX3CL1 stimulation after cardiac I/R. To study the monocyte NFκB response to CX3CL1/CX3CR1 stimulation, the human monocyte cell lines THP-1, MM6 and U937 were studied followed by freshly isolated human monocytes from whole peripheral blood.

The first aim of this work was to immunophenotype the relative expression levels of CX3CR1 by human monocyte cell lines and freshly isolated human classical, intermediate and non-classical monocytes. This was performed to determine if the monocyte population expressed adequate CX3CR1 for CX3CL1 to induce activation of downstream signalling. The second aim was to investigate activation of the NFκB

pathway by CX3CL1 stimulation by measuring expression levels of NFκB pathway proteins by western blot analysis and FACS. As NFκB is arguably one of the most important regulators of pro-inflammatory gene expression, several techniques have been developed to monitor its activity at multiple stages of NFκB pathway activation [370]. A large amount of published information on the NFκB signalling cascade has however focussed on the two best-understood phosphorylation targets within the NFκB p65 subunit, S276 and S536 [371]. In the NFκB signaling cascade, phosphorylation of p65 is required for nuclear translocation and transcriptional activation, but different sites of phosphorylation have different significance in this regard; phosphorylation at the serine 536 position is required for nuclear translocation while phosphorylation of serine 529 affects transcriptional activity, and serine 276 is involved in co-activator recruitment at target gene promoters [372-374]. Induction of the NFκB pathway in THP-1 monocytes by CX3CL1 stimulation was therefore firstly determined by measuring phosphorylation of p65 at Ser-536. The final aim of this work was to determine if CX3CL1 stimulation regulates the expression of NFκB target genes in THP-1 monocytes. The NFκB pathway has a broad spectrum of target genes, however the focus in this study was to evaluate the expression of pro-inflammatory genes IL-1β , IL-6, IL-8 and IκBα in monocytes using qPCR.

6.2 Results

6.2.1 Immunophenotyping Human Monocyte Cell Line THP-1 Marker Expression Compared to Human Circulating Monocyte Subpopulations

The THP-1 human monocyte cell line is a widely used model for the study of monocyte function *in vitro*, and may therefore be a useful tool to study monocyte signalling pathways downstream of the CX3CL1/CX3CR1 axis. The existence of three distinct monocyte subpopulations in the human circulation prompted the initial aim of this work, which was to investigate THP-1 expression of the monocyte markers CD16, CD14, CCR2, CX3CR1 to identify whether these cells fall into the classification of classical, intermediate, or non-classical human monocytes. To address this, human PBMCs from volunteer peripheral whole blood were isolated by Ficoll separation, and analysed by FACS. In parallel, cultured THP-1 cells were analysed for monocyte marker expression.

The results of this analysis showed that human blood monocyte subpopulations expressed their respective characteristic levels of monocyte markers; classical monocytes ($CD16^{-}CD14^{++}CCR2^{hi}CX3CR1^{lo}$), intermediate monocytes ($CD16^{+}CD14^{+}CCR2^{mid}CX3CR1^{mid}$), and non-classical monocytes ($CD16^{++}CD14^{lo}CCR2^{lo}CX3CR1^{hi}$) (Figure 6.2). Immunophenotyping of THP-1 monocytes revealed that these cells were $CD16^{-}CD14^{++}CCR2^{mid\text{-}hi}CX3CR1^{lo}$ (Figure 6.1, 6.2). THP-1 monocytes therefore expressed monocyte markers CD16, CD14, CCR2 and CX3CR1 at levels that were comparable with classical monocytes (Figure 6.2B, C). Total PBMCs were also phenotyped for monocyte marker expression (Figure 6.3).

The results of this initial profiling of the THP-1 human monocyte cell line therefore concluded that these cells resemble human circulating classical monocytes much more closely than non-classical or intermediate monocyte subsets.

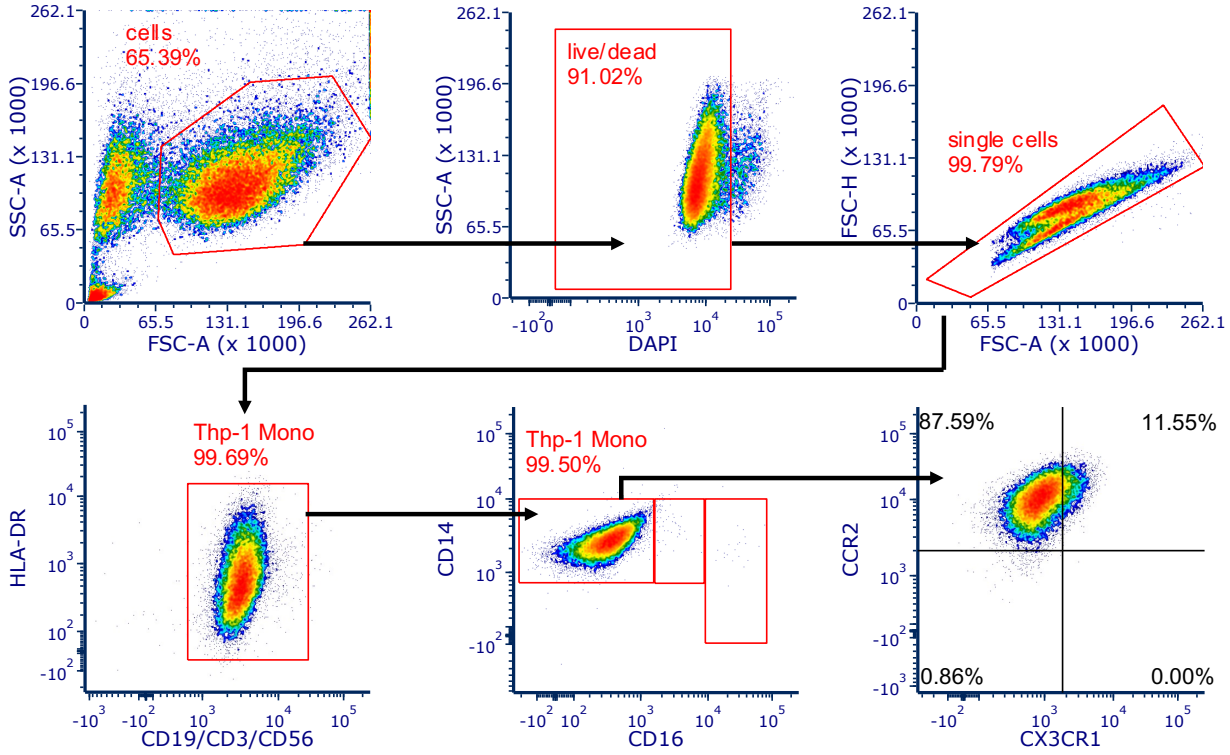

Figure 6. 1. Flow Cytometry analysis of THP-1 human monocytic cell line.

THP-1 human monocytes were characterised as $CD16^{-}CD14^{hi}CCR2^{hi}CX3CR1^{lo}$ cells and therefore closely resembled human circulating classical monocytes.

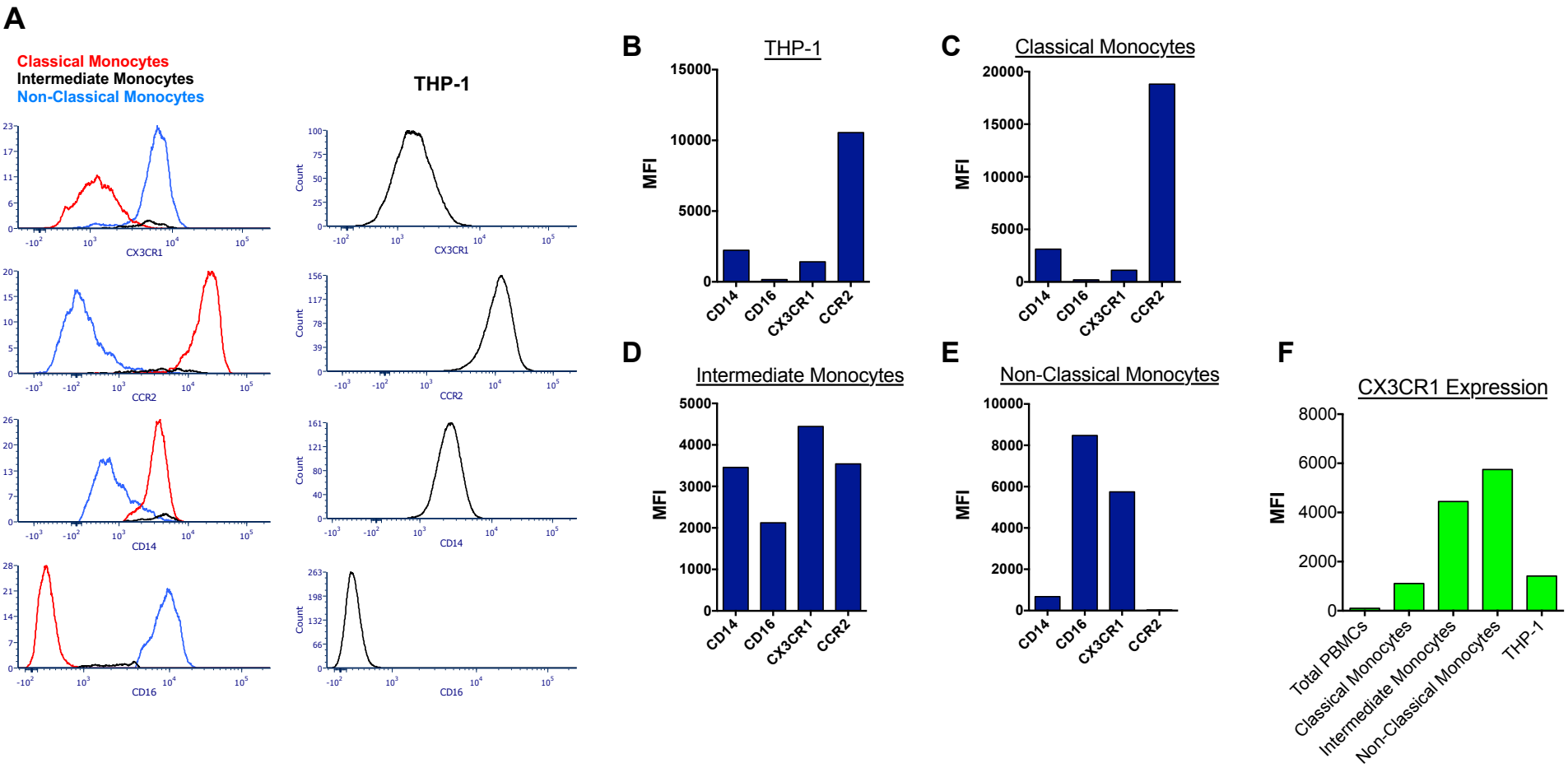
A
Classical Monocytes
Intermediate Monocytes
Non-Classical Monocytes
THP-1
Count
CX3CR1
CCR2
CD14
CD16
B
THP-1
MFI
CD14
CD16
CX3CR1
CCR2
C
Classical Monocytes
D
Intermediate Monocytes
E
Non-Classical Monocytes
F
CX3CR1 Expression
Total PBMCs
Classical Monocytes
Intermediate Monocytes
Non-Classical Monocytes
THP-1

Figure 6. 2. Immunophenotyping of the THP-1 human monocyte cell line compared with fresh whole blood human monocyte subpopulations (classical, intermediate, and non-classical).

A-E. MFI of CX3CR1, CCR2, CD14, and CD16 expressed by human blood monocyte subpopulations (classical, intermediate, non-classical), compared with the THP-1 human monocyte cell line. F. Comparison of CX3CR1 expression between human blood monocyte subpopulations and THP-1 monocytes showed that the THP-1 monocyte cell line closely resembles human classical monocytes with relation to CX3CR1 expression.

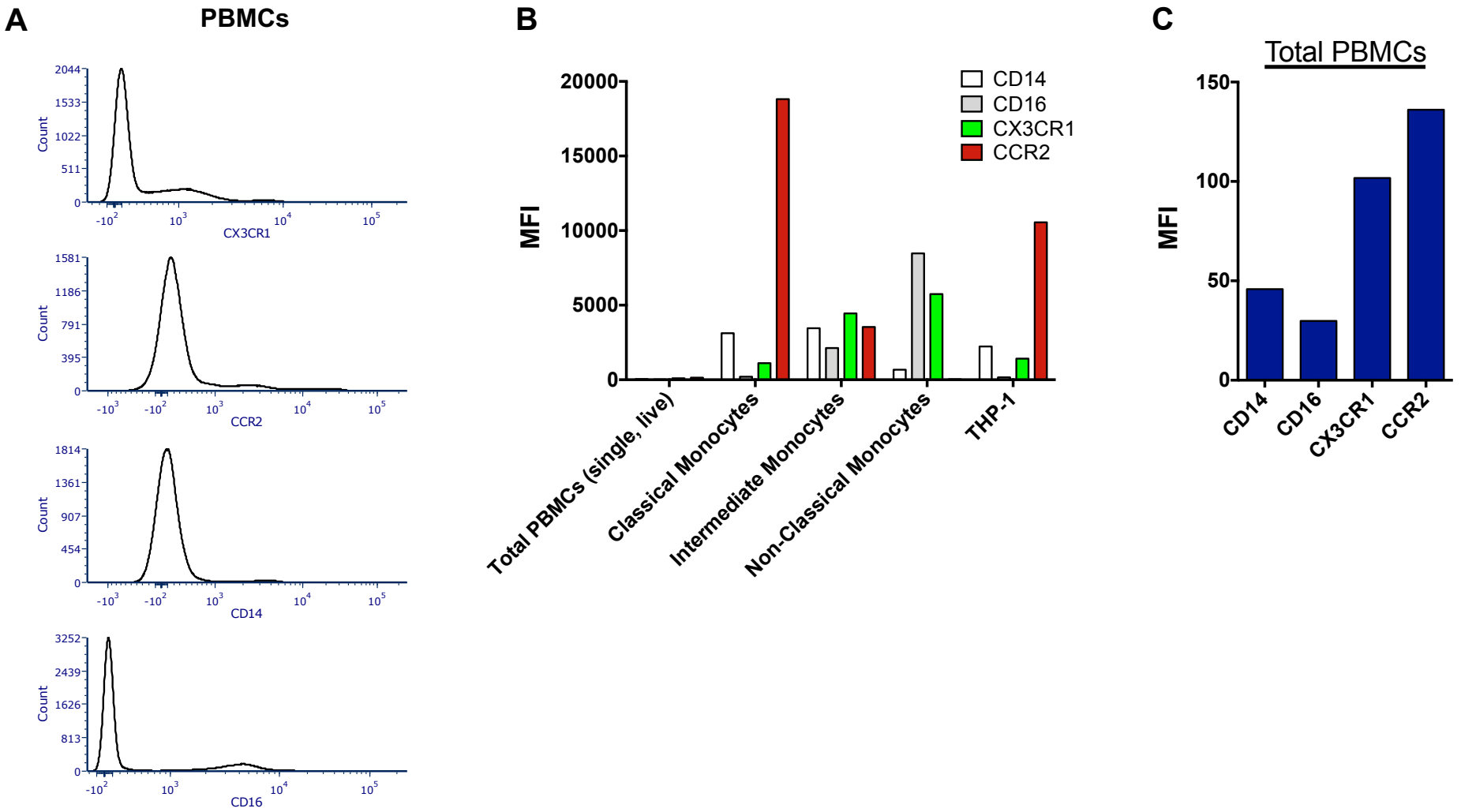
A
PBMCs
Count
CX3CR1
CCR2
CD14
CD16
B
MFI
CD14
CD16
CX3CR1
CCR2
Total PBMCs (single, live)
Classical Monocytes
Intermediate Monocytes
Non-Classical Monocytes
THP-1
C
Total PBMCs
MFI
CD14
CD16
CX3CR1
CCR2

Figure 6. 3. Immunophenotyping of human PBMCs.

A, C. MFI of CX3CR1, CCR2, CD14 and CD16 expressed by human PBMCs. B. Comparison of monocyte marker CD14, CD16, CX3CR1 and CCR2 expression by human PBMCs, human blood monocyte subpopulations (classical, intermediate, and non-classical), and THP-1 human monocytes.

6.2.2 Immunophenotyping of Human Monocytic Cell Lines THP-1, MonoMac6, and U937

In addition to THP-1 cells, MonoMac6 (MM6) and U937 cell lines are frequently used as models for investigating human monocyte function, regulation, and signalling pathways in vitro [375-377]. These monocyte lines were immunophenotyped for monocyte markers as performed for THP-1 cells, with the aim to identify a human monocyte cell line that expresses high levels of CX3CR1 and therefore more closely resembles the human circulating non-classical monocyte population.

The results of this analysis showed that U937 monocyte expression of CX3CR1 was 1.7-fold greater than THP-1 cells (Figure 6.4A). The MM6 cell line also expressed greater levels of CX3CR1 than THP-1 cells by approximately 2-fold. However, comparison of CX3CR1 MFI with human peripheral blood monocyte subpopulations showed that the expression of CX3CR1 by all these monocytic cell lines was still lower than that of peripheral blood classical monocytes. Expression of CX3CR1 by THP-1, U937 and MM6 cells was 30.3%, 51.4%, and 60.4% of that of classical monocytes, respectively (Figure 6.4B). Furthermore, non-classical monocytes expressed 12.9-fold greater levels of CX3CR1 than THP-1 cells, 7.6-fold more than U937, and 6.5-fold more than MM6 monocytes.

Therefore, of the three monocyte cell lines studied, there was no obvious choice for studying non-classical monocyte NFκB signalling in response to CX3CL1. The THP-1 cell line was carried forward for signalling experiments on the basis that these monocytes were more robust and practical to culture.

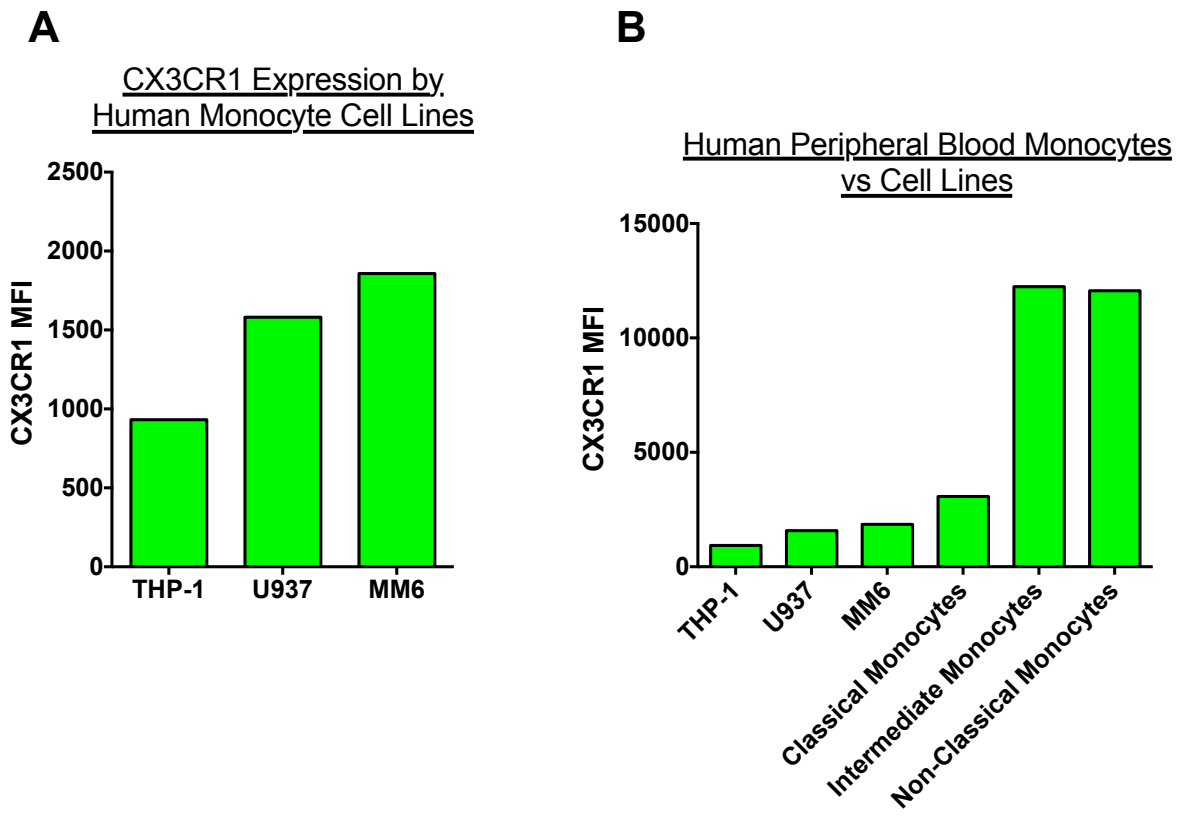

Figure 6. 4. Profiling CX3CR1 expression by human monocyte cell lines THP-1, U937 and MM6 compared to human peripheral blood fresh monocyte subpopulations (classical, intermediate, non-classical).

6.2.3 Optimisation of CX3CL1 Dose and Time Stimulation for Phosphorylation of the NFκB subunit p65 in THP-1 Monocytes

To date, the signalling pathways that are activated downstream of CX3CR1 stimulation by CX3CL1 are poorly understood. Initial insights have pointed towards activation of the NFκB pathway [378-381] by CX3CL1/CX3CR1 in a range of cell types including microglia, intestinal epithelial cells, and neurons. The evidence reporting CX3CR1-induced activation of NFκB specifically in monocytes however is lacking. In this chapter, I therefore hypothesised that CX3CL1 binding to its receptor CX3CR1 induces NFκB activation in human monocytes, which leads to an increased pro-inflammatory response of these cells. Through this upregulation of NFκB and pro-inflammatory response in monocytes, CX3CL1 may exert its detrimental effect on myocardial repair following cardiac I/R.

To investigate this, cultured THP-1 monocyte cells were stimulated with CX3CL1 ligand and NFκB activation was evaluated by measuring the levels of phosphorylated p65. Phosphorylation of p65 is a widely used measure of NFκB signalling activation; under normal conditions, the p65 subunit of NFκB is retained in the cytoplasm with the inhibitory protein IκB; however, when NFκB is activated by stimuli such as TNF-α, the phosphorylated p65 subunit of NFκB translocates into the nucleus to regulate the expression of inflammatory mediators and MMPs [382, 383]. Activation of NFκB is known to be induced by pro-inflammatory cytokines such as TNF-α, which results in nuclear translocation of the p50/p60 heterodimers [384]. Based on this known phenomenon, TNF-α stimulation was employed as a positive control in this study.

Optimisation of the dose and time of CX3CL1 stimulation was firstly performed. A number of studies showing CX3CL1-induced survival of human monocytes provided insight into the range of CX3CL1 required to elicit an anti-apoptotic response, which were initially used to determine a dose range of CX3CL1 [220, 357, 379, 384]. These studies used CX3CL1 concentrations ranging from 1-1000ng/ml. On the basis of this, I firstly investigated THP-1 p65 phosphorylation in response to 10, 50, and 100ng/ml CX3CL1, for either 60min or 120min. This initial experiment showed that TNF-α

(15min, 10ng/ml) stimulated a large increase in the levels of phosphorylated p65, as expected (Figure 6.5A). CX3CL1 stimulation induced modest phosphorylation of p65 at both 60min and 120min, which was not notably different between 10, 50, and 100ng/ml concentrations of CX3CL1 at either time point. Based on this observation, 10ng/ml and 50ng/ml CX3CL1 concentrations were taken forward for subsequent analysis.

The modest response of NFκB to CX3CL1 stimulation observed at 60min and 120min suggested that phosphorylation of the NFκB subunit p65 by CX3CL1 may occur at an earlier time point. To investigate this, THP-1 monocytes were stimulated with 10ng/ml and 50ng/ml CX3CL1 for either 15min, 30min, 60min, or 180min. The latter time point was included to examine prolonged versus transient phosphorylation of p65. At 10ng/ml, CX3CL1 did not induce significant phosphorylation of p65 at either 15, 30, 60, or 180min (Figure 6.5B, D). Of all the time points studied, THP-1 monocytes showed a slight increase in phosphorylated p65 at 60min compared to that of untreated cells, though this increase was modest and not significant. TNF-α-treated cells showed a significant increase in phosphorylated p65 ($p<0.01$). At a higher concentration of 50ng/ml, CX3CL1 also did not stimulate significant p65 phosphorylation (Figure 6.5C, D). As observed for 10ng/ml CX3CL1, 50ng/ml CX3CL1 induced modest phosphorylation of p65 at 60min, though again this was only marginal compared to untreated THP-1 monocytes.

Based on these findings, stimulation of THP-1 monocytes with CX3CL1 at a concentration of 10ng/ml for 60 minutes was repeated to identify whether the modest NFκB response observed under these conditions was reproducible and therefore valid. Following repeated experiments, this optimised dose and timing of CX3CL1 at 10ng/ml for 60 minutes induced modest significant phosphorylation of the NFκB subunit p65 compared untreated cells ($p<0.01$) (Figure 6.6). The findings of this work therefore concluded that CX3CL1 stimulation of THP-1 monocytes leads to low levels of NFκB activation as determined by increased phosphorylation of p65.

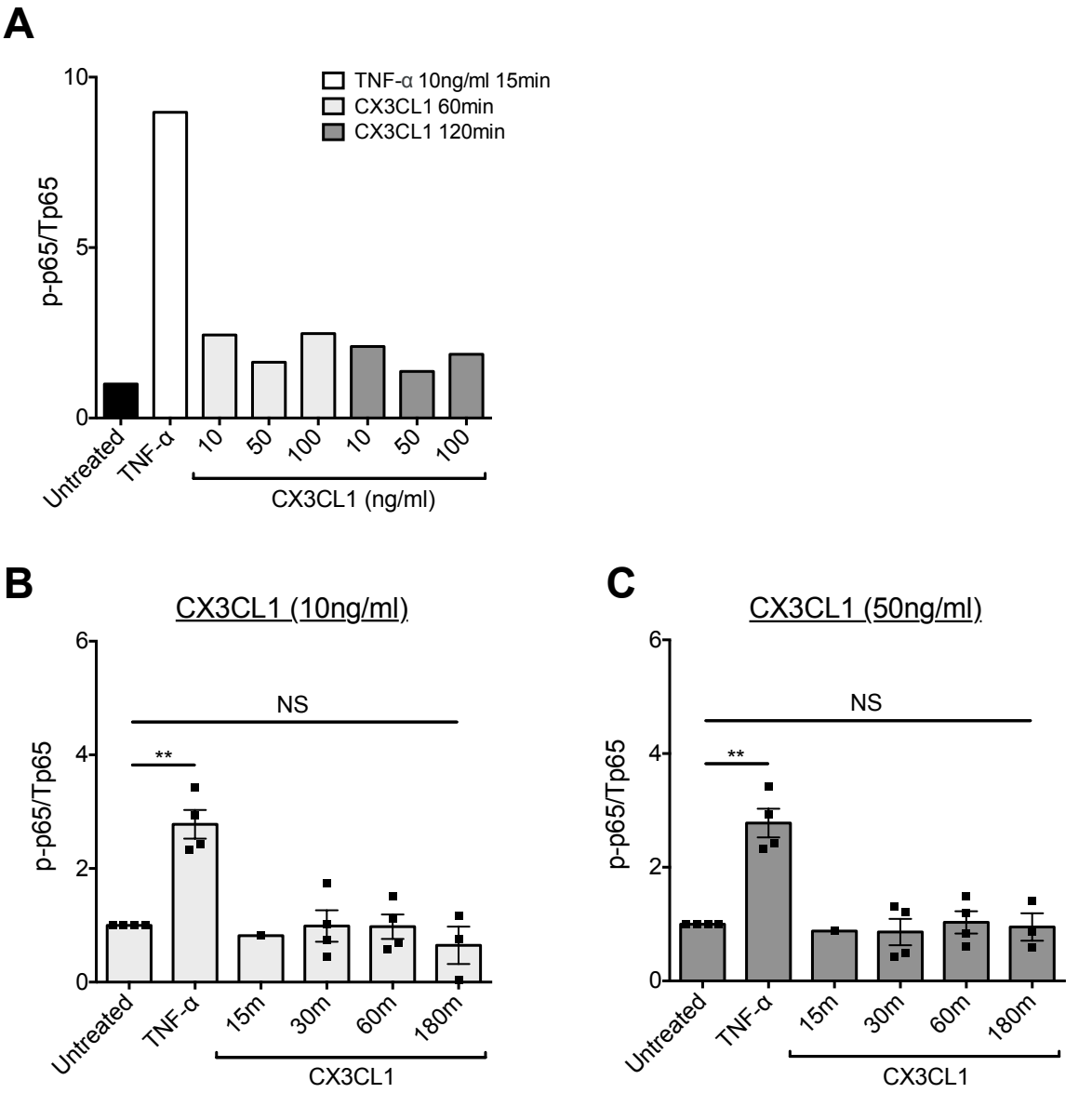
A
TNF-α 10ng/ml 15min
CX3CL1 60min
CX3CL1 120min
p-p65/Tp65
10
5
0
Untreated
TNF-α
10
50
100
10
50
100
CX3CL1 (ng/ml)
B
CX3CL1 (10ng/ml)
NS
**
p-p65/Tp65
6
4
2
0
Untreated
TNF-α
15m
30m
60m
180m
CX3CL1
C
CX3CL1 (50ng/ml)
NS
**
p-p65/Tp65
6
4
2
0
Untreated
TNF-α
15m
30m
60m
180m
CX3CL1
D
- 30 - 60 - 180 - - Mins CX3CL1 10ng/ml
- - 30 - 60 - 180 - Mins CX3CL1 50ng/ml
- - - - - - - 15 Mins TNF-α 10ng/ml
p-p65 (S536)
Total p65
α-tubulin (p-p65)

Figure 6. 5. Optimisation of CX3CL1 stimulation dose and time in THP-1 cells for activation of the NFκB pathway measured by phosphorylation of the NFκB subunit p65.

TNF-α was used as a positive control which is known to induce phosphorylation of p65 after 15min at 10ng/ml. A. Dose response to CX3CL1 at 10, 50, and 100ng/ml for 60min or 120min. B. Time response to CX3CL1 at 10ng/ml for 15, 30, 60 and 180min. C. Time response to CX3CL1 at 50ng/ml for 15, 30, 60 and 180min. One-way Anova with Tukey's multiple comparison test. Data refers to mean ± SEM. **p<0.01. D. Western blot showing phosphorylated p65 in response to CX3CL1 or TNF-α stimulation at the time and dose stated. Levels of phosphorylated p65 were normalised to total p65 and α-tubulin was detected as a loading control.

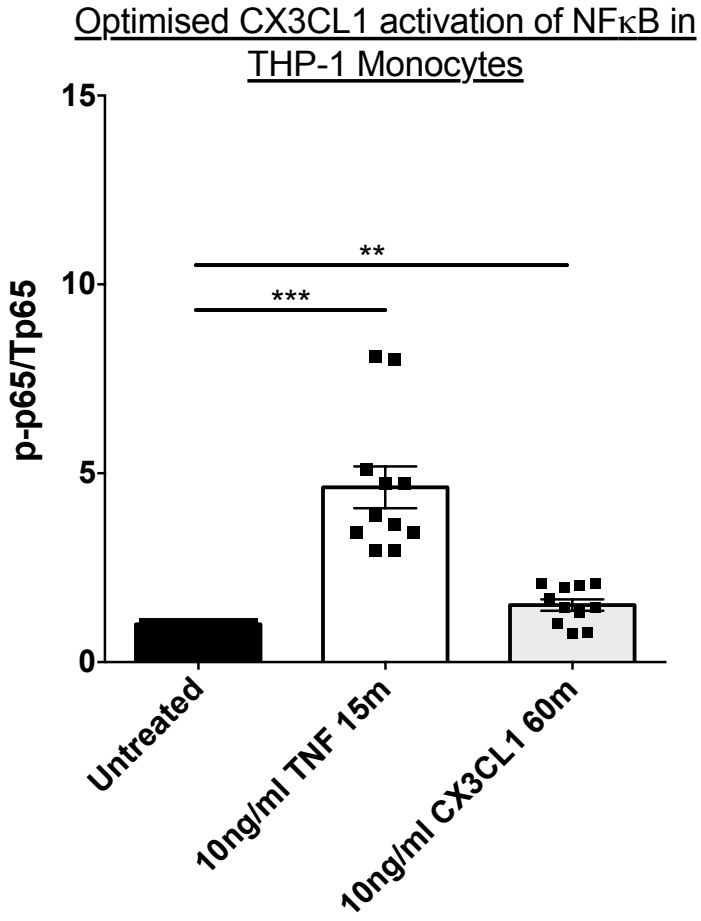

Figure 6. 6. Optimised dose and timing of CX3CL1 stimulation of THP-1 human monocytes at 10ng/ml for 60 minutes induces significant phosphorylation of NFκB p65 subunit. Levels of phosphorylated p65 were normalised to total p65. One-way Anova with Tukey's multiple comparison test. Data refers to mean ± SEM. **p<0.01, ***p<0.001.

6.2.4 Human CX3CR1 inhibitor KAN567 (Compound 18a, AZD8797) and NFκB inhibitor BI605906 dose response inhibition of CX3CL1-induced p65 phosphorylation

Following the observation that CX3CL1 can induce modest phosphorylation of p65 during optimal conditions (10ng/ml CX3CL1, 60min), the next aim of this work was to determine if this response could be blocked in the presence of a i) NFκB pathway inhibitor and ii) CX3CR1 inhibitor. To inhibit the NFκB pathway, the molecule BI605906 was used. BI605906 is a selective IKKβ inhibitor (IC50 = 380nM), which displays no effect on a panel of 100 kinases, except IGF1 (IC50 = 7.6μM). A range of inhibitor doses (0.5-10μM) was decided based on those that are reported to effectively inhibit IKKβ; Clark et al [385] showed inhibition of p65 phosphorylation at 2-40μM BI605906, while Zhang et al [386] show inhibition of IKKβ by BI605906 at 5μM. In addition to IKKβ, a number of kinases have been identified that phosphorylate p65-Ser536 including RSK1, IKKα, IKKe, and NAK/TBK1 [366, 387-389]. The conditions and consequences of p65-Ser536 phosphorylation appear to depend on the physiological context. Pre-incubation of CX3CL1-treated THP-1 cells with BI605906 was therefore also useful to confirm that CX3CL1-induced phosphorylation of p65 occurs via IKKβ, as oppose to other upstream signalling molecules.

THP-1 cells were treated with either 10ng/ml 60min CX3CL1 alone, or with 0.5, 1, 2.5, 5, or 10μM BI605906 for 30 minutes prior to CX3CL1 stimulation (Figure 6.7A, B). A control group of THP-1 cells were treated with DMSO only as the BI605906 inhibitor was stored in DMSO. At the lowest concentration of BI605906 of 0.5μM, levels of phosphorylated p65 were not significantly different from CX3CL1-only treated cells. At 1μM BI605906 however, CX3CL1-induced p65 phosphorylation was significantly reduced ($p<0.05$). Treatment with higher concentrations of the IKKβ inhibitor BI605906 at 2.5μM and 10μM further decreased phosphorylated levels of p65, to below that of CX3CL1-only treated cells ($p<0.01$). Notably, inhibition of IKKβ by BI605906 at all doses tested reduced levels of phospho-p65 to below that of CX3CL1-treated and untreated cells, suggesting that BI605906 may inhibit a p65 response that is stimulated by factors other than CX3CL1.

Secondly, to determine if the previously observed p65 phosphorylation was truly a response to CX3CL1 and not any other confounding stimuli, the CX3CR1 antagonist KAN567 was used to treat THP-1 cells prior to stimulation with CX3CL1 (10ng/ml, 60min). KAN567 is a human CX3CR1 inhibitor **(**Compound 18a, AZD8797). As the NFκB pathway is known to be activated by a broad range of stimuli, it was important as part of this study to determine whether CX3CL1-induced phosphorylation of p65 under optimal conditions was a specific response to CX3CL1, and could therefore be inhibited upon blockade of CX3CR1 by KAN567. Concentrations of KAN567 between 40nM-10μM have been shown to inhibit CX3CL1 binding to CX3CR1 [390]. A dose range of 1nM-1μM was therefore employed in this study. A vehicle only treated sample was used as a control, which is the buffer used by the manufacturer (Kancera) to dissolve the inhibitor.

In contrast to incubation with the IKKβ inhibitor BI605906, pre-incubation with the CX3CR1 inhibitor KAN567 for 30 minutes prior to CX3CL1 treatment did not significantly reduce p65 phosphorylation induced by CX3CL1 stimulation (10ng/ml 60min) (Figure 6.7C, D). At doses of 1, 10, 100, 500, and 1000nM, KAN567 had no significant inhibitory effect on CX3CL1-induced phosphorylation of p65. Such findings suggested that activation of the NFκB pathway observed in the presence of CX3CL1 (10ng/ml 60min) may in part be due to the presence of other stimuli which also induce this pathway, which is discussed in more detail in section 6.3. This is also suggested by the subtle induction of p65 phosphorylation observed in vehicle only-treated THP-1 cells (Figure 6.7 C, D).

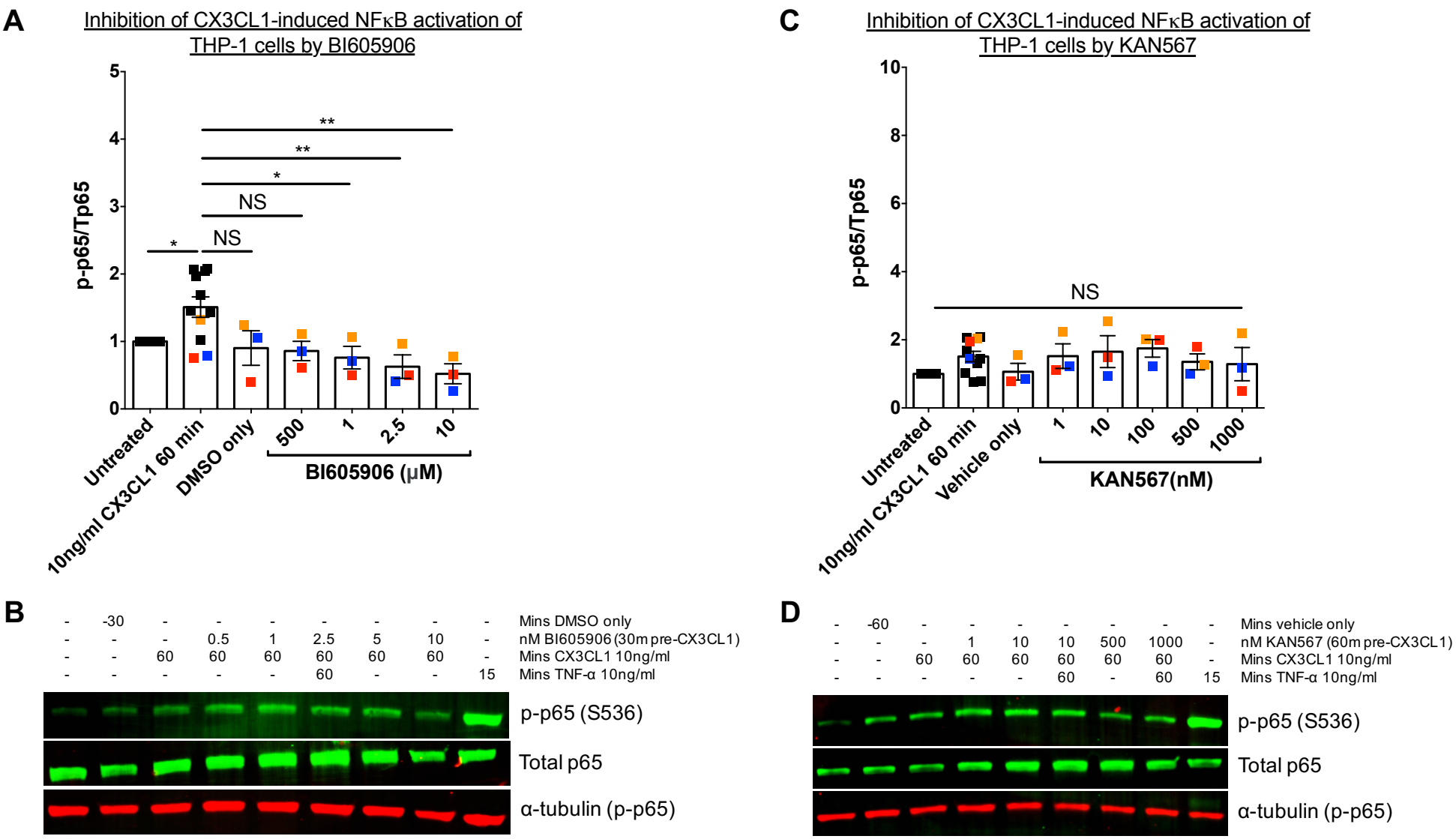
A
Inhibition of CX3CL1-induced NFκB activation of THP-1 cells by BI605906
p-p65/Tp65
0
1
2
3
4
5
**
**
*
NS
NS
*
Untreated
10ng/ml CX3CL1 60 min
DMSO only
500
1
2.5
10
BI605906 (μM)
C
Inhibition of CX3CL1-induced NFκB activation of THP-1 cells by KAN567
p-p65/Tp65
0
2
4
6
8
10
NS
Untreated
10ng/ml CX3CL1 60 min
Vehicle only
1
10
100
500
1000
KAN567(nM)
B
- -30 - - - - - - - Mins DMSO only
- - - 0.5 1 2.5 5 10 - nM BI605906 (30m pre-CX3CL1)
- - 60 60 60 60 60 60 - Mins CX3CL1 10ng/ml
- - - - - 60 - - 15 Mins TNF-α 10ng/ml
p-p65 (S536)
Total p65
α-tubulin (p-p65)
D
- -60 - - - - - - - Mins vehicle only
- - - 1 10 10 500 1000 - nM KAN567 (60m pre-CX3CL1)
- - 60 60 60 60 60 60 - Mins CX3CL1 10ng/ml
- - - - - 60 - 60 15 Mins TNF-α 10ng/ml
p-p65 (S536)
Total p65
α-tubulin (p-p65)

Figure 6. 7. Inhibition of CX3CL1-induced p65 phosphorylation by NFκB and CX3CR1 inhibitors.

A. Selective IKKβ inhibitor BI605906 dose response inhibition of CX3CL1-induced p65 phosphorylation. n=3/dose of BI605906; additional n=8 without BI605906 inhibitor. DMSO only control was included as BI605906 was dissolved in DMSO. One-way Anova with repeated measures analysis**.** Data refers to mean ± SEM. *p<0.05, **p<0.01. B. Western blot showing dose response inhibition of CX3CL1-induced p65 phosphorylation in the presence of the selective IKKβ inhibitor BI605906. C. CX3CR1 antagonist KAN567 (Compound 18a, AZD8797) dose response inhibition of CX3CL1-induced p65 phosphorylation. n=3/dose KAN567; additional n=8 without KAN567 inhibitor. Vehicle only control was included as KAN567 was dissolved in this buffer. One-way Anova with repeated measures analysis**.** Data refers to mean ± SEM. B. Western blot showing dose response inhibition of CX3CL1-induced p65 phosphorylation in the presence of the CX3CR1 antagonist KAN567. Levels of phosphorylated p65 were normalised to total p65 and α-tubulin was used as a loading control throughout.

6.2.5 Expression of NFκB Target Genes IL-8, IκBα, IL-β, and IL-6 by CX3CL1

A well-recognized function of NFκB is the regulation of inflammatory responses. NFκB is an inducible transcription factor which upon activation, targets inflammation by directly increasing the production of pro-inflammatory cytokines, chemokines, and adhesion molecules. NFκB also regulates cell proliferation, apoptosis, morphogenesis and differentiation [391]. Among the most well-established inducers of NFκB in the context of inflammation are members of the TNF family of cytokines [392, 393]. TNF-α is known to upregulate transcription of pro-inflammatory genes IL-8, IL-6, and IL-1β via activation of the NFκB pathway. Gene transcription of TNF-α's target genes is known to occur at 2-6h following stimulation, at a concentration of 10ng/ml [394, 395]. NFκB is also known to regulate its own pathway in a negative feedback loop; activation of NFκB for example by TNF-α induces IκBα gene transcription. In THP-1 monocytes, Gomes et al have shown that the NFκB pathway is activated by LPS stimulation, which leads to increased production of the inflammatory cytokines TNF-α, IL-1β, IL-6, and -8 [396]. Monocyte activation of the NFκB pathway specifically in response to CX3CL1 has however not been explored to date. Based on the previous observation that CX3CL1 stimulation can lead to slight induction of p65 phosphorylation in THP-1 monocytes, the next part of this work was to identify downstream target genes of NFκB signalling that are regulated by CX3CL1 stimulation. Elucidation of such target genes would help to understand how the CX3CL1/CX3CR1 axis contributes to monocyte function following cardiac I/R.

To investigate this, THP-1 cells were seeded on day 0 and left to culture for 48h at 37°C in normal media. This time frame allowed for any effect of fresh serum on NFκB pathway activation to plateau before stimulation with CX3CL1. THP-1 monocytes were lysed for total RNA at either 2h, 6h, or 16h following CX3CL1 stimulation and reverse transcription was performed to obtain cDNA. Real-time PCR was then carried out probing for NFκB target genes IL-8, IL-6, IL-1β and IκBα. GAPDH and RPL13A were included as housekeeper reference genes. Results were normalized using the ΔΔCT method. Concentrations of CX3CL1 of 10ng/ml and 50ng/ml were used on the basis of the modest phosphorylation of p65 observed previously at these concentrations of

the ligand. Time points of 2h, 6h, and 16h were chosen on the basis that gene transcription changes are known to occur within this time frame. The well-established inducer of NFκB target gene expression, TNF-α, was used as a positive control in this study.

Data shown in Figure 6.8A shows that IL-8 expression was increased by TNF-α stimulation for either 2h or 6h at 10ng/ml compared to untreated cells, however this was not significant. Stimulation of THP-1 cells with CX3CL1 for 2h did not significantly change the expression levels of IL-8 at either concentration of CX3CL1 tested. A longer stimulation of CX3CL1 at 10ng/ml for 6h however lead to a significant increase in IL-8 expression ($p = 0.039$) (Figure 6.8A). Analysis of three of the independent experiments showed that this upregulation of IL-8 expression was greater at the lower dose of 10ng/ml CX3CL1 ($p = 0.011$), than 50ng/ml CX3CL1 ($p = 0.037$) (Figure 6.8B). Investigation of IL-8 gene expression following an extended CX3CL1 stimulation of 16h showed that the expression of this chemokine was not significantly increased at this time point.

Stimulation of THP-1 monocytes with TNF-α for both 2h and 6h at 10ng/ml significantly increased the expression of NFκB gene targets IκBα and IL-1β (Figure 6.8C, D). TNF-α stimulation increased IκBα expression more significantly at 2h ($p = 0.0003$) than 6h ($p = 0.001$). Expression of IL-1β was upregulated significantly to a similar extent at 2h ($p = 0.0007$) and 6h ($p= 0.0003$) following TNF-α expression. Stimulation with CX3CL1 for either 2h, 6h, or 16h at the two concentrations of the ligand tested did not however significantly change the expression of NFκB targets IκBα (Figure 6.8C) and IL-1β (Figure 6.8D).

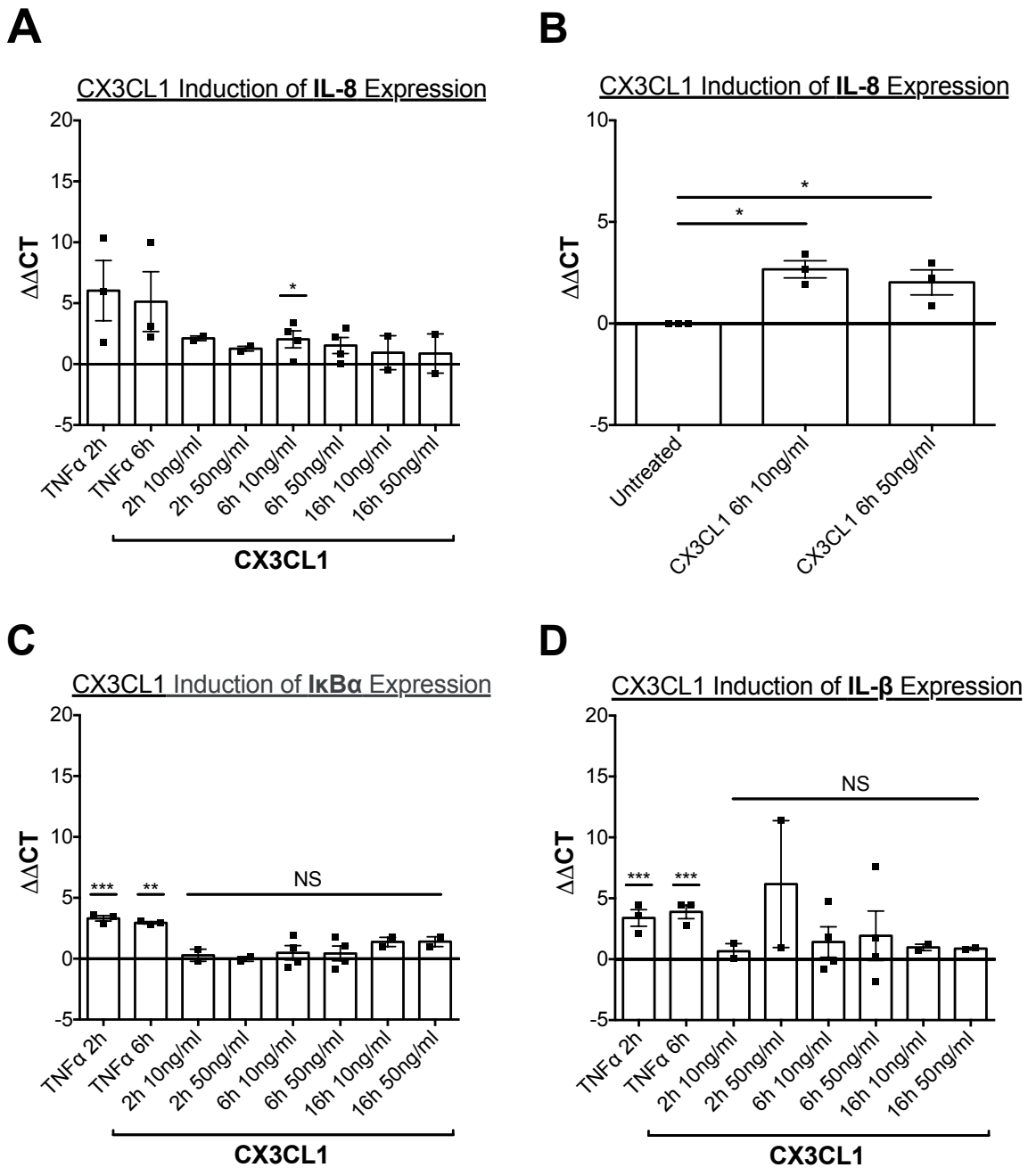

Figure 6. 8. CX3CL1 induction of NFκB target genes in THP-1 monocytes.

THP-1 cells were stimulated with either 10 or 50ng/ml CX3CL1 for either 2h (n=2), 6h (n=4), or 16h (n=2) to study the regulation of NFκB inflammatory target genes IL-8 (A, B), IκBα (C), and IL-1β (D). TNF-α stimulation at 10ng/ml for 2h or 6h was used as a positive control (n=3/time point). One-way Anova with Tukey's test for multiple comparisons. Data refers to mean ± SEM. *p<0.05, **p<0.01, ***p<0.001.

6.2.6 Purification of Human Whole Peripheral Blood Monocytes

In the previous section I showed that THP-1 human monocytes show a slight induction of p65 phosphorylation in response to CX3CL1 stimulation (10ng/ml 60min). Downstream of this activation, THP-1 monocytes showed modest upregulation of IL-8 expression following 6h stimulation with 10ng/ml CX3CL1. Based on these observations it is plausible that CX3CL1 ligand binding to its receptor CX3CR1 induces minor activation of the NFκB pathway in THP-1 monocytes. Such a modest response may be explained by the low levels of CX3CR1 expressed by THP-1 monocytes shown in section 6.2.2. Immunophenotyping of these cells previously showed that expression of CX3CR1 by these cells resembles that of human $CX3CR1^{lo}$ classical monocytes. Due to their high expression levels of CX3CR1, non-classical monocytes would provide an ideal model to study NFκB activation by CX3CL1/CX3CR1 signalling. Current available human monocyte cell lines however, like THP-1 monocytes, possess a mature classical monocyte phenotype, as shown in this study for MM6 and U937 cells and by others [397]. As such, there is no existing human cell line available which represents non-classical monocytes. Attempts to mature the most advance cell line (MonoMac6) [398, 399] to become CD16-positive have not been successful thus far. Furthermore, gene expression data, CD marker profile and functional chemotaxis assays suggest that the monocyte cell lines THP-1 and U937 only partly resemble freshly isolated human classical $CD14^{+}$ monocytes in their undifferentiated state [400]. With this in mind, it appears that the most appropriate method of studying CX3CL1-induced NFκB activation in non-classical monocytes is to purify these cells from fresh human whole blood/PMBCs. Techniques to isolate monocytes from human whole blood are fairly established, however there is evidence that the choice of monocyte enrichment protocol significantly affects the yield, purity, relative abundance of monocyte subsets, and the resulting phenotype of cultured monocytes [401, 402]. Among monocyte isolation methods, negative selection of monocytes appears to be the most effective, whereby the distribution of monocyte subsets is not substantially altered [403].

Based on these reports, this study used a negative human monocyte selection protocol. This approach is based on the labeling of non-monocytes with biotin-

conjugated antibodies and subsequent depletion of the labeled cells by binding to streptavidin-conjugated magnetic beads, while monocytes remain untouched. The Monocyte Isolation Kit II (Miltenyi Biotec, #130-091-153) contains anti-CD3 and anti-CD7 to label T cells, anti-CD16 (granulocytes), anti-CD19 (B cells), anti-CD56 (NK cells), anti-CD123 (granulocytes), as well as anti-CD235a to label red blood cells. Using this approach, the count of non-classical monocytes that could be obtained from a specified volume of human whole blood was determined to plan subsequent NFκB protein and gene expression analysis experiments accordingly.

EDTA anti-coagulated blood was obtained from healthy volunteers after informed consent and in accordance with the ethical guidelines of the institution. Monocytes were extracted as described in section 3. The purity of human monocytes was evaluated by fluorescent staining with the previously established human monocyte marker antibody panel (CD14, CD16, HLA-DR, CD3, CD19, CD56, CCR2, CX3CR1) and FACS analysis.

The extracted PBMC cell suspension corresponded to a yield of $1x10^7$ PBMCs/ml of whole blood as determined by manual counting, and was made up of a heterogeneous population of immune cells including T-cells, B-cells, NK-cells, and monocytes (Figure 6.9A). FACS analysis of the isolated PBMCs showed that the total monocyte population ($HLA\text{-}DR^+$ Lin^-) represented 4.3% of total PBMCs (Figure 6.9B), and therefore yielded ~$4.3x10^5$ monocytes/ml blood. The PBMC sample was then enriched for monocytes by depletion of non-monocytic cell types. The obtained yield of purified monocytes represented 95.7% of total cells (Figure 6.9C), which was approximately 4.9x higher than that achieved from peripheral whole blood and 22.3x higher than PMBC total monocytes. The non-monocyte fraction of PBMCs was analysed to confirm the effective extraction of monocytes (Figure 6.9D). This population contained 2% monocytes among all other leukocytes, further confirming successful extraction of the monocyte population. Furthermore, as this protocol only involved one stage of immune-magnetic separation, there was high viability of purified monocytes of >95% (Figure 6.10B). Isolated human classical, intermediate, and non-classical monocytes expressed characteristic expression of CCR2 and CX3CR1, demonstrating that the extraction process did not affect the expression of these chemokine markers (Figure

6.10A). Of the purified total monocyte population, classical monocytes represented ~85%, non-classical monocytes 5-10% and intermediate monocytes <5% (Figure 6.10B). Considering that 4.3×10^5 monocytes could be obtained per ml of blood, the hypothetical isolation yield of non-classical monocytes which represent 5-10% of total monocytes was $2.15x10^4$-$4.3x10^4$ cells/ml blood. These findings were obtained from two independent experiments using whole blood from two different volunteers.

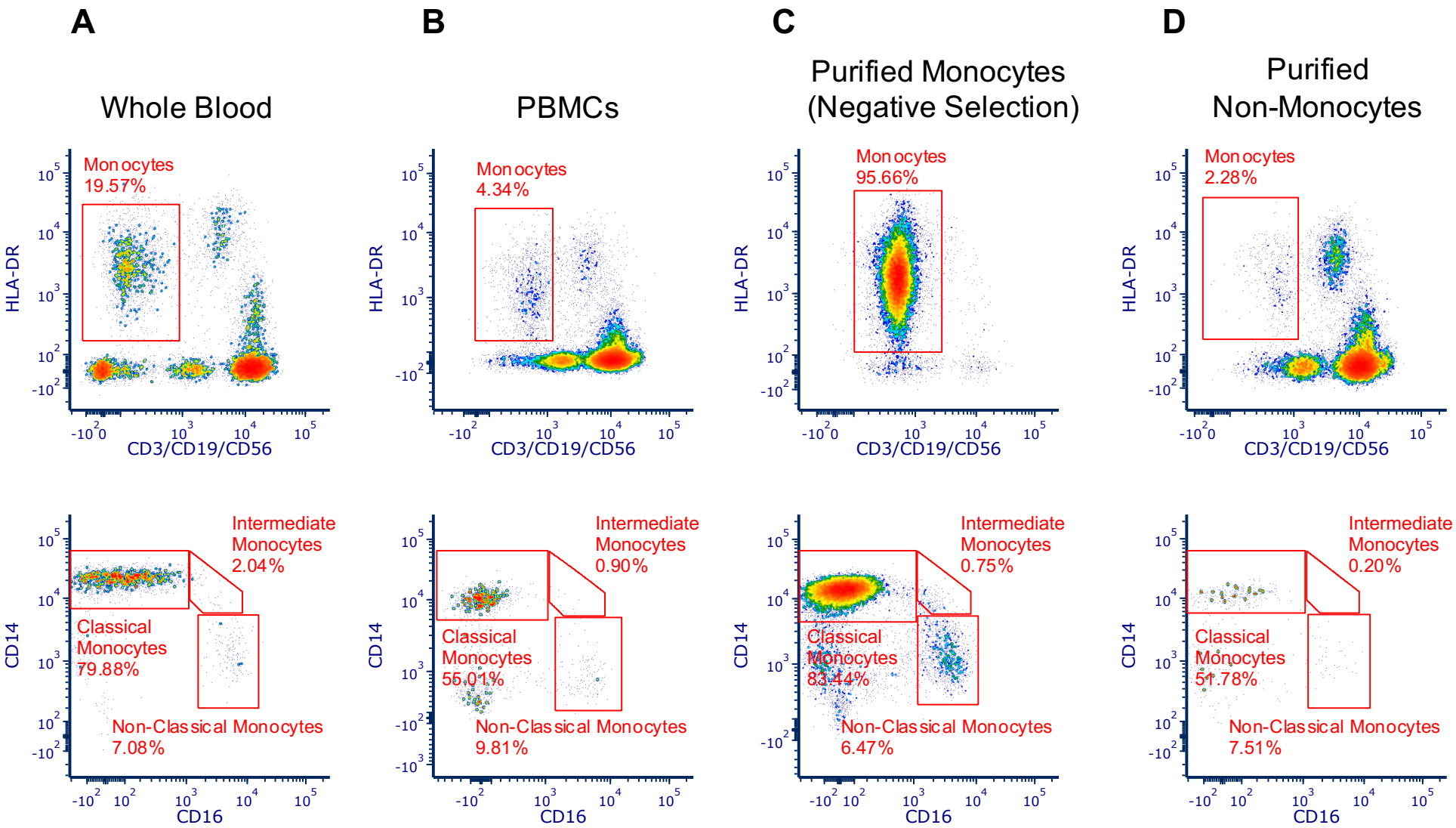
A
Whole Blood
Monocytes
19.57%
HLA-DR
CD3/CD19/CD56
Intermediate
Monocytes
2.04%
Classical
Monocytes
79.88%
Non-Classical Monocytes
7.08%
CD14
CD16
B
PBMCs
Monocytes
4.34%
HLA-DR
CD3/CD19/CD56
Intermediate
Monocytes
0.90%
Classical
Monocytes
55.01%
Non-Classical Monocytes
9.81%
CD14
CD16
C
Purified Monocytes
(Negative Selection)
Monocytes
95.66%
HLA-DR
CD3/CD19/CD56
Intermediate
Monocytes
0.75%
Classical
Monocytes
83.44%
Non-Classical Monocytes
6.47%
CD14
CD16
D
Purified
Non-Monocytes
Monocytes
2.28%
HLA-DR
CD3/CD19/CD56
Intermediate
Monocytes
0.20%
Classical
Monocytes
51.78%
Non-Classical Monocytes
7.51%
CD14
CD16

Figure 6. 9 Purification of human whole peripheral blood monocytes by negative selection beads.

PBMCs were firstly removed by centrifugation of whole blood over Histopaque (Sigma Aldrich, #10771), followed by erythrocyte lysis using Lysing Buffer (BD Pharm Lyse, #555899). PBMCs were then subject to monocyte negative selection using the Monocyte Isolation Kit II and manual columns (Miltenyi Biotec, #130-042-201). Flow Cytometry was used to analyse the total monocyte population in A. human whole blood, B. extracted PBMCs, C. purified monocyte population obtained by negative selection, D. purified non-monocyte population.

.

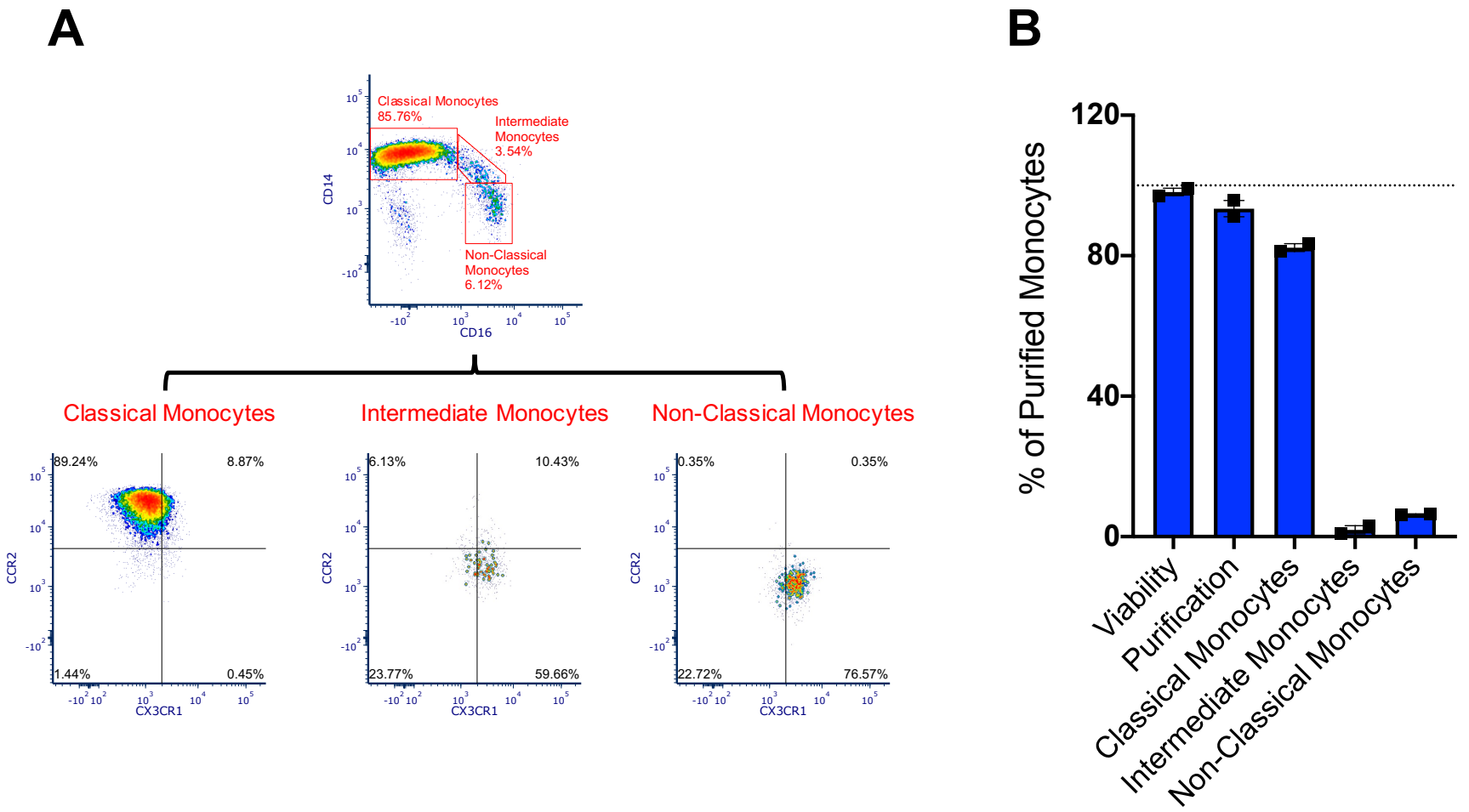
A
Classical Monocytes
85.76%
Intermediate
Monocytes
3.54%
Non-Classical
Monocytes
6.12%
CD14
CD16
Classical Monocytes
Intermediate Monocytes
Non-Classical Monocytes
89.24%
8.87%
1.44%
0.45%
6.13%
10.43%
23.77%
59.66%
0.35%
0.35%
22.72%
76.57%
CCR2
CX3CR1
B
% of Purified Monocytes
120
80
40
0
Viability
Purification
Classical Monocytes
Intermediate Monocytes
Non-Classical Monocytes

Figure 6. 10. Purification, viability, subpopulation composition and chemokine marker expression of extracted human blood monocytes.

A. Expression of chemokine receptors CCR2 and CX3CR1 by purified human blood monocytes. This magnetic-separation process does not alter the expression of these key monocyte markers. B. The viability, purification, and composition of purified total monocytes from human whole blood. This monocyte isolation protocol yielded a high purity of monocytes of >95%, of which classical monocytes represented ~85%, non-classical monocytes 5-10% and intermediate monocytes <5%. Data representative of two independent experiments (two human volunteer blood samples). Data refers to mean ± SEM.

6.2.7 FACS Analysis of NFκB subunit p65 Phosphorylation by CX3CL1 stimulation of Monocytes

The purification of monocytes from human whole blood described in the previous section was performed to establish the counts of monocytes that could be obtained from a specified volume of blood and thus determine the sample required for subsequent protein and gene expression experiment analysis. It was initially hypothesized that the CX3CR1^{+} non-classical monocyte proportion of this purified total monocyte population would show a stronger NFκB response to CX3CL1 stimulation than that observed for THP-1 monocytes, due to their higher expression levels of CX3CR1 (Figure 6.10A). However, the yield of non-classical monocytes that could theoretically be obtained ($2.15x10^4$-$4.3x10^4$ / ml blood), would not permit the study of p-p65 expression by western blot protein analysis as performed using THP-1 monocytes, as this required a minimum of $1x10^6$ cells per treatment.

Due to this low count of non-classical monocytes, it was decided to first investigate the total monocyte NFκB response to CX3CL1 by western blot analysis. As 1ml of blood yielded 4.3×10^5 total purified monocytes, 60ml of volunteer blood was obtained, as this would give a theoretical yield of ~$2.5x10^7$ monocytes. Once the sample was obtained, PBMCs were isolated, and monocytes were purified as described in section 6.2.6. An excess volume of blood was included to allow for loss of some cells during PBMC isolation and monocyte purification. From the purified total monocyte population, $3x10^6$ cells were cultured per condition (untreated, CX3CL1 and TNF-α) in serum-free RPMI-1640 to avoid the induction of the NFκB pathway by serum. Cells were cultured briefly for 30min prior to stimulation with CX3CL1 or TNF-α. Following treatment, it was observed that all monocytes were no longer viable leading to termination of the experiment. This is likely due to the effect of serum-starvation which has been shown to induce apoptosis of monocytes. CX3CL1 has been shown to rescue cells from starvation-induced apoptosis, though interestingly there was no pro-survival effect observed in CX3CL1-treated cells during this experiment. Other methods of culturing purified human monocytes must therefore be tested in future work.

An alternative approach to study activation of the NFκB pathway by CX3CL1 rather than protein expression analysis is to analyse levels of phosphorylated p65 by FACS. This method would also permit analysis of p-p65 expression specifically by the non-classical monocyte subpopulation, since these cells could be gated and defined as $CD14^{+}CD16^{++}CX3CR1^{hi}CCR2^{lo}$ cells. This technique required optimisation, as a complex method of fixation and permeablisation of cells is required to permit both monocyte surface marker antibody binding and detection of intracellular p-p65. This optimization was carried out using the MM6 monocyte cell on the basis that these cells express slightly higher levels of CX3CR1 and thus a response to CX3CL1 would be more obvious if present. The protocols tested are summarized in Table 6.1. Protocol 1 highlighted in green was the most effective. This work was completed with the help of post-doc Dr. Catherine Park.

As per protein expression analysis, TNF-α treatment was used as a positive control to compare with optimized CX3CL1 treatment (10ng/ml for 60 min), with or without 30min pre-treatment with the CX3CR1 inhibitor KAN567 (10nM). This preliminary analysis showed that untreated MM6 cells showed slight induction of the NFκB pathway as determined by increased levels of p-p65 (Figure 6.11, 6.12), which reflected the findings observed in the previous THP-1 protein analysis. Treatment with TNF-α (10ng/ml, 15m) further increased the percentage of $p\text{-}p65^{+}$ MM6 monocytes, though this response was not as striking as that observed in THP-1 p-p65 protein analysis. Stimulation of MM6 monocytes with CX3CL1 (10ng/ml 60min) lead to no difference in p-p65 activation compared with untreated cells (Figure 6.11, 6.12), in contrast to the modest p-p65 response observed in THP-1 cells by western blot analysis.

To test if this lack of response was a reflection of the low CX3CR1 expression by MM6 monocytes, this protocol was decided to be performed on human whole blood samples, which would permit examination of the specific $CX3CR1^{hi}$ non-classical monocyte NFκB response to CX3CL1, by gating on $CD14^{+}CD16^{++}$ cells. This work was unfortunately prevented by Institute shutdown relating to the COVID-19 pandemic, but represents a starting point for future work building on this preliminary research.

Protocol	Step 1	Step 2	Step 3	Step 4	Step 5
1	Stain Monocytes (CD16, CD14)	Fix (PFA)	Permeabilisation (Methanol)	p-p65 Primary Antibody Stain	p-p65 Secondary Antibody Stain
2	Stain Monocytes (CD16, CD14)	Fix (PFA)	Permeabilisation (Triton-X)	p-p65 Primary Antibody Stain	p-p65 Secondary Antibody Stain
3	Fix (PFA)	Stain Monocytes (CD16, CD14)	Permeabilisation (Methanol)	p-p65 Primary Antibody Stain	p-65 Secondary Antibody Stain
4	Fix (PFA)	Stain Monocytes (CD16, CD14)	Permeabilisation (Triton-X)	p-p65 Primary Antibody Stain	p-p65 Secondary Antibody Stain

Table 6. 1. Protocols tested for FACS analysis of phosphorylated p65 (p-p65) in MM6 cells treated with CX3CL1.

Protocol 1 gave the clearest results and is also the method recommended by Cell Signalling [404]. All protocols were also tested for non-specific binding of the p-p65 secondary antibody by running a no p65 primary antibody control. This analysis showed no off-target binding of the secondary antibody.

Unstained

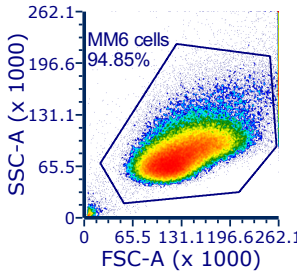

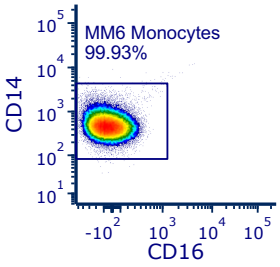

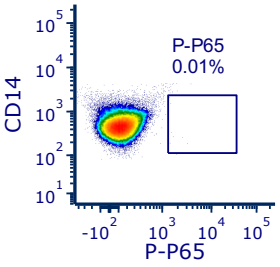

Untreated

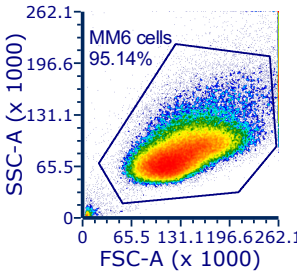

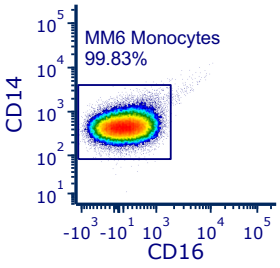

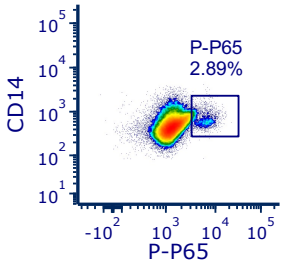

TNFα
10ng/ml
15m

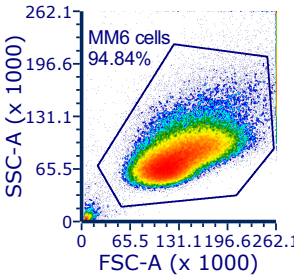

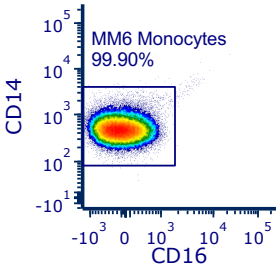

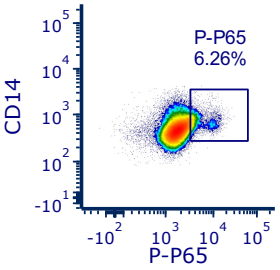

CX3CL1
10ng/ml
60m

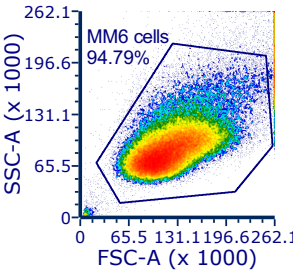

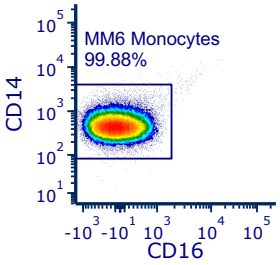

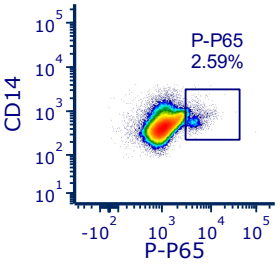

CX3CL1
10ng/ml
60m
+
KAN567
10nM

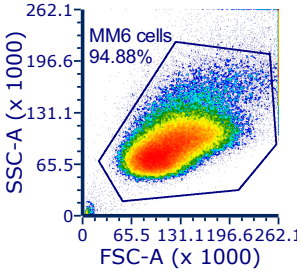

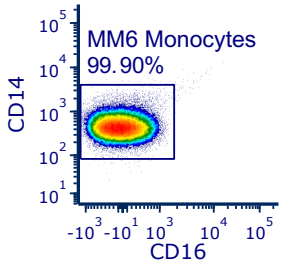

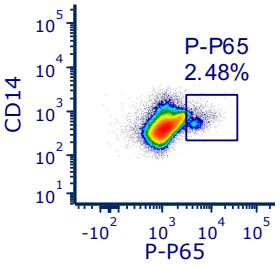

Figure 6. 11. FACS analysis of MM6 monocyte expression of phosphorylated p65 (p-p65) following CX3CL1 treatment (10ng/ml 60min).

Untreated cells showed low levels of p-p65 which are comparable with the levels observed following treatment with CX3CL1 at 10ng/ml for 60 min. This response is not blocked in the presence of the CX3CR1 inhibitor KAN567, suggesting induction of the NFκB pathway by factors other than CX3CL1. TNF-α treatment stimulated slightly higher phosphorylation of p65 than untreated cells and CX3CL1 treatment.

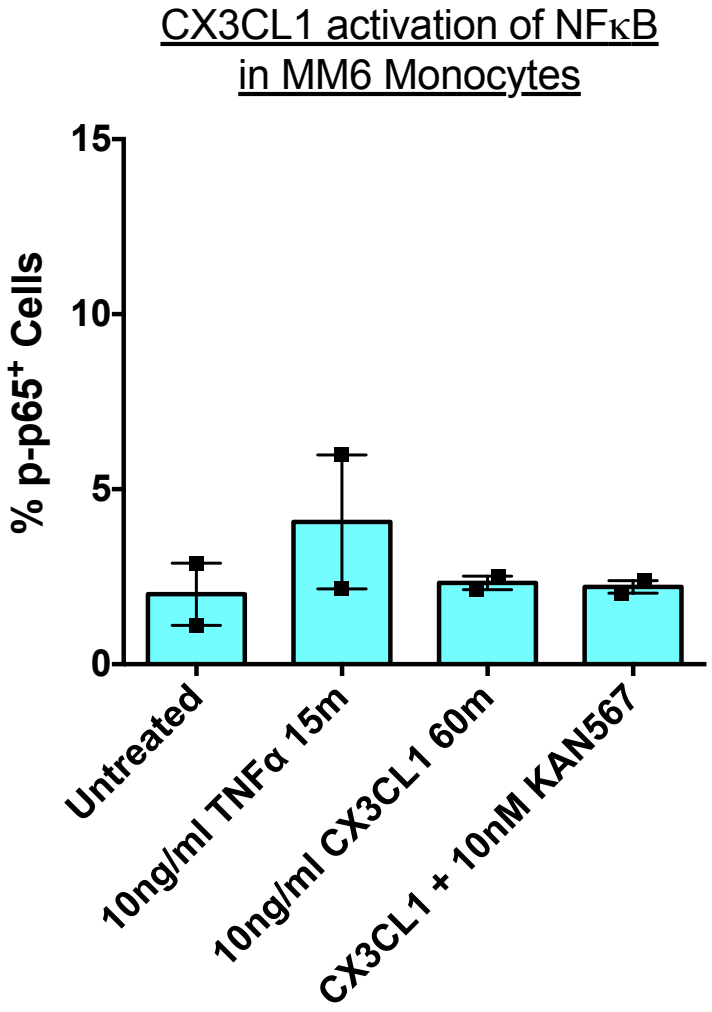

Figure 6. 12. Optimized protocol to investigate the levels of phosphorylated p65 (p-p65) in MM6 monocytes in response to CX3CL1 (10ng/ml 60min) stimulation.

Following stimulation with CX3CL1 (10ng/ml 60min), MM6 cells were stained for the monocyte markers CD16 and CD14, followed by fixation in PFA. Cells were then permeabilised using methanol to allow subsequent primary and secondary staining of intra-cellular p-p65. Pilot optimisation data from two independent experiments. Data refers to mean ± SEM.

6.3 Discussion

In this chapter I investigated how stimulation of CX3CR1^{+} monocytes with CX3CL1 ligand, which is known to increase in the circulation following STEMI, may activate the downstream pro-inflammatory NFκB signalling cascade. Elucidation of the mechanisms of CX3CL1/CX3CR1 signalling in non-classical monocytes will help to explain their exact function following cardiac I/R, and therefore help to understand the mechanistic link between their dynamics in the circulation and myocardial function following STEMI.

The data presented in this chapter indicates that CX3CL1 treatment of THP-1 monocytes at the optimal time and dose (10ng/ml for 60 minutes) can induce modest phosphorylation of the NFκB subunit p65, which leads to a small significant upregulation of the pro-inflammatory gene IL-8. CX3CL1 stimulation however had no significant effect on the expression of other NFκB pro-inflammatory target genes, IL-6 and IL-1β. It is plausible that the modest phosphorylation of p65 at Ser536 precedes the induction of IL-8 expression; studies have shown that transfection of the S536D form of p65 induces IL-8 transcription, while the S536A form, which cannot be phosphorylated at the p65-Ser536 site, does not [405]. As previously mentioned, the low induction of p65 phosphorylation and IL-8 expression by CX3CL1 stimulation shown in this work may be related to the low CX3CR1 expression levels by the THP-1 cell line; CX3CR1 expression is 12.9-fold lower in THP-1 monocytes compared to that of human peripheral blood non-classical monocytes. It is therefore conceivable that stimulation of human CX3CR1^{hi} non-classical monocytes by CX3CL1 would induce stronger activation of the NFκB pathway due to the considerably higher expression of CX3CR1 by this monocyte subset. Investigation of this non-classical monocyte NFκB response to CX3CL1 stimulation is however restricted to the use of freshly isolated human non-classical monocytes, due to the lack of an established non-classical monocyte cell line. The only evidence of a non-classical monocyte-resembling cell line is MonoMac1 cells, the sibling cell line of MonoMac6 monocytes, can have induced expression of CD16 in response to Macrophage Colony-Stimulating Factor (M-CSF) [406]. Purification of monocytes from human whole peripheral blood can be performed successfully, as demonstrated in this study using negative selection.

Activation of NFκB pathway by CX3CL1 stimulation specifically in non-classical monocytes can then be achieved by FACS analysis of p-p65. In this thesis, I present a preliminary protocol for investigating this, which was optimized on the MM6 monocyte cell line. Future work should focus on establishing a successful method of culturing human purified monocytes, which can then be used for this analysis.

While it is possible that the minimal response of THP-1 monocytes to CX3CL1 is related to low CX3CR1 expression, another consideration to make is the effect of serum on the activation of the NFκB signalling cascade. It is well established that activation of this pathway can be induced by a broad range of stimuli, each of which mediates a specific pathway of NFκB activation to induce a specific downstream function. A number of reports have suggested that exposure of cells to fresh media influences NFκB activation [407] and target gene expression. To avoid the confounding effects of serum on NFκB activation in this study, THP-1 cells were cultured with fresh media 48h prior to CX3CL1 stimulation, allowing the effects of serum on NFκB signalling to plateau before treatment with CX3CL1. Furthermore, the background level of p65 phosphorylation could be ascertained from untreated control cells, which had a significantly lower level of phosphorylated p65 than CX3CL1-treated cells (10ng/ml 60min), thereby supporting the subtle induction of the NFκB pathway by CX3CL1. An alternative method of using serum-free media could be employed to distinguish the relative effects of CX3CL1 and serum on NFκB activation if required, however this starvation of cells would also introduce confounding factors; serum starvation itself can lead to activation of the NFκB pathway. Frankenberger at al showed that DNA binding activity of NFκB in monocytes was detected without specific stimulation; constitutive NFκB activity was detected in the monocyte cell lines HL60, U937, THP-1, MonoMac1 and MonoMac6, in serum-free conditions [408]. Analysis of human primary cells also identified substantial constitutive NFκB activity in blood monocytes. It is therefore arguable that treatment of THP-1 cells with fresh media 48h prior to CX3CL1 stimulation is a more valid approach than serum-free media to investigate the THP-1 NFκB response to CX3CL1. Future work should however test reduced serum concentrations, between 0.1-10% to identify the effect on basal p65 phosphorylation events, or substitute serum with BSA.

It must also be acknowledged that the slight induction of IL-8 by CX3CL1 in THP-1 monocytes observed in this study does not occur for other target genes IL-1β, IL-6 and IκBα. Sasaki et al discuss that in U937 monocytes and human PBMCs, nuclear IκBα inhibits recruitment of Ser-536-p-p65 to the TNF-α, IL-1β, and IL-6 promoters, but does not repress the IL-8 promoter. [369]. As such, it is possible that induction of IL-8 expression in monocytes may still occur during inhibition of the NFκB pathway. Future work should therefore investigate CX3CL1-induced upregulation of IL-8 by THP-1 monocytes in the presence of the CX3CR1 antagonist KAN567. It is also possible that a higher concentration of CX3CL1 ligand is required to induce greater upregulation of IL-8; most chemokines bind optimally to their receptor between concentrations of 10-30nM (~100-300 ng/ml), however the concentrations of CX3CL1 used herein are at the lower end of this range.

A reproducible effect of CX3CL1 on NFκB-mediated IL-8 expression would help to explain the function of CX3CR1 monocytes following cardiac I/R, since IL-8 is heavily implicated in cardiovascular disease [409]. Following MI, IL-8 induces homing of neutrophils that contribute to myocardial injury [410]. It could therefore be hypothesized that increased CX3CL1 ligand in the circulation following STEMI induces NFκB activation in the vascular pool of $CX3CR1^{+}$ non-classical monocytes, which leads to increased production of IL-8 and therefore potentiated pro-inflammatory neutrophil recruitment to the infarct. Future experiments should therefore examine IL-8 production by cultured non-classical monocytes in response to CX3CL1, and migration of neutrophils in response to this. IL-8 is also involved in the establishment and preservation of an inflammatory microenvironment of the insulted vascular wall, and participates in all stages of atherosclerosis from vascular inflammation to cardiac remodeling after myocardial infarction [411]. The IL-8 cytokine also promotes and sustains the shift from an acute to a chronic inflammatory reaction in the vessel wall by mediating the release of the monocyte chemoattractant CCL2 and the shedding of IL-6Rα from neutrophils in the inflammatory infiltrate [411]. IL-8 is also an important modulator of monocyte-endothelial interaction under flow conditions; IL-8 can rapidly cause rolling monocytes to firmly adhere to endothelial-expressed E-selectin [412]. Inhibition of IL-8 in rabbit model lead to reduced myocardial injury after cardiac I/R

[413]. Furthermore in STEMI patients, high circulating concentrations of IL-8 is associated with large infarct size, impaired recovery of LV function, and adverse clinical outcome [414].

CX3CL1-induced IL-8 expression through NFκB activation in THP-1 monocytes may therefore result in different effects on the immune response to cardiac I/R. Since CX3CL1 is known to peak at 90 minutes following reperfusion in STEMI patients [209], CX3CL1 may induce the greatest expression of IL-8 at this time point, leading to increased production of IL-8 6h following stimulation, as shown in this study. This may lead to increased adhesion of non-classical monocytes to the endothelium, or cause exaggerated neutrophil recruitment to the injured myocardium and prolong the inflammatory response, leading to further myocardial damage.

Chapter 7.0. Discussion

7.1 Summary of Findings

7.1.1 Introduction

The primary aim of this research was to further understand the role of non-classical monocytes following acute cardiac I/R and the importance of the CX3CL1/CX3CR1 axis in this response. To date, research has documented the CX3CR1-mediated patrolling function of these cells along the vascular endothelium in both human and mouse, though their function outside of this immune surveillance in the acute response to cardiac I/R is unknown. In mouse models of cardiac I/R, $Ly6C^{lo}$ non-classical monocytes are known to dominate the second, reparative phase of repair at day 5-9 post-MI. These cells largely arise from the maturation of $Ly6C^{hi}$ classical monocytes which mediate the inflammatory phase of repair (day 1-3 post-MI). Recent work however suggests an earlier role of $CX3CR1^{+}$ non-classical monocytes, specifically of the 'patrolling vascular pool' of these cells, which have been observed in the injured myocardium within the first 3h of reperfusion [161, 163]. This thesis therefore hypothesized that $CX3CR1^{+}$ non-classical monocytes have a key role in the acute response (up to 24h) to cardiac I/R via CX3CL1/CX3CR1signalling, which influences cardiac repair and therefore cardiac function following myocardial I/R.

7.1.2 Acute depletion of circulating $CX3CR1^{+}$ non-classical monocytes at 90 minutes post-PCI is associated with STEMI patient infarct size and LVEF

In two studies of retrospective and prospective STEMI patients, I performed a detailed analysis of non-classical monocyte dynamics in the circulation at acute time points after reperfusion (15min, 30min, 90min, 180min, 24h). This study presents a novel analysis as there has been no previous investigation of monocyte dynamics during this immediate post-reperfusion period among published studies to date. The prospective study described in chapter 4 also provides a highly accurate quantification of STEMI patient circulating monocyte counts, due to the robust and reproducible

FACS method of defining monocyte subpopulations. In contrast, other published work has been criticized due to the inaccurate definition of each monocyte population [286].

The prevailing result from these studies was that non-classical monocytes are dramatically depleted in the circulation of STEMI patients at 90 minutes' post-reperfusion. This finding was consistent in both retrospective and prospective STEMI patient cohorts. These changes were not observed in the NSTEMI patient group, so was therefore specific for cases of acute I/R rather than a PCI-procedurally induced observation. Classical monocytes and intermediate monocytes did not demonstrate the same dramatic depletion at 90 minutes' post reperfusion that was observed for non-classical monocytes. Classical monocytes showed minor drop, which was slightly increased in intermediate monocytes. In this sense, a greater depletion of monocyte subpopulations was seen with increasing levels of CX3CR1 expression. Analysis of myocardial function in STEMI patients by cardiac MRI revealed that these acute post-reperfusion non-classical monocyte dynamics (pre-90min) were significantly associated with both patient infarct size and LVEF, whereby a greater depletion of $CX3CR1^{+}$ non-classical monocytes predicted larger infarct size and lower LVEF. As there was no significant association between monocyte subpopulation dynamics and MVO, this study suggests that monocyte kinetics during the acute 24h post-reperfusion are more related to infarct size than to microvascular damage. This is in contrast to the post-reperfusion lymphocyte response, whereby an early decrease (90min post-PCI) in STEMI patient circulating T cell counts is significantly associated with the extent of MVO [209].

The nature of this relationship is unclear, however a possible mechanism is that a larger infarct size stimulates a greater inflammatory cascade, involving increased cleavage of endothelium-expressed transmembrane CX3CL1 into soluble CX3CL1, which in turn which stimulates a greater depletion of non-classical monocytes from the circulation as they are recruited to the injured myocardium, as illustrated in Figure 7.1. This is particularly plausible since the concentration of circulating CX3CL1 in STEMI patients has been shown to peak at 90 minutes post-PCI [209], thus coinciding with non-classical monocyte depletion. This increased response of non-classical

monocytes may promote further leukocyte recruitment and potentiate the inflammatory response to I/R, leading to a compromised LVEF.
This research has therefore provided a basis for future clinical studies to investigate the relationship between non-classical monocyte dynamics and cardiac outcome in a much larger cohort of STEMI patients, and validate the findings presented in this thesis.

7.1.3 Genetic knockout of CX3CR1 affects the counts of circulating non-classical monocytes, but not their infiltration into the injured myocardium or cardiac function following myocardial I/R.

A large proportion of this thesis is focused on a murine model of cardiac I/R to investigate the effect of genetic CX3CR1 knockout on the monocyte response to myocardial I/R. This model provided two main powerful tools that were unavailable in the clinical setting; direct access to injured heart tissue, and a model of $CX3CR1^{-/-}$ monocytes, using the CX3CR1-GFP mouse line. To draw comparisons with the observed STEMI patient depletion of circulating non-classical monocytes following reperfusion, mouse circulating monocyte subpopulations were quantified at 2h following induced cardiac I/R. Mouse $Ly6C^{lo}$ non-classical monocytes were depleted in the circulation, as observed in the clinical setting. This however was not confined to non-classical monocytes but was also observed for classical and intermediate populations, which may relate to the similar expression levels of CX3CR1 between subsets, as discussed in Chapter 5. When analyzing the effect of CX3CR1 knockout on mouse blood monocyte populations, the data presented here confirms those findings reported by others; CX3CR1 knockout mice have significantly reduced counts of circulating non-classical monocytes at baseline, due to the absence of CX3CR1-mediated survival signals. Interestingly in this study, I showed that the extent of non-classical monocyte depletion from the circulation at 2h was significantly greater in CX3CR1 knockout mice than in wild-type mice. Further research is required to confirm if this is due to the reduced survival of these cells, or a greater recruitment of $CX3CR1^{-/-}$ non-classical monocytes to the injured heart tissue.

Analysis of immune cell infiltration into the injured myocardium showed that monocyte infiltration dramatically increases in the infarct at day 3 following I/R compared to 2h and 24h. Based on the data presented here, genetic CX3CR1 knockout does not significantly affect the infiltration of total monocytes into the injured myocardium at 2h, 24h, or day 3 following cardiac I/R. Sub-classification of monocytes into classical and non-classical monocytes based on GFP expression showed that non-classical monocyte counts in the injured myocardium at 24h were significantly lower in CX3CR1 knockout mice compared to *Cx3cr1*$^{+/GFP}$ control mice. The reduced counts of infiltrated non-classical monocytes at 24h in CX3CR1$^{-/-}$ mice were followed up by examining monocyte adhesion to myocardial LV veins at 2h post I/R. CX3CR1 is widely reported to be crucial for monocyte adhesion and thus CX3CR1$^{-/-}$ mice were hypothesized to have reduced counts of endothelial-adhered monocytes in the major veins of the injured myocardial tissue. Monocyte adhesion at 2h post-I/R was found to be specific to the I/R region, but was not significantly different between control Cx3cr1$^{+/GFP}$ and CX3CR1$^{-/-}$ mice. Following these findings, it was concluded that CX3CR1 knockout mice have reduced infiltration of non-classical monocytes at 24h, which is not due to impaired adhesion at 2h post-I/R, and subsequently recovers at day 3 I/R. This data was based on a comparison between *Cx3cr1*$^{+/GFP}$ and *Cx3cr1*$^{GFP/GFP}$ mice, therefore future work is required to investigate monocyte behaviour in wild-type mice. The methodological limitations regarding monocyte subset definition by immunofluorescence microscopy in this study also require these findings to be confirmed using more robust methods of non-classical monocyte definition in the heart tissue such as time-lapse imaging, intra-vital microscopy, or confocal microscopy. Future work should also build on the existing findings from this thesis showing that mouse circulating non-classical monocytes express significantly greater levels of PD-L1 than their classical monocyte counterpart. If this distinction in PD-L1 expression between monocyte subsets prevails in the mouse heart tissue, such a tool may allow more accurate identification of infiltrated non-classical monocytes than the methods used herein.

Analysis of macrophage subpopulations in the day 3 I/R heart showed that M1 macrophages are significantly more abundant than M2 macrophages, which is in line with current concepts. Comparison between *Cx3cr1*$^{+/GFP}$ control mice with CX3CR1

knockout hearts showed no effect of CX3CR1 knockout on macrophage subpopulations at day 3. A lack of phenotype was also observed in the assessment of mouse myocardial function at 6 weeks following cardiac I/R by MRI; wild-type, *Cx3cr1*$^{+/GFP}$ and CX3CR1 knockout mice showed no significant differences in ESV, EDV, and LVEF parameters. As discussed in detail in chapter 5, the absence of a striking phenotype in CX3CR1$^{-/-}$ mice may be explained by the development of compensatory mechanisms to overcome the lack of this key receptor. Investigation of CX3CL1/CX3CR1 inhibition through other mechanism such as pharmacological inhibition of CX3CR1 or CX3CL1, which would not be confounded by compensatory mechanisms, should therefore be investigated in future research. Other studies have demonstrated the effect of anti-CX3CL1 treatment on cardiac repair following I/R, therefore it would be of great interest to see how this method of inhibition influences the non-classical monocyte response to myocardial I/R.

7.1.4. CX3CL1/CX3CR1 signalling induces modest activation of the NFκB pro-inflammatory pathway

The third aim of this project was to investigate activation of the NFκB pathway downstream of CX3CL1/CX3CR1 stimulation in human monocytes. Both the NFκB pathway and the CX3CL1/CX3CR1 axis have been implicated in the extent of myocardial damage following cardiac I/R, therefore it was hypothesized that CX3CL1 stimulation of non-classical monocyte-expressed CX3CR1 activates downstream NFκB signalling, leading to upregulated pro-inflammatory functions of non-classical monocytes. Immunophenotyping of human monocyte cell lines THP-1, MM6 and U937 cells demonstrated that all three cell lines resembled human circulating classical monocytes in terms of CX3CR1, CD16, and CD14 expression. Following time and dose-response optimisation of CX3CL1 stimulation, I showed that THP-1 monocytes show modest activation of the NFκB subunit p65 in response to CX3CL1 treatment (10ng/ml 60 minutes). Under these optimised conditions, THP-1 monocytes also showed modest but significant upregulation of the pro-inflammatory cytokine IL-8. Since IL-8 is an established chemotactic factor for neutrophil recruitment to injured or infected tissue, these findings support a working hypothesis that activation of the vascular pool of non-classical monocytes by circulating CX3CL1 following cardiac I/R

may lead to activation of the NFκB cascade and upregulated production of IL-8 by non-classical monocytes (Figure 7.1), which subsequently promotes exaggerated recruitment of neutrophils to the injured myocardium. Such a heightened neutrophil response may potentiate the inflammatory response in the injured myocardium and therefore exacerbate injury.

The modest levels of NFκB activation in response to CX3CL1 witnessed in this study may be reflective of the low expression of CX3CR1 by THP-1 monocytes. Such a response may be greater in non-classical monocytes which express considerably higher levels of CX3CR1. Since there is no existing cell line that represents non-classical monocytes, these cells must be isolated from human whole blood. In this thesis I validated a method of purifying total monocytes from human whole peripheral blood using negative selection beads, which yielded a high purity (>95%) of monocytes. While this method achieved a high purity of total monocytes, culturing of these cells in serum-free mediate to prevent serum-activation of the NFκB induced monocyte cell death in a matter of hours. In an alternative approach, I then optimised a protocol to investigate NFκB activation by CX3CL1 in non-classical monocytes by FACS analysis. This method was optimized on the monocyte cell line MM6, with the intent to progress to experiments using human whole blood. Using this technique, non-classical monocyte p-p65 expression could be distinguished from that of other monocyte subsets by gating on $CD14^{+}CD16^{++}$ cells during FACS analysis. Future work should therefore utilise this optimised protocol to investigate NFκB activation specifically in human $CX3CR1^{hi}$ non-classical monocytes in response to CX3CL1 stimulation. Identification of a heightened NFκB response in these cells compared to MM6 classical-like monocytes would suggest CX3CL1-specific induction of the NFkB pathway. Another approach to investigate this in future work would be to transfect human monocyte cells with CX3CR1, and identify robust, specific upregulation of NFκB by binding of CX3CL1.

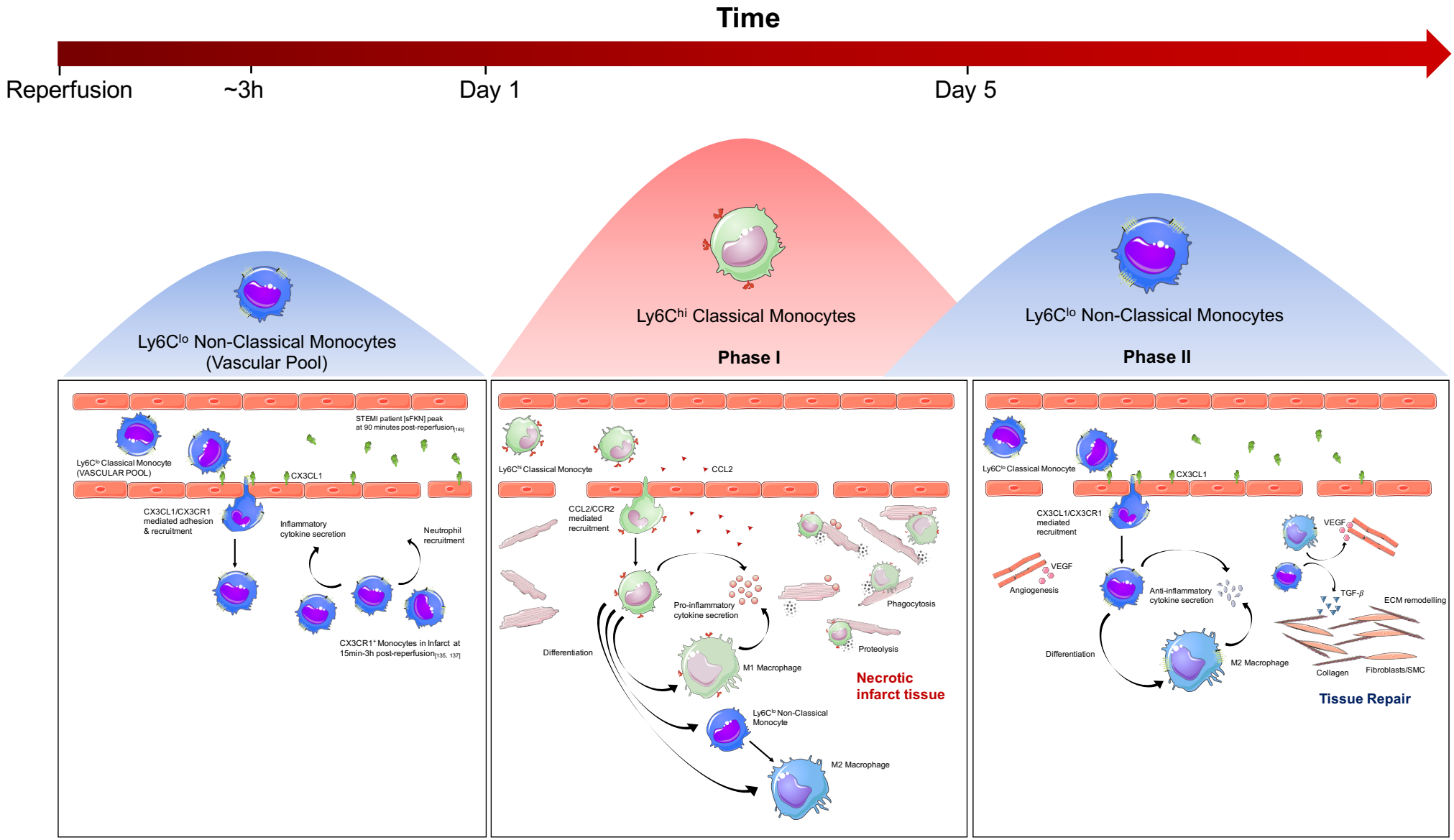
Time
Reperfusion
~3h
Day 1
Day 5
Ly6C^lo Non-Classical Monocytes (Vascular Pool)
Ly6C^hi Classical Monocytes
Phase I
Ly6C^lo Non-Classical Monocytes
Phase II
Ly6C^lo Classical Monocyte (VASCULAR POOL)
CX3CL1
STEMI patient [sFKN] peak at 90 minutes post-reperfusion[183]
CX3CL1/CX3CR1 mediated adhesion & recruitment
Inflammatory cytokine secretion
Neutrophil recruitment
CX3CR1+ Monocytes in Infarct at 15min-3h post-reperfusion[135, 137]
Ly6C^hi Classical Monocyte
CCL2
CCL2/CCR2 mediated recruitment
Pro-inflammatory cytokine secretion
Phagocytosis
Proteolysis
Differentiation
M1 Macrophage
Necrotic infarct tissue
Ly6C^lo Non-Classical Monocyte
M2 Macrophage
Ly6C^lo Classical Monocyte
CX3CL1
CX3CL1/CX3CR1 mediated recruitment
VEGF
Angiogenesis
Anti-inflammatory cytokine secretion
VEGF
TGF-β
ECM remodelling
Differentiation
M2 Macrophage
Collagen
Fibroblasts/SMC
Tissue Repair

Figure 7. 1. The Monocyte Response to MI.

Adapted from Nahrendorf et al 2007, 2010. The monocyte response to myocardial infarction in mouse, based on Nahrendorf's time course of biphasic monocyte subpopulation recruitment and function in the infarct myocardium. Phase I of healing is an inflammatory response dominated by CCL2-recruited Ly6C^{hi} classical monocytes from the spleen which infiltrate the heart at day 1-3 post-MI. Once in the heart tissue, Ly6C^{hi} classical monocytes undergo differentiation into M1 macrophages. Ly6C^{hi} classical monocytes and M1 macrophages secrete proinflammatory cytokines such as TNF-α, and carry out phagocytosis and proteolysis to clear necrotic infarct material. The second phase of healing is reparative and pro-fibrotic, occurring at day 5-9 post-MI. This phase is mediated by Ly6C^{lo} non-classical monocytes which are recruited to the heart from the circulation via a CX3CL1 chemokine gradient. Ly6C^{lo} non-classical monocytes can also arise from differentiation of Ly6C^{hi} monocytes. Ly6C^{lo} non-classical monocytes differentiate into the M2 class of macrophages, both of which terminate the inflammatory response by releasing anti-inflammatory mediators such as IL-10 and TGF-β. Ly6C^{lo} and M2 macrophages coordinate angiogenesis and promote blood supply in the forming granulation tissue. Type I collagen is synthesized by myofibroblasts which strengthens the infarct and protects it against rupture. More recent studies have demonstrated a possible earlier role of non-classical monocytes in the acute 24h following cardiac I/R; CX3CR1^{+} monocytes have been shown to be present in the infarct as early as 15m following reperfusion may be derived from a vascular pool of patrolling non-classical monocytes. It is possible that this early wave of infiltrating non-classical monocytes mediates the acute neutrophil response and thereby influences the extent of inflammation following myocardial injury.

7.2 Limitations

7.2.1 Assessment of Injury in Mouse Model of Cardiac I/R

One of the key limitations of this work concerns the lack of assessment of injury in the model of cardiac I/R, which may have impacted the data and therefore interpretation of this study. The extent of cardiac injury following cardiac I/R can be determined using a range of measures including assessment of infarct size by plasma biomarkers such as creatine kinase and troponins. Other studies investigating a mouse model of cardiac I/R indeed have utilized these measures; 24h after induction of MI, a blood sample is collected from the tail vein into a tube containing sodium citrate buffer for assay of troponin I by ELISA (Life Diagnostics High Sensitivity Mouse Cardiac Troponin-I ELISA kit) to assess the extent of ischemic injury [415, 416]. Cardiovascular magnetic resonance (CMR) with gadolinium-based contrast agents to image late gadolinium enhancement (LGE) is also used for tissue characterisation after cardiac I/R, which is considered the gold standard to assess infarct size in experimental MI models [417].

7.2.2 Sample Size and Missing Power Analysis

When investigating monocytes in the mouse spleen and bone marrow following cardiac I/R, inadequate number of animals in certain groups prevented statistical analysis. Further experiments are therefore required increase n numbers to ensure rigor and reproducibility and the validation of results.

7.3. Future Studies of Human and Mouse Monocytes

eGFP expression on classical and non-classical monocytes in Cx3cr1$^{+/GFP}$ mice lead to the traditional nomenclature that classical monocytes are CX3CR1^{lo} and non-classical monocytes CX3CR1^{hi}. However more recent studies have now shown that eGFP expression does not correlate with CX3CR1 surface protein expression on classical and non-classical monocytes. A recent study has shown that eGFP level in Cx3cr1$^{+/GFP}$ mice does not reflect CX3CR1 expression (as measured using anti-CX3CR1 antibody) [419], and consequently CX3CR1 expression does not discriminate mouse classical monocytes from non-classical monocytes using a multi-parametric analysis of mouse blood monocytes in steady state or inflammatory conditions (measured by either anti-CX3CR1 antibody or CX3CL1-AF647 uptake). As such, the cytosolic reporter eGFP is an indirect measure of CX3CR1 surface expression, and the previous definition of CX3CR1^{lo} classical monocytes and CX3CR1^{hi} non-classical monocytes can therefore no longer be used in mice. Furthermore, as the half-life of GFP is >24h, cells that no longer express CX3CR1 are likely to harbor residual GFP because of the extended half-life of the GFP protein. This study did however identify that the marker CD43 can discriminate mouse monocyte subsets, unlike CX3CR1; in the blood, bone marrow, spleen, and lung, classical monocytes are Ly6C^{hi} CD43$^{-/lo}$, while non-classical monocytes are Ly6C^{lo} CD43^{hi}.

Another recent study showed that CX3CR1 mRNA and protein expression is not significantly different between mouse classical and non-classical monocytes, however is significantly increased on non-classical monocytes in the bone marrow, indicating a loss of this receptor expression on non-classical monocytes in the blood [420]. By contrast in humans, CX3CR1 expression is significantly greater on non-classical monocytes than classical monocytes in the blood, bone marrow, spleen, and lung, and can therefore accurately differentiate human monocyte subsets in these compartments. This work also identified CD43 as a better marker than CX3CR1 to use with Ly6C for defining mouse monocyte subpopulations.

7.4. Conclusion

The research presented in this thesis builds on recent findings demonstrating an earlier role of non-classical monocytes following cardiac I/R than originally believed. STEMI patient non-classical monocyte dynamics immediately following PCI are associated with myocardial function, suggesting a mechanistic link between these cells and cardiac repair while also offering a potential biomarker to stratify patients. This project established in pre-clinical mouse models of cardiac I/R that monocyte adhesion to myocardial venous endothelium occurs over a similar time point to these distinct STEMI patient non-classical monocyte dynamics. This early post-reperfusion role of non-classical monocytes may be linked to the acute neutrophil response to MI, through CX3CL1-induced upregulation of IL-8 production by non-classical monocytes via the NFκB pathway. Such findings provide the foundation to explore the acute post-reperfusion role of non-classical monocytes in further depth, to understand their exact role. These findings are of significant clinical relevance, as there is currently no approved therapeutic treatment for ischaemia reperfusion injury in STEMI patients following PCI to improve outcome; currently approved therapeutics are restricted to anti-clotting strategies, which do not target ischemia reperfusion injury. Harnessing the CX3CL1/CX3CR1-mediated non-classical monocyte response in the acute post-reperfusion period may offer a key avenue to prevent a detrimental I/R-induced inflammatory response, at clinically feasible time point while STEMI patients are still hospitalised.

References

1. Singh, R.B., et al., *Pathogenesis of atherosclerosis: A multifactorial process.* Journal of Clinical and Experimental Cardiology, 2002. **7**(1): p. 40–53.
2. Sayols-Baixeras, S., et al., Pathogenesis of coronary artery disease: focus on genetic risk factors and identification of genetic variants. The Application of Clinical Genetics, 2014(7): p. 15–32.
3. Skålén, K., et al., Subendothelial retention of atherogenic lipoproteins in early atherosclerosis. Nature, 2002(417): p. 750-754
4. Insull, W., The Pathology of Atherosclerosis: Plaque Development and Plaque Responses to Medical Treatment. The American Journal of Medicine, 2009. **122**(1): p. S3–S14.
5. Galkina, E. and K. Ley, *Immune and Inflammatory Mechanisms of Atherosclerosis.* Annual Review of Immunology, 2009(27): p. 165–197.
6. Finn, A.V., et al., *Concept of Vulnerable/Unstable Plaque.* Arteriosclerosis, Thrombosis, and Vascular Biology, 2010(30): p. 1282-1292.
7. van der Wal, A.C. and A.E. Becker, *Atherosclerotic plaque rupture – pathologic basis of plaque stability and instability.* Cardiovascular Research, 1999. **41**(2): p. 334-344.
8. Ambrose, J.A., Plaque disruption and the acute coronary syndromes of unstable angina and myocardial infarction: if the substrate is similar, why is the clinical presentation different? Journal of the American College of Cardiology, 1992. **19**(7): p. 1653-8.
9. Sheridan, P.J. and D.C. Crossman, *Critical review of unstable angina and non-ST elevation myocardial infarction* Postgraduate Medical Journal, 2002. **78**(926): p. 717–726.
10. Fuster V, et al., Atherosclerotic plaque rupture and thrombosis. Evolving concepts. Circulation, 1990. **82**(3 Suppl): p. 47-59.
11. Thygesen, K., et al., *Third Universal Definition of Myocardial Infarction.* Circulation, 2012. **126**(16): p. 2020-2035.
12. Reichlin, T., et al., *Early Diagnosis of Myocardial Infarction with Sensitive Cardiac Troponin Assays.* The New England Journal of Medicine, 2009. **361**: p. 858-867.

13. Jneid, H., et al., Redefining Myocardial Infarction: What Is New In The ESC/ACCF/AHA/WHF Third Universal Definition Of Myocardial Infarction? Methodist DeBakey Cardiovascular Journal, 2013. **9**(3): p. 169–172.
14. Xu, R.Y., et al., *High-sensitive cardiac troponin T.* Journal of Geriatric Cardiology, 2013. **10**(1): p. 102–109.
15. Anderson, J.L., et al., ACC/AHA 2007 Guidelines for the Management of Patients With Unstable Angina/Non–ST-Elevation Myocardial Infarction. Circulation, 2007. **116**: p. e148-e304.
16. Steg, P.G., et al., ESC Guidelines for the management of acute myocardial infarction in patients presenting with ST-segment elevation: The Task Force on the management of ST-segment elevation acute myocardial infarction of the European Society of Cardiology (ESC). European Heart Journal, 2012. **33**(20): p. 2569-619.
17. van de Loo, A., et al., Primary percutaneous coronary intervention in acute myocardial infarction: direct transportation to catheterization laboratory by emergency teams reduces door-to-balloon time. Clinical Cardiology, 2006. **29**(3): p. 112-6.
18. Keeley, E.C., J.A. Boura, and C.L. Grines, Primary angioplasty versus intravenous thrombolytic therapy for acute myocardial infarction: a quantitative review of 23 randomised trials. Lancet, 2003. **361**(9351): p. 13-20.
19. Harper, R.W. and J. Lefkovits, Prehospital thrombolysis followed by early angiography and percutaneous coronary intervention where appropriate — an underused strategy for the management of STEMI. The Medical Journal of Australia, 2010. **193**(4): p. 234-237.
20. Van de Werf, F., et al., Management of acute myocardial infarction in patients presenting with ST-segment elevation. The Task Force on the Management of Acute Myocardial Infarction of the European Society of Cardiology. European Heart Journal, 2003. **24**(1): p. 28-66.
21. Lip, G.Y.H., B.S.P. Chin, and N. Prasad, *Antithrombotic therapy in myocardial infarction and stable angina.* British Medical Journal, 2002. **325**(1287).
22. Stouffer, G.A. Percutaneous Coronary Intervention (PCI) Technique. 2016 [cited 2017 05-05-17].
23. Raos, V., et al., Anti-ischemic therapy in patients with STEMI or NSTEMI treated at county and university hospitals. Acta Med Croatica, 2009. **63**(1): p. 53-8.

24. Hausenloy, D.J. and D.M. Yellon, *Myocardial ischemia-reperfusion injury: a neglected therapeutic target.* The Journal of Clinical Investigation, 2013. **123**(1): p. 92-100.

25. Zhang, H. and S. Sun, *NF-kappaB in inflammation and renal diseases. .* Cell Biosci 2015(5): p. 63.

26. Braunwald, E. and R.A. Kloner, *Myocardial reperfusion: a double-edged sword?* The Journal of Clinical Investigation, 1985. **76**(5): p. 1713–1719.

27. Buja, L.M., *Myocardial ischemia and reperfusion injury* Cardiovascular Pathology, 2005. **14**(4): p. 170–175.

28. Simonis, G., R.H. Strasser, and B. Ebner, *Reperfusion injury in acute myocardial infarction.* Journal of Critical Care, 2012. **16**((Suppl 2)): p. A22.

29. Heusch, G., Treatment of Myocardial Ischemia/Reperfusion Injury by Ischemic and Pharmacological Postconditioning. Comprehensive Physiology, 2015. **5**(3): p. 1123-45.

30. Ibáñez, B., et al., *Evolving Therapies for Myocardial Ischemia/Reperfusion Injury* The Journal of the American College of Cardiology, 2015. **65**(14): p. 1454–1471.

31. Fordyce, C.B., et al., Novel therapeutics in myocardial infarction: targeting microvascular dysfunction and reperfusion injury. Trends in Pharmalogical Sciences, 2015. **36**(9): p. 605-16.

32. Spath, N.B., N.L. Mills, and N.L. Cruden, Novel cardioprotective and regenerative therapies in acute myocardial infarction: a review of recent and ongoing clinical trials. Future Cardiology, 2016. **12**(6): p. 655-672.

33. BHF. *CVD STATISTICS – BHF UK FACTSHEET*. 2016 27-03-2016 09-05-2017].

34. Minicucci, M.F., et al., Heart Failure After Myocardial Infarction: Clinical Implications and Treatment. Clinical Cardiology, 2011. **34**(7): p. 410-4.

35. Dargie, H., Heart failure post-myocardial infarction: a review of the issues Heart, 2005. **91**(Suppl 2): p. ii3–ii6.

36. Pfeffer, M.A. and E. Braunwald, Ventricular remodeling after myocardial infarction. Experimental observations and clinical implications. Circulation, 1990. **81**(4): p. 1161-72.

37. Galli, A. and F. Lombardi, Postinfarct Left Ventricular Remodelling: A Prevailing Cause of Heart Failure. Cardiology Research and Practice, 2016.

38. Ajello, L., et al., Diagnosis and Treatment of Asymptomatic Left Ventricular Systolic Dysfunction after Myocardial Infarction. ISRN Cardiology, 2013. **2013**(731285).
39. Seropian, I.M., et al., Anti-Inflammatory Strategies for Ventricular Remodeling Following ST-Segment Elevation Acute Myocardial Infarction. The Journal of the American College of Cardiology, 2014. **63**(16): p. 1593-603.
40. Boudonas, G.E., *β-Blockers in coronary artery disease management.* Hippokratia, 2010. **14**(4): p. 231–235.
41. Patten, R.D., J.E. Udelson, and M.A. Konstam, *Ventricular remodeling and its prevention in the treatment of heart failure.* Current Opinion in Cardiology, 1998. **13**(3): p. 162-7.
42. Granrud, G.A. and P.J. Vatterott, *Arrhythmias and acute myocardial infarction.* Postgraduate Medical Journal, 1991. **90**(6): p. 85-96.
43. Kumar, V., et al., *Study of cardiac arrhythmias in acute myocardial infarction within 48 hours.* International Journal of Advances in Medicine, 2017. **4**(1): p. 103-107.
44. Perron, A.D. and T. Sweeney, *Arrhythmic complications of acute coronary syndromes.* Emergency Medicine Clinics of North America, 2005. **23**(4): p. 1065-82.
45. Gorenek, B., et al., Cardiac arrhythmias in acute coronary syndromes: position paper from the joint EHRA, ACCA, and EAPCI task force. EuroIntervention, 2015. **10**(9): p. 1095-108.
46. Cannon, R., III Mechanisms, management and future directions for reperfusion injury after acute myocardial infarction. Nat Clin Pract Cardiovasc Med., 2005(2): p. 88-94.
47. LM., B., *Myocardial ischemia and reperfusion injury. .* Cardiovasc Pathol. , 2005(14): p. 170–175.
48. Inserte, J., et al., Contribution of delayed intracellular pH recovery to ischemic postconditioning protection. Antioxid Redox Signal. , 2011. **14**(5): p. 923-39.
49. Inserte, J., et al., cGMP/PKG pathway mediates myocardial postconditioning protection in rat hearts by delaying normalization of intracellular acidosis during reperfusion. J Mol Cell Cardiol. , 2011. **50**(5): p. 903-9.
50. Hausenloy, D. and D. Yellon, Remote ischaemic preconditioning: underlying mechanisms and clinical application. Cardiovasc Res. , 2008. **79**(3): p. 377-86.

51. Gritsopoulos, G., et al., Remote postconditioning is more potent than classic postconditioning in reducing the infarct size in anesthetized rabbits. Cardiovasc Drugs Ther. , 2009. **23**(3): p. 193-8.
52. Hausenloy, D., et al., Investigating the signal transduction pathways underlying remote ischemic conditioning in the porcine heart. Cardiovasc Drugs Ther., 2012. **26**(2): p. 87-93.
53. Götberg, M., et al., A pilot study of rapid cooling by cold saline and endovascular cooling before reperfusion in patients with ST-elevation myocardial infarction. Circ Cardiovasc Interv., 2010. **3**(5): p. 400-7.
54. Rupprecht, H., et al., Cardioprotective effects of the Na(+)/H(+) exchange inhibitor cariporide in patients with acute anterior myocardial infarction undergoing direct PTCA. Circulation., 2000. **101**(25): p. 2902-8.
55. Yamada, K., et al., Reduction of myocardial infarct size by SM-20550, a novel Na(+)/H(+) exchange inhibitor, in rabbits. Eur J Pharmacol. , 2000. **404**(1-2): p. 201-12.
56. Karmazyn, M., *NHE-1: still a viable therapeutic target.* J Mol Cell Cardiol. , 2013. **61**: p. 77-82.
57. Das, A., et al., PDE5 inhibitors as therapeutics for heart disease, diabetes and cancer. . Pharmacol Ther., 2015. **147**: p. 12–21.
58. Padilla, F., et al., Intravenous administration of the natriuretic peptide urodilatin at low doses during coronary reperfusion limits infarct size in anesthetized pigs. Cardiovasc Res. , 2001. **51**: p. 592–600.
59. Selker, H., et al., Out-of-hospital administration of intravenous glucose-insulin-potassium in patients with suspected acute coronary syndromes: The IMMEDIATE randomized controlled trial. . JAMA., 2012. **307**: p. 1925–1933.
60. Lønborg, J., et al., Exenatide reduces reperfusion injury in patients with ST-segment elevation myocardial infarction. Eur Heart J., 2012. **33**: p. 1491–1499.
61. Ross, A., et al., AMISTAD-II Investigators: A randomized, double-blinded, placebo-controlled multicenter trial of adenosine as an adjunct to reperfusion in the treatment of acute myocardial infarction (AMISTAD-II). J Am Coll Cardiol. , 2005. **45**: p. 1775–1780.

62. Garcia-Dorado, D., et al., Intracoronary injection of adenosine before reperfusion in patients with ST-segment elevation myocardial infarction: A randomized controlled clinical trial. Int J Cardiol., 2014. **177**: p. 935–941.
63. Piot, C., et al., Effect of cyclosporine on reperfusion injury in acute myocardial infarction. . N Engl J Med. , 2008. **359**: p. 473–481.
64. Ghaffari, S., et al., The effect of prethrombolytic cyclosporine-A injection on clinical outcome of acute anterior ST-elevation myocardial infarction. Cardiovasc Ther., 2013. **31**: p. e34–e39.
65. Hausenloy, D. and D. Yellon, *Targeting myocardial reperfusion injury - the search continues.* N Engl J Med., 2015. **373**: p. 1073–1075.
66. Ibanez, B., et al., Effect of early metoprolol on infarct size in ST-segment-elevation myocardial infarction patients undergoing primary percutaneous coronary intervention: The Effect of Metoprolol in Cardioprotection During an Acute Myocardial Infarction (METOCARD-CNIC) trial. . Circulation., 2013. **123**: p. 1495–1503. .
67. Sorrentino, S., et al., Nebivolol exerts beneficial effects on endothelial function, early endothelial progenitor cells, myocardial neovascularization, and left ventricular dysfunction early after myocardial infarction beyond conventional β1-blockade. J Am Coll Cardiol. , 2011. **57**: p. 601–611.
68. Rakowski, T., et al., Early abciximab administration before primary percutaneous coronary intervention improves infarct-related artery patency and left ventricular function in high-risk patients with anterior wall myocardial infarction: A randomized study. Am Heart J., 2007. **153**: p. 360–365.
69. Thiele, H., et al., Intracoronary compared with intravenous bolus abciximab application in patients with ST-elevation myocardial infarction undergoing primary percutaneous coronary intervention: The randomized Leipzig immediate percutaneous coronary intervention abciximab IV versus IC in ST-elevation myocardial infarction trial. . Circulation., 2008. **118**: p. 49–57.
70. Ambrosio, G., et al., GRACE Investigators: Chronic nitrate therapy is associated with different presentation and evolution of acute coronary syndromes: Insights from 52,693 patients in the Global Registry of Acute Coronary Events. Eur Heart J., 2010. **31**: p. 430–438.
71. Leesar, M., et al., Delayed preconditioning-mimetic action of nitroglycerin in patients undergoing coronary angioplasty. . Circulation., 2001. **103**: p. 2935–2941.

72. Epelman, S., P. Liu, P,, and D.L. Mann, *Role of Innate and Adaptive Immunity in Cardiac Injury and Repair.* Nature Reviews Immunology, 2015. **15**(2): p. 117–129.
73. Frangogiannis, N.G., *The inflammatory response in myocardial injury, repair and remodeling.* Nature Reviews Cardiology, 2014. **11**(5): p. 255–265.
74. van der Laan, A.M., M. Nahrendorf, and J.J. Piek, Healing and adverse remodelling after acute myocardial infarction: role of the cellular immune response. Heart, 2012. **98**(18): p. 1384-1390.
75. Talman, V. and H. Ruskoaho, Cardiac fibrosis in myocardial infarction—from repair and remodeling to regeneration. Cell Tissue Res., 2016. **365**(3): p. 563–581.
76. Arslan, F., et al., Myocardial ischemia/reperfusion injury is mediated by leukocytic toll-like receptor-2 and reduced by systemic administration of a novel anti-toll-like receptor-2 antibody. Circulation, 2010. **121**(1): p. 80-90.
77. Favre, J., et al., Toll-like receptors 2-deficient mice are protected against postischemic coronary endothelial dysfunction. Arteriosclerosis, Thrombosis, and Vascular Biology, 2007. **27**(5): p. 1064-71.
78. Oyama, J., et al., Reduced myocardial ischemia-reperfusion injury in toll-like receptor 4-deficient mice. Circulation, 2004. **109**(6): p. 784-9.
79. Timmers, L., et al., Toll-like receptor 4 mediates maladaptive left ventricular remodeling and impairs cardiac function after myocardial infarction. Circulation Research, 2008. **102**(2): p. 257-64.
80. Hill, J.H. and P.A. Ward, *The phlogistic role of C3 leukotactic fragments in myocardial infarcts of rats.* The Journal of Experimental Medicine, 1971. **133**(4): p. 885-900.
81. Yasojima, K., et al., Complement gene expression by rabbit heart: upregulation by ischemia and reperfusion. Circulation Research, 1998. **82**(11): p. 1224-30.
82. Wysoczynski, M., et al., Complement Component 3 is Necessary to Preserve Myocardium and Myocardial Function in Chronic Myocardial Infarction. Stem Cells, 2014. **32**(9): p. 2502–2515.
83. Hori, M. and K. Nishida, *Oxidative stress and left ventricular remodelling after myocardial infarction.* Cardiovascular Research, 2009. **81**(3): p. 457-64.
84. Andrassy, M., et al., High-mobility group box-1 in ischemia-reperfusion injury of the heart. Circulation, 2008. **117**(25): p. 3216-26.

85. Lugrin, J., et al., Interleukin-1 alpha is a crucial danger signal triggering acute myocardial inflammation during myocardial infarction. The Journal of Immunology, 2015. **194**(2): p. 499–503.
86. Chenn, C., et al., Role of Extracellular RNA and TLR3Trif Signaling in Myocardial Ischemia–Reperfusion Injury. Journal of the American Heart Association, 2014. **3**(1): p. e000683.
87. Tak, P.P. and G.S. Firestein, *NF-κB: a key role in inflammatory diseases.* The Journal of Clinical Investigation, 2001. **107**(1): p. 7-11.
88. Ma, Y., A. Yabluchanskiy, and M.L. Lindsey, *Neutrophil roles in left ventricular remodeling following myocardial infarction.* Fibrogenesis Tissue Repair. , 2013. **6**(11): p. 1755-1536-6-11.
89. Frangogiannis, N.G., *The role of the chemokines in myocardial ischemia and reperfusion.* Current Vascular Pharmacology, 2004. **2**(2): p. 163-74.
90. Cavalera, M. and N.G. Frangogiannis, *Targeting the chemokines in cardiac repair.* Current Pharmaceutical Design, 2014. **20**(12): p. 1971–1979.
91. Saxena, A., I. Russo, and N.G. Frangogiannis, Inflammation as a therapeutic target in myocardial infarction: learning from past failures to meet future challenges. Translational Research, 2016. **167**(1): p. 152–166.
92. Dobaczewski, M., et al., CCR5 signaling suppresses inflammation and reduces adverse remodeling of the infarcted heart, mediating recruitment of regulatory T cells. The American Journal of Pathology, 2010. **176**(5): p. 2177-87.
93. Cochain, C., et al., The chemokine decoy receptor D6 prevents excessive inflammation and adverse ventricular remodeling after myocardial infarction. Arteriosclerosis, Thrombosis, and Vascular Biology, 2012. **32**(9): p. 2206-13.
94. Dobaczewski, M., W. Chen, and N. Frangogiannis, *Transforming growth factor (TGF)-β signaling in cardiac remodeling.* J Mol Cell Cardiol., 2011. **51**(4): p. 600-6.
95. Bujak, M., et al., Aging-related defects are associated with adverse cardiac remodeling in a mouse model of reperfused myocardial infarction. J Am Coll Cardiol., 2008. **51**(14): p. 1384-92.
96. Frangogiannis, N.G., *Regulation of the inflammatory response in cardiac repair.* Circulation Research, 2012. **110**(1): p. 159–173.

97. Ono, K., et al., Cytokine gene expression after myocardial infarction in rat hearts: possible implication in left ventricular remodeling. Circulation, 1998. **98**(2): p. 149-56.
98. Su, C., et al., Non-synaptic inhibition between grouped neurons in an olfactory circuit. Nature, 2012. **492**(7427): p. 66–71.
99. Majmudar, M.D., et al., Monocyte-directed RNAi targeting CCR2 improves infarct healing in atherosclerosis-prone mice. Circulation, 2013. **127**(20): p. 2038–2046.
100. Cardilo-Reis L, W.J., Binder CJ., *When monocytes come (too) close to our hearts.* Journal of the American College of Cardiology, 2010. **55**(15): p. 1639-41.
101. Hayashidani, S., et al., Anti-monocyte chemoattractant protein-1 gene therapy attenuates left ventricular remodeling and failure after experimental myocardial infarction. Circulation, 2003. **108**(17): p. 2134-40.
102. Kaikita, K., et al., Targeted Deletion of CC Chemokine Receptor 2 Attenuates Left Ventricular Remodeling after Experimental Myocardial Infarction. The American Journal of Pathology, 2004. **165**(2): p. 439–447.
103. Dewald, O., et al., CCL2/Monocyte Chemoattractant Protein-1 regulates inflammatory responses critical to healing myocardial infarcts. Circulation Research, 2005. **96**(8): p. 881-9.
104. Leuschner, F., et al., *Therapeutic siRNA silencing in inflammatory monocytes in mice.* Nature Biotechnology, 2011. **29**: p. 1005–1010.
105. Maekawa, Y., et al., Prognostic significance of peripheral monocytosis after reperfused acute myocardial infarction:a possible role for left ventricular remodeling. Journal of the American College of Cardiology, 2002. **39**(2): p. 241–246.
106. Takahashi, T., et al., Relationship of admission neutrophil count to microvascular injury, left ventricular dilation, and long-term outcome in patients treated with primary angioplasty for acute myocardial infarction. Official Journal of the Japanese Circulation Society, 2008. **72**(6): p. 867-72.
107. Fullerton, J.N., A.J. O'Brien, and D.W. Gilroy, *Pathways mediating resolution of inflammation: when enough is too much.* The Journal of Pathology, 2013. **231**(1): p. 8–20.

108. Frangogiannis, N.G., L.H. Michael, and M.L. Entman, Myofibroblasts in reperfused myocardial infarcts express the embryonic form of smooth muscle myosin heavy chain (SMemb). Cardiovascular Reseach, 2000. **48**(1): p. 89-100.

109. Willems, I.E., et al., *The alpha-smooth muscle actin-positive cells in healing human myocardial scars.* The American Journal of Pathology, 1994. **145**(4): p. 868-75.

110. van den Borne, S.W., et al., *Myocardial remodeling after infarction: the role of myofibroblasts.* National Reviews. Cardiology., 2010. **7**(1): p. 30-7.

111. Fan, D., et al., Cardiac fibroblasts, fibrosis and extracellular matrix remodeling in heart disease. Fibrogenesis & Tissue Repair, 2012. **5**(1): p. 15.

112. Deb, A. and E. Ubil, *Cardiac fibroblast in development and wound healing.* Journal of Molecular and Cellular Cardiology, 2014(70): p. 47-55.

113. van Amerongen, M.J., et al., Macrophage Depletion Impairs Wound Healing and Increases Left Ventricular Remodeling after Myocardial Injury in Mice. The American Journal of Pathology, 2007. **170**(3): p. 818–829.

114. Chen, W. and N.G. Frangogiannis, *Fibroblasts in post-infarction inflammation and cardiac repair.* Biochimica et Biophysica Acta, 2013. **1833**(4): p. 945-53.

115. Talman, V. and H. Ruskoaho, *Cardiac fibrosis in myocardial infarction—from repair and remodeling to regeneration.* Cell and Tissue Research, 2016. **365**(3): p. 563–581.

116. Ingersoll, M., et al., *Monocyte trafficking in acute and chronic inflammation. .* Trends Immunol, 2011(32): p. 470–477.

117. Oberbarnscheidt, M., et al., *Non-self recognition by monocytes initiates allograft rejection.* J Clin Invest 2014(124): p. 3579–3589.

118. Bigley, V., et al., The human syndrome of dendritic cell, monocyte, B and NK lymphoid deficiency. . J Exp Med, 2011(208): p. 227–234.

119. Hashimoto, D., J. Miller, and M. Merad, *Dendritic cell and macrophage heterogeneity in vivo.* Immunity, 2011(35): p. 323–335.

120. Mitchell, A., B. Roediger, and W. Weninger, *Monocyte homeostasis and the plasticity of inflammatory monocytes.* Cell Immunol, 2014(291): p. 22–31.

121. Ziegler-Heitbrock, L., *Monocyte subsets in man and other species. .* Cell Immunol 2014(289): p. 135–139.

122. Geissmann, F., et al., *Development of monocytes, macrophages and dendritic cells.* Science, 2010. **327**(5966): p. 656–661.
123. Heitbrock, L., Blood Monocytes and Their Subsets: Established Features and Open Questions. 2015(6): p. 423.
124. Wong, K.L., et al., Gene expression profiling reveals the defining features of the classical, intermediate, and nonclassical human monocyte subsets. Blood, 2011. **118**(5): p. e16-31.
125. Thomas, G., et al., *Nonclassical Patrolling Monocyte Function in the Vasculature.* Arteriosclerosis, Thrombosis, and Vascular Biology, 2015. **35**(6): p. 1306-1316.
126. Varol, C., et al., Monocytes give rise to mucosal, but not splenic, conventional dendritic cells. J Exp Med, 2007. **1**(204): p. 171-80. .
127. Varol, C., S. Yona, and S. Jung, *Origins and tissue-context-dependent fates of blood monocytes.* Immunol Cell Biol, 2009(87): p. 30–38.
128. Yona, S., et al., Fate mapping reveals origins and dynamics of monocytes and tissue macrophages under homeostasis. Immunity, 2013. **38**(1): p. 79-91.
129. Sunderkötter, C., et al., Subpopulations of mouse blood monocytes differ in maturation stage and inflammatory response. J Immunol., 2004. **172**(7): p. 4410-7.
130. Yrlid, U., C. Jenkins, and G. MacPherson, Relationships between distinct blood monocyte subsets and migrating intestinal lymph dendritic cells in vivo under steady-state conditions. J Immunol., 2006. **176**(7): p. 4155-62.
131. Thomas, G., et al., Deleting an Nr4a1 Super-Enhancer Subdomain Ablates Ly6C^{low} Monocytes while Preserving Macrophage Gene Function. Immunity., 2016. **45**(5): p. 975-987.
132. de Bruijn, M., et al., Distinct mouse bone marrow macrophage precursors identified by differential expression of ER-MP12 and ER-MP20 antigens. Eur. J. Immunol, 1994. . **24**(10): p. 2279-84.
133. Randolph, G., et al., Differentiation of phagocytic monocytes into lymph node dendritic cells in vivo. Immunity., 1999 **11**(6): p. 753-61.
134. Van Furth, R. and H. Diesselhoff-den Dulk, Quantitative study on the production and kinetics of mononuclear phagocytes during an acute inflammatory reaction. J. Exp. Med, 1973(138): p. 1314.

135. Terry, R.L. and S.D. Miller, *Molecular control of monocyte development.* Cellular Immunology, 2014. **291**(0): p. 16–21.
136. Kurotaki, D., et al., Essential role of the IRF8-KLF4 transcription factor cascade in murine monocyte differentiation. Blood, 2013. **121**(10): p. 1839-49.
137. Alder, J.K., et al., Kruppel-like factor 4 is essential for inflammatory monocyte differentiation in vivo. Journal of Immunology, 2008. **180**(8): p. 5645-52.
138. Hanna, R.N., et al., The transcription factor NR4A1 (Nur77) controls bone marrow differentiation and survival of Ly6C− monocytes. Nature Reviews Immunology, 2011. **12**(8): p. 778–785.
139. Cros, J., et al., Human CD14dim monocytes patrol and sense nucleic acids and viruses via TLR7 and TLR8 receptors. Immunity., 2010. **33**(3): p. 375-86.
140. Geissmann, F., S. Jung, and D. Littman, Blood monocytes consist of two principal subsets with distinct migratory properties. . Immunity, 2003(19): p. 71–82.
141. Patel, A., et al., The fate and lifespan of human monocyte subsets in steady state and systemic inflammation. . J Exp Med, 2017(214): p. 1913–23.
142. Yona, S., et al., Fate mapping reveals origins and dynamics of monocytes and tissue macrophages under homeostasis. . Immunity, 2013(38): p. 79–91.
143. Gamrekelashvili, J., et al., Regulation of monocyte cell fate by blood vessels mediated by Notch signalling. Nat Commun, 2016(7): p. 12597.
144. Auffray, C., et al., Monitoring of blood vessels and tissues by a population of monocytes with patrolling behavior. Science, 2007. **317**(5838): p. 666-70.
145. O'Connell, K., et al., Practical Murine Hematopathology: A Comparative Review and Implications for Research. Comp Med., 2015. **65**(2): p. 96–113.
146. Serbina, N. and E. Pamer, Monocyte emigration from bone marrow during bacterial infection requires signals mediated by chemokine receptor CCR2. . Nat. Immunol., 2006(7): p. 311–317.
147. Auffray, C., M. Sieweke, and F. Geissmann, *Blood monocytes: development, heterogeneity, and relationship with dendritic cells.* Annu Rev Immunol., 2009(27): p. 669–92.
148. Shi, C. and E.G. Pamer, *Monocyte recruitment during infection and inflammation.* Nature Reviews Immunology, 2011. **11**(11): p. 762–774.
149. Buscher, K., et al., Patrolling Mechanics of Non-Classical Monocytes in Vascular Inflammation. Front Cardiovasc Med., 2017. **4**(80).

150. Auffray, C., et al., Monitoring of blood vessels and tissues by a population of monocytes with patrolling behavior. Science, 2007. **317**(5838): p. 666-70.
151. Jakubzick, C., et al., Blood monocyte subsets differentially give rise to CD103+ and CD103- pulmonary dendritic cell populations. Journal of Immunology, 2008. **180**(5): p. 3019-27.
152. Carlin, L.M., et al., Nr4a1-Dependent Ly6Clow Monocytes Monitor Endothelial Cells and Orchestrate Their Disposal. Cell, 2013. **153**(2): p. 362–375.
153. Ingersoll, M.A., et al., Comparison of gene expression profiles between human and mouse monocyte subsets. Blood, 2010. **115**(3): p. e10-9.
154. Cros, J., et al., Human CD14dim Monocytes Patrol and Sense Nucleic Acids and Viruses via TLR7 and TLR8 Receptors. Immunity, 2010. **33**(3): p. 375–386.
155. Swirski, F.K., et al., Identification of Splenic Reservoir Monocytes and Their Deployment to Inflammatory Sites. Science, 2010. **325**(5940): p. 612–616.
156. Pittet, M.J., M. Nahrendorf, and F.K. Swirski, *The journey from stem cell to macrophage.* Annals of the New York Academy of Sciences, 2014. **1319**(1): p. 1–18.
157. Tsou, C.L., et al., Critical roles for CCR2 and MCP-3 in monocyte mobilization from bone marrow and recruitment to inflammatory sites. The Journal of Clinical Investigation, 2007. **117**(4): p. 902–909.
158. Dutta, P. and M. Nahrendorf, *Monocytes in myocardial infarction.* Arteriosclerosis, Thrombosis, and Vascular Biology, 2015. **35**(5): p. 1066-70.
159. Luscinskas FW, et al., Monocyte rolling, arrest and spreading on IL-4-activated vascular endothelium under flow is mediated via sequential action of L-selectin, beta 1-integrins, and beta 2-integrins. The Journal of Cell Biology, 1994. **125**(6): p. 1417–1427.
160. Hilgendorf, I., et al., Ly-6Chigh monocytes depend on Nr4a1 to balance both inflammatory and reparative phases in the infarcted myocardium. Circulation Research, 2014. **114**(10): p. 1611-22.
161. Jung, K., et al., Endoscopic Time-Lapse Imaging of Immune Cells in Infarcted Mouse Hearts. Circ Res. , 2013. **112**(6).
162. Kreisel, D., et al., *In vivo two-photon imaging reveals monocyte-dependent neutrophil extravasation during pulmonary inflammation. .* Proceedings of the National Academy of Sciences of the United States of America., 2010(107): p. 18073–18078.

163. Li, W., et al., Intravital 2-photon imaging of leukocyte trafficking in beating heart. J Clin Invest. , 2012. **122**(7): p. 2499–2508.
164. Belge, K.U., et al., *The proinflammatory CD14+CD16+DR++ monocytes are a major source of TNF.* The Journal of Immunology, 2002. **168**(7): p. 3536-42.
165. Chimen, M., et al., Monocyte Subsets Coregulate Inflammatory Responses by Integrated Signaling through TNF and IL-6 at the Endothelial Cell Interface. The Journal of Immunology, 2017. **198**(7): p. 2834-2843.
166. Mukherjee, R., et al., Non-Classical monocytes display inflammatory features: Validation in Sepsis and Systemic Lupus Erythematous. Scientific Reports, 2015. **5**(13886).
167. Yang, J., et al., Monocyte and macrophage differentiation: circulation inflammatory monocyte as biomarker for inflammatory diseases. Biomarker Research, 2014. **2**(1): p. 1.
168. Anbazhagan, K., et al., Transcriptomic Network Support Distinct Roles of Classical and Non-Classical Monocytes in Human. International Reviews of Immunology, 2014. **33**(6).
169. Ruparelia, N., et al., Acute myocardial infarction activates distinct inflammation and proliferation pathways in circulating monocytes, prior to recruitment, and identified through conserved transcriptional responses in mice and humans. . European Heart Journal, 2015. **36**(29): p. 1923-34.
170. Tsujioka H, I.T., Ikejima H, Kuroi A, Takarada S, Tanimoto T, Kitabata H, Okochi K, Arita Y, Ishibashi K, Komukai K, Kataiwa H, Nakamura N, Hirata K, Tanaka A, Akasaka T., *Impact of heterogeneity of human peripheral blood monocyte subsets on myocardial salvage in patients with primary acute myocardial infarction.* Journal of the American College of Cardiology, 2009. **54**(2): p. 130-8.
171. Tsujioka, H., et al., Post-reperfusion Enhancement of CD14(+)CD16(-) Monocytes and Microvascular Obstruction in ST-segment Elevation Acute Myocardial Infarction. Circ J., 2010. **74**(6): p. 1175-82.
172. van der Laan , A., et al., A Proinflammatory Monocyte Response Is Associated With Myocardial Injury and Impaired Functional Outcome in Patients With ST-segment Elevation Myocardial Infarction: Monocytes and Myocardial Infarction. Am Heart J, 2012. **163**(1): p. 57-65.

173. Tapp , L., et al., The CD14++CD16+ Monocyte Subset and Monocyte-Platelet Interactions in Patients With ST-elevation Myocardial Infarction. J Thromb Haemost, 2012. **10**(7): p. 1231-41.
174. Rogacev, K., et al., CD14++CD16+ monocytes independently predict cardiovascular events: a cohort study of 951 patients referred for elective coronary angiography. J Am Coll Cardiol. , 2012(60): p. 1512–1520.
175. Frantz, S., et al., Monocytes/macrophages prevent healing defects and left ventricular thrombus formation after myocardial infarction. FASEB J., 2013. **27**(3): p. 871-81.
176. Urra, X., et al., Monocyte subtypes predict clinical course and prognosis in human stroke. . J Cereb Blood Flow Metab., 2009(29): p. 994–1002.
177. Kaito, M., et al., Relevance of distinct monocyte subsets to clinical course of ischemic stroke patients. . PLoS one, 2013(8): p. e69409.
178. Urra, X., et al., Monocytes are major players in the prognosis and risk of infection after acute stroke. Stroke. , 2009(40): p. 1262–1268.
179. Moser, B., et al., *Chemokines: multiple levels of leukocyte migration control.* Trends in Immunology, 2004. **25**(2): p. 75-84.
180. Zlotnik, A.a.O., Yoshie., Chemokines: A New Classification System and Their Role in Immunity.". Immunity, 2000. **12**(2): p. 121–127.
181. Fernandez, E.J.a.E.L., *Structure, Function, and Inhibition of Chemokines.* Annual Review of Pharmacology and Toxicology, 2002(42): p. 469-499.
182. Olson, T.S.a.K., Ley., *Chemokines and chemokine receptors in leukocyte trafficking.* American Journal of Physiology - Regulatory, Integrative and Comparative Physiology, 2002. **238**(1).
183. Ransohoff, R.M., Chemokines and chemokine receptors: Standing at the crossroads of immunobiology and neurobiology. Immunity, 2009. **31**(5): p. 711–721.
184. Graham, G., T. Handel, and A. Proudfoot, *Leukocyte Adhesion: Reconceptualizing Chemokine Presentation by Glycosaminoglycans.* Trends Immunol., 2019. **40**(6): p. 472-481.
185. Imai, T., et al., Identification and molecular characterization of fractalkine receptor CX3CR1, which mediates both leukocyte migration and adhesion. Cell., 1997. **91**(4): p. 521-30.

186. Hundhausen, C., A. Schulte, and B. Schulz, Regulated shedding of transmembrane chemokines by the disintegrin and metalloproteinase 10 facilitates detachment of adherent leukocytes. J Immunol., 2007. **178**(12): p. 8064.
187. Ludwig, A., et al., Fractalkine is expressed by smooth muscle cells in response to IFN-gamma and TNF-alpha and is modulated by metalloproteinase activity. J Immunol., 2002. **168**(2): p. 604-12.
188. Fong, A., et al., Fractalkine and CX3CR1 mediate a novel mechanism of leukocyte capture, firm adhesion, and activation under physiologic flow. . J. Exp. Med, 1998(188): p. 1413–1419.
189. Nicholson, M., et al., Affinity and kinetic analysis of L-selectin (CD62L) binding to glycosylation-dependent cell-adhesion molecule-1. J Biol Chem. , 1998. **273**(2): p. 763-70.
190. Muller, W., *Getting Leukocytes to the Site of Inflammation.* Vet Pathol. , 2013. **50**(1): p. 7-22.
191. Bogen, S., et al., Monoclonal antibody to murine PECAM-1 (CD31) blocks acute inflammation in vivo. J. Exp. Med, 1994. **179**(3): p. 1059–1064.
192. Geissmann, F., S. Jung, and D. Littman Blood monocytes consist of two principal subsets with distinct migratory properties. Immunity., 2003. **19**(1): p. 71-82.
193. Carlin, L., et al., Nr4a1-dependent Ly6C(low) monocytes monitor endothelial cells and orchestrate their disposal. Cell, 2013. **153**(2): p. 362-75.
194. Haskell, C., M. Cleary, and I. Charo, Molecular uncoupling of fractalkine-mediated cell adhesion and signal transduction. Rapid flow arrest of CX3CR1-expressing cells is independent of G-protein activation. J Biol Chem., 1999. **274**(15): p. 10053-8.
195. Rennert, K., et al., Recruitment of CD16(+) monocytes to endothelial cells in response to LPS-treatment and concomitant TNF release is regulated by CX3CR1 and interfered by soluble fractalkine. Cytokine, 2016(83): p. 41-52.
196. Wildgruber, M., et al., The "Intermediate" CD14++CD16+ monocyte subset increases in severe peripheral artery disease in humans. Sci Rep., 2016(6): p. 39483.
197. Garton, K., et al., Tumor necrosis factor-alpha-converting enzyme (ADAM17) mediates the cleavage and shedding of fractalkine (CX3CL1). J Biol Chem., 2001. **276**(41): p. 37993-8001.

198. O'Sullivan, S., et al., Fractalkine shedding is mediated by p38 and the ADAM10 protease under pro-inflammatory conditions in human astrocytes. J Neuroinflammation., 2016. **13**(1): p. 189.
199. Marsh, S., H. Arthur, and S. I., *The secret life of nonclassical monocytes.* Cytom. Part A, 2017. **91**(11): p. 1055–1058.
200. Ancuta, P., et al., *Fractalkine Preferentially Mediates Arrest and Migration of CD16+ Monocytes.* The Journal of Experimental Medicine, 2003. **197**(12): p. 1701–1707.
201. Ferretti, E., V. Pistoia, and A. Corcione, Role of fractalkine/CX3CL1 and its receptor in the pathogenesis of inflammatory and malignant diseases with emphasis on B cell malignancies. Mediators Inflamm., 2014: p. 480941.
202. Jones, B., M. Beamer, and S. Ahmed, *Fractalkine/CX3CL1: a potential new target for inflammatory diseases.* Mol Interv., 2010. **10**(5): p. 263-70.
203. Xuan, W., et al., Detrimental effect of fractalkine on myocardial ischaemia and heart failure. Cardiovascular Research, 2011. **92**(3): p. 385-93.
204. Altin, S. and P. Schulze, *Fractalkine: a novel cardiac chemokine?* Cardiovasc Res., 2011. **92**(3): p. 361–362.
205. Ali, M., et al., A novel CX3CR1 antagonist eluting stent reduces stenosis by targeting inflammation. Biomaterials., 2015(69): p. 22-9.
206. Yao, K., et al., Changes in fractalkine in patients with ST-elevation myocardial infarction. Coron Artery Dis., 2015. **26**(6): p. 516-20.
207. Bay, M., et al., NT-proBNP: a new diagnostic screening tool to differentiate between patients with normal and reduced left ventricular systolic function. Heart. , 2003. **89**(2): p. 150–154.
208. Husberg, C., et al., Cytokine expression profiling of the myocardium reveals a role for CX3CL1 (fractalkine) in heart failure. J Mol Cell Cardiol., 2008. **45**(2): p. 261-9.
209. Boag, S.E., et al., T lymphocytes and fractalkine contribute to myocardial ischemia/reperfusion injury in patients. Journal of Clinical Investigation, 2015. **125**(8): p. 3063-76.
210. Xu, B., et al., Prognostic value of fractalkine/CX3CL1 concentration in patients with acute myocardial infarction treated with primary percutaneous coronary intervention. Cytokine, 2019. **113**: p. 365-370.

211. Moatti, D., et al., Polymorphism in the fractalkine receptor CX3CR1 as a genetic risk factor for coronary artery disease. Blood., 2001. **97**(7): p. 1925-8.
212. Pucci, S., et al., CX3CR1 Receptor Polymorphisms, Th1 Cell Recruitment, and Acute Myocardial Infarction Outcome: Looking for a Link. Biomed Res Int., 2013: p. 451349.
213. Lavergne, E., et al., Adverse associations between CX3CR1 polymorphisms and risk of cardiovascular or cerebrovascular disease. Arterioscler Thromb Vasc Biol., 2005. **25**(4): p. 847-53.
214. Lesnik, P., C. Haskell, and I. Charo, Decreased atherosclerosis in CX3CR1–/– mice reveals a role for fractalkine in atherogenesis. J Clin Invest. , 2003. **111**(3): p. 333–340.
215. Rowinska, Z., et al., Role of the CX3C chemokine receptor CX3CR1 in the pathogenesis of atherosclerosis after aortic transplantation. PLoS One, 2017. **12**(2): p. e0170644.
216. Zhou, J., et al., DEC205-DC targeted DNA vaccine against CX3CR1 protects against atherogenesis in mice. PLoS One., 2018. **13**(4): p. e0195657.
217. Riopel, M., et al., Chronic fractalkine administration improves glucose tolerance and pancreatic endocrine function. J Clin Invest. , 2018. **128**(4): p. 1458-1470.
218. Landsman, L., et al., CX3CR1 is required for monocyte homeostasis and atherogenesis by promoting cell survival. Blood, 2009. **113**(4): p. 963-72.
219. Zhao, T., et al., Hypoxia-Inducible Factor-1α Regulates Chemotactic Migration of Pancreatic Ductal Adenocarcinoma Cells through Directly Transactivating the CX3CR1 Gene. PLoS One. , 2012. **7**(8): p. e43399.
220. Kim, K., et al., In vivo structure/function and expression analysis of the CX3C chemokine fractalkine. Blood, 2011. **118**(22): p. e156–e167.
221. Boehme, S., et al., The chemokine fractalkine inhibits Fas-mediated cell death of brain microglia. J. Immunol, 2000. **165**(1): p. 397–403.
222. White, G., et al., Fractalkine has anti-apoptotic and proliferative effects on human vascular smooth muscle cells via epidermal growth factor receptor signalling. Cardiovasc Res. , 2010. **85**(4): p. 825–835.
223. Chandrasekar, B., et al., Fractalkine (CX3CL1) stimulated by nuclear factor kappaB (NF-kappaB)-dependent inflammatory signals induces aortic smooth muscle cell proliferation through an autocrine pathway. Biochem. J., 2003. **373**: p. 547–58.

224. Meucci, O., et al., Expression of CX3CR1 chemokine receptors on neurons and their role in neuronal survival. Proc. Natl. Acad. Sci., 2000. **97**(14): p. 8075–8080.
225. Lee, S., et al., Fractalkine stimulates angiogenesis by activating the Raf-1/MEK/ERK- and PI3K/Akt/eNOS-dependent signal pathways. Am. J. Physiol. Circ. Physiol., 2006. **291**(6): p. H2836–H2846.
226. Cook DN, et al., Generation and analysis of mice lacking the chemokine fractalkine. Mol Cell Biol., 2001. **21**(9): p. 3159-65.
227. Wang, H., et al., Fractalkine/CX3CR1 induces apoptosis resistance and proliferation through the activation of the AKT/NF-κB cascade in pancreatic cancer cells. Cell Biochem Funct. , 2017. **35**(6): p. 315-326.
228. Cambien, B., et al., Signal transduction pathways involved in soluble fractalkine-induced monocytic cell adhesion. Blood, 2001. **97**(7): p. 2031-7.
229. Liu, Y., et al., Macrophage/monocyte-specific deletion of Ras homolog gene family member A (RhoA) downregulates fractalkine receptor and inhibits chronic rejection of mouse cardiac allografts. . The Journal of Heart and Lung Transplantation, 2017. **36**(3): p. 340-354.
230. Gevrey, J.C., B.M. Isaac, and D. Cox, *Syk is required for monocyte/macrophage chemotaxis to CX3CL1 (Fractalkine).* Journal of Immunology, 2005. **175**(6): p. 3737-45.
231. Green, S.R., et al., The CC chemokine MCP-1 stimulates surface expression of CX3CR1 and enhances the adhesion of monocytes to fractalkine/CX3CL1 via p38 MAPK. Journal of Immunology, 2006. **176**(12): p. 7412-20.
232. Taube, D., et al., *Fractalkine depresses cardiomyocyte contractility.* PLoS One., 2013. **8**(7): p. e69832.
233. Sun, S., *Non-canonical NF-kappaB signaling pathway. .* Cell Res, 2011(21): p. 71–85.
234. Vallabhapurapu, S. and M. Karin, Regulation and function of NF-kappaB transcription factors in the immune system. . Annu Rev Immunol 2009(27): p. 693–733.
235. Hamid, T., et al., Cardiomyocyte NF-{kappa}B p65 promotes adverse remodelling, apoptosis, and endoplasmic reticulum stress in heart failure. . Cardiovasc Res., 2011(89): p. 129–138.

236. Busam, K., et al., Staphylococcus aureus and derived exotoxins induce nuclear factor kappa B-like activity in murine bone marrow macrophages. Infection and immunity, 1992. **60**(5): p. 2008-15.
237. Lemercier, G., S. Roman-Roman, and G. Rawadi, A Mycoplasma fermentans derived synthetic lipopeptide induces AP-1 and NF-kappaB activity and cytokine secretion in macrophages via the activation of mitogen-activated protein kinase pathways. The Journal of biological chemistry., 1998. **273**(51): p. 34391-8.
238. Berberich, I., G. Shu, and E. Clark, *Cross-linking CD40 on B cells rapidly activates nuclear factor-kappa B.* Journal of immunology 1994. **153**(10): p. 4357-66.
239. Hayden, M. and S. Ghosh, NF-κB, the first quarter-century: remarkable progress and outstanding questions. Genes Dev., 2012. **26**(3): p. 203–234.
240. Pahl, H., Activators and target genes of Rel/NF-kappaB transcription factors. Oncogene, 1999. **18**(49): p. 6853-6866.
241. Mercurio, F. and A. Manning, *NF-kappaB as a Primary Regulator of the Stress Response.* Oncogene, 1999. **18**(45): p. 6163-71
242. D'Ignazio, L. and S. Rocha, *Hypoxia Induced NF-κB.* Cell, 2016. **5**(1): p. 10.
243. Senftleben, U., et al., Activation by IKKα of a second, evolutionary conserved, NF-κ B signaling pathway. . Science, 2001(293): p. 1495–1499.
244. Dejardin, E., et al., The lymphotoxin-β receptor induces different patterns of gene expression via two NF-κB pathways. . Immunity, 2002(17): p. 525–535.
245. Bonizzi, G. and M. Karin, The two NF-κB activation pathways and their role in innate and adaptive immunity. . Trends Immunol, 2004(25): p. 280–288.
246. Novack, D., et al., The IκB function of NF-κB2 p100 controls stimulated osteoclastogenesis. . J Exp Med, 2003(198): p. 771–781.
247. Matsushima, A., et al., Essential role of nuclear factor NF-κB-inducing kinase and inhibitor of κB (IκB) kinase α in NF-κB activation through lymphotoxin β receptor, but not through tumor necrosis factor receptor. J Exp Med, 2001(193): p. 631–636.
248. Dejardin, E., et al., The lymphotoxin-β receptor induces different patterns of gene expression via two NF-κB pathway. Immunity, 2002(17): p. 525–535
249. Bonizzim G, et al., Activation of IKKα target genes depends on recognition of specific κB binding sites by RelB:p52 dimers. . Embo J 2004(23): p. 4202–4210.
250. Lawrence, T., *The Nuclear Factor NF-κB Pathway in Inflammation.* Cold Spring Harb Perspect Biol., 2009. **6**(1): p. a001651.

251. Sun, S., J. Chang, and J. Jin, *Regulation of nuclear factor-kappaB in autoimmunity. .* Trends Immunol, 2013(34): p. 282–289.
252. Ghosh, S. and M. Karin, *Missing pieces in the NF-kappaB puzzle. .* Cell, 2002(109): p. S81–S96.
253. Hayden, M. and S. Ghosh, *NF-kappaB in immunobiology. .* Cell Res, 2011(21): p. 223–244.
254. Wang, N., H. Liang, and K. Zen, Molecular mechanisms that influence the macrophage m1-m2 polarization balance. Front Immunol., 2014(5): p. 614.
255. Sutterwala, F., S. Haasken, and S. Cassel, *Mechanism of NLRP3 inflammasome activation.* Ann N Y Acad Sci 2014(1319): p. 82–95.
256. Liu, T., et al., *NF-κB signaling in inflammation.* Signal Transduct Target Ther., 2017(2): p. 17023.
257. Zhang, Q., M. Lenardo, and D. Baltimore, *30 Years of NF-κB: A Blossoming of Relevance to Human Pathobiology.* Cell, 2017. **168**(1-2): p. 37-57.
258. Sun, S. and S. Ley, *New insights into NF-kappaB regulation and function.* Trends Immunol, 2008(29): p. 469–478.
259. Karin, M. and M. Delhase, The I kappa B kinase (IKK) and NF-kappa B: key elements of proinflammatory signalling. Semin Immunol, 2000(12): p. 85–98.
260. Hayden, M. and S. Ghosh, *Shared principles in NF-kappaB signaling. .* Cell, 2008(132): p. 344–362.
261. Israel, A., *the IKK complex, a central regulator of NF-kappaB activation.* Cold Spring Harb Perspect Biol 2010(2): p. a000158.
262. Oeckinghaus, A. and S. Ghosh, *The NF-κB Family of Transcription Factors and Its Regulation.* Cold Spring Harb Perspect Biol., 2009. **1**(4): p. a000034.
263. Marchant, D., et al., *Inflammation in Myocardial Diseases.* Circ Res, 2012. **110**(1): p. 126-44.
264. Venkatachalam, K., et al., Neutralization of interleukin-18 Ameliorates Ischemia/Reperfusion-Induced Myocardial Injury. J Biol Chem., 2009. **284**(12): p. 7853-65.
265. Moss, N., et al., IKKbeta Inhibition Attenuates Myocardial Injury and Dysfunction Following Acute Ischemia-Reperfusion Injury. Am J Physiol Heart Circ Physiol, 2007. **293**(4): p. H2248-53.

266. Frantz, S., et al., Tissue-Specific Effects of the Nuclear Factor κB Subunit p50 on Myocardial Ischemia-Reperfusion Injury. Am J Pathol., 2007. **171**(2): p. 507–512.
267. Zeng, M., et al., *Suppression of NF-κB Reduces Myocardial No-Reflow.* PLoS One. , 2012. **7**(10): p. e47306.
268. Maimaitiaili, A., et al., Inhibition of nuclear factor kappa B pathway protects myocardial ischemia/reperfusion injury in rats under treatment with abnormal savda munziq. Am J Transl Res., 2018. **10**(1): p. 77–85.
269. Gordon, J., J. Shaw, and L. Kirshenbaum, *Multiple Facets of NF-κB in the Heart: To Be or Not to NF-κB.* Circ Res, 2011. **108**(9): p. 1122-32.
270. Galán-Ganga, M., Á. García-Yagüe, and I. Lastres-Becker, *Role of MSK1 in the Induction of NF-κB by the Chemokine CX3CL1 in Microglial Cells.* Cell Mol Neurobiol. , 2019. **39**(3): p. 331-340.
271. Raspé, C., et al., NF-κB-mediated inverse regulation of fractalkine and CX3CR1 during CLP-induced sepsis. Cytokine., 2013. **61**(1): p. 97-103.
272. Chandrasekar, B., et al., Fractalkine (CX3CL1) stimulated by nuclear factor kappaB (NF-kappaB)-dependent inflammatory signals induces aortic smooth muscle cell proliferation through an autocrine pathway. Biochem J., 2003. **373**: p. 547-58.
273. Meucci, O., et al., Expression of CX3CR1 chemokine receptors on neurons and their role in neuronal survival. Proc Natl Acad Sci U S A. , 2000. **97**(14): p. 8075–8080.
274. Brand, S., et al., Fractalkine-mediated signals regulate cell-survival and immune-modulatory responses in intestinal epithelial cells. Gastroenterology., 2002. **122**(1): p. 166-77.
275. Chen, Y., et al., Inhibition by pentoxifylline of TNF-alpha-stimulated fractalkine production in vascular smooth muscle cells: evidence for mediation by NF-kappa B down-regulation. Br J Pharmacol. , 2003. **138**(5): p. 950-8.
276. O'Sullivan , S., et al., Fractalkine shedding is mediated by p38 and the ADAM10 protease under pro-inflammatory conditions in human astrocytes. J Neuroinflammation. , 2016. **13**(1): p. 189.
277. Jung, S., et al., Analysis of Fractalkine Receptor CX3CR1 Function by Targeted Deletion and Green Fluorescent Protein Reporter Gene Insertion. Mol Cell Biol., 2000. **20**(11): p. 4106–4114.
278. Tsuchiya, S., et al., Establishment and Characterization of a Human Acute Monocytic Leukemia Cell Line (THP-1). Int J Cancer, 1980. **26**(2): p. 171-6.

279. Ziegler-Heitbrock, H., et al., Establishment of a Human Cell Line (Mono Mac 6) With Characteristics of Mature Monocytes. Int J Cancer, 1988. **41**(3): p. 456-61.
280. Sundstrom, C. and K. Nilsson, Establishment and characterisation of a human histocytic lymphoma cell line (U937). . Int J Cancer 1976(17): p. 565–577.
281. Nahrendorf, M., et al., The healing myocardium sequentially mobilizes two monocyte subsets with divergent and complementary functions. Journal of Experimental Medicine, 2007. **204**(12): p. 3037–3047.
282. Hilgendorf, I., et al., Ly-6Chigh monocytes depend on Nr4a1 to balance both inflammatory and reparative phases in the infarcted myocardium. Circ Res, 2014. **114**(10): p. 1611-22.
283. Bosch X, et al., Monocyte Subsets Are Differently Associated with Infarct Size, Left Ventricular Function, and the Formation of a Potentially Arrhythmogenic Scar in Patients with Acute Myocardial Infarction. J Cardiovasc Transl Res., 2019.
284. Di Stefano, R., et al., Inflammatory markers and cardiac function in acute coronary syndrome: difference in ST-segment elevation myocardial infarction (STEMI) and in non-STEMI models. . Biomed Pharmacother., 2009. **63**(10): p. 773-80.
285. Mukherjee, R., et al., Non-Classical monocytes display inflammatory features: Validation in Sepsis and Systemic Lupus Erythematous. Scientific Reports, 2015. **5**(13886).
286. Thomas, G., et al., Human Blood Monocyte Subsets: A New Gating Strategy Defined Using Cell Surface Markers Identified by Mass Cytometry. Arterioscler Thromb Vasc Biol., 2017. **37**(8): p. 1548-1558.
287. Lesnik P, Haskell CA, and C. IF, Decreased atherosclerosis in CX3CR1-/- mice reveals a role for fractalkine in atherogenesis. J Clin Invest., 2003. **111**(3): p. 333-40.
288. Xuan, W., et al., Resveratrol improves myocardial ischemia and ischemic heart failure in mice by antagonizing the detrimental effects of fractalkine. Critical Care Medicine, 2012. **40**(11): p. 3026-33.
289. Gu, X., et al., Fractalkine neutralization improves cardiac function after myocardial infarction. Experimental Physiology, 2015. **100**(7): p. 805–817.
290. Moatti, D., et al., Polymorphism in the fractalkine receptor CX3CR1 as a genetic risk factor for coronary artery disease. . Blood, 2001. **97**(7): p. 1925-8.

291. Wu, J., et al., Two Polymorphisms in the Fractalkine Receptor CX3CR1 Gene Influence the Development of Atherosclerosis: A Meta-Analysis. Disease Markers, 2014. **2014**: p. 913678.
292. Daubert MA and J. A., The utility of troponin measurement to detect myocardial infarction: review of the current findings. Vasc Health Risk Manag. , 2010(6): p. 691-9.
293. Ziegler-Heitbrock, L., Blood Monocytes and Their Subsets: Established Features and Open Questions. . Front Immunol. , 2015. **6**(423).
294. Sampath, P., et al., Monocyte Subsets: Phenotypes and Function in Tuberculosis Infection. Front Immunol., 2018. **9**(1726).
295. Hübl, W., et al., Value of neutrophil CD16 expression for detection of left shift and acute-phase response. Am J Clin Pathol., 1997. **107**(2): p. 187-96.
296. Romee, R., et al., NK cell CD16 surface expression and function is regulated by a disintegrin and metalloprotease-17 (ADAM17). . Blood, 2013. **121**(18): p. 3599-608.
297. Marimuthu, R., et al., Characterization of Human Monocyte Subsets by Whole Blood Flow Cytometry Analysis. J Vis Exp, 2018. **17**(140).
298. Manz, M. and S. Boettcher, *Emergency granulopoiesis.* Nat Rev Immunol. , 2014. **14**(5): p. 302-14.
299. Sreejit, G., et al., Neutrophil-Derived S100A8/A9 Amplify Granulopoiesis Following Myocardial Infarction. Circulation. , 2020.
300. Ghaffari, S., et al., The predictive Value of Total Neutrophil Count and Neutrophil/Lymphocyte Ratio in Predicting In-hospital Mortality and Complications after STEMI. J Cardiovasc Thorac Res. , 2014. **6**(1): p. 35–41.
301. Cignarella, A., et al., The continuum of monocyte phenotypes: Experimental evidence and prognostic utility in assessing cardiovascular risk. J Leukoc Biol., 2018.
302. Ong, S., et al., A Novel, Five-Marker Alternative to CD16-CD14 Gating to Identify the Three Human Monocyte Subsets. Front Immunol., 2019. **10**(1761).
303. Shantsila, E., et al., Monocyte subsets in coronary artery disease and their associations with markers of inflammation and fibrinolysis. Atherosclerosis. , 2014. **234**(1): p. 4-10.

304. van Kranenburg, M., et al., Prognostic value of microvascular obstruction and infarct size, as measured by CMR in STEMI patients. JACC: Cardiovascular Imaging, 2014. **7**(9): p. 930-9.
305. de Waha, S., et al., Impact of early vs. late microvascular obstruction assessed by magnetic resonance imaging on long-term outcome after ST-elevation myocardial infarction: a comparison with traditional prognostic markers. European Heart Journal, 2010. **31**(21): p. 2660-8.
306. Hombach, V., et al., Sequelae of acute myocardial infarction regarding cardiac structure and function and their prognostic significance as assessed by magnetic resonance imaging. Eur Heart J., 2005. **26**(6): p. 549-57.
307. Tsujioka, H., et al., Post-reperfusion enhancement of CD14(+)CD16(-) monocytes and microvascular obstruction in ST-segment elevation acute myocardial infarction. Circ J., 2010. **74**(6): p. 1175-82.
308. REINISCH, W., et al., Donor dependent, interferon-γ induced HLA-DR expression on human neutrophils in vivo. Clin Exp Immunol., 2003. **133**(3): p. 476–484.
309. Naeim, F. and R. Phan, Atlas of Hematopathology. Principles of Immunophenotyping. 2.1.5.2 CD14. Second ed. 2018.
310. Johnston, B., et al., Chronic inflammation upregulates chemokine receptors and induces neutrophil migration to monocyte chemoattractant protein-1. J Clin Invest., 1999(103): p. 1269–1276.
311. Talbot, J., F. Bianchini, and D. Nascimento, CCR2 Expression in Neutrophils Plays a Critical Role in Their Migration Into the Joints in Rheumatoid Arthritis. . Arthritis Rheumatol., 2015. **67**(7): p. 1751–1759.
312. Yan, X., et al., Temporal Dynamics of Cardiac Immune Cell Accumulation Following Acute Myocardial Infarction. J Mol Cell Cardiol., 2013(62): p. 24-35.
313. Jung, K., et al., Endoscopic Time-Lapse Imaging of Immune Cells in Infarcted Mouse Hearts. Circulation Research, 2013. **112**(6).
314. Hilgendorf, I., et al., Ly-6C high monocytes depend on Nr4a1 to balance both inflammatory and reparative phases in the infarcted myocardium. Circ Res 2014(114): p. 1611–1622.
315. Hettinger, J., et al., *Origin of monocytes and macrophages in a committed progenitor.* Nature Reviews Immunology, 2013. **14**: p. 821-830.

316. Swirski, F.K., et al., Identification of splenic reservoir monocytes and their deployment to inflammatory sites. Science, 2009. **325**(5940): p. 612-6.
317. Tsou, C., et al., Critical roles for CCR2 and MCP-3 in monocyte mobilization from bone marrow and recruitment to inflammatory sites.J. Clin Invest., 2007(117): p. 902–909.
318. ., Z.-H.L., The CD14+ CD16+ blood monocytes: their role in infection and inflammation. . Leukoc Biol., 2007. **81**(3): p. 584–592.
319. Geissmann, F., S. Jung, and D. Littman, Blood monocytes consist of two principal subsets with distinct migratory properties. . Immunity, 2003. **19**(1): p. 71-82.
320. Tacke, F. and G. Randolph, *Migratory fate and differentiation of blood monocyte subsets.* Immunobiology., 2006. **211**(6-8): p. 609–618.
321. Gordon, S. and P. Taylor, *Monocyte and macrophage heterogeneity. .* Nat Rev Immunol. , 2005. **5**(12): p. 953–964.
322. White, G., et al., *Fractalkine promotes human monocyte survival via a reduction in oxidative stress.* Arterioscler Thromb Vasc Biol., 2014. **34**(12): p. 2554-62.
323. dela Paz, N. and P. D'Amore, *Arterial versus venous endothelial cells.* Cell Tissue Res., 2009. **335**(1): p. 5–16.
324. Peet, C., et al., Cardiac monocytes and macrophages after myocardial infarction. . Cardiovasc Res. , 2019.
325. Heidt, T., et al., Differential contribution of monocytes to heart macrophages in steady- state and after myocardial infarction. Circ Res., 2014(115): p. 284–95.
326. Murray, P., et al., Macrophage activation and polarization: nomenclature and experimental guidelines. Immunity, 2014. **41**(1): p. 14-20.
327. Ma, Y., A. Mouton, and M. Lindsey, Cardiac macrophage biology in the steady-state heart, the aging heart, and following myocardial infarction. Transl Res. , 2018(191): p. 15-28.
328. Yang, J., et al., Monocyte and macrophage differentiation: circulation inflammatory monocyte as biomarker for inflammatory diseases. Biomark Res, 2014. **2**(1).
329. Ishida, Y., J. Gao, and P. Murphy, Chemokine receptor CX3CR1 mediates skin wound healing by promoting macrophage and fibroblast accumulation and function. . Immunol, 2008(180): p. 569–579.

330. Donnelly, D., et al., Deficient CX3CR1 signaling promotes recovery after mouse spinal cord injury by limiting the recruitment and activation of Ly6Clo/iNOS+ macrophages. J. Neurosci., 2011(31): p. 9910–9922.
331. Yona, S., et al., Fate mapping reveals origins and dynamics of monocytes and tissue macrophages under homeostasis. Immunity., 2013. **38**(1): p. 79-91.
332. Arnold, L., et al., Inflammatory monocytes recruited after skeletal muscle injury switch into antiinflammatory macrophages to support myogenesis. J Exp Med, 2007. **204**(5): p. 1057-69.
333. Little, M., R. Hurst, and K. Else, Dynamic changes in macrophage activation and proliferation during the development and resolution of intestinal inflammation. J Immunol. , 2014. **93**(9): p. 4684-95.
334. Morris, L., C. Graham, and S. Gordon, Macrophages in haemopoietic and other tissues of the developing mouse detected by the monoclonal antibody F4/80. Development, 1991. 112(2): p. 517-26.
335. Lin, H., et al., The macrophage F4/80 receptor is required for the induction of antigen-specific efferent regulatory T cells in peripheral tolerance. J Exp Med. , 2005. **201**(10): p. 1615–1625.
336. Lee, M., et al., Tissue-specific Role of CX3CR1 Expressing Immune Cells and Their Relationships with Human Disease. Immune Network, 2018. **18**(1): p. e5.
337. Eriksson, E., et al., *Powerful inflammatory properties of large vein endothelium in vivo.* Arterioscler Thromb Vasc Biol, 2005. **25**(4): p. 723-8.
338. Ijsselsteijn, M., et al., A 40-Marker Panel for High Dimensional Characterization of Cancer Immune Microenvironments by Imaging Mass Cytometry. . Front Immunol. , 2019(10): p. 2534.
339. Kubo, N., et al., Leukocyte CD11b expression is not essential for the development of atherosclerosis in mice. J Lipid Res, 2000. **41**(7): p. 1060-6.
340. Lee, P., et al., *Ly6 family proteins in neutrophil biology.* J Leukoc Biol., 2013. **94**(4): p. 585-94.
341. Christensen, J., et al., CD11b expression as a marker to distinguish between recently activated effector CD8(+) T cells and memory cells. Int Immunol., 2001. **13**(4): p. 593-600.
342. Chu, H., et al., *Role of CCR2 in inflammatory conditions of the central nervous system.* J Cereb Blood Flow Metab., 2014. **34**(9): p. 1425–1429.

.
343. Oliva-Martin, M., et al., Evaluation of a method for murine monocyte isolation by bone marrow depletion. Anal Biochem., 2015(480): p. 42-8.
344. Rose, S., A. Misharin, and H. Perlman1, *A novel Ly6C/Ly6G-based strategy to analyze the mouse splenic myeloid compartment.* Cytometry A. , 2012. **81**(4): p. 343–350.
345. Swartz, K. *Expected Cell Frequencies*. Available from: https://www.biolegend.com/en-us/blog/expected-cell-frequencies.
346. Bianchini M, et al., PD-L1 expression on nonclassical monocytes reveals their origin and immunoregulatory function. Sci Immunol, 2019. **4**(36).
347. Kratofil, R., P. Kubes, and J. Deniset, *Monocyte Conversion During Inflammation and Injury. .* Arterioscler Thromb Vasc Biol. , 2017. **37**(1): p. 35-42. .
348. Poupel, L., et al., Pharmacological inhibition of the chemokine receptor, CX3CR1, reduces atherosclerosis in mice. Arterioscler Thromb Vasc Biol., 2013. **33**(10): p. 2297-305. .
349. Tomczyk M, K.I., Szade K, Bukowska-Strakova K, Meloni M, Jozkowicz A, Dulak J, Jazwa A. , Splenic Ly6Chi monocytes contribute to adverse late post-ischemic left ventricular remodeling in heme oxygenase-1 deficient mice. Basic Res Cardiol, 2017. **112**(4): p. 39.
350. Lu, R., et al., Dynamic changes of peripheral blood monocyte subsets after myocardial ischemia/reperfusion in rats. 30, 2014. **2**(131-4).
351. Haskell, C., M. Cleary, and I. Charo, Molecular uncoupling of fractalkine-mediated cell adhesion and signal transduction: rapid flow arrest of CX3CR1-expressing cells is independent of G-protein activation. . J. Biol. Chem. , 1999(274): p. 10053–10058.
352. Umehara, H., et al., *Fractalkine in vascular biology: from basic research to clinical disease.* Arterioscler Thromb Vasc Biol., 2004. **24**(1): p. 34-40.
353. Nakano Y, M.T., Tokutome M, Funamoto D, Katsuki S, Ikeda G, Nagaoka K, Ishikita A, Nakano K, Koga J, Sunagawa K, Egashira K., *Nanoparticle-Mediated Delivery of Irbesartan Induces Cardioprotection from Myocardial Ischemia-Reperfusion Injury by Antagonizing Monocyte-Mediated Inflammation.* Sci Rep, 2016. **6**(29601).

354. Boyette, L., et al., Phenotype, function, and differentiation potential of human monocyte subsets. PLoS One., 2017. **12**(4): p. e0176460.
355. O'Rourke, S., A. Dunne, and M. Monaghan, The Role of Macrophages in the Infarcted Myocardium: Orchestrators of ECM Remodeling. Front Cardiovasc Med., 2019. **6**(101).
356. Lee, Y., et al., CX3CR1 differentiates F4/80low monocytes into pro-inflammatory F4/80high macrophages in the liver. . Sci Rep., 2018. **8**(1): p. 15076.
357. White, G. and D. Greaves, *Fractalkine: a survivor's guide: chemokines as antiapoptotic mediators.* Arterioscler Thromb Vasc Biol., 2012. **32**(3): p. 589-94.
358. Biswas, S., A. Sica, and C. Lewis, Plasticity of macrophage function during tumor progression: regulation by distinct molecular mechanisms. J Immunol., 2008(180): p. 2011–7.
359. Murray, P. and T. Wynn, *Protective and pathogenic functions of macrophage subsets.* Nat Rev Immunol., 2011(11): p. 723–37.
360. Bianchini, M., et al., PD-L1 Expression on Nonclassical Monocytes Reveals Their Origin and Immunoregulatory Function. Sci Immunol, 2019. **4**(36).
361. Ingersoll, M., et al., Comparison of gene expression profiles between human and mouse monocyte subsets. Blood, 2010. **115**(3): p. e10–e19.
362. Kis, A., D. Yellon, and G. Baxter, Role of nuclear factor-kappa B activation in acute ischaemia-reperfusion injury in myocardium. Br J Pharmacol 2003(138): p. 894–900.
363. Meldrum, D., et al., On-pump coro- nary artery bypass surgery activates human myocardial NF-kappaB and increases TNF-alpha in the heart. J Surg Res, 2003(112): p. 175–179.
364. Carlson, D., et al., IkB overexpression in cardiomyocytes prevents NF- B translocation and provides cardioprotection in trauma. . Am J Physiol Heart Circ Physiol 2003(284): p. H804–H814.
365. Morishita, R., et al., In vivo transfection of cis element “decoy” against nuclear factor-kappaB binding site prevents myocardial infarction. Nat Med, 1997(3): p. 894 – 899.
366. Lawrence, T., et al., Ikk[Alpha] Limits Macrophage Nf-[Kappa]B Activation and Contributes to the Resolution of Inflammation. . Nature, 2005(434): p. 1138–1143.

367. Moss, N., et al., IKKbeta inhibition attenuates myocardial injury and dysfunction following acute ischemia-reperfusion injury. Am J Physiol Heart Circ Physiol, 2007. **293**(4): p. H2248-53.
368. Li, H., et al., Targeted cardiac overexpression of A20 improves left ventricular performance and reduces compensatory hypertrophy after myocardial infarction. Circulation, 2007. **115**(14): p. 1885-94.
369. Frantz, S., et al., Tissue-Specific Effects of the Nuclear Factor κB Subunit p50 on Myocardial Ischemia-Reperfusion Injury. Am J Pathol. , 2007. **171**(2): p. 507–512.
370. Ernst, O., S. Vayttaden, and Fraser IDC, *Measurement of NF-κB activation in TLR-activated macrophages.* Methods Mol Biol. , 2018(1714): p. 67–78.
371. Christian, F., E. Smith, and R. Carmody, *The Regulation of NF-κB Subunits by Phosphorylation.* Cells, 2016. **5**(1): p. 12.
372. Mattioli, I., et al., Transient and selective NF-kappa B p65 serine 536 phosphorylation induced by T cell costimulation is mediated by I kappa B kinase beta and controls the kinetics of p65 nuclear import. . J Immunol., 2004. **172**: p. 6336–6344.
373. Wang D and B.A. Jr., Activation of nuclear factor-kappaB-dependent transcription by tumor necrosis factor-alpha is mediated through phosphorylation of RelA/p65 on serine 529. . The Journal of biological chemistry. , 1998(273): p. 29411–29416.
374. Zhong, H., R. Voll, and S. Ghosh, Phosphorylation of NF-kappa B p65 by PKA stimulates transcriptional activity by promoting a novel bivalent interaction with the coactivator CBP/p300. . Molecular cell, 1998(1): p. 661–671.
375. Bosshart, H. and M. Heinzelmann, *THP-1 cells as a model for human monocytes.* Ann Transl Med. , 2016. **4**(21): p. 438.
376. Sundström C and N. K., Establishment and characterization of a human histiocytic lymphoma cell line (U-937). Int J Cancer. , 1976 **17**(5): p. 565-77.
377. Ziegler-Heitbrock, H., et al., Establishment of a human cell line (Mono Mac 6) with characteristics of mature monocytes. Int J Cancer., 1988. **41**(3): p. 456-61.
378. Castro-Sánchez, S., et al., CX3CR1-deficient microglia shows impaired signalling of the transcription factor NRF2: Implications in tauopathies. Redox Biol, 2019.

379. Brand, S., et al., Fractalkine-mediated signals regulate cell-survival and immune-modulatory responses in intestinal epithelial cells. Gastroenterology. , 2002. **122**(1): p. 166-77.
380. Meucci, O., et al., Expression of CX3CR1 chemokine receptors on neurons and their role in neuronal survival. . Proc Natl Acad Sci U S A., 2000. **97**(14): p. 8075–8080.
381. Hou, S., C. Hou, and J. Liu, CX3CL1 promotes MMP-3 production via the CX3CR1, c-Raf, MEK, ERK, and NF-κB signaling pathway in osteoarthritis synovial fibroblasts.
. Arthritis Res Ther., 2017. **19**(1): p. 282.
382. Liu, F., et al., Interleukin (IL)-23 p19 expression induced by IL-1beta in human fibroblast-like synoviocytes with rheumatoid arthritis via active nuclear factor-kappaB and AP-1 dependent pathway. . Rheumatology, 2007. **46**(8): p. 1266–73.
383. Montaseri, A., et al., IGF-1 and PDGF-bb suppress IL-1beta-induced cartilage degradation through down-regulation of NF-kappaB signaling: involvement of Src/PI-3 K/AKT pathway. PLoS One, 2011. **6**(12): p. e28663.
384. Awane, M., et al., NF-kappa B-inducing kinase is a common mediator of IL-17-, TNF-alpha-, and IL-1 beta-induced chemokine promoter activation in intestinal epithelial cells. . J Immunol, 1999. **162**: p. 5337–5344.
385. Clark, K., et al., Novel cross-talk within the IKK family controls innate immunity. Biochem J. , 2011. **434**(1): p. 93-104.
386. Zhang, J., et al., An unexpected twist to the activation of IKKβ: TAK1 primes IKKβ for activation by autophosphorylation. Biochem J. , 2014. **461**(3): p. 531-7.
387. Buss, H., et al., Constitutive and Interleukin-1-Inducible Phosphorylation of P65 Nf-Kb at Serine 536 Is Mediated by Multiple Protein Kinases Including Iκb Kinase (Ikk)-A, Ikkβ, Ikkϵ, Traf Family Member-Associated (Tank)-Binding Kinase 1 (Tbk1), and an Unknown Kinase and Couples P65 to Tata-Binding Protein-Associated Factor Ii31-Mediated Interleukin-8 Transcription. J. Biol. Chem, 2004(279): p. 55633–55643.
388. Sakurai, H., et al., Iκb Kinases Phosphorylate Nf-Kb P65 Subunit on Serine 536 in the Transactivation Domain. J. Biol. Chem, 1999(274): p. 30353–30356.
389. Sizemore, N., et al., Distinct Roles of the Ikappa B Kinase Alpha and Beta Subunits in Liberating Nuclear Factor Kappa B (Nf-Kappa B) from Ikappa B and in

Phosphorylating the P65 Subunit of Nf-Kappa B. J. Biol. Chem, 2002(277): p. 3863–3869.

390. Cederblad, L., et al., AZD8797 is an allosteric non-competitive modulator of the human CX3CR1 receptor. Biochem J., 2016. **473**(5): p. 641-9.

391. Liu, T., et al., *NF-κB signaling in inflammation.* Signal Transduct Target Ther., 2017. **2**(17023).

392. Hayden, M. and S. Ghosh, *Regulation of NF-κB by TNF Family Cytokines.* Semin Immunol., 2015. **26**(3): p. 253–266.

393. Schütze, S., et al., *TNF-induced activation of NF-kappa B.* Immunobiology., 1995. **193**(2-4): p. 193-203.

394. Turner, N., et al., Mechanism of TNFα-induced IL-1α, IL-1β and IL-6 expression in human cardiac fibroblasts: Effects of statins and thiazolidinediones Cardiovascular Research, 2007. **76**(1): p. 81–90.

395. Chiewchengchol, D., et al., Differential changes in gene expression in human neutrophils following TNF-α stimulation: Up-regulation of anti-apoptotic proteins and down-regulation of proteins involved in death receptor signaling. Immun Inflamm Dis., 2016. **4**(1): p. 35–44.

396. Gomes , A., et al., Inhibition of NF-kB activation and cytokines production in THP-1 monocytes by 2-styrylchromones. Med Chem, 2015. **11**(6): p. 560-6.

397. Ziegler-Heitbrock, H., et al., Establishment of a human cell line (Mono Mac 6) with characteristics of mature monocytes. Int J Cancer., 1998. **41**(3): p. 456-61.

398. Heitbrock, Z., *Mono Mac 6.* International Journal of Cancer, 1998(41): p. 456-461.

399. Neustock, P., et al., Cytokine production of the human monocytic cell line Mono Mac 6 in comparison to mature monocytes in peripheral blood mononuclear cells. Immunobiology., 1993. **188**(3): p. 293-302.

400. Riddy, D., et al., Comparative genotypic and phenotypic analysis of human peripheral blood monocytes and surrogate monocyte-like cell lines commonly used in metabolic disease research. PLoS One., 2018. **13**(5): p. e0197177.

401. R, M., et al., Non-classical monocytes display inflammatory features: validation in sepsis and systemic lupus erythematous. Sci. Rep, 2015(5): p. 13886.

402. Nielsen, M., M. Andersen, and H. Møller, Monocyte isolation techniques significantly impact the phenotype of both isolated monocytes and derived macrophages in vitro. Immunology., 2020. **159**(1): p. 63-74.
403. Fendl, B., et al., Storage of human whole blood, but not isolated monocytes, preserves the distribution of monocyte subsets. Biochem Biophys Res Commun, 2019. **517**(4): p. 709-714.
404. Signalling, C. *Phospho-NF-κB p65 (Ser536) (93H1) Rabbit mAb #3033*. 2020 29012020]; Available from: https://www.cellsignal.co.uk/products/primary-antibodies/phospho-nf-kb-p65-ser536-93h1-rabbit-mab/3033.
405. Sasaki, C., et al., Phosphorylation of RelA/p65 on serine 536 defines an I{kappa}B{alpha}-independent NF-{kappa}B pathway. J Biol Chem., 2005. **280**(41): p. 34538-47.
406. Vakili, S., T. Fischer, and J. Rappaport, M2 differentiation of MonoMac-1 cell line induced by M-CSF and glucocorticoid pathways. . J Cell Physiol, 2020.
407. Yu, M., J. Yeh, and C. van Waes, Protein Kinase CK2 Mediates Inhibitor-Kappa B Kinase and Aberrant Nuclear Factor-κB Activation by Serum Factor(s) in Head and Neck Squamous Carcinoma Cells. Cancer Res. , 2006. **66**(13): p. 6722–6731.
408. M, F., et al., Constitutive nuclear NF-kappa B in cells of the monocyte lineage. Biochem J. , 1994. **304**: p. 87-94.
409. Apostolakis, S., et al., *Interleukin 8 and cardiovascular disease.* Cardiovasc Res. , 2009. **84**(3): p. 353-60.
410. Riesenberg, K., et al., Neutrophil superoxide release and interleukin 8 in acute myocardial infarction: distinction between complicated and uncomplicated states. Eur J Clin Invest. , 1997(27): p. 398-404.
411. Marin, V., F. Montero-Julian, and S. Gres, The IL-6-soluble IL-6Ralpha autocrine loop of endothelial activation as an intermediate between acute and chronic inflammation: an experimental model involving thrombin. J Immunol., 2001(167): p. 3435-3442.
412. Gerszten, R., et al., MCP-1 and IL-8 trigger firm adhesion of monocytes to vascular endothelium under flow conditions,. Nature, 1999. **398**: p. 718-723.
413. Boyle, E., et al., Inhibition of interleukin-8 blocks myocardial ischemia-reperfusion injury, . J Thorac Cardiovasc Surg, 1998. **116**: p. 114-121.

414. Shetelig C1, L.S., Hoffmann P3, Seljeflot I4, Gran JM5, Eritsland J6, Andersen GØ6., *Association of IL-8 With Infarct Size and Clinical Outcomes in Patients With STEMI.* J Am Coll Cardiol. , 2018. **72**(2): p. 187-198.

415. White, C., et al., Cardiomyocyte and Vascular Smooth Muscle-Independent 11β-Hydroxysteroid Dehydrogenase 1 Amplifies Infarct Expansion, Hypertrophy, and the Development of Heart Failure After Myocardial Infarction in Male Mice. Endocrinology., 2016. **157**(1): p. 346–357.

416. O'Brien, P., D. Smith, and T. Knechtel, Cardiac troponin I is a sensitive, specific biomarker of cardiac injury in laboratory animals. . Lab Anim., 2006. **40**: p. 153–171.

417. Haberkorn, S., et al., Cardiovascular Magnetic Resonance Relaxometry Predicts Regional Functional Outcome After Experimental Myocardial Infarction. Circ Cardiovasc Imaging, 2017. **10**(8): p. e006025.

418. Xu, Z., et al., A Murine Model of Myocardial Ischemia-reperfusion Injury through Ligation of the Left Anterior Descending Artery. J Vis Exp. , 2014(86): p. 51329.

419. Meghraoui-Kheddar, A., et al., Revising CX3CR1 Expression on Murine Classical and Non-classical Monocytes. Front Immunol. , 2020. **11**: p. 1117.

420. Cassetta, L., et al., Mouse Classical and Non-Classical Monocytes Express Comparable Levels of Chemokine Receptor CX3CR1. bioRxiv, 2020.